Carbon nanotubes: synthesis and functionalization.

Robert Andrews

Degree of Doctor of Philosophy

The University of Edinburgh

2006

Abstract

This thesis focuses on two of the major challenges of carbon nanotube (CNT) research: understanding the growth mechanism of nanotubes by chemical vapour deposition (CVD) and the positioning of nanotubes on surfaces.

The mechanism of growth of single–walled nanotubes (SWNTs) has been studied in two ways. Firstly, a novel iron nanoparticle catalyst for the production of single–walled nanotubes was developed. CVD conditions were established that produced high quality tubes. These optimised CVD conditions were then used as the basis of several comparative CVD experiments showing that the quality of nanotubes and the yield of carbon depended on the availability of carbon to react. The availability could be controlled by the varying concentration of methane in the gas phase or the residence time of the methane over the catalyst. Evidence is presented that the diameters of the tubes produced were affected by the availability of methane.

A second mechanistic investigation was carried out to study the validity of the previously proposed *ring addition mechanism* for the growth of carbon nanotubes from camphor. In this mechanism, the formation of tubes is thought to occur through the addition of preformed carbon rings: so it would be expected that there would be a relationship between the molecular structure of the precursor and the resulting SWNTs. To explore this relationship, comparative CVDs were carried out to produce SWNTs with several different cyclic and acyclic compounds similar in structure to camphor. The vapour pressure and the chemical stability of the precursor were found to be important to the formation of nanotubes, while the compound's structure was not related to the quality of tubes produced. The lack of a relationship between the structure of the precursor and the production of SWNTs suggests that preformed rings are not vital to the production of SWNTs. Differences in the growth of SWNT from benzene and methane were related to the stability of each compound. In particular, differences in the distributions of the diameters of the tubes formed from methane and benzene have been observed. These differences have been explained in

terms of the relative kinetic stabilities of these molecules, and in terms of a competition between end–cap and sidewall growth.

Positioning of nanotubes on surfaces has been explored using two approaches. In the first approach, commercially obtained SWNTs were functionalized by a sulfur plasma so that the products would form bonds with gold surfaces. The nanotubes were found to selectively deposit themselves onto gold surfaces from ethanolic dispersions of the functionalized samples. This selective deposition of the nanotubes allowed the production of prototype carbon nanotube field–effect transistors with higher device yields than were obtained with unfunctionalized tubes.

In a second approach to positioning of carbon nanotubes, the growth of tubes on surfaces by CVD was explored. Iron nitrate and different magnesium compounds were dip–coated onto SiO_2 surfaces so that MgO supported–Fe catalysts would be formed by calcination. SWNTs were grown on the surfaces by CVD. Surface area measurements of the equivalent powdered catalysts showed that a high surface area was vital to produce dense growth of high quality SWNTs. The morphology of the surface was also found to play a key role in the growth of the tubes. Patterned growth of carbon nanotubes was accomplished using soft lithography techniques to control the localization of catalyst deposition onto a surface. A long calcination step (10 h, 950 °C) before CVD, was found to improve the quality of nanotubes grown. Catalysts that had been calcined for 10 hours were also found to produce smaller diameter nanotubes than uncalcined samples. The formation of smaller diameter tubes was explained in terms of the formation of $MgFe_2O_4$ alloys, consistent with results reported previously in the literature. In addition, Raman spectroscopy of the calcined catalysts with 3% w/w loadings of Fe was used to confirm directly the presence of $MgFe_2O_4$.

Declaration

I declare that all the work in this thesis is my own unless stated by reference.

Robert Jonathan Andrews

Signed

Date

Acknowledgements

I would to thank my supervisor, Dr. Andrew Alexander, for all his advice and help throughout the years. Thanks also to the rest of the group, Gavin Forrest, especially for help with figures and excel spreadsheets. Also thanks are owed to all the project students and visitors: Catriona (Katy then, now Cate) Smith, Mary Finnegan, J. Edward Forbes. and the rest.

Thanks Iris Coe for giving me her old PDMS stamps and advice on Contact printing. Thanks also to Hugh Vass and Jason Crain for collecting Raman spectra for me. For assistance with TEM John Findlay and Chris Jeffree should be thanked. For training me and helping me use the SEM, Nicola Cayzer, Paula McDade and John Craven thanks to you all (especially for the tea and biscuits – and the ducks). A large debt of gratitude to Dr. Ronald Brown (Uncle Ron) for help with running isotherms and XPS samples but also help with the TGA set-up.

I would like to show my gratitude to Dr. Rebecca Cheung, Dr. Natalie Plank and all the rest at the SMC, for all their help with microfabrication and the imaging.

Natalie deserves special thanks for being such a good friend and collaborator even though she did seem to always leave her wallet in the office at teatime.

Of course, there are lots of people I'd like to thank for letting me ignore them for most of four years such as my family: Mum, Dad, (Misty), Matthew, Marianne and Jane. Old friends that need to be thanked are Ali and Jenny (my favourite almost married couple), Dr. Richard Alexander, Kathryn, Emma, Rita Sa, Rita, Fi and all the rest. Also thanks to Dr. Black's family Keisha, Jim and all the rest.

Thanks to the interests outside research, Les Escogriffes, especially Véro for all her support and help. Rudsambee for making me sing again. Thanks especially to Chris, Ollie and Jenny (& family).

Thanks to Paul, Liz, Colin and Lesley for all the help and fun with the Chemical Connection

At work, I'd really like to thank Trish, Kat (and Duncan), Gaynor, Marica, Stuart, Eve, Elin, Lorna, David Peggy (not so crazy Dave), Dave Sanders, Dave Gibson, Emmelyn, Alice, Ian, Dilek and all the rest of the people I've shared an office or some tea.

Biggest thanks and affection to Dr. Black, who has been wonderful throughout this time. All my love, I am very lucky.

Glossary

AFM	Atomic force microscopy
BE	Binding energy
C_h	Chiral vector
CNT	Carbon nanotube
CVD	Chemical vapour deposition
D	Debye
DCC	Dicyclohexylcabodiimide
E_g	Band gap energy
eV	Electron volt
FET	Field effect transistor
HiPco	High pressure carbon monoxide
HREELS	High resolution electron energy loss spectroscopy
I_D / I_G	Ratio of intensities of D and G bands
IPA	Isopropanol
IR	Infra-red
KE	Kinetic energy
MWNT	Multi-walled nanotube
OES	Optical emission spectroscopy
p	(Vapour) Pressure
PDMS	Poly(dimethylsiloxane)
PTFE	Polytetrafluoroethylene
R	Universal gas constant
RBM	Radial breathing mode
sccm	Standard cubic centimetres per minute
SEM	Scanning electron microscopy
SWNT	Single-walled carbon nanotube
T	Temperature
T_b	Boiling point
TEM	Transmission electron microscopy
TGA	Thermogravimetric analysis
XPS	X-ray photoelectron spectroscopy

γ_0	Tight binding overlap energy
ΔH_{vap}	Enthalpy of vaporization
φ	Work-function
$\omega+$	High frequency contribution to the G band
$\omega-$	Low frequency contribution to the G band
ω_{RBM}	Wavenumber of radial breathing mode

Table of contents

1 Introduction to carbon nanotubes

1.1 Discovery of carbon nanotubes

Research into carbon fibres has been carried out for over a century. One of the first fibres prepared was used by Edison to improve the incandescent lamp.[1] The discovery of carbon nanotubes is widely thought to have occurred in 1991. In that year, a paper by Sumio Iijima was published in the journal Nature, detailing the discovery of a new form of the carbon needle with concentric layers of carbon.[2] Many articles cite Iijima's paper as being the "discovery" of carbon nanotubes. Although the importance of this Nature paper should not be belittled, there is plenty of evidence to say that carbon nanotubes had been reported before the Iijima paper.[1,3] Indeed, a recent editorial in the journal Carbon has suggested that the first report of nanoscale carbon fibres with hollow internal cavities, which the editors equate with carbon nanotubes, was in 1952.[4] The editorial goes on to point out that the structure of concentric layers of carbon that are characteristic for multi–walled nanotubes (MWNTs) was observed in 1958. Indeed the company Hyperion Catalysis International, Inc. (Cambridge, MA) began producing MWNTs since the early eighties as additives for polymers to improve the polymer conductivity.[5]

Although carbon nanotubes may have been prepared and characterised before 1991, it does not seem that their structure and interesting properties were understood. The real break–through that Iijima made in his 1991 paper was relating carbon nanotubes to fullerenes. The discovery of fullerenes[6] had encouraged many researchers to study the properties of closed–cage carbon structures (Figure 1.1).[2] Indeed, there were some theoretical investigations that described the properties of extended fullerene–like molecules, which were carried out before Iijima's work.[1,4,6-9] Without the discovery of fullerenes, the amazing properties and structures of nanotubes may never have been explored.

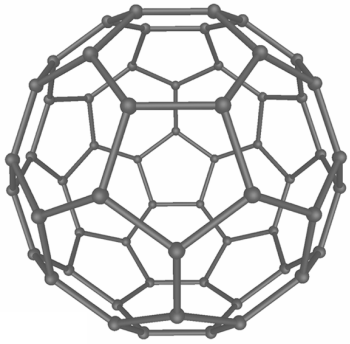

Figure 1.1. Structure of the buckminsterfullerene (C_{60}).[10] The discovery of C_{60} and the other fullerenes created interest in all–carbon molecules. This interest allowed the structure of nanotubes to be understood.

1.2 Scope of this introduction

The introductory chapter to this thesis cannot cover the entire the field of carbon nanotubes research. Since carbon nanotubes caught the imagination of scientists and engineers in the early 1990s, there has been an *incredible* volume of research carried out. Searching the Thomson ISI Web of Knowledge database for articles with the topic "carbon nanotube*" (the asterisk allowing for the plural) yields the over 21,000 references.[11] Analyzing these references by publication year, we can see that there is an exponential growth in number with time as is shown in Figure 1.2. In fact, the total number of references that have been published in the years 2003 – 2006 is over 14,000. So, since the research for this thesis started in 2002, the number of research papers has increased by more than 200%.

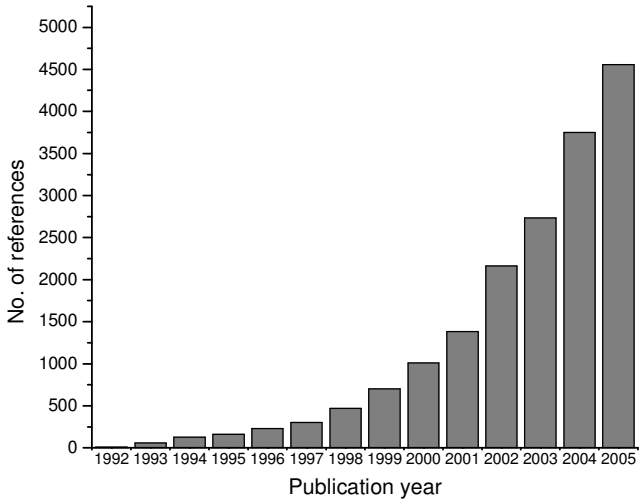

Figure 1.2. The number of references returned for a search for "carbon nanotube*" analyzed by publication year. It is clear that there is a great interest in carbon nanotubes that has been growing over the passed few years.

The intention of this introduction is not to exhaustively examine all the work that has been done on carbon nanotubes. Instead, the topic of nanotubes is introduced in the context of the research to be presented. The research has been mainly focussed on growth of carbon nanotubes: therefore, in Section 1.5 the synthesis of carbon nanotubes is discussed. In Sections 1.5.3 and 1.5.4, chemical vapour deposition is explored in more detail, as it was the method used to produce tubes in this work. In Section 1.3 we talk about the structure of the tubes. Section 1.4 discusses the properties and the applications that carbon nanotubes may be suited. A brief introduction to functionalization is given in Section 1.6. A more detailed discussion of the common characterization techniques is deferred to Chapter 2, although we shall make references to such techniques throughout this Introduction.

1.3 Structure of carbon nanotubes

Carbons atoms form strong bonds to each other, and the variety of hybridization that the atom can adopt (sp, sp^2, sp^3) allows there to be many different forms of all–carbon materials.[12,13] The two well known allotropes of carbon are diamond and

grapthite. Their structures are shown in Figure 1.3. Graphite is made up of flat, extended sheets of carbon atoms. Each of the carbon atoms is sp^2 hybridized, and the σ–bonding using the sp^2 orbitals between neighbouring carbon atoms makes a network of hexagons. The p orbitals on the carbon atoms form an extended π system that allows graphite to conduct. This is in contrast to the other well known allotrope, diamond, where the carbon atoms are all sp^3 hybridized and bonded to four other carbon atoms in a tetrahedral arrangement.

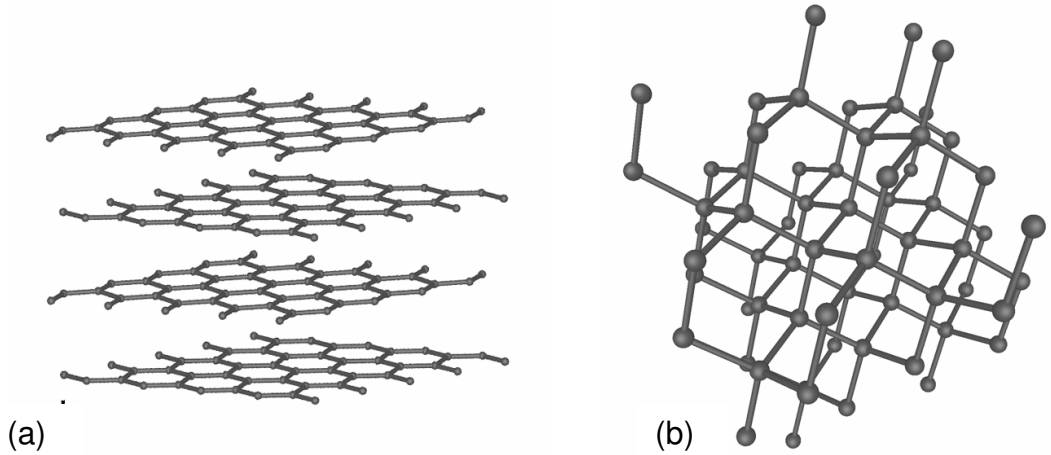

Figure 1.3. The structures of graphite (a) and diamond (b).[10] Graphite is made up of many extended flat sheets of carbon atoms. Each carbon atom in graphite is directly bonded to three others (except at edges of sheets). Each of the carbon atoms also has a p orbital: these combine to form a extended π system above and below each sheet of atoms. The carbon atoms in diamond are all sp^3 hybridized and are bonded covalently to four other atoms. This arrangement of bonding produces a three dimensional network.

The structure of carbon nanotubes is closely related to graphite. A single, finite sheet of atoms from graphite is known as graphene. A carbon nanotube can be simply thought of as sheet of graphene that has been rolled up to form a seamless cylinder with a hollow core as shown in Figure 1.4 .[14] The ends of the tubes can either be open, or capped with a fullerene–like (hemispherical shaped) structure. Indeed, nanotubes are sometimes described as extended fullerenes.

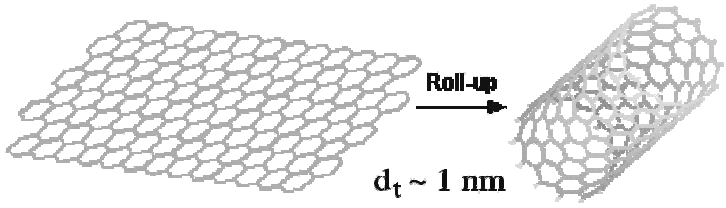

Figure 1.4. Rolling–up of graphite sheet to form a carbon nanotube.[15]

There are two major classes of carbon nanotubes: single–walled and multi–walled tubes. As shown in Figure 1.5, a single graphitic sheet rolled–up would give a single–walled nanotube (SWNT), while several sheets that are rolled–up around a common axis would give a multi–walled nanotube (MWNT). A nanoparticle can be defined as an object that is less than 100 nm in any of its dimensions. Although there are no hard rules about the diameters of SWNTs and MWNTs, it is usually found that SWNTs are less than 2 nm in diameter. Due to the large cooperative van der Waals forces and π–stacking, SWNTs have a tendency to form ropes, or bundles of tubes.[16] The electrons in the π system allow nanotubes to conduct, and make them very polarizable. For example, the induced dipole moment for a SWNT that is 10 μm in length, in a 1 V μm^{-1} electric field, has been estimated at about 10^6 D.[14] MWNTs can be much wider but are usually less than 100 nm in diameter.[3]

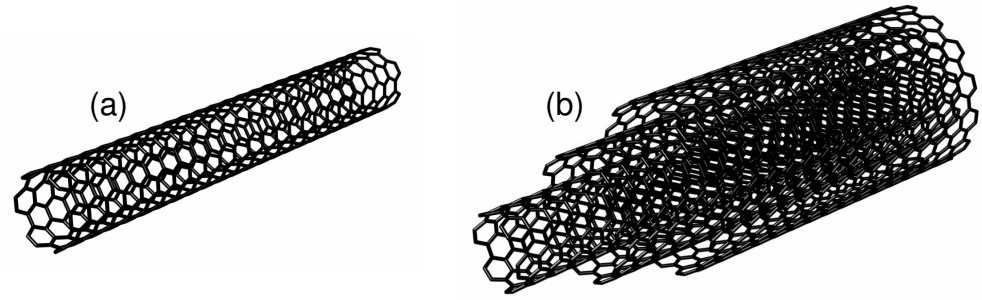

Figure 1.5. Structures of idealized single–walled (a), and multi–walled (b) nanotubes.

Nanotubes form as many different structures as there are many different ways that a graphene sheet can be rolled up to form a nanotube. The chiral vector, or Hamada vector, ($\mathbf{C}_h$) of a tube is used to describe its particular structure. As shown in Figure 1.6, the chiral vector can be thought of as describing the circumference of the tube in terms of the graphite lattice vectors ($\mathbf{a}_1$ and $\mathbf{a}_2$).[17]

$$\mathbf{C}_h = (n\mathbf{a}_1 + m\mathbf{a}_2) \quad (1.1)$$

This describes how to travel from a point on the surface of a tube around the circumference and back to the original point. Usually the chiral vector is reported in the shorter form of (n,m) values where n and m are the integer coefficient of the lattice vectors. By convention, chiral vectors are reported so that n > m. The vector **T** defines the translational symmetry along the tube surface and is parallel to the tubes axis. The rectangle with $\mathbf{C}_h$ and **T** as edges, is the unit cell of the tube. The chiral vector is related to the diameter of a tube (d_t) by

$$d_t = C_h/\pi = \sqrt{3}a_{c-c}(n^2+nm+m^2)^{1/2}/\pi \quad (1.2)$$

where a_{c-c} is the nearest neighbour C–C distance, which is usually to be assumed to be the same as in graphite (1.421 Å),[17] and C_h is the length of the chiral vector $\mathbf{C}_h$. The structure of a tube is sometimes simply known as its chirality.

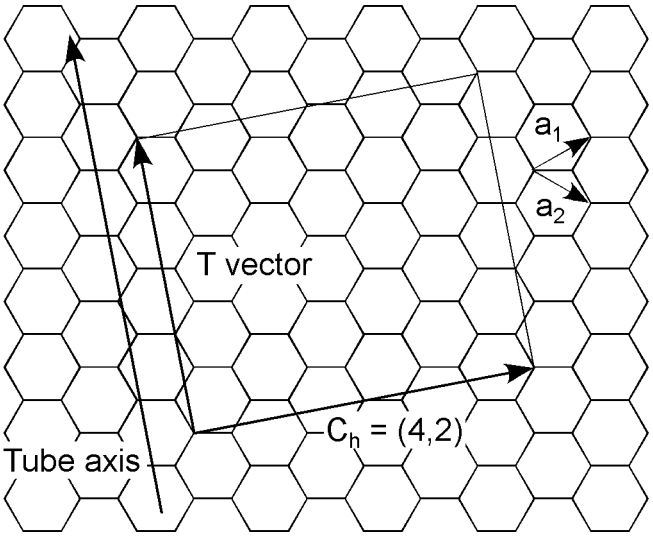

Figure 1.6. The chiral vector (C_h) of a (4,2) carbon nanotube. The chiral vector defines the circumference of the tube in terms of the lattice vectors of graphite (a_1 and a_2). The vector T defines the translational symmetry along the surface of the tube parallel to the tube axis. The rectangle defined by these two vectors is the unit cell of the nanotube.

The reason behind the term "chiral" vector is due to the fact that in some tubes there is no plane of symmetry that includes the axis of the tube, and the tubes have a handedness. The carbon atoms of the tube can be thought of as making helices of carbon around the axis of the tube. The chirality of a tube is sometimes known as the tube's helicity. The absolute configuration (*i.e.*, the enantiomer) of a tube is not usually considered. Some chiral vectors define achiral tubes that have been

categorized into two groups.[17] Achiral tubes with vectors having values (n,n) are termed armchair tubes, while those with vectors equal to (n,0) are called zigzag tubes. All other tubes, with $n \neq m$ and $m \neq 0$, are known as chiral tubes. Examples of the way that a sheet of graphite can be rolled up to give different tubes are illustrated in Figure 1.7.

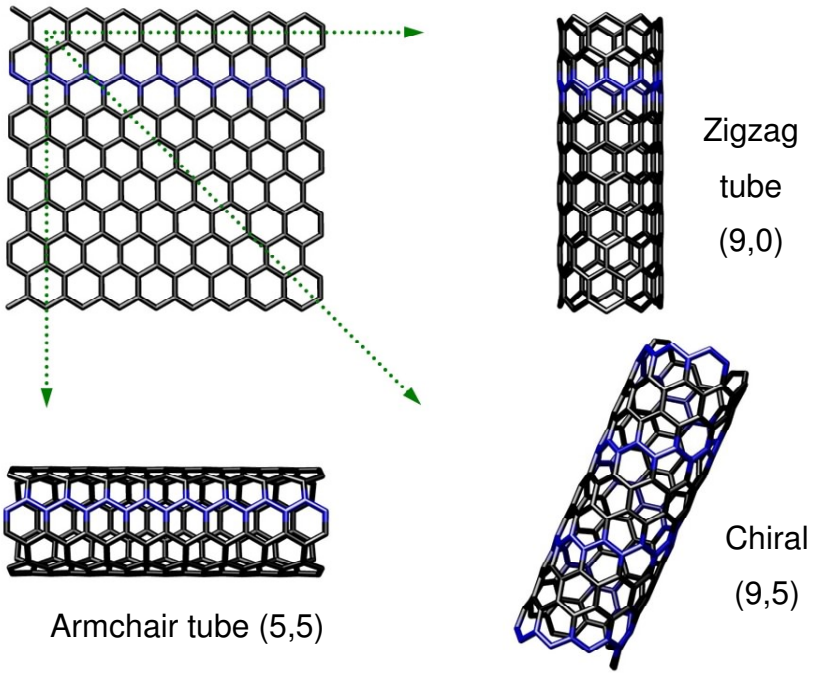

Figure 1.7. Different tubes are constructed by rolling a graphene sheet in different ways.[18] The armchair and the zigzag tubes have planes of symmetry that include the tube axis, while chiral tubes do not.

In addition to the way that the hexagons tessellate on the surface of the tubes, the structure of the tube is unique in other ways. Single–walled nanotubes can be grown centimetres in length.[19] As they have diameters of around 1 nm, they can possess incredibly large aspect ratios. The small diameters of nanotubes and their large aspect ratios have made carbon nanotubes interesting to many scientists as they are quasi–one dimensional systems.[14] Nanotubes have used as model system to investigate the quantum phenomena of 1–D solids.[14]

1.4 Properties and uses of carbon nanotubes

Although carbon nanotubes are fundamentally interesting to scientists due to their low–dimensional nature, it is undoubtedly their properties, and their potential uses, that have driven the great amount of research in this area. One of the most striking features of carbon nanotubes is electrical properties. As a result of the 1–D nature of carbon nanotubes, electrons can be conducted in nanotubes without being scattered. The mean free path of the electron in a nanotube can be longer than the distance that the electron is being transported. The absence of scattering of the electrons during conduction is known as ballistic transport and allows the nanotube to conduct without dissipating energy as heat.[20] Carbon nanotubes have been shown to carry current densities up to 10^9 A cm^{-2}.[20] For comparison, copper is estimated to be able to only carry around 10^6 A cm^{-2}.[20]As noted above, the company Hyperion Catalysis International, Inc. already uses carbon nanotubes to produce plastics that are conducting.[5] These plastics are used in applications where the build–up of static electricity is a problem, such as car parts that are to be spray–painted, or containers for electrical components that may be damaged by an electric discharge.

An interesting aspect of carbon nanotubes is the fact that their structure (their chirality) is intimately linked to their electrical properties. The electrical properties of a tube can be determined from the chiral vector.[1] If (n – m) = 3q where q is an integer, then the tube is metallic, otherwise the tube is semiconducting. For a sample of tubes, it would be expected that around a third of the tubes would be metallic. As the chiral vector of an armchair tube is (n,n), all armchair tubes are metallic. The band gap (E_g) of semiconducting tubes has been seen to be inversely proportional to the diameter of the tube.[1] The band–gap energy decreases as the tubes increase in diameter, as they start resemble graphite, which is a zero band–gap material (semi–metal).

Due to their small diameters and unique electrical properties, there has been much interest in using nanotubes as electronic devices.[21,22] It is hoped that it will be possible to produce electronic devices such as transistors that will consume less energy and produce less heat. The most popular design of nanotube transistors is the

field effect transistor (FET). A diagram of a typical nanotube device is shown in Figure 1.8: this type of device will be discussed more in Chapter 5 of this thesis. In Figure 1.9, there is a false–colour image of an actual individual SWNT nanotube device obtained using atom force microscopy.[22] In this sort of device, the current between the source and the drain electrode is changed by applying an electric field, supplied at a gate electrode, to vary the amount of charge carriers able to carry the current.[23]

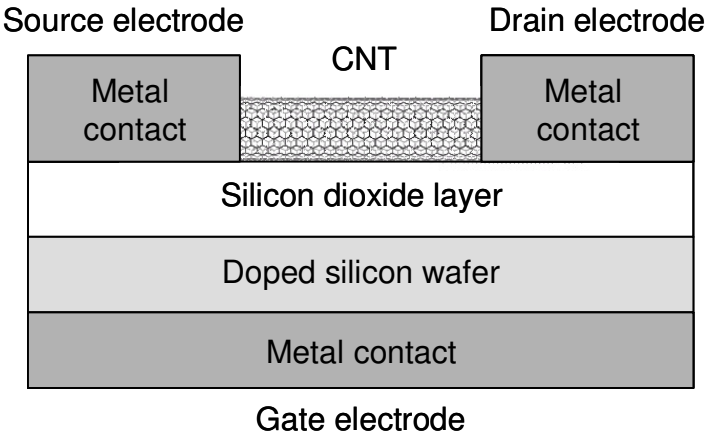

Figure 1.8. Diagram of a nanotube field effect transistor (FET). The current between the source and drain electrodes is controlled by applying an electric field at the gate electrode, which changes the number of charge carriers able to conduct from the source to the drain electrodes.

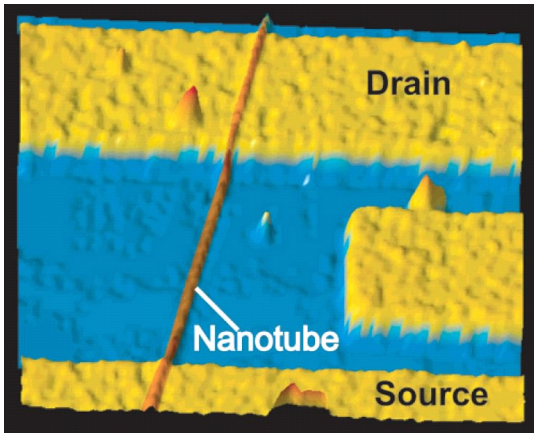

Figure 1.9. Atomic force microscope image of an individual SWNT making up a FET.[22]

The use of carbon nanotubes in electronics still faces many obstacles. Carbon nanotubes are difficult to position, and it is difficult to make reliable contacts with other materials.[14] As FETs can only be made with semiconducting tubes,[23] another

difficulty is in trying to produce nanotube materials that contain only semiconducting tubes. Currently, it is difficult to separate tubes by their electrical characteristics,[24] and it is not possible to control the growth of tubes to produce semiconducting tubes preferentially.[25,36]

Due to their high conductivity and small diameters, carbon nanotubes have good electron–emission properties.[27] If a nanotube is tethered to a cathode, its small diameter and large aspect ratio will generate large electric fields at the tip of the tube, so that electrons will be easily emitted.[28] It is hoped that carbon nanotube field–emission guns will find uses in such applications such a flat panel displays.[5]

As well as being good conductors of electricity, nanotubes have very high thermal conductivity. The thermal conductivity of a single tube has been measured as 6600 W m^{-1} K^{-1} at room temperature.[29] For comparison, diamond, which is one of the best thermal conductors due to its network structure and strong bonds,[29] has a thermal conductivity of 1000 W m^{-1} K^{-1} at 0°C.[30] Figure 1.10 shows that bundles of tubes show a greater thermal conductivity parallel, rather than perpendicular, to the axis of the tubes.[31]

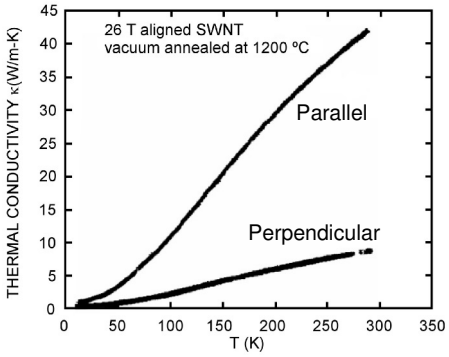

Figure 1.10. Thermal conductivity of a magnetically aligned mat of carbon nanotubes.[31] The thermal conductivity of the mat is much larger parallel to the tube axes than perpendicular. Transport of heat occurs faster along tubes than transfer between them.[25]

The mechanical properties of carbon nanotubes have also attracted great interest. Many carbon materials, such as diamond and carbon fibres, are known to be very strong due to the strong covalent bonds that contribute to their structure. The mechanical properties of a material are often measured by applying a force (F) over

an area (A) and then measuring the amount that the material extends. The data is usually plotted as a stress (F/A) against strain (dx/x) where x is the original length of the material and dx is the change. Stress–strain plots are usually linear with small strains[32]. The gradient of the linear portion is called the Young's modulus and is a commonly used measure of strength of a material.[32] The Young's moduli of individual nanotubes have been measured using techniques such as atomic force microscopy.[3] From these measurements, a value of 1 TPa has been estimated, which is comparable to the value of 1.2 TPa for diamond. Nanotubes have also been shown to have high tensile strengths of around 45 GPa, which is the maximum stress that can be applied before the material breaks. For comparison, the tensile strength of steel varies from 0.4 – 0.76 GPa.[34]

Carbon nanotubes have low densities compared to other strong materials. This, and the fact that single–walled tubes are flexible perpendicular to the tubes axis, has fuelled interest in trying to produce new strong materials, particularly in making polymer composites.[16,5] There has been some success in using nanotubes to control a polymer's mechanical properties. It has been found that to produce the same increase in Young's Modulus and tensile strength for a polymer, a smaller quantity of nanotubes could be added compared to other carbon fibres.[35] However, many composites have actually shown worse properties compared to the pure polymer. Carbon nanotubes are difficult to disperse in polymer.[16] The bundles of nanotubes in the polymer introduce weak points because the tubes are only held together by weaker non–covalent forces.[36] In many of the composites, the strength is also not increased, as there is little adhesion between the polymer and the nanotubes. This lack of adhesion means that forces applied to the composite are not transmitted to the tubes.[16] Currently, a large part of research into polymer composites is focussed on using functionalization of tubes to make them easier to disperse in polymers, and to increase the adhesion of polymer and nanotubes by forming covalent bonds between them.[16] One of the great challenges of this approach is to find methods to functionalize the tubes in such a way that does not damage the tubes. By definition, chemical functionalization will cause some disruption to the sp^2 C network of the

tube. This may fatally disrupt the tubes so that they no longer posses the properties required.[16]

Activated carbons have found many uses due to their high surface areas. Carbon nanotubes can also have high surface area, and the internal cavities of tubes can become accessible to adsorbates if the end–caps of the tubes are removed, perhaps by oxidation. The main thrust of nanotube research for gas storage has been looking at storing hydrogen as an energy source.[37,38] One of the great hopes for carbon nanotubes was that they would provide a way to store hydrogen safely and economically for such applications as transport.[39] Unfortunately, due to the lack of reproducibility of hydrogen storage when experiments were carried out by different research groups, there now seems to be little hope that carbon nanotubes could be used in this application.[40]

There are still many challenges facing the use of nanotubes to produce new products that make use of their incredible properties. Some of these challenges lie in the processing of the tubes into a useful form. However, there is still much work to be done to understand how to control the growth process. Currently, it is difficult to grow tubes in a predetermined position[41-43] and there is no way to control the chiralities (structures) of the tubes produced.[26] It is hope that by studying the mechanism of the growth of tubes it will be possible to gain insight into ways to control the growth.

1.5 Synthesis of carbon nanotubes

There are many different ways that carbon nanotubes and nanofibres have been produced. The most common are described here. Carbon nanotube syntheses can be classed as either high–energy methods or catalytic methods.[3] The formation of nanotubes is thought to involve atomic carbon or at least small carbon molecules, like C_2.[26] The high energy methods, like arc–discharge and laser ablation, use large amounts of energy to vapourize a solid carbon source, usually graphite.[1] The catalytic methods, such as chemical vapour deposition (CVD), use metal catalysts to break down the carbon–containing precursors, typically hydrocarbons, to form the

carbon species that go on to from the carbon nanotubes.[43] In this section, we look at the common growth methods in more detail.

1.5.1 Arc discharge

Arc discharge was the method originally used by Iijima et al. to prepare nanotubes.[2] The setup and experimental conditions are similar to those used for preparation of fullerenes. The setup is shown in Figure 1.11. To produce nanotubes, a voltage is applied between two graphite electrodes that are held separated by about 1 mm in an atmosphere of inert gas such as helium at a pressure of 500 torr.[3] A voltage of 20 – 25 V is applied to the electrodes with a current of 50 – 120 A and an arc occurs between the electrodes. The carbon evaporates from the electrodes into the plasma of the discharge where the nanotubes form. The tubes collect on the cathode while the anode decreases in size. The electrodes are moved during the experiment to keep the same electrode distance. Doping of the electrode with metals such as Co, Ni, Fe, Y and Gd has produced single–walled tubes.[1] Arc discharge usually produces other carbon impurities and carbon–coated metal nanoparticles in addition to nanotubes.[3]

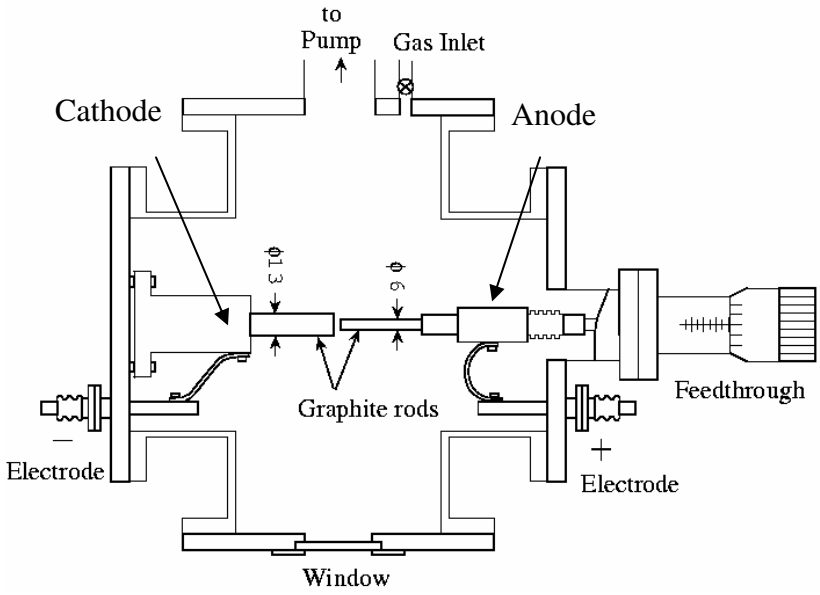

Figure 1.11. Diagram of Arc Discharge equipment to produce carbon nanotubes.[1] A voltage is applied across the electrodes that produces an arc between the carbon cathode and anode. The carbon nanotubes formed, collect on the cathode.

1.5.2 Laser ablation

Laser ablation is a more efficient method of producing tubes than arc discharge. It has been claimed that high yields with > 70 – 90 % conversion of the graphite to nanotubes are possible with the technique.[45] A diagram of the setup is shown in Figure 1.12. A laser is used to vapourize carbon from a graphite target that has been heated in a furnace to high temperature (~ 1200 ºC) in an inert gas. The flow of gas carries the nascent tubes away from the target, and the tubes collect on the walls of the setup.

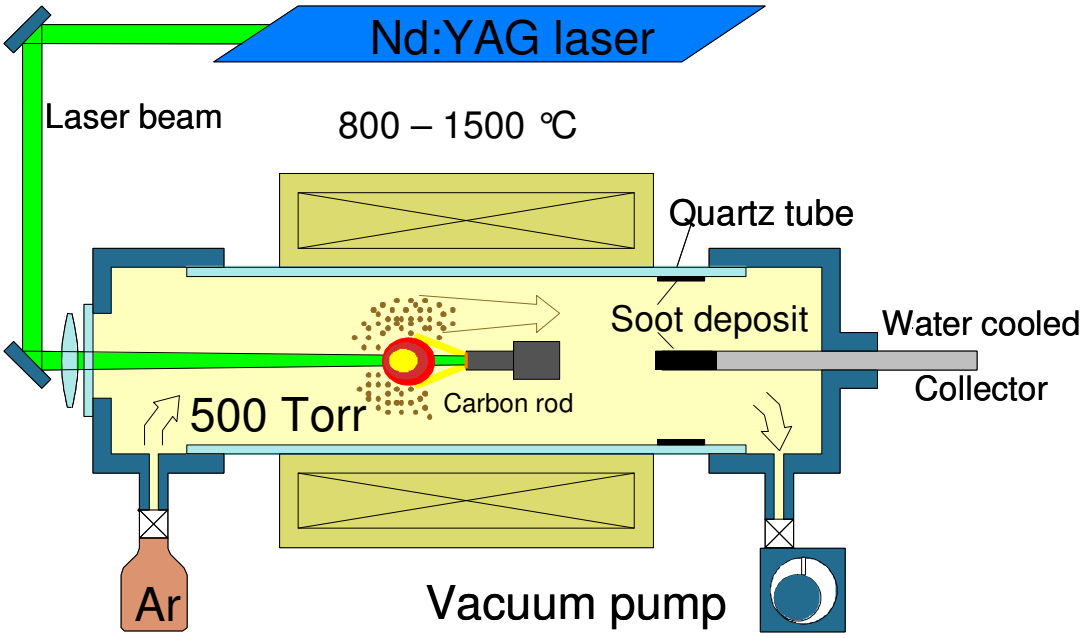

Figure 1.12. Diagram of laser ablation set–up.[15] Nanotubes are formed by vaporising carbon the surface of a graphite target with a powerful laser.

1.5.3 Chemical vapour deposition

Chemical vapour deposition (CVD) to produce carbon nanotubes has become a popular topic of research:[46] this is partly due to the simple setup required, as shown in Figure 1.9. The simplicity of CVD also suggested that it would be possible to scale it up for industrial production of tubes. Moreover, it is hoped CVD could give greater control over the growth of tubes due to the greater scope for controlling reaction conditions, such as designing catalysts.[14,46] CVD is the method of nanotube growth that is explored in this thesis.

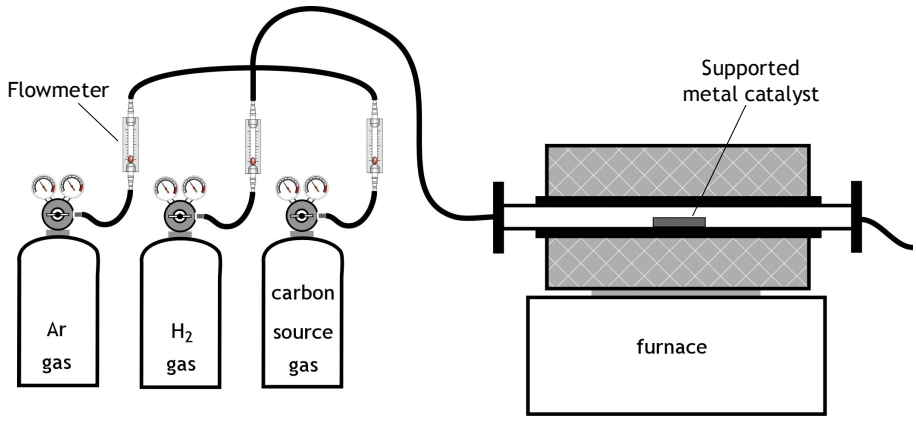

Figure 1.13. Diagram of a CVD setup.[18] The simple equipment required make CVD an attractive method to produce carbon nanotubes.

Chemical vapour deposition is a catalytic method in that it uses metal catalysts to breakdown the carbon–containing precursors to form nanotubes.[26,44,46] As such, it is sometimes referred to as catalytic chemical vapour deposition (CCVD) although more often the word "catalytic" is omitted. In a typical CVD experiment, a supported–metal catalyst (for examples, see below) is heated in a furnace to between 600 and 1000 ºC.[44] The carbon–containing precursor is then passed over the catalyst to form the tubes. The catalyst is then allowed to cool down under an inert gas to avoid etching away the nanotubes by reaction with oxygen. Many different carbon–containing molecules have been used to make carbon nanotubes.[47] For the synthesis of single–walled nanotubes, the use of small molecules, such as carbon monoxide or methane, has been found to be effective.[44] There has also been great variety in the catalyst systems that have been used.[44,46] However the most popular metals in the literature are iron, nickel, cobalt and molybdenum.[44] There has also been success in growing nanotubes using mixtures of these metals, particularly mixtures of molybdenum with one of other metals. Mostly the metal particles are supported on some metal oxide, such as silica and alumina.[46] This approach is used in this work, and different catalysts were prepared with aluminium oxide and magnesium oxide as supports.

There are several ways that powdered catalysts for CVD can be produced.[46] A common way to prepare catalysts is by ion impregnation, where the support is exposed to a solution of metal salts and then the solvent is removed.[50] There is also

interest in using pre–formed nanoparticles that could control the diameter of the nanotubes produced.[51] When CVD is used to grow tubes on surfaces,[14] the metal catalysts can be produced on the surface in several ways. Examples include applying solutions of metal salts onto the surface[52] and evaporating thin metals to form thin films to of the catalyst.[53] Pre–formed nanoparticles have also been dispersed on surfaces.[54]

Some syntheses do not use a support, and the reaction takes place with the particles suspended in the gas. This approach is sometimes known as an aerosol synthesis.[44] The most important example of this kind of synthesis is known as the high pressure carbon monoxide process (HiPco).[48] In this synthesis carbon nanotubes are formed by the disproportionation of carbon monoxide (the Boudouard reaction) with an iron catalyst at high temperature (900 – 1100 °C) and pressure (30 – 50 atm).[49] The iron catalyst is supplied as iron pentacarbonyl that decomposes to iron nanoparticles in the gas phase to form iron nanoparticles.[49] The HiPco process is used by Carbon Nanotechnologies, Inc. (CNI, Houston, TX) to produce SWNTs commercially. HiPco SWNTs purchased from CNI were used in the functionalization experiments described in Chapter 5.

One advantage that CVD has over the other synthesis methods is the possibility of growing tubes on surfaces. Catalysts can be dispersed on a surface that is then exposed to CVD so that nanotubes grow directly on the surface.[14] It is hoped that these techniques will be useful in the production of field emission devices. Perhaps, if the catalyst can be patterned, it would be possible produce electronic devices such as FETs or chemical sensors directly, without the need to purify or position the nanotubes first.[14]

1.5.4 Mechanism of nanotube growth in chemical vapour deposition

There have been many mechanisms proposed to explain the formation of carbon nanotubes.[26] Here, the focus is concentrated on the efforts to understand growth of nanotubes in CVD. A brief background will be given in this introduction, more

details are presented in Chapters 3 and 4, where the discussion deals with more intricate features of the growth mechanism.

In the most popular model of nanotube growth by CVD, the metal catalyst is in the form of nanoparticles deposited on the surface of the support.[46] The carbon precursor breaks down catalytically on the surface of a nanoparticle. The carbon produced then goes on to form the nanotube. There are two possible ways in which this can happen. In one, the carbon dissolves into the liquid–like interior of the particle until it becomes saturated and then the carbon precipitates out as a nanotube.[44,46,55] In the other, the carbon diffuses round the surface of the particle until it meets and adds itself to the edge of the growing tube.[56,57] In addition to breaking down the precursor, the nanoparticle is thought to stabilize the dangling bonds of the growing tube and act as a "template" for the forming tube. The diameters of catalyst nanoparticles have been related to the diameters of the nanotubes that grow from them.[14,46,58,59] Although the growth of several SWNTs has been seen from a single catalytic particle.[7]

Two models of the growth process are shown in Figure 1.14. Evidence of growth by such mechanisms is shown in Figure 1.15. If the nanoparticle remains attached to the surface of the support, due to some strong interaction between the two, the growth is sometimes described as *base growth*.[50] If the particle leaves the support, trailing a nascent tube behind it, the growth is termed *tip growth*. It has been asserted that base growth is more common for the formation of single–walled nanotubes as samples of such tubes have been commonly found to have complete encapsulated ends without a metal particle.[48-50]

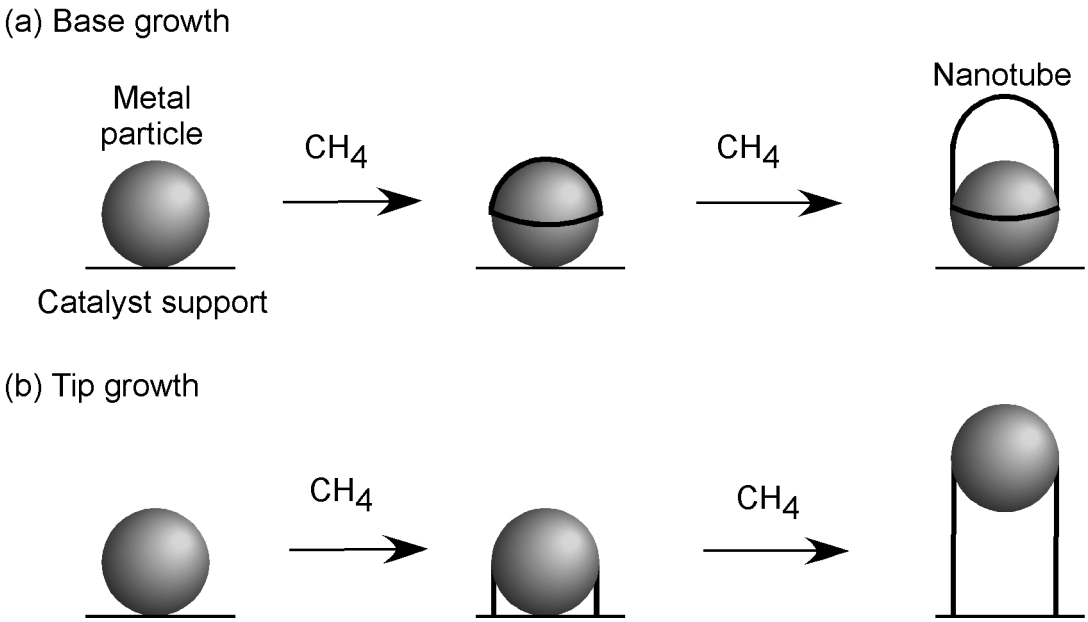

Figure 1.14. Two models of nanotube growth. In the base growth model (a), the metal nanoparticle stays attached to the support as the nanotube grows, while in the tip growth model (b) the particle is pushed from the surface as the tube grows. Methane is shown as the carbon source.

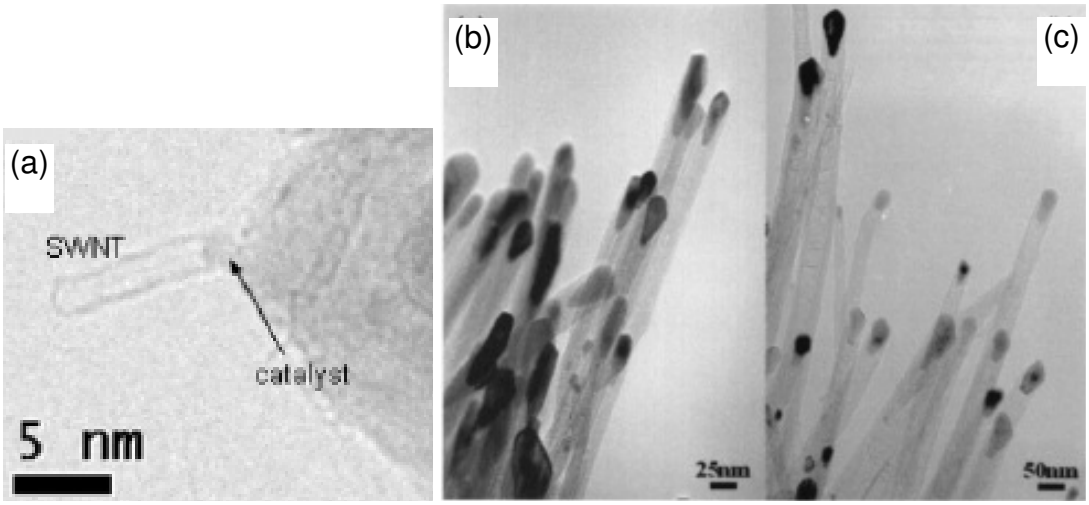

Figure 1.15. TEM images of tubes grown by base growth (a) and tip growth mechanisms (b, c).[60,61] In the base growth, seen here for a SWNT, the particle remains attached to the surface of the catalyst support . In the tip growth, shown here for MWNTs, the nanoparticle is pushed off the surface.

A different mechanism of tube growth that has been suggested will be studied in more detail later (Chapter 4). This mechanism is thought to proceed through the addition of preformed carbon rings.[62,63] This mechanism was proposed for the growth of MWNTs from benzene at fairly low CVD temperature (700 °C). It was found, by mass spectrometry, that during the growth of the MWNTs no carbon–containing fragments (e.g., C_nH_y) were produced, and only H_2 was detected.[62] Figure 1.18 shows a schematic of the mechanism proposed. The benzene is thought to adsorb onto the surface of the metal nanoparticles. Once adsorbed, the benzene rings can then react to form nanotubes through the loss of H_2.[63] The so–called *ring addition mechanism* has the interesting feature that it would appear that it should be possible to design a good precursor for carbon nanotube growth. It has been suggested that the ring addition mechanism occurs in the growth of SWNTs when camphor is used as a precursor, as will be discussed later.[63]

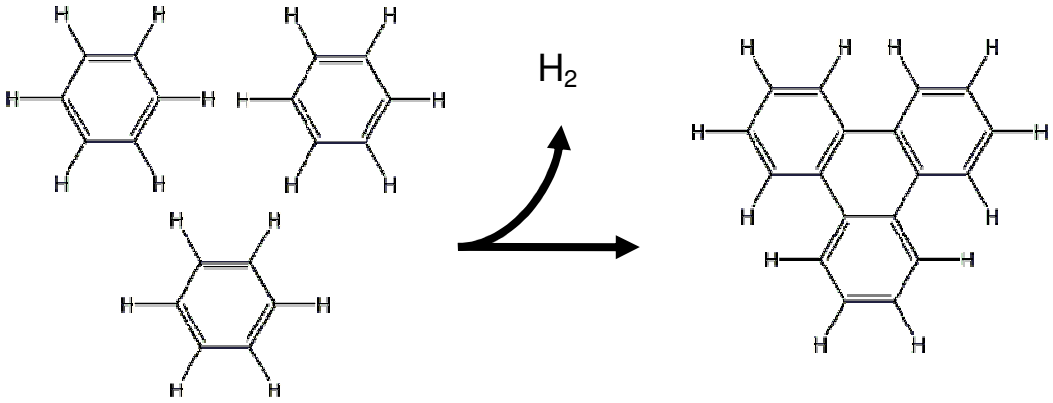

Figure 1.16. The proposed mechanism of tube growth from benzene. The benzene rings are thought to adsorb onto the surface of a metal particle where they can react to form nanotubes by the loss of H_2.

1.6 Functionalization of carbon nanotubes

A large area of interest in carbon nanotubes is functionalization. It is hoped that functionalization may allow nanotubes to be used to produce both new devices[65] and new materials.[16] For example, the solubility of carbon nanotubes has been increased through covalent functionalization. Functionalization of carbon nanotubes can be categorized in two different types.[66] In one type, reactions occur with the intrinsic structure of the tube: the sidewalls of the tube. As these sidewall of the carbon

nanotube are quite inert,[67] highly reactive intermediates are needed to attack the carbon nanotubes.[15] A good example of this approach is the direct reaction of carbon nanotubes with fluorine.[68] Stoichiometries of C_2F can be achieved, meaning that the entire length of the nanotubes can be functionalized. The second type of reaction uses carboxylic acid functional groups that are present on the tube due to defects. The number of defects on the nanotubes can be increased by oxidising the tubes.[65] The carboxylic acid groups present at the defects can be functionalised using well–known reactions to form, for example, amines and esters.[65]

In this thesis, carbon nanotubes have been functionalized with sulfur–containing groups in order to aid their positioning onto gold surfaces (Chapter 5). The use of the sulfur–gold bond to position tubes has been studied previously. One approach has been to attach thiol (–SH) containing groups through carboxylic acid groups at defects sites.[69,70] In the work of Liu *et al.*[70] carbon nanotubes were oxidised using concentrated sulphuric and nitric acids. These shortened tubes were thought to have a high concentration of carboxylic acid groups at the ends of the tubes, where the less–stable caps had been removed. The shortened tubes were then functionalized with cysteamine (C_2H_7NS) using dicyclohexylcarbodiimide as a coupling reagent: see Figure 1.17

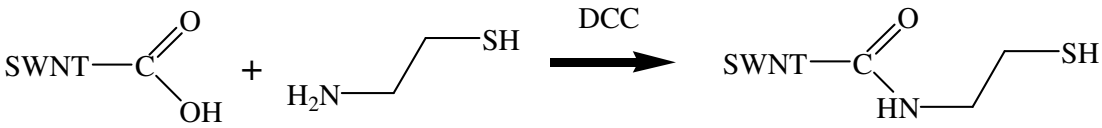

Figure 1.17. Reaction scheme of oxidation carbon nanotubes and cysteamine. The oxidation of carbon nanotubes introduces carboxylic acid groups that can be used to attach different molecules. Here an amide bond is formed using dicyclohexylcarbodiimide (DCC).

When the functionalized tubes were exposed to a gold surface it was found that they assembled themselves onto the gold so that the axis of the tube was perpendicular to the gold surface as shown in Figure 5.1 (Chapter 5). It was thought that the tubes positioned themselves in this way to maximise the sulfur–gold interaction and the van der Waals forces between the side–walls of the tubes.

1.7 References

1) R. Saito, G. Dresselhaus, M. S. Dresselhaus. Physical Properties of Carbon Nanotubes. 1998, Imperial College Press, UK.

2) S. Iijima. Helical microtubules of graphitic carbon. *Nature*, 1991, **354**, 56.

3) P. J. F. Harris. *Carbon Nanotubes and Related Structures*. 1999, Cambridge University Press.

4) M. Monthioux, V. L. Kuznetsov. Who should be given the credit for the discovery of carbon nanotubes? *Carbon*, 2006, **44**, 1621.

5) V. Jamieson. An open secret. *New Scientist* 15th March 2003, pp 30

6) H. W. Kroto, J. R. Heath, S. C. O'Brien, R. F. Curl, R. E. Smalley. C60: Buckminsterfullerene. *Nature* 1985, **318**, 162.

7) P. W. Fowler. Carbon Cylinders : A Class of Closed–shell Clusters. *J. Chem. Soc. Faraday Trans*. 1990, **86**, 2073.

8) J. W. Mintmire, B.I. Dunlap, C.T. White. Are fullerene tubules metallic? *Phys. Rev. Lett.* 1992, **68**, 631.

9) M. S. Dresselhaus, G. Dresselhaus, R. Saito. Carbon fibers based on C60 and their symmetry. *Phys. Rev. B*, 1992, **45**, 6234

10) Image courtesy of Michael Ströck.

11) Thomson ISI Web of Knowledge database. Searched was performed at 13:43 11/9/06 using search term “carbon nanotube*”.

12) F. A. Cotton, G. Wilkinson, C. A. Murillo, M. Bochmann. *Advanced Inorganic Chemistry*, (6 ed.), 1999, John Wiley & Sons, Inc.

13) N. N. Greenwood, A. Earnshaw. *Chemistry of the Elements* (2 Ed.), 1998 Butterworth Heinemann.

14) H. Dai. Carbon Nanotubes: Synthesis, Integration, and Properties. *Acc. Chem. Res.* 2002, **35**, 1035.

15) Image courtesy of M. S.Dresselhaus.

16) C. A. Dyke, J. M. Tour. Covalent Functionalization of Single–Walled Carbon Nanotubes for Materials Applications. *J. Phys. Chem. A,* 2004, **108**, 11151.

17) M. S. Dresselhaus, G. Dresselhaus, R. Saito, A. Jorio. Raman spectroscopy of carbon nanotubes. *Physics Reports*, 2005, **409**, 47.

18) Image courtesy of G. A. Forrest.

19) S. Huang, X. Cai, J. Liu. Growth of Millimeter–Long and Horizontally Aligned Single–Walled Carbon Nanotubes on Flat Substrates. *J. Am. Chem. Soc.* 2003, **125**, 5636.

20) S. Frank, P. Poncharal, Z.L. Wang, W.A. de Heer. Carbon Nanotube Quantum Resistors. *Science* 1998, **280**, 1744.

21) M. Ouyang, J.–L. Huang, C. M. Lieber. Fundamental Electronic Properties and Applications of Single–Walled Carbon Nanotubes *Acc. Chem. Res*. 2002, **35**, 1018.

22) Ph. Avouris. Molecular Electronics with Carbon Nanotubes *Acc. Chem. Res.* 2002, **35**, 1026.

23) Ph. Avouris, J. Chen. Nanotube electronics and optoelectronics. *Mater. Today*, 2006, **9(10)**, 46.

24) R. Krupke, F. Hennrich. Separation Techniques for Carbon Nanotubes. *Advanced Engineering Materials* 2005, **7**, 111.

25) F Beuneu. Solid State Communications Nucleation and growth of single wall carbon nanotubes. *Solid State Comm.,* 2005, **136**, 62.

26) R. B. Little. Mechanistic Aspects of Carbon Nanotube Nucleation. *J. Cluster Sci.,* 2003, **14**, 135.

27) A. G. Rinzler, J. H. Hafner, P. Nikolaev, L. Lou, S. G. Kim, D. Tomanek, P. Nordlander, D. T. Colbert, R. E. Smalley Unraveling Nanotubes: Field Emission from an Atomic Wire. *Science,* 1995, **269**, 1550.

28) N. S. Xua, S. E. Huq. Novel cold cathode materials and applications. *Materials Science and Engineering R,* 2005, 48, 47.

29) S. Berber, Y.-K. Kwon, D. Tománek. Unusually High Thermal Conductivity of Carbon Nanotubes. *Phys. Rev. Lett*., 2000, **84**, 4613.

30) D. R. Linde (ed). Thermal Concductivity of Crystalline Dielectrics. In: *Handbook of Chemistry and Physics*. Boca Raton CRC Press, 2006, 12–201.

31) J. E. Fischer, W. Zhou, J. Vavro, M. C. Llaguno, C. Guthy, R. Haggenmueller, M. J. Casavant, D. E. Walters, R. E. Smalley. Magnetically aligned single wall carbon nanotube films: Preferred orientation and anisotropic transport properties. *J.Appl. Phys.*, 2003, **93**, 2157.

32) J. M. G. Cowie. *Polymers: Chemistry and Physics of Modern Materials* (2ed.), 1991, Stanley Thornes (Publishers) Ltd.

33) M.-F. Yu, B. S. Files, S. Arepalli, R. S. Ruoff. Tensile Loading of Ropes of Single Wall Carbon Nanotubes and their Mechanical Properties. *Phys. Rev. Lett*., 2000, **84**, 5552.

34) D. A. Walters, L. M. Ericson, M. J. Casavant, J. Liu, D.T. Colbert, K.A. Smith, R.E. Smalley. Elastic strain of freely suspended single–wall carbon nanotube ropes. *Appl. Phys. Lett.,* 1999, **74**, 3803.

35) D. Qian, E. C. Dickey, R. Andrews, T. Rantell. Load transfer and deformation mechanisms in carbon nanotube–polystyrene composites *Appl. Phys. Lett.*, 2000, **76**, 2868.

36) O. Lourie, H. D. Wagner. Transmission electron microscopy observations of fracture of single–wall carbon nanotubes under axial tension. *Appl. Phys. Lett.*, 1998, **73**, 3527.

37) G. Q. Ning, F. Wei, G. H. Luo, Q. X. Wang, Y. L. Wu, H. Yu, Hydrogen storage in multi–wall carbon nanotubes using samples up to 85 g *Appl. Phys. A*, 2004, **78**, 955.

38) A. C. Dillon, K. M. Jones, T. A. Bekkedahl, C. H. Kiang, D. S. Bethune, M. J. Heben. Storage of hydrogen in single–walled carbon nanotubes. *Nature*, 1997, **386**, 377.

39) H.-M. Cheng, Q.-H. Yang, C. Liu. Hydrogen storage in carbon nanotubes. *Carbon*, 2001, **39,** 1447.

40) H.-M. Cheng, Q.-H. Yang, C. Liu. Hydrogen storage in carbon nanotubes. *Carbon*, 2001, **39,** 1447.

41) C. Zhou, J. Kong, H. Dai. Electrical measurements of individual semiconducting single–walled carbon nanotubes of various diameters. *Appl. Phys. Lett.,* 2000, **76**, 1597.

42) S. Fan, M. G. Chapline, N. R. Franklin, T. W. Tombler, A. M. Cassell, H. Dai. Self–Oriented Regular Arrays of Carbon Nanotubes and Their Field Emission Properties. *Science,* 1999, **283**, 512.

43) A. M. Cassell, N. R. Franklin, T. W. Tombler, E. M. Chan, J. Han, H. Dai. Directed growth of free–standing single–walled carbon nanotubes. *J. Am. Chem. Soc*., 1999, **121**, 7975.

44) A. Moisala, A. G. Nasibulin, E. I. Kauppinen. The role of metal nanoparticles in the catalytic production of single–walled carbon nanotubes — a review. *J Phys: Condens. Matter*, 2003, **15**, s3011.

45) A. Thess, R. Lee, P. Nikolaev, H. Dai, P. Petit, J. Robert, C. Xu, Y. H. Lee, S. G. Kim, A. G. Rinzler, D. T. Colbert, G. E. Scuseria, D. Tománek, J. E. Fischer, R. E. Smalley. Crystalline Ropes of Metallic Carbon Nanotubes. *Science*, 1996, **273**, 483.

46) A.-C. Depuis. The catalyst in the CCVD of carbon nanotubes—a review. *Prog. Mater. Sc.i*, 2005, **50**, 929

47) Q. Li, H. Yan, J. Zhang, J. Liu. Effect of hydrocarbons precursors on the formation of carbon nanotubes in chemical vapor deposition. *Carbon,* 2004, **42**, 829.

48) A. M. Cassell, J. A. Raymakers, J. Kong, H. Dai. Large scale CVD synthesis of single–walled carbon nanotubes. *J. Phys. Chem. B,* 1999, **103**, 6484.

49) H. Ago, S. Imamura, T Okazaki, T. Saito, M. Yumura, M. Tsuji. CVD growth of single–walled carbon nanotubes with narrow diameter distribution over Fe/MgO catalyst and their fluorescence spectroscopy. *J. Phys. Chem., B* 2005, **109**, 10035.

50) H. Kind, J.-M. Bonard, L. Forro, K. Kern. Printing Gel–like Catalysts for the Directed Growth of Multiwall Carbon Nanotubes. *Langmuir*, 2000, 16, 6877.

51) D. N. Futaba, K. Hata, T. Yamada, K. Mizuno, M. Yumura, S. Iijima. Kinetics of Water–Assisted Single–Walled Carbon Nanotube Synthesis Revealed by a Time–Evolution Analysis. *Phys. Rev. Lett.*, 2005, **95**, 056104.

52) Y. Zhang, Y. Li, W Kim, D Wang, H Dai. Imaging as–grown single–walled carbon nanotubes originated from isolated catalytic nanoparticles. *Appl. Phys. A,* 2002, **74**, 325

53) P. Nikolaev, M. J. Bronikowski, R. K. Bradley, F. Rohmund, D. T. Colbert, K. A. Smith, R. E. Smalley. *Chem. Phys. Lett.*, 1999, **313**, 91.

54) M. J. Bronikowski, P. A. Willis, D. T. Colbert, K. A. Smith, R. E. Smalley. Gas–phase production of carbon single–walled nanotubes from carbon monoxide via the HiPco process: A parametric study. *J. Vac. Sci. Tech. A*, 2001, **19**, 1800.

55) R. T. K. Baker, M. A. Barber, R. J. Waite, P.S. Harris, F.S. Feates, *J. Catal.*, 1972, **26**, 51.

56) V. Vinceguerra, F. Buonocore, G. Panzera, L. Occhipinti, N*anotech.*, 2003, **14**, 655.

57) S. Maruyama, R Kojima, Y Miyauchi, S Chiashi, M Kohno. Low temperature synthesis of high–purity single–walled carbon nanotubes from alcohol. *Chem. Phys. Lett.,* 2002, **360**, 229.

58) C. L. Cheung, A. Kurtz, H. Park, C. M. Lieber. Diameter–Controlled Synthesis of Carbon Nanotubes. *J. Phys. Chem. B,* 2002, **106,** 2429.

59) Y. Zhang, Y. Li, W Kim, D Wang, H Dai. Imaging as–grown single–walled carbon nanotubes originated from isolated catalytic nanoparticles. *Appl. Phys. A,* 2002, **74**, 325.

60) M. Lin, J. Pei, Y. Tan, C. Boothroyd, K. P. Loh, E. S. Tok, Y.-L. Foo. Direct Observation of Single–Walled Carbon Nanotube Growth at the Atomistic Scale. *Nano. Lett.*, 2006, **6**, 449.

61) C. Ducati, I. Alexandrou, M. Chhowalla, J. Robertson, G. A. Amaratunga. The role of the catalytic particle in the growth of carbon nanotubes by plasma enhanced chemical vapor deposition. *J. Appl. Phys.*, 2004, **95**, 6387.

62) Y. Tian, Z. Hu, Y. Yang, X. Wang, X. Chen, H. Xu. In situ TA–MS study of the six–membered–ring–based growth of carbon nanotubes with benzene precursor. *J Am. Chem. Soc.,* 2004, **126**, 1180.

63) Y. Tian, Z. Hu, Y. Yang, X. Chen, W. Ji, Y. Chen. Thermal analysis–mass spectroscopy coupling as a powerful technique to study the growth of carbon nanotubes from benzene. *Chem. Phys. Lett.,* 2004, **388**, 259.

64) M. Kumar, Y. Ando. Controlling the diameter distribution of carbon nanotubes grown from camphor on a zeolite support. *Carbon,* 2005, **43**, 533.

65) D. Tasis, N. Tagmatarchis, A. Bianco, M. Prato. Chemistry of Carbon Nanotubes. *Chem. Rev.,* 2006, **106,** 1105

66) Y. P. Sun, K. Fu, Y. Lin, W. Huang. Functionalized Carbon Nanotubes: Properties and Applications. *Acc. Chem. Res.*, 2002, **35**, 1096.

67) S. Niyogi, M. A. Hamon, H. Hu, B. Zhao, P. Bhowmik, R. Sen, M. E. Itkis, R. C. Haddon. Chemistry of Single–Walled Carbon Nanotubes. *Acc. Chem. Res.,* 2002, **35**, 1105.

68) V. N. Khabashesku, W. E. Billups, J. L. Margrave. Fluorination of Single–Wall Carbon Nanotubes and Subsequent Derivatization Reactions. *Acc. Chem. Res.,* 2002, **35**, 1187.

69) J. Liu, A. G. Rinzler, H. Dai, J. H. Hafner, R. K. Bradley, P. J. Boul, A. Lu, T. Iverson, K. Shelimov, C. B. Huffman, F. Rodriguez-Macias, Y.-S. Shon, T. R. Lee, D. T. Colbert, R. E. Smalley. Fullerene pipes. *Science,* 1998, **280**, 1253.

70) Z. Liu, Z. Shen, T. Zhu, S. Hou, L. Ying, Z. Shi, Z. Gu. Organizing Single–Walled Carbon Nanotubes on Gold Using a Wet Chemical Self–Assembling Technique. *Langmuir,* 2000, **16,** 3569

2 Experimental techniques

Due to their unique size and structure, carbon nanotubes require very different analysis techniques to small molecules. For example, electron microscopy has played a vital part in their characterization. Several different experimental techniques have been used in the present work, which will now be briefly introduced. The aim of the chapter is introduce the reader to the techniques commonly used, and to highlight any specific features that are particular to the analysis of carbon nanotubes.

2.1 Raman spectroscopy

Raman spectroscopy of carbon nanotubes yields a wealth of information about structure of the tubes in the sample, such as the type of tube (SWNTs, or MWNTs) or a measure of the number of defects in the tube.[1] It is also a quick and non–destructive technique that allows a large area of a sample to be examined.

2.1.1 Raman scattering

When light is scattered by a molecule, it can do so either elastically, without a change in energy of the photon, or inelastically, where the light loses energy to the molecule or gains energy from it.[2] In Raman spectroscopy, information about the energy levels of a system, vibrational levels in the case of nanotubes, is obtained from the frequencies of the inelastically scattered light. Due to their extended structure, the vibrations of carbon nanotubes are normally described in terms of phonons.[1]

The scattering process can be described in terms of exciting a molecule to a virtual state that then emits a photon when it relaxes. Three possible ways that this process can occur are shown in Figure 2.1. If the photon emitted has same energy as the incoming photon, then molecule returns to the same state as before the scattering of the photon. This process is Rayleigh scattering.[2] If the emitted photon leaves with less energy then the molecule has been left in an excited state, in this case a vibrational excitation: this process is termed Stokes scattering. Where the photon absorbs a phonon, is known as anti–Stokes scattering. For anti–Stokes scattering to

occur, the molecule must be in an excited vibrational state when it absorbs the photon. Anti–Stokes scattering is usually less intense because at room temperature, the population of the excited state will be lower than that of the ground state. As the scattering is more intense, it is usually the Stokes scattering spectrum that is collected. All the spectra collected in this work are the Stokes scattering spectra.

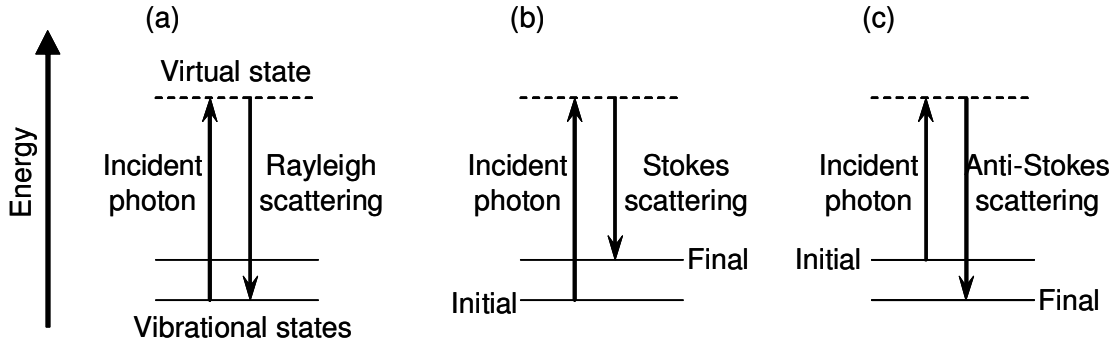

Figure 2.1. Different photon scattering processes. In Rayleigh scattering (a), there is no change in energy in the photon or the molecule, while in Stokes scattering (b) the molecule gains energy from the incident photon. In anti–Stokes scattering, the scattered photon has higher energy, as the molecule loses a quantum of energy.

Typically, a laser is used in Raman experiments as the monochromatic light makes it easier to separate the inelastically scattered light from the elastically scattered. The use of a laser also helps to produce a measurable intensity of the inelastically scattered photons due to the large flux of photons produced by the laser. The inelastic scattering occurs fairly infrequently (around 1 in 10^7 scattering events is inelastic), so the Raman signals can be weak.[2] Carbon nanotubes can have very large Raman signals. In fact, the signal is so great that Raman spectroscopy can be carried out on single nanotubes on surfaces.[3] The large Raman signal of nanotubes is partly due to the large polarizability and their ordered structure.[3] The Raman signal of nanotubes is also often resonantly enhanced, which is discussed in 2.1.6.

2.1.2 Raman spectroscopy of carbon nanotubes

The selection rules for Raman spectroscopy are different to those for infrared spectroscopy, where the photon is absorbed directly by the molecule. For a vibrational mode to be Raman active, it needs to give rise to a change in the polarizability of the molecule.[2] Group theory has been used to shown that for any

particular single–walled nanotube, it will have either 15 or 16 Raman active vibrational modes,[4] depending on the symmetry of the tube. The intensity of many of these modes is quite weak and many of the peaks overlap. In fact, there are 4 features in a Raman spectrum that are commonly observed and are described below: the radial breathing modes (RBMs), and the D, G and G' bands.

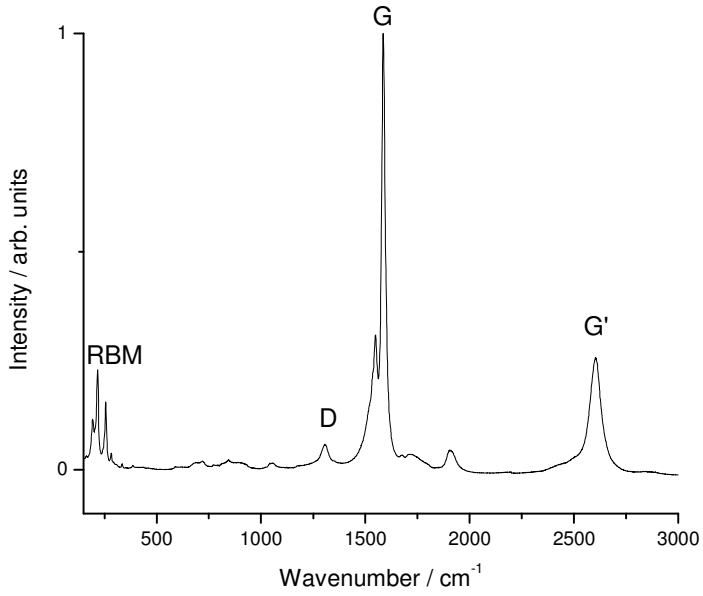

Figure 2.2. A typical Raman spectrum of single–walled nanotubes. Raman spectra of SWNTs are characterized by a small D band and radial breathing modes (RBMs).

2.1.3 Radial breathing modes

Typical spectra for single–walled and multi–walled nanotubes are shown in Figure 2.2. The peaks at low wavenumber, < 350 cm^{-1}, are called the radial breathing modes (RBMs).[1] These modes arise from the symmetrical expansion and contraction of the tubes around the tube axis by the carbon atoms moving radially, and they are unique to carbon nanotubes. The presence of RBMs is evidence that a sample contains single–walled nanotubes. RBMs are not observed in the Raman spectra of multi–walled nanotubes because RBMs of large tubes are not very intense, and because the peaks are broadened by the interactions between the layers.[1] The frequency of a radial breathing mode is inversely proportional to the diameter of the nanotube from

which it arises. It has been found empirically that the diameter of tube (d_t) can related to the frequency of the radial breathing mode (ω_{RBM})[3] by

$$d_t / \mathrm{nm} \approx \frac{248}{\omega_{RBM} / \mathrm{cm}^{-1}} \ . \qquad (2.1)$$

As there are usually many different diameters of tubes present in a sample of single–walled tubes, their Raman spectra show several different radial breathing modes: as can be seen by the several peaks at the left of the spectrum in Fig.2.2.

2.1.4 The G band

The most intense feature in the spectrum of carbon nanotubes is the G band that is found around 1590 cm^{-1}.[5] The G band is a feature of all sp^2 bonded carbon materials.[1] In graphite the G band can be fitted to a single Lorentzian lineshape,[6] but the curvature in a nanotube splits the G band into 2 peaks, which are not always resolved. The higher wavenumber peak is labelled ω^+ and is associated with vibration of carbon atoms along the tube axis. It can be fitted to a single Lorentzian centred around 1590 cm^{-1}. The lower wavenumber peak ω^- is associated with vibration of atoms round the circumference of the tube. The shape of the ω^- peak depends on the electrical characteristics of the tube. For semiconducting tubes, the ω^- peak is fitted by a single Lorentzian, while metallic tubes require a Breit–Wigner–Fano lineshape, which is usually much broader than the semiconducting ω^- peak.[5] The ω^- peak of metallic tubes occurs at slightly lower wavenumbers than that of semiconducting tubes, but the frequency of both also depends on the tube's diameter.[5] For spectra of individual tubes, the differences in the shape of the G band can be used to determine if the tube is metallic or semiconducting.[3,5] Examples of Raman spectra from individual nanotubes are shown in Figure 2.3. The shape of the G band can be seen to be different for semiconducting and metallic nanotubes.

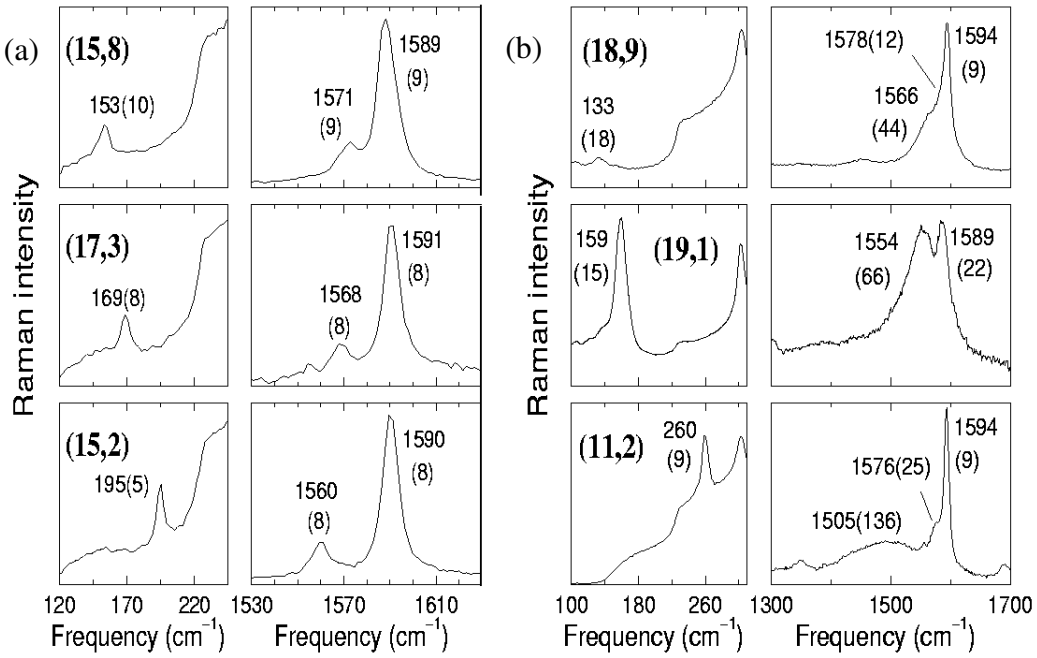

Figure 2.3. Raman spectra for isolated, individual semiconducting (a) and metallic (b) nanotubes.[6] The numbers are the wavenumbers of peaks while the numbers in parenthesis are the linewidths. The G bands in all the spectra can be seen to be made up of, at least, two peaks. The metallic tubes (b) have a much wider G band due to the much wider and intense ω^- peak. Note that the G bands of the semiconducting nanotube spectra are plotted on a different scale than for the metallic tubes.

2.1.5 The D band G' bands

While the G band is associated with high order in sp^2 bonded carbon materials, the D band is associated with disorder.[7] The D band is different from the radial breathing modes and the G band in that it is a defect–mediated mode.[1,7] The mechanism by which the D band arises involves the absorption of a photon by an electron that then loses energy and excites the D band vibration. The electron is then scattered by a defect in the structure, such as a vacancy in the lattice or an sp^3 bonded carbon, that allows the system to emit a photon.[1] The D band occurs around 1330 cm^{-1} and has been associated with a Raman band found in the spectrum of diamond:[8] thus, the D band has been often attributed to sp^3 bonding defects in the nanotubes. The D band is always associated with disorder in the structure of the carbon nanotubes and is intense for many carbon impurities that are found in samples of single–walled nanotubes, such as amorphous carbon. A common measure of the quality of a sample

of nanotubes is the ratio of the intensity of the D band to the G band, I_D / I_G.[9,10.] Pure, defect–free single–walled nanotubes have low I_D / I_G ratios. If a sample's spectrum has a large I_D / I_G ratio then it indicates the presence of a large amount of impurities in the sample, or defects in the nanotubes. Samples that have low I_D / I_G are sometimes described as being *well graphitized*, meaning that the carbon atoms are sp^2 bonded with few defects.

Another strong feature in the Raman spectra of carbon nanotubes is the G' band.[1] It is sometimes called the overtone of the D band as it appears at double the frequency of the D band. However, the G' band is produced in a different way from the D band so they have different behaviour. The G' band occurs when a photon excites the nanotube and then emits two of the same phonons that are excited in the production of the D band. The system can then emit a photon with out the need of a defect to mediate the process, as would happen with the D band. The intensity of the G' band does not depend on the density of defects in the tubes, and is seen in all carbon materials with sp^2 bonding.[1] The G' band was not usually recorded in this research, because it did not contain more data than could be obtained from the D and G bands.

2.1.6 Resonance–enhanced Raman spectroscopy

Carbon nanotubes can generate very large signals during Raman spectroscopy. Large polarizabilities and their largely defect–free structure partly explains these large intensities.[3] However, the signals are also enhanced through resonance. Resonance enhancement in Raman spectroscopy occurs when absorption of a photon promotes the molecule to a real state rather than a virtual one.[3] As discussed in Chapter 1, nanotubes are quasi–one dimensional systems due to their large aspect ratios and small diameters. Figure 2.4 shows a calculated density of electronic states plot for a carbon nanotube.[11] There are several large, sharp peaks in the plot that are known as van Hove singularities that are characteristic of 1–D systems.[12] When the laser energy is equal to the difference in energy between two of these singularities, resonance enhancement can occur due to promotion of an electron from one of these singularities in the valence band to the equivalent (mirror–image) peak in the conductance band.[3] As these singularities are sharp, the resonance window is small,

< ~ 10 meV for isolated tubes.[13] When the tubes are bundled, the resonance window has found to be larger ~ 100 meV.[13] So for a sample of single–walled tubes containing many different chiralities, only some of the tubes present will be in resonance in with laser such that their signals are enhanced. Figure 2.5 shows that different RBMs and different shapes of the G band can be seen in the spectra for a sample that is collected with different laser wavelengths.[14]

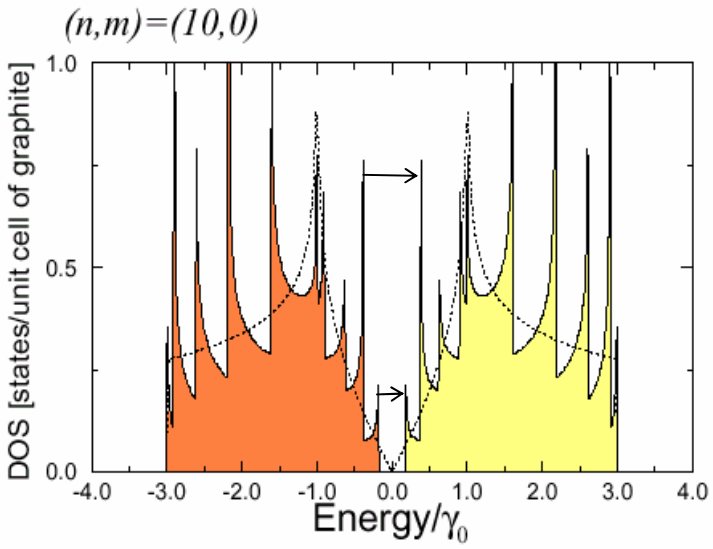

Figure 2.4. The density of states of a (10,0) carbon nanotube.[11] The large peaks are known as van Hove singularities. Large enhancements in the Raman signal occur when the energy of the laser photon corresponds to the energy difference between a peak in the valence band (shaded grey) and its corresponding peak in conductance band. The arrows show two of these transitions. The term γ_0 is the nearest–neighbour carbon–carbon tight binding overlap energy which is taken to be 2.9 eV.[5] The dashed line is the density of electronic states of graphite.

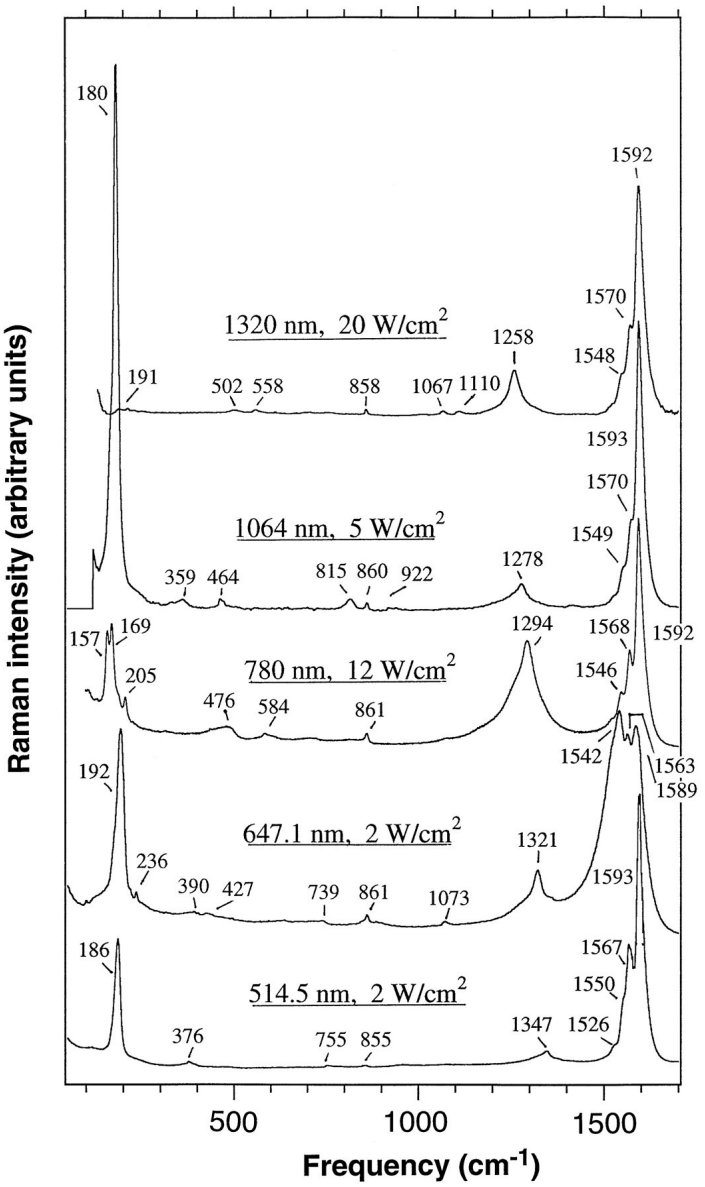

Figure 2.5. Raman spectra of a sample of single nanotubes taken at different excitation energies.[14] As the energy of the excitation photon changes, a different set of tubes comes into resonance to have an enhanced signal. Each spectrum shows RBMs at different frequencies, and the shape of the G band also varies.

Values for the energy difference between van Hove singularties have been calculated using the tight binding approximation.[15] Such a plot, known as a Kataura plot, is shown in Figure 2.6. This plot contains information that can be used to identify chiralities of nanotubes present in a sample. If it is assumed that the only RBM that arises from a nanotube is one in resonance with the laser energy, then an assignment of chiral vector (n,m) can be made by comparing the transition energy with the

diameter of the tube that is can be calculated for the wavenumber of the RBM using Equation 2.1.

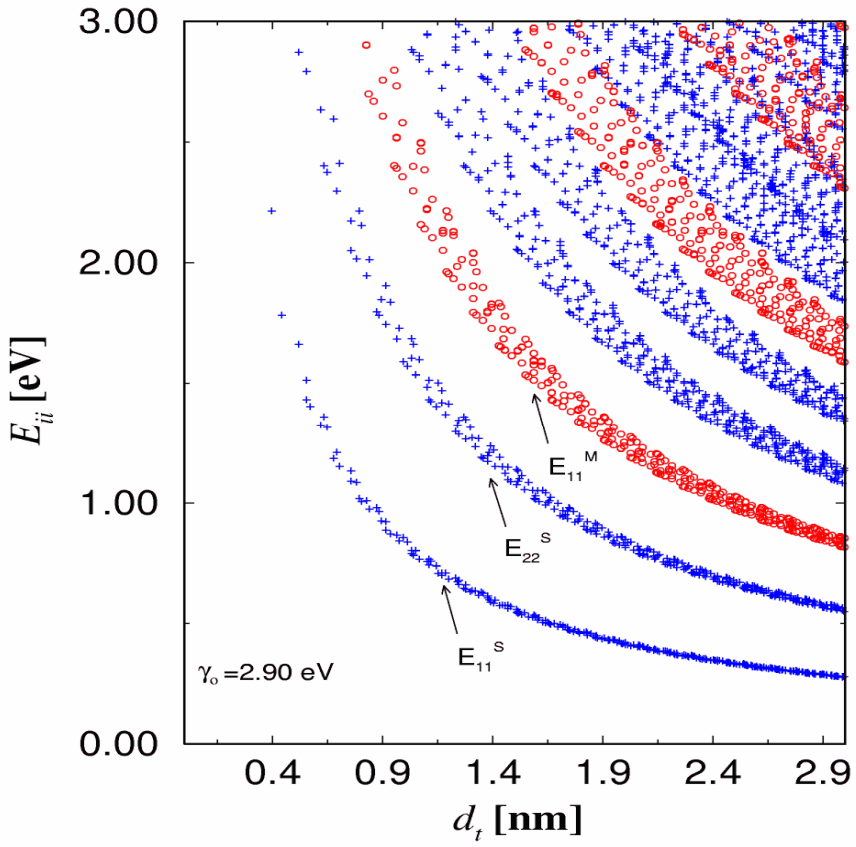

Figure 2.6. Plot of diameter of nanotube against transition energy between corresponding van hove singularties calculated using the tight binding approximation .[15] The red circles are metallic tubes while the blue crosses are semiconducting tubes. This kind of plot, known as a Kataura plot, is often used to assign the chirality of individual nanotubes by assuming that the laser energy of the Raman laser is equal to that of the transition energy.

2.1.7 Summary of Raman spectroscopy of carbon nanotubes

Raman spectroscopy is well suited to the study of carbon nanotubes. It can provide a great deal of information about sample, the type of tubes present and quality of the sample in terms of the amount of defects and impurities. In this work, most Raman spectra were collected using a Labram 300 (Jobin–Yvon Horiba) with a He–Ne laser (633 nm) with a laser power of 13 mW.

2.2 Thermogravimetric analysis

In thermogravimetric analysis (TGA), the mass of a sample is measured while it is heated, usually in some sort of controlled atmosphere, so that mass can be plotted against temperature. Sometimes, the derivative of the mass loss with temperature is also plotted to aid in the identification of the temperature at which a loss occurs. As different processes, such as the oxidation of a material or the evaporation of compound, occur at different temperatures, it is possible to determine the composition of a sample by interpreting the mass–temperature plot. In this work, TGA was used to determine the amount of carbon deposited on a sample during chemical vapour deposition. During a TGA experiment, the sample, typically < 10 mg, was heated from room temperature (~ 20 ºC) to 1000 ºC at 10 ºC min^{-1} in a flow of air. A typical TGA is shown in Figure 2.7. At low temperatures (< 250 ºC) the mass loss is attributed to loss of adsorbed water. Carbon materials have been found to begin to oxidise in air between 400 °C and 600 ºC. Usually the major weight loss for a sample would occur at this temperature due to the oxidation of the carbon materials, which are then lost from the sample as carbon dioxide gas. In the thesis, the percentage mass carbon (% mass C) of a sample is often reported and was determined using the formula

$$\% \text{ mass C} = ((m_1 - m_2) / m_2) \times 100, \qquad (2.2)$$

where m_1 is the mass of the sample just before the carbon oxidation (around 350 °C) and m_2 is the mass just after (around 600 °C). An increase in mass at higher temperature (> 800 ºC) was thought to be due to the oxidation of metallic iron in the sample. A TG762 thermobalance (Stanton Redcroft) was used through the course of this research.

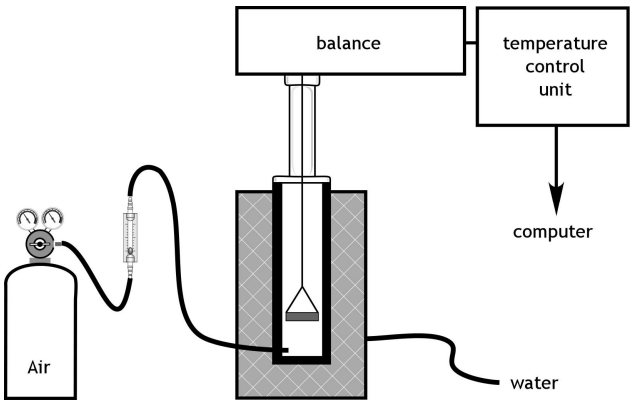

Figure 2.7. Diagram of the thermogravimetric analysis equipment. The sample is placed in the pan of the balance and is constantly weighed while it is heated in a water–cooled furnace. A flow of air is passed through the furnace while the sample is heated. The temperature in the furnace and the mass of the sample are recorded against time.

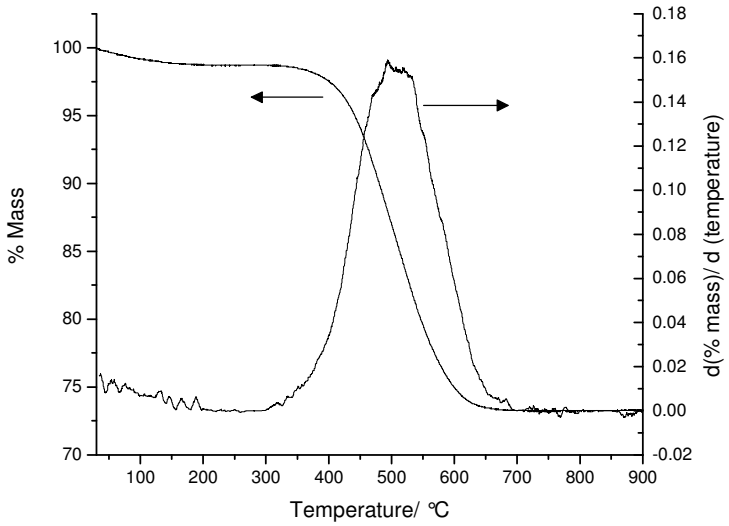

Figure 2.8. A typical plot of TGA data. The plot of mass against temperature and its derivative are shown. The derivative is taken as it can be used to determine if two mass losses are occurring at around the same temperature. As the sample is heated the first mass loss (~ 100 ºC) is due to the loss of water. The loss in carbon mass occurs typically between 300 ºC and 700 ºC and is due to the oxidation of carbon. Sometimes an increase in mass is observed at higher temperature, which is attributed to the oxidation of residual metallic catalyst.

2.3 Electron microscopy

2.3.1 Scanning electron microscopy

In scanning electron microscopy (SEM), a beam of electrons, typically with energies of between 1 keV and 30 keV, is used to probe the surface of a sample.[16] The electrons in the beam, when they strike the surface, are scattered by the atoms in the surface. Some of the energy from the electron beam causes the ejection of lower energy electrons (< 50 eV) from the sample that are known as secondary electrons.[17] These secondary electrons are collected and are converted into a signal that is used to build up an image of the surface as the electron beam is scanned across the surface of the sample. The brightness of area in a secondary electron image is proportional to the amount of electrons that reached the detector from that point, so raised areas that are closer to the detector appear brighter.[17] SEM using secondary electrons is said to contrast by height. The geometry of edges allows the escape of more electrons than a flat surface so edges often appear bright.[16] All the SEM images in this thesis are secondary electron images.

There are many other kinds of electrons and electromagnetic radiation that can be collected from the interaction of the electron beam and the sample. Each of them contains different information: e.g., backscattered electrons, which are electrons from the beam that have been elastically scattered by the atoms of the sample, can also be used to form an image of the sample.[17] As the number of backscattered electrons increases with the atomic number of the atoms involved, the image produced can show the variation in chemical composition across a sample.

As the electron beam is scanned across the sample, it is important that the sample is conducting so that charge does not build up on it that would affect the imaging. Non–conducting samples are usually coated with carbon or gold to increase their conductivity. All samples in this thesis were sputter–coated with gold before viewing. A Philips XL30CP scanning electron microscope with a tungsten filament was used to obtain all the SEM images used in this thesis, usually with a working distance of 10 mm and an accelerating voltage of 30 kV.

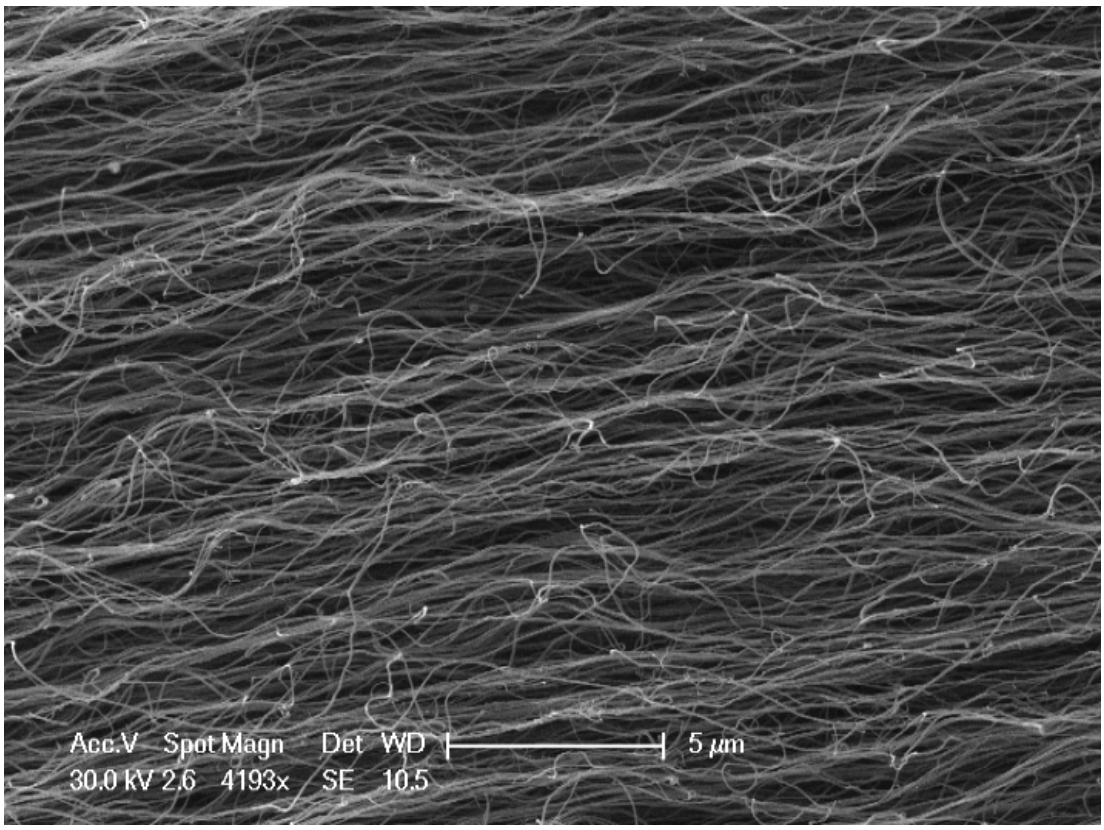

Figure 2.9. SEM of aligned multi–walled tubes and nanofibres. SEM can give a detailed view of the surface a sample. Here we can observe the individual nanotubes and fibres are bundled together to form a mat of tubes. The fibre/tubes have a diameter of around 50 nm.

2.3.2 Transmission electron microscopy

In transmission electron microscopy (TEM), a beam of electrons is focussed on a very thin sample, and the image is formed by the electrons that are transmitted through the sample onto a phosphor screen so that the image can be viewed. A schematic of TEM is shown in Figure 2.10. The electrons in the beam that are scattered by the sample, at some angle to the beam, are removed by using an aperture.[18] For the image to be recorded, the image is projected onto a photographic plate or CCD camera. In the most common form of TEM, called bright field imaging, the differences in the amount of electrons that pass through the different areas of sample without scattering, create the image.[16] Only bright field imaging was used throughout this thesis. This form of TEM is similar to light microscopy.[16] As the electrons pass through the sample, TEM can give information about the internal structure of nanotubes, such as the way that the graphene sheets make up the side–wall.[4,,8,19]

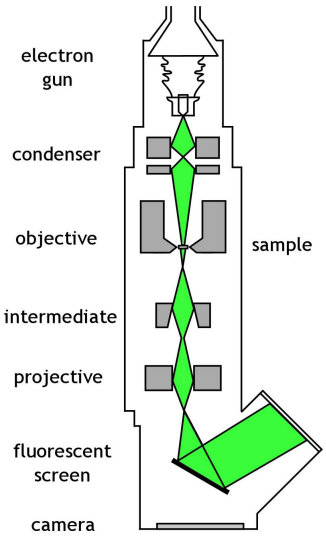

Figure 2.10. Schematic of a TEM. The set up is quite similar to that of a light microscope. The illumination source is an electron gun that produces a beam. This beam is collimated by the condenser onto the sample. The intermediate (or objective) lens forms the first image which is then magnified by the projective lens to its final size. As, of course, the electrons cannot be viewed directly, the image is formed a fluorescent screen or a camera is used to capture the image.

Samples in this thesis were viewed using a Philips CM120 Biotwin TEM in the Institute of Molecular Plant Sciences at the University of Edinburgh, using an accelerating voltage of 100 kV.

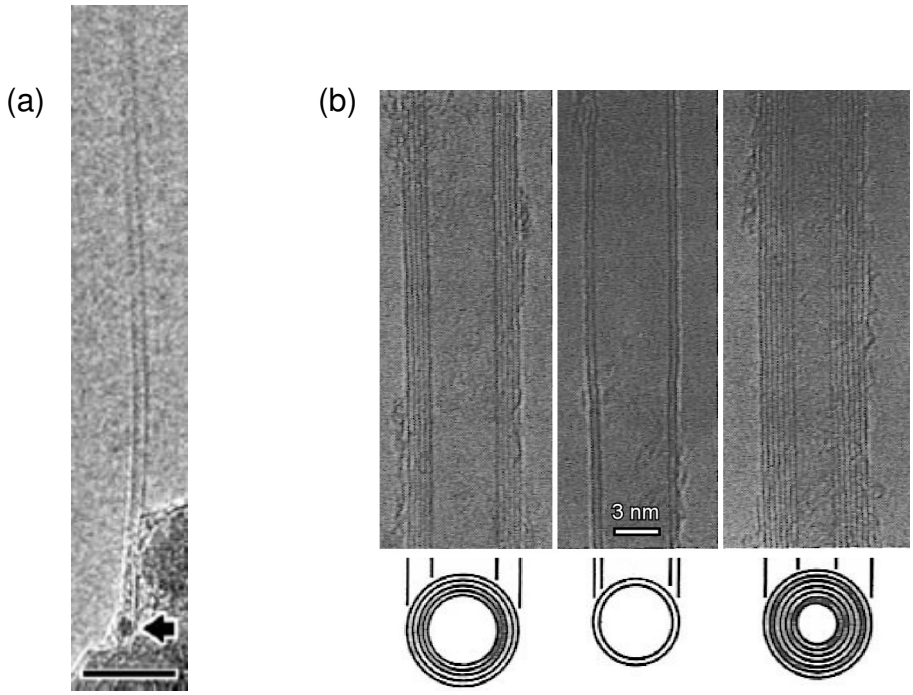

Figure 2.11. TEM can be used to look at individual SWNTs (a)[20] and resolve the different sheets of graphite that make up a MWNT(b).[21]

2.4 X–ray photoelectron spectroscopy

X–ray photoelectron spectroscopy (XPS) can be used as a form of elemental analysis for surfaces.[22] If an atom is ionised by an x–ray, the kinetic energy of the electron (KE) can be related to the binding energy (BE) of the orbital from which the electron had been ejected by

$$KE = h\upsilon - BE - \varphi, \qquad (2.2)$$

where $h\upsilon$ is the energy of the x–ray and φ is the work function of material.[22]

In an XPS experiment, the sample is exposed to monochromatic x–rays that eject electrons from the sample with different kinetic energies. The electrons only have a mean free path of a few nanometres in the sample, so only electrons from the surface are detected. XPS is therefore a surface specific technique.[23] The number of ejected electrons with a particular kinetic energy is measured for many different kinetic energies, so that a plot of electron intensity against binding energy, using Equation 2.2, can be made. The binding energy of a peak is characteristic for each element, so

a peak at a certain energy can be used to identify the presence of a certain element. The area under a peak is proportional to the amount of that element present in the sample.[24] The relative amount of element present can be calculated if the areas are adjusted to take into account the sensitivity of the particular element to the x–rays used.[24] The binding energies of the elements can be changed by the oxidation state of the atom and its environment. An element in a high oxidation state will tend to have a higher binding energy than one in a low oxidation state, as the atom or ion will have a greater positive charge to attract the electron.[22] These differences in the binding energies allow the identification of different functional groups.

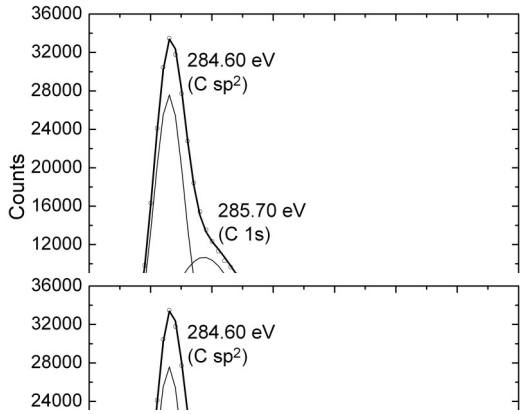

Figure 2.12. XPS of a sample of oxidized SWNTs The C 1s has several different contributions the largest at 284.60 eV is due to sp^2 bonded carbon, while the peak at 285.70 eV is sp^3 bonded. The broader peak at higher biding energies arises from carbon bonded to oxygen atoms.[26]

As the samples are ionised during the analysis, a charge can build up on them that changes the kinetic energy of the electron. To account for this drift in kinetic energy, and also if the work function φ is not known, the binding energies are shifted so that the peak of a known element is at the correct binding energy. For example in carbon nanotube samples, the spectrum is adjusted so that the maximum of the carbon 1s peak is at 284.6 eV, which corresponds to sp^2 bonded carbon.[26] XPS was carried out in this research using a VG Scientific Sigma Probe XPS instrument with a monochromatic Al (Kα) x–ray source.

2.5 References

1) M. S. Dresselhaus, G. Dresselhaus, R. Saito, A. Jorio. Raman spectroscopy of carbon nanotubes. *Physics Reports*, 2005, **409**, 47

2) A. K. Brisdon. *Inorganic Spectroscopic Methods*, 1998, Oxford University Press.

3) M. S. Dresselhaus, G. Dresselhaus, A. Jorio, A. G. Souza Filho, M. A. Pimenta, R. Saito. Single Nanotube Raman Spectroscopy. *Acc. Chem. Res.,* 2002, **35,** 1070.

4) R. Saito, G. Dresselhaus, M. S. Dresselhaus. *Physical Properties of Carbon Nanotubes*, 1998, Imperial College Press, UK

5) M. S. Dresselhaus. G. Dresselhaus, A. Jorio, A. G. Souza Filho, R. Saito. Raman spectroscopy on isolated single wall carbon nanotubes. *Carbon*, 2002, **40**, 2043

6) A. Jorio, A. G. Souza Filho, G. Dresselhaus, M. S. Dresselhaus, A. K. Swan, M. S. Unlu, B. B. Goldberg,M. A. Pimenta, J. H. Hafner, C. M. Lieber, R. Saito. G–band resonant Raman study of 62 isolated single–wall carbon nanotubes. *Phys. Rev. B*, 2002, **65**, 155412.

7) M. A. Pimenta, A. Jorio, S. D. M. Brown, A. G. Souza Filho, G. Dresselhaus, J. H. Hafner, C. M. Lieber, R. Saito, M. S. Dresselhaus. Diameter dependence of the Raman D–band in isolated single–wall carbon nanotubes. *Phys. Rev. B*, 2001, **64**, 041401.

8) P. J. F. Harris. *Carbon Nanotubes and related Structures*, 1999, Cambridge University Press.

9) W. Qian, T. Liu, F. Wei, H. Yuan. Quantitative Raman characterization of the mixed samples of the single and multi–wall carbon nanotubes. *Carbon,* 2003, **41**, 1851.

10) H. Athalin, S. Lefrant. A correlated method for quantifying mixed and dispersed carbon nanotubes: analysis of the Raman band intensities and evidence of wavenumber shift. *J. Raman Spec*. 2005, **36**, 400.

11) R. Saito, G. Dresselhaus,M. S. Dresselhaus. Trigonal warping effect of carbon nanotubes. *Phys. Rev.* B, 2000, **61**, 2981.

12) S. R. Elliot. *The Physics and Chemistry of Solids.*1998, John Wiley & sons.

13) C. Fantini, A. Jorio, M. Souza, M. S. Strano, M. S. Dresselhaus, M. A. Pimenta. Optical Transition Energies for Carbon Nanotubes from Resonant Raman Spectroscopy: Environment and Temperature Effects. *Phys. Rev. Lett*., 2004, **93**, 47406.

14) A. M. Rao, E. Richter, S. Bandow, B. Chase, P. C. Eklund, K. A. Williams, S. Fang, K. R. Subbaswamy, M. Menon, A. Thess, R. E. Smalley, G. Dresselhaus, M. S. Dresselhaus. Diameter–Selective Raman Scattering from Vibrational Modes in Carbon Nanotubes. *Science*, 1997, **275**, 187.

15) H. Kataura, Y. Kumazawa, Y. Maniwa, I. Umezu, S. Suzuki, Y. Ohtsuka,Y. Achiba. Optical Properties of Single–Wall Carbon Nanotubes. *Synth. Met.,* 1999, **103**, 2555.

16) D. Chescoe, P. J. Peterhew. *The operation of Transmission and Scanning Electron Microscopes*, 1990, Oxford University Press.

17) J. I. Goldstein, D. E. Newbury, P. Echlin, D. C. Joy, A. D. Romig, C. E. Lyman, C. Fiori, E. Lifshin. *Scanning Electron Microscopy and X–ray Microanalysis* (2nd Ed.), 1992, Plenum Press.

18) A. W. Agar, R. H. Alderson, D. Chescoe. *Principles and Practice Electron Microscope Operation*, 1974, North–Holland Publishing Company.

19) Ph. Lambin, A. Loiseau, C. Culot, L. P. Biro. Structure of carbon nanotubes by local and global probes. *Carbon*, 2002, 1635–1645.

20) H. Dai. Carbon Nanotubes: Synthesis, Integration, and Properties. *Acc. Chem. Res.* 2002, **35,** 1035

21) S. Iijima. Helical microtubules of graphitic carbon. *Nature*, 1991, **354**, 56

22) G. Attard, C. Barnes. *Surfaces*, 1998, Oxford University Press.

23) P. W. Atkins, J. de Paula. *Physical Chemistry* (7 th Ed.), 2002, Oxford University Press.

24) D. Briggs, M. P. Seah. *Practical Surface Analysis by Auger and X–Ray photoelectron spectroscopy*, 1987, John Wiley and Sons Ltd.

25) G. A. Forrest. University of Edinburgh. Unpublished results.

26) C. J. Powell. Elemental binding energies for X–ray photoelectron spectroscopy. *Appl. Surf. Sci.,* 1995, **89,** 141.

3 Chemical vapour deposition of carbon nanotubes from a supported iron oxide nanoparticle catalyst

3.1 Introduction

3.1.1 Chemical vapour deposition

Chemical vapour deposition (CVD) is an important method of synthesizing carbon. All methods of producing CNTs are thought to form atomic carbon (or at least very small fragments such as C_2), which then condense to form the tubes.[1-3] The key to the formation of CNTs at low temperatures by CVD is the use of a catalyst that allows the decomposition of a carbon containing molecule to produce the necessary carbon. By comparison, in the laser ablation and arc discharge methods a great deal of energy is applied to graphite to produce the atomic carbon or small carbon molecules in the gas phase. For all growth methods, the condensation of the carbon into nanotubes must be under kinetic control, as the most thermodynamically stable form of carbon that could form would be graphite.[3] The catalyst in the CVD process is thought to play an additional role, as the nanoparticles of the catalytic metal can template the formation of a tube; the metal particle can stabilise the dangling bonds at the growing edge of the tube.[4]

Although methods for growing carbon fibres and filaments have been known for many years, there is still little that is widely agreed about the mechanism[3]. It is hoped that if real insight into the mechanism can be gained, this would allow the selective production of tubes with particular structures[2] (diameters and chiral vectors). It is known that a tube's structure controls its properties, and the properties of a tube will—of course—determine its potential applications. Since separating tubes by length, width or electrical properties is difficult at present, it would be valuable to understand the growth mechanism to such an extent that the growth of particular tubes could be achieved.

3.1.2 Rationale for focus on SWNT growth

Our main goal was to produce a large amount catalyst that could be used to produce CNTs by CVD, so that the comparative experiments could be carried out that would

give some insight into the mechanism of CNT formation. The focus was on production of SWNTs, as they are arguably of greater interest due to their small diameters and simple structure. Also SWNTs would be easier to analyse: e.g., the diameters of MWNTs can only be estimated by electron microscopy at present. Only TEM can determine whether the tubes produced are in fact true MWNTs, where the graphitic sheets are parallel to the axis of the tube, rather than carbon fibres.[5] In addition, the thicknesses of the sidewalls of MWNTs (the distance from the outside of the tube to the central cavity or the number of graphitic sheets that make up the tube's wall) can only be determined by TEM. Although SWNTs are smaller in diameter and therefore more difficult to image in TEM, their unique structure gives them a Raman spectrum that can be related to diameter. The frequency of radial breathing modes (RBMs) are inversely related to the diameter of the tube from which they originate.[6] This allows Raman spectroscopy to be used to estimate the width distribution of tubes produced. Information about the chiralities of tubes can also be inferred from Raman spectroscopy.

3.1.3 Design of catalyst to produce single–walled nanotubes

Design of our catalyst was guided by the literature. Many catalysts described in the literature were prepared from metal salts, often the nitrate or acetate, which are dispersed onto an inert oxide support such as silica or alumina.[1] There is evidence that SWNTs grow from single metal nanoparticles that have sizes comparable to the tubes formed.[1,2,7-10] The metal salts in the catalyst are thought to form nanoparticles as the catalyst is heated, either in a special calcination step or during the initial stages of growth by CVD.

It is difficult to predict the size of particles formed by methods using metal salts. In order to reduce variation in the size of particles produced, it was decided that nanoparticles would be prepared first, so that they could be dispersed onto a variety of support materials. This would facilitate measurements of the diameters of the nanoparticles before they are dispersed onto the catalyst support. Measurements of the size of particles, once having been dispersed on the support, would be impractical with the TEM available to us. It is well known that the most successful catalysts for

the growth of SWNTs are prepared from transition metals such as iron, cobalt, nickel, molybdenum, or alloys of these metals.[1,2] Carbon is soluble in all of these metals when they are liquid, and their ability to produce nanotubes is often ascribed to this solubility of carbon.[2] Several examples of the preparation of nanoparticles that form SWNTs under CVD conditions can be found in the literature.[1,2,7-12] Initailly, two different approaches were adopted that had been reported previously in the literature as methods of preparing nanoparticles suitable for the growth of carbon nanotubes. The syntheses of nanoparticles included precipitation of iron metal from the decomposition of iron pentacarbonyl at high temperature, [7] and chemical reduction of metal salts in the presence of surfactant molecules that promoted the formation of nanoparticles.[8] No suitably active catalysts were produced from the metal particles synthesized by these methods. The metal particles formed were found to be very air sensitive. Large amounts of surfactant hindered the imaging of the particles by TEM, and seemed to stop the growth of CNTs when the particles were dispersed onto surfaces.

Due to the difficulties presented by surfactants, and by reactivity of metal particles, another strategy was employed to form nanoparticles Here a very simple synthesis to prepare magnetite (Fe_3O_4) nanoparticles without surfactant was adopted from the literature (see Appendix A.1).[13] This original synthesis was part of an investigation into the synthesis of magnetic nanoparticles for data storage media that we adapted to make CNT catalysts. The magnetite particles were found to produce SWNTs by CVD, and were used as the catalyst for all of our comparative CVD studies.

The choice of catalyst support has found to be important in the production of nanotubes. Two popular supports for CNT catalysts are aluminium oxide and magnesium oxide.[14,15] Both of these materials were tested as supports for the present work. Another factor that was considered was the surface area of the support for the catalyst. Catalyst supports with large surface areas have been found to be good at producing SWNTs.[16] This is usually explained by the greater area of the support hindering the coalescing of the nanoparticles.[11] In order to maximise the surface area

of the catalysts produced, nanopowdered Al_2O_3 and MgO were used: details are given in Appendix A.2.

Once a suitable catalyst was prepared, the comparative CVDs were carried out using methane as the source of carbon as it is probably the most popular and most–studied precursor for producing SWNTs.[1,2,14]

3.2 Experimental

A brief summary of the experiments carried out are given here, all experimental details can be found in Appendices A.1 to A.3.

3.2.1 Nanoparticle synthesis

Nanoparticles were prepared as an aqueous dispersion by precipitating a solution of Fe(II) and Fe(III) chlorides (1:2 molar ratio) in a solution of ammonium hydroxide, in a similar manner to the synthesis of Kang et al.[13] The particles were then washed to remove the excess ammonium hydroxide. The particles were characterized by TEM.

3.2.2 Catalyst preparation

Catalysts were prepared by rotary evaporating an aqueous dispersion of the support material with the required amount of the as–prepared nanoparticle dispersion. The resulting powder was then dried in an oven and ground with a pestle and mortar in order to break up agglomerations.

3.2.3 Growth of carbon nanotubes by chemical vapour depostion

Chemical vapour deposition was carried out by heating up a sample of catalyst (~ 0.1 g in all experiments) in a tube furnace. Once the furnace had reached a working temperature between 600 °C and 1000 °C, methane was passed over the catalyst. Sometimes hydrogen and argon were used to dilute the methane. The furnace was initially heated and cooled under a flow of argon. The CVD product was

characterized with thermogravimetric analysis (TGA), Raman spectroscopy and electron microscopy.

3.3 Results and discussion

3.3.1 Nanoparticle synthesis

The nanoparticles were synthesised as a black suspension in water that would typically settle out after a few days. Over time, the black precipitate would turn brown, suggesting the oxidation of the magnetite to maghemite (γ-Fe_2O_3). Magnetite ($Fe(II)Fe_2(III)O_4$) has an inverse spinel structure.[17] In magnetite, the oxide ions form a cubic close–packing lattice. This arrangement of ions has two different sites, tetrahedral and octahedral, that the iron ions can inhabit.[18] Half of the Fe(III) ions and all the Fe(II) occupy tetrahedral sites in the lattice while the other half of the Fe(III) ions occupy octahedral sites.[17] By contrast, in a normal spinel the doubly charge ions would reside in the tetrahedral sites and the triply charged ions in the octahedral.[18] In maghemite, the Fe(III) ions are distributed randomly over the octahedral and tetrahedral sites. Oxidation of magnetite leads to formation of maghemite (γ-Fe_2O_3) rather than haematite (α-Fe_2O_3) because in both structures the oxide ions are in a cubic close–packing lattice. Conversion to haematite from magnetite is not favoured, as the oxide ions in haematite are arranged in a hexagonal close–packed arrangement.[17] The particles were characterised by TEM. Figure 3.1 shows the particles as being roughly spherical in shape.

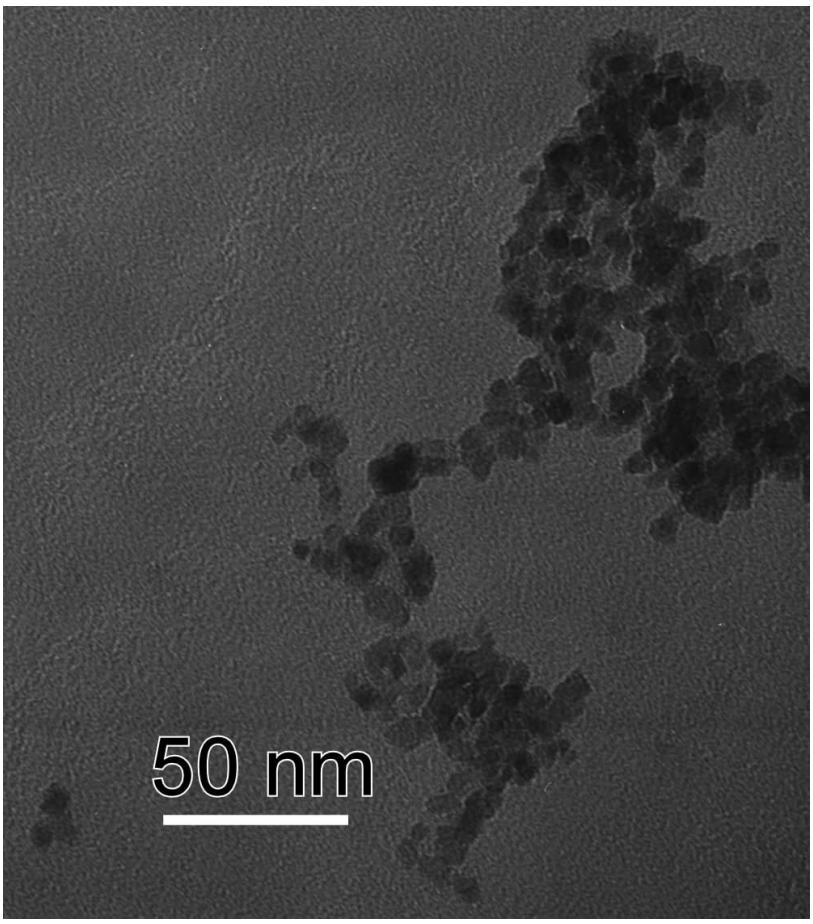

Figure 3.1. TEM image of iron oxide catalyst nanoparticles synthesised. The nanoparticles can be seen to be roughly spherical.

From the measurement of over 300 particles, the average diameter (measured across widest part) was found to be 10.6 nm with a standard deviation of 3.4 nm. A histogram of the diameters of the particles is shown in Figure 3.2.

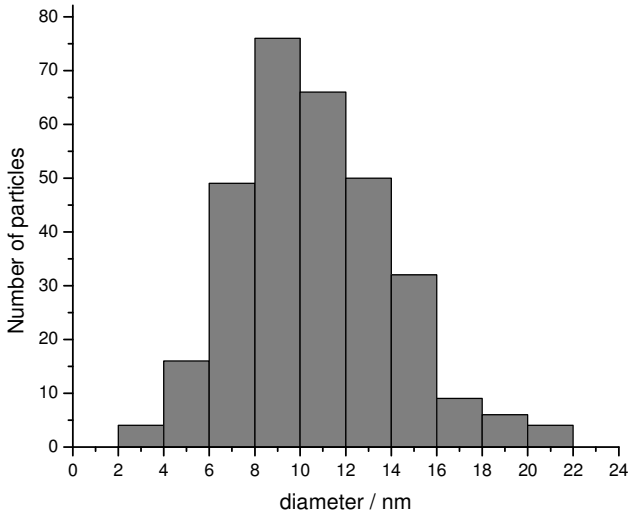

Figure 3.2. Histogram of the diameters of iron oxide nanoparticles synthesised. The nanoparticles were not entirely spherical, so were measured across the widest section visible.

It has been suggested by several different authors that small catalyst particles are much more useful in producing SWNTs, because larger particles can produce MWNTs in addition to SWNTs.[7] It has even been suggested that as nanoparticle diameter decreases, there comes a size of particles that only produces SWNTs: this is thought to be somewhere between 4 nm and 6 nm.[7] Assuming that the unit cell volumes of the nanoparticle magnetite and iron are the same as the bulk,[19] and that the nanoparticles are spherical, the diameter of an iron nanoparticle expected from the corresponding iron oxide particle can be estimated. If we take our average diameter of an iron oxide particle as being 10.6 nm then we get a diameter of reduced iron particle of 4 nm. The actual average diameter of a reduced particle is probably slightly less than 4 nm because the iron oxide particles are not entirely spherical. The particles were measured at their widest visible section, therefore the volume of the particles will be over–estimated.

3.3.2 Characterisation of CVD products

Primarily, both thermogravimetric analysis (TGA) and Raman spectroscopy were used to characterise the products from the CVDs. TGA was used to determine the percentage mass of carbon of the CVD products. All TGA plots showed a mass

decrease due to the oxidation and loss of carbon from the sample, usually between 350 °C and 700 °C. The mass % C of the sample was calculated as

$$\text{mass \% C} = 100 \times (m_1 - m_2) / m_1, \qquad (3.1)$$

where m_1 and m_2 are the mass of the sample before and after the carbon mass loss, respectively. Unfortunately, it was not possible to estimate the relative amounts of the different types of carbon present (i.e., SWNTs, MWNTs, amorphous carbon) as the plots of mass against time generally only show one gradual decrease between 400 °C and 600 °C.

Raman spectroscopy was used to establish the presence of graphitic carbon by the presence of the G band (at ~ 1590 cm^{-1}) which is attributed to sp^2 bonded carbon, and the D band (~ 1300 cm^{-1}) which is a disorder–activated band that is associated with sp^3 bonded carbon and defects in graphitic structures.[5] A measure of the graphitization, or quality, of the tubes that is often used, is the ratio of the integrated intensity of the D band to the G band (I_D / I_G). So that the calculated I_D / I_G ratios were representative of the products, several spectra were recorded for each sample and the I_D / I_G ratio was calculated as an average of at least six spectra. Low frequency modes between 150 – 350 cm^{-1} (RBMs) are attributed to the presence of SWNTs.

3.3.3 Preliminary experiments

Once the nanoparticles had been synthesised, catalysts were prepared using different supports. Alumina (Degussa aluminoxid C) and MgO (Aldrich) nanopowder were used as supports. When comparing the supports, it is difficult to judge what would be a fair comparison as several attributes can be different, e.g., surface area. Here, the same molar ratios of Fe:Al and Fe:Mg (~ 1:30) were prepared for both supports. The mass loadings for each catalyst were 3.4 % w/w Fe for the alumina catalyst, and 4.6 % w/w Fe for the MgO catalyst. CVD was carried out at 900 °C for 30 min with a flowrate of 1.4 l min^{-1} methane and 0.8 l min^{-1} hydrogen.

3.3.3.1 Characterization of CVD products

Support	Average I_D / I_G ratio	Mass % C
Al_2O_3	1.24	11
MgO	0.13	13

Table 3.1. Average I_D / I_G ratios and mass % C for the Al_2O_3 and MgO supported catalysts.

Results of characterization for the CVD products produced are presented in Table 3.1. As can be seen from the representative Raman spectra in Figure 3.3, the MgO supported catalyst gave much better tubes, as the D band is much smaller than that for the Al_2O_3 supported catalyst. The average I_D / I_G ratios are shown in Table 3.1. In addition, RBMs were observed in all the spectra from the MgO supported catalyst, while in some of the spectra for the Al_2O_3 supported catalyst there were none. The catalysts gave comparable yields of carbon for MgO (13 %) compared to the Al_2O_3 (11 %). However, as the MgO catalyst did have a slightly greater proportion (4.6 % w/w iron) of iron weight for weight than the other catalyst, it is expected that it could give a larger C yield.

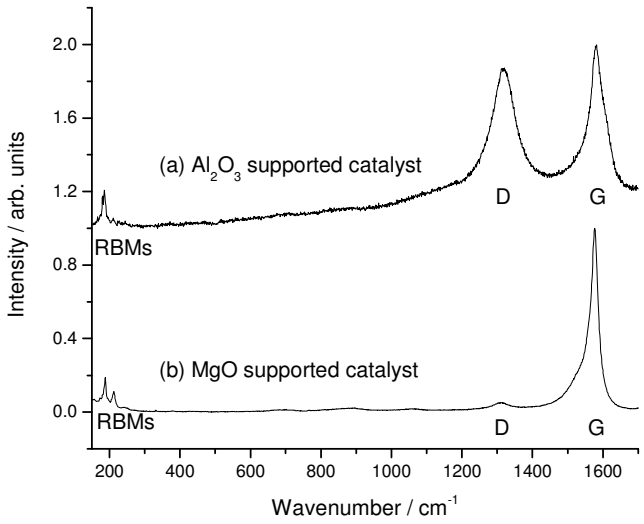

Figure 3.3. Representative Raman spectra of CVD products of (a) Al_2O_3 supported catalyst, and (b) MgO supported catalyst. The RBMs which can be seen at low wavenumbers indicate that SWNTs have been produced. The more intense features at higher wavenumber, the D and G bands, are related to amorphous and graphitized carbon respectively. In this way the relative intensities of these features can be used a measure of "quality" of the tubes produced. The small D band compared to the G band for the MgO catalyst suggests that more graphitized and less amorphous carbon has been produced by this catalyst.

The TEM image, Figure 3.4, of the CVD product made from the magnesium oxide supported catalyst shows clearly the SWNTs in bundles.

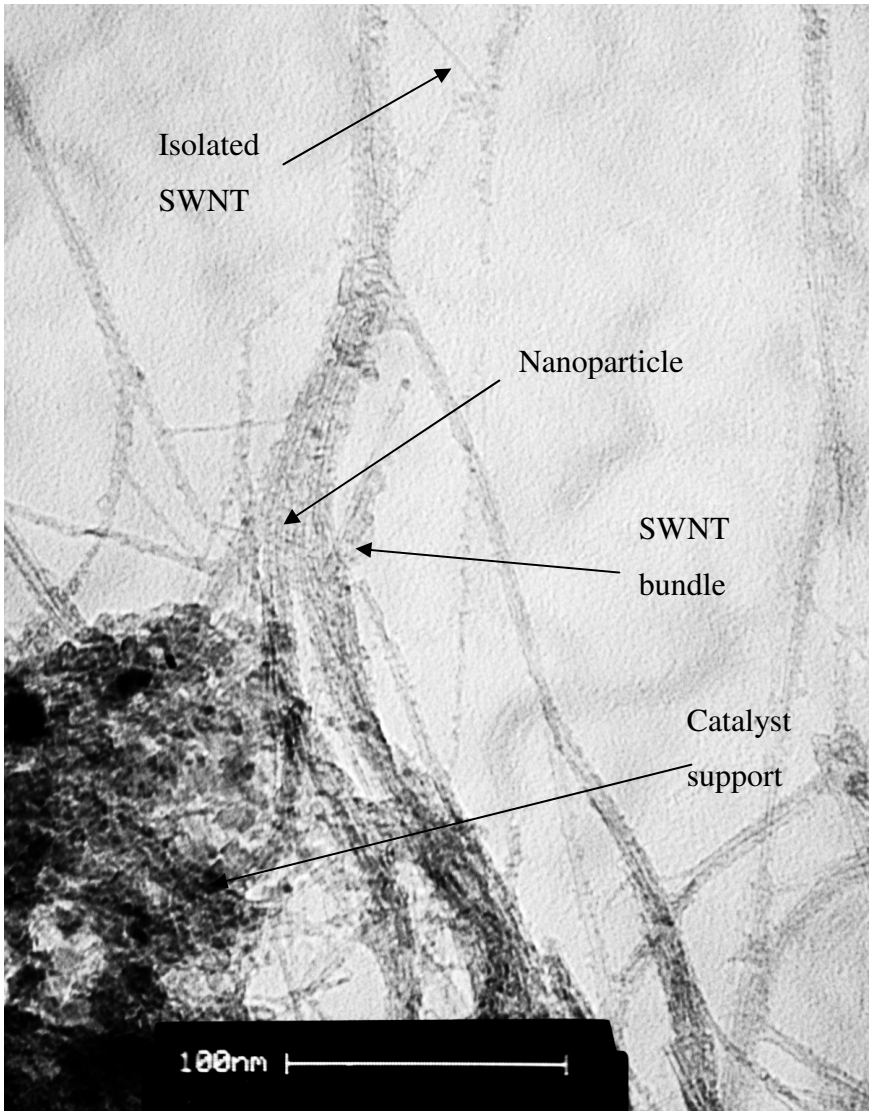

Figure 3.4. TEM image of SWNT bundles produced by MgO supported catalyst. Bundles of SWNTs can be seen as indicated by an arrow. An isolated SWNT with a diameter of 1.3 nm can also been seen at the top of the image. The large feature in the lower left hand corner is thought to be the catalyst support. The small dark particles that can be seen on some of the bundles are nanoparticles (diameters < 3 nm) which, due to their greater contrast, are thought to be iron or magnesium oxide.

3.3.3.2 Surface area measurements

The surface areas of the supported catalysts were determined by plotting adsorption data using N_2 with the Brunauer, Emmet and Teller (BET) isotherm.[20] The results are presented in Table 3.2. As can be seen, the catalyst with the MgO support has the highest surface area. It is not obvious why the MgO supported catalyst has a higher surface area than the MgO support alone, whereas the surface area of the alumina supported catalyst is lower than alumina only. It is known that catalysts with greater surface areas are better at growing CNTs. However, the differences in the surface areas between the different catalysts do not seem large enough to explain the very large difference in the quality of tubes grown. It has been suggested that MgO may be a particularly good support for growing carbon nanotubes due to the strong interaction of the MgO with the iron. These interactions can be described in terms of Lewis acid / base interactions between metal oxide supports and metal catalyst particles,[1] and it is known that MgO has a high surface basicity compared to other metal oxides commonly used as supports.[21]

Sample	BET surface area ($m^2 g^{-1}$)
MgO supported catalyst	132.5
MgO support	107.5
Alumina supported catalyst	105.4
Alumina support	120.7

Table 3.2. BET surface areas for catalysts and supports. The catalyst supported on the MgO nanopowder has a larger surface area than the alumina supported catalyst.

In summary, The MgO supported catalyst was found to produce high quality SWNTs. To study the growth of SWNTs under various conditions, a large amount of this catalyst was prepared so that many CVDs could be carried out: the results are detailed in the next section.

3.3.4 Comparative syntheses of single–walled nanotubes

The MgO supported catalyst was found to produce high quality SWNTs. Due to air oxidation of the nanoparticles, it would be difficult to make a catalyst with exactly

the same amount of iron each time. Also it is difficult to measure the dispersal of the nanoparticles over the support. So, in order to minimise any difference between the catalysts used in the comparative CVDs, a large stock batch of the nanoparticles on MgO was prepared, using the methods detailed in Appendix A.1.

3.3.4.1 Initial optimisation of gas flows

Experiments were carried out to establish a suitable set of flowrate conditions to grow tubes, which could be used in the experiments where the temperature and the time were varied. Three trial CVDs were carried out to establish the flow rates that were suitable for growth of SWNTs. All three CVDs were carried out at 900 °C for 30 min with the flowrates of gas used as shown in Table 3.3. As shown below, the CVD carried out without a flow of hydrogen gave worse tubes in terms of a higher I_D / I_G ratio, but with a higher yield of carbon. However, when the flow of H_2 was increased from 0.8 l min^{-1} to 3.8 l min^{-1}, the quality of the tubes decreased and so did the yield. All Raman spectra from these samples, shown in Figure 3.5, showed RBMs. The mass % carbon of the samples is comparable to the values obtained from other Fe/MgO catalysts in the literature[15,22,23] (prepared with salts of the catalytic metal) which range in value from 55 wt % C down to 6 %. No experimental data on the amount of carbon deposited on Fe / MgO catalyst prepared with iron nanoparticles has been published.[11,23,24]

Methane flowrate / l min^{-1}	Hydrogen flowrate / l min^{-1}	Mass % C	Average I_D / I_G ratio
1.4	0	23	0.51
1.4	0.8	9	0.09
1.4	3.8	7	0.37

Table 3.3. Flowrates of gas as used in the CVD experiments carried out at 900 °C for 30 minutes. The average I_D / I_G ratio and the mass % C for each sample are also shown. The sample produced with 1.4 l min^{-1} methane and 0.8 l min^{-1} hydrogen had the smallest I_D / I_G ratio.

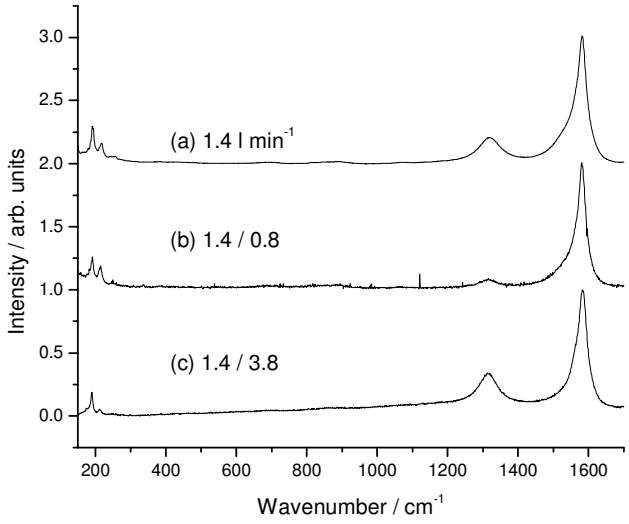

Figure 3.5. Representative Raman spectra for three different CVD experiments. All CVDs were carried out under the same conditions (900 °C for 30 minutes and a methane flowrate of 1.4 l min^{-1}) but they differed in the flowrate of hydrogen as follows: (a) no flow of hydrogen, (b) 0.8 l min^{-1}, and (c) 3.8 l min^{-1} of hydrogen.

The improvement in CNT growth from the presence of hydrogen during CVD has been explained in several different ways.[1,10,26-30] It has been suggested that the presence of hydrogen during the synthesis reduces the amount of pyrolysis of the carbon precursor,[10] which could lead to the formation of carbon impurities. Some works suggest that hydrogen helps to etch away impurities, such as amorphous carbon, to leave the pristine carbon nanotubes.[28-30] Others suggest that the hydrogen

helps to activate the catalyst by reducing the particles to metal.[1,26,27] In summary, from these experiments it was found that the best flow rate was 1.4 l min^{-1} of methane and 0.8 l min^{-1} of hydrogen.

3.3.4.2 Growth at different temperatures

Several CVDs were carried out at different temperatures with methane / hydrogen flowrates at 1.4 / 0.8 l min^{-1} for 30 minutes. SEM of the prepared samples revealed the presence of tube–like growth on all the samples except the one grown at 600 °C: see Figure 3.6 to Figure 3.10. By the SEM images, it can be seen that the CVD at 900 °C produced the densest growth of carbon nanotubes on the surface of the catalyst. The Raman spectra of all samples grown, shown in Figure 3.11, contain D and G bands, and RBMs suggesting that SWNTs are present. However, the quality of the tubes does depend on the temperature of the CVD. Table 3.4 shows the average I_D / I_G ratios for each sample. It can be seen that the CVD carried out at 900 °C produced the tubes with lowest I_D / I_G ratio, and therefore the highest quality tubes. Table 3.4 also shows the mass % carbon of each sample, and it should be pointed out that the sample that grew at 600 °C actually showed barely measurable growth. The Raman spectra collected on this sample came from very small isolated patches of carbon growth that were found on the surface of the catalyst. No growth of tubes was observed by SEM for this sample, and only bare catalyst was imaged as shown in Figure 3.6. It is difficult to explain why there should be patches of growth: it may be because there were some areas of support with a higher concentration of iron that were more conducive to tube growth.

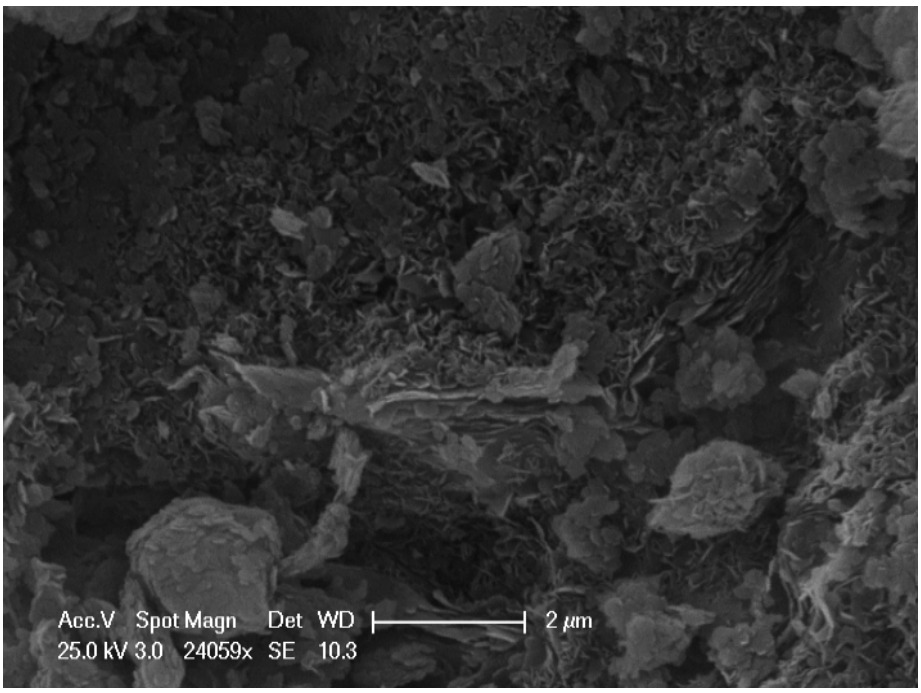

Figure 3.6. When CVD was carried out 600 °C, no growth of tubes could be seen on the surface of the catalyst.

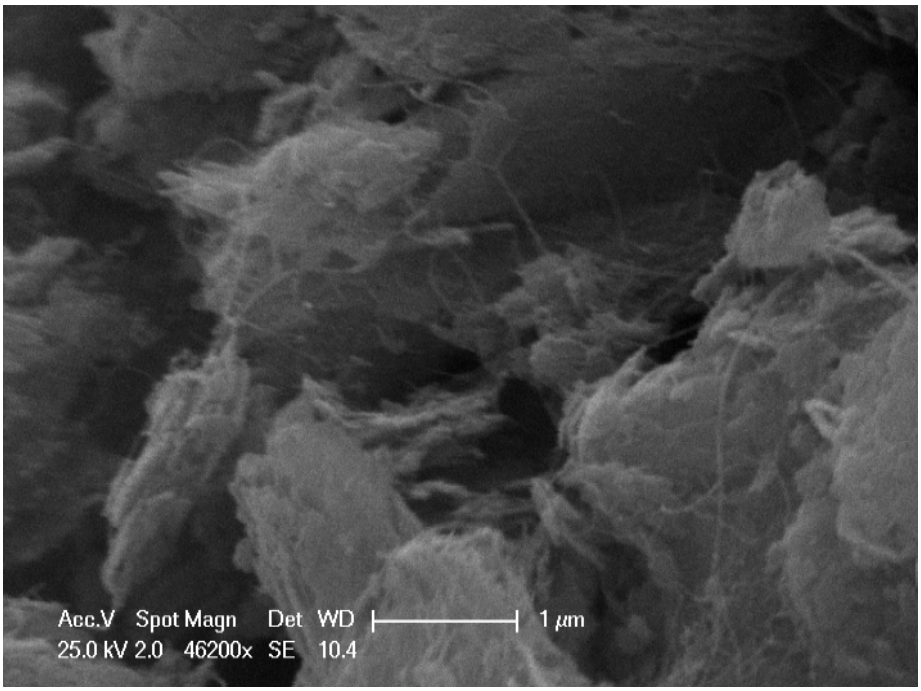

Figure 3.7. For the sample grown at 700 °C, there was growth of tubes visible on the surface.

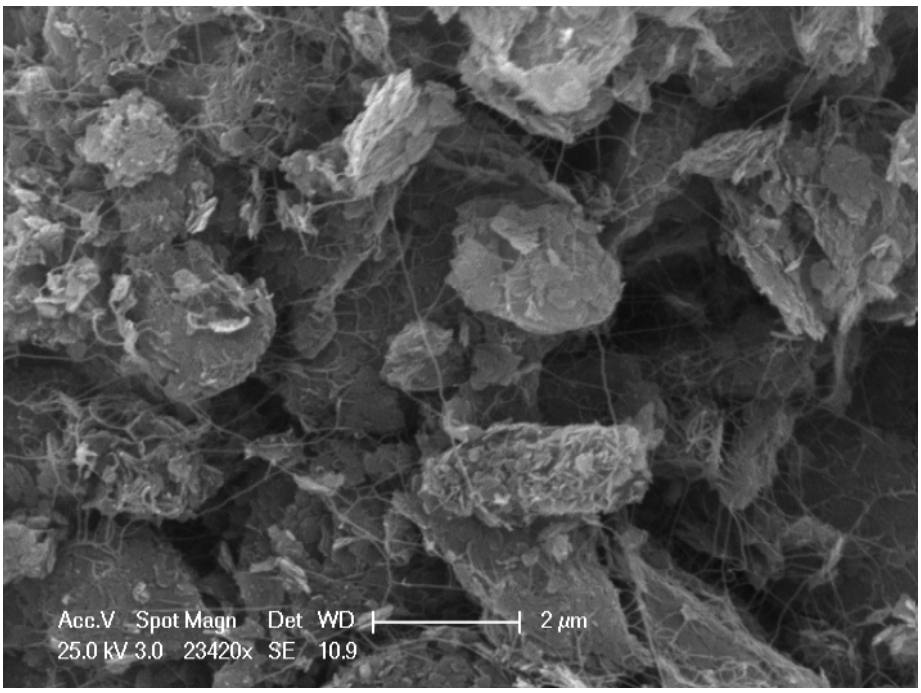

Figure 3.8. Growth of tubes on the sample, which was heated 800 °C during CVD, appears similar to that of the 700 °C sample.

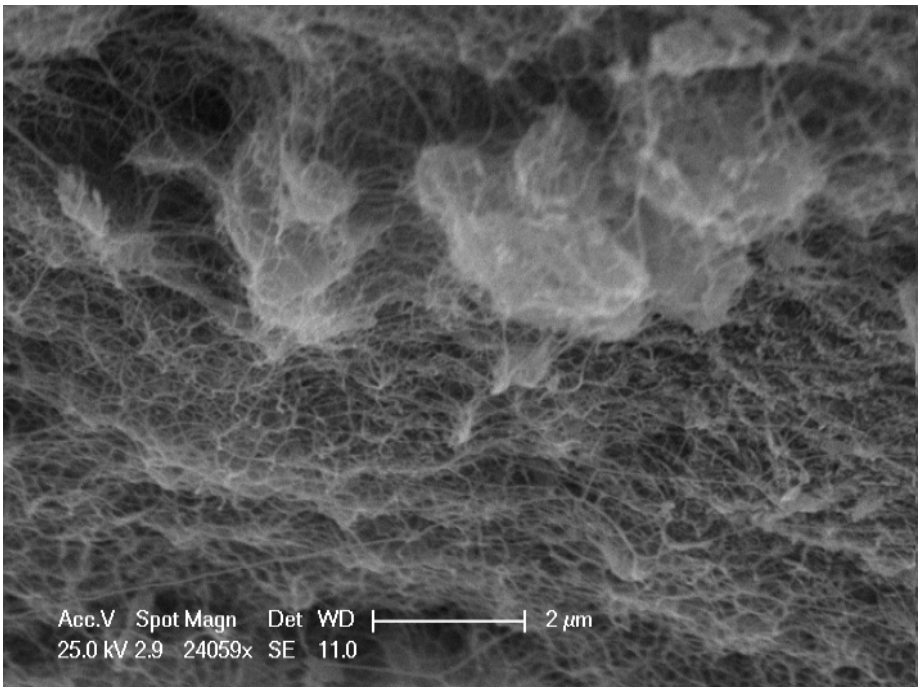

Figure 3.9. The 900 °C sample showed dense growth of tubes all over its surface.

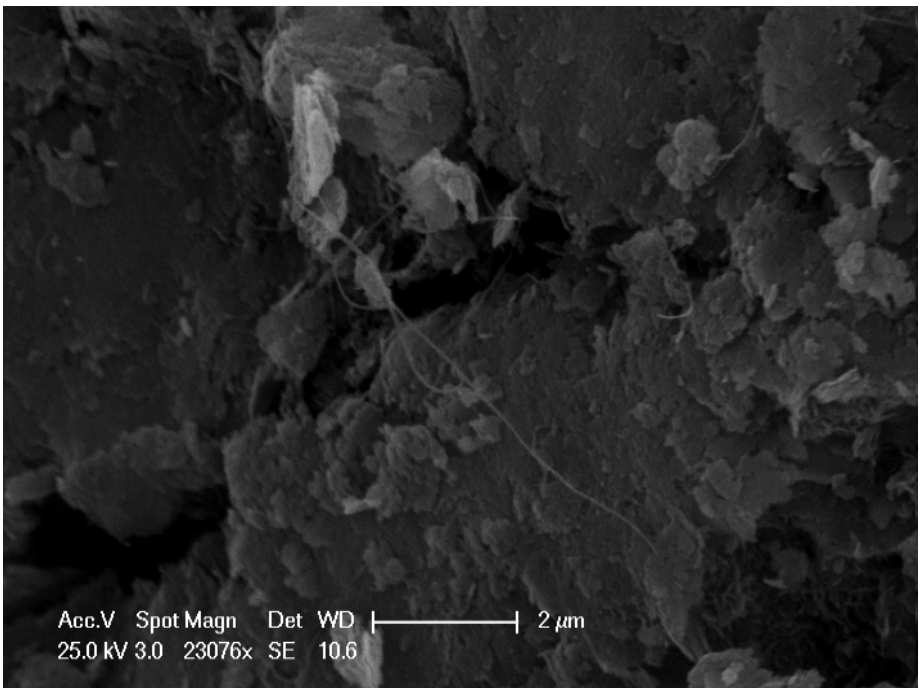

Figure 3.10. When CVD was carried out 1000 °C, only sparse growth of tubes could be seen. The rest of the carbon deposited on the catalyst must be in the form of impurities such as amorphous carbon.

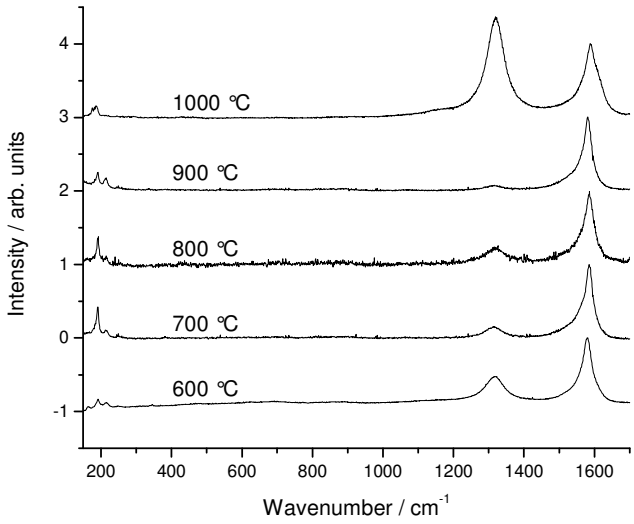

Figure 3.11. Raman spectra for CVD experiments carried out at different temperatures. It should be noted that all samples, except that grown at 600°C, were covered in carbon growth. The 600 °C sample showed very little growth; the Raman spectra in this case were obtained from selected small isolated patches of growth.

Temperature / °C	Mass % C	Average I_D / I_G ratio
600	0	0.80
700	2	0.25
800	2	0.36
900	7	0.09
1000	11	2.23

Table 3.4. Mass % C and average I_D / I_G ratios of CVD products grown at different temperatures.

There was a sharp increase in the amount of carbon deposited when the temperature was increased from 800 °C to 900 °C. Also, there was an increase in the graphitization of the sample, as demonstrated by a decrease in the I_D / I_G ratio. An increase in the growth of tubes was apparent by SEM, as can be seen by comparing Figure 3.8 and Figure 3.9. Figure 3.9, the sample prepared at 900 °C, shows much denser growth of tubes.

There is evidence that SWNT growth is enhanced by the catalyst particles being in a liquid state.[31] However, it should be noted that all the samples produced did have Raman spectra that showed RBMs. The presence of RBM peaks suggests that some SWNTs do form at any of these temperatures: if liquid nanoparticles are *necessary* for SWNT formation, then there must be some present at all these temperatures. A similar catalyst system of iron on MgO has also been shown to grow SWNTs at 600 °C, and even at 550 °C: in that work, the authors claim that this is the lowest temperature reported for growth of SWNTs. [11] Recently, there has been a report of growth of SWNTs at 550 °C, but this was carried out with acetylene, which is much more reactive.[12] All these low temperature syntheses, where growth occurs below 600 °C, were carried out with preformed metal nanoparticles as catalysts. We suggest that high temperatures are generally required in CVD to aid the formation of small nanoparticles: if preformed nanoparticles are used, lower temperatures can be used.

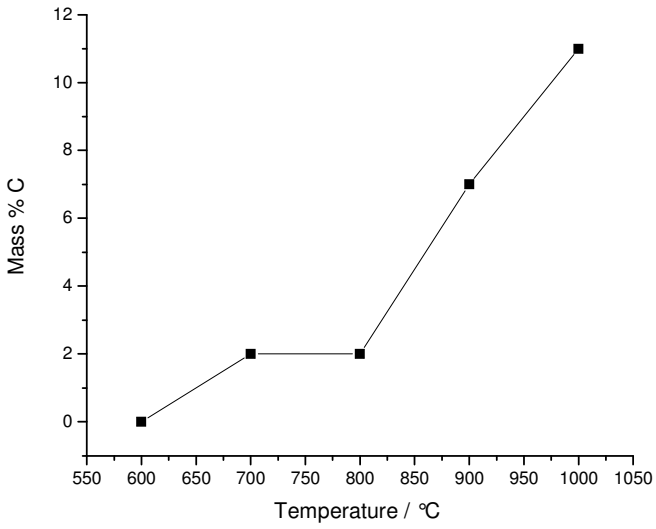

Figure 3.12. Plot of % mass carbon against temperature. The amount of carbon deposited on the catalyst during CVD increases with temperature.

At 1000 °C more carbon is deposited (Figure 1.12), and the CVD product is less graphitized than those grown at lower temperatures. SEM (Figure 3.10) showed that few tubes were visible on the catalyst, which suggests that a great deal of the carbon deposited was some form of non–graphitized carbon. The results at higher temperatures can be explained by non–catalytic reactions, which would form non–graphitic carbon impurities. At the catalyst, the increased decomposition rate forces too much carbon to be precipitated, which could give defective MWNTs or even terminate the growth of the tubes. At the higher temperature, the rate of etching by the reaction gases may also be increased so that any tubes produced will contain more defects.

To sum up, it was seen that the lowest I_D / I_G ratio and therefore the highest quality was produced in our experiments at 900 °C. This was chosen as the temperature that would be used for further experiments.

3.3.4.3 Variation in growth of single–walled nanotubes with time

To determine the effect of the duration of time that the methane is passed over the catalyst during CVD, we carried out a set of timed experiments. In this set of experiments the flowrate of methane and hydrogen were kept the same, 1.4 and 0.8 l

min^{-1} respectively, and the temperature was chosen to be 900 °C. From the plot of mass % C against time, presented in Figure 3.13 and Table 3.5, it can be seen that at first (< 45 min) the rate of deposition was roughly constant. At longer times (> 45 min) it can be seen that much less carbon was deposited on the catalyst. As the reaction conditions were the same (except for time) the decrease in carbon deposited at longer times suggests that after 45 min, the solid carbon formed is being etched by the gases. The composition of the gases was the same throughout, so we might assume that the etching is occurring constantly, as long as some carbon has been deposited. During the first 45 min, the total rate of carbon deposition (including nanotubes and other carbon impurities) must be larger than the rate of etching.

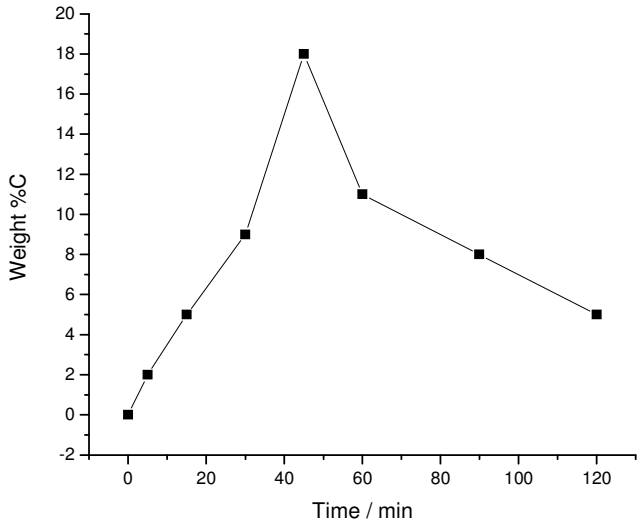

Figure 3.13. Plot of mass % C against duration of CVD.

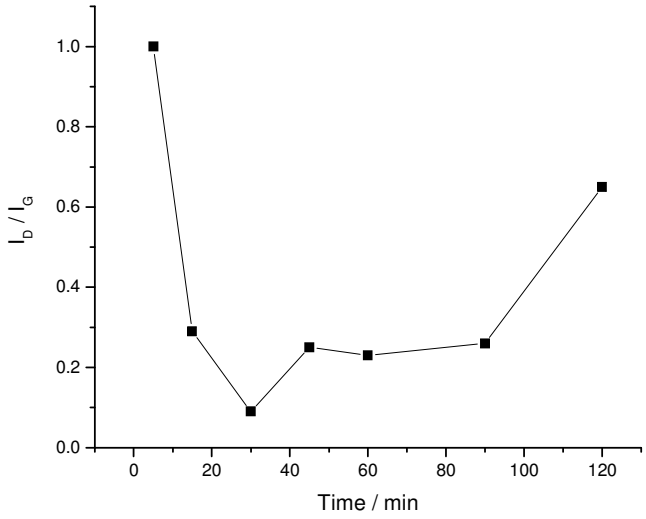

Figure 3.14. Plot of average I_D / I_G ratio against duration of CVD.

During the period of increasing carbon deposition, the I_D / I_G ratio in the Raman spectra decreases with time, as demonstrated in Figure 3.14, which suggests that mostly well–graphitized carbon was being produced. The presence of SWNTs was confirmed by the presence of RBMs in the Raman spectra, as presented in Figure 3.15. Carbon impurities such as MWNTs will also be formed during the CVD, but if their formation dominated then the I_D / I_G ratio would not decrease. The Raman spectra of the CVD product from the shortest time (5 min) show large I_D / I_G ratios: indicating that poorly graphitized carbon is produced. Interestingly, SEM showed that some tubes could be seen on the surface of the catalyst, Figure 3.16. The presence of RBMs in the Raman spectra suggests that some of the tubes visible in the SEM may be bundles of SWNTs (perhaps well graphitized). However, the large I_D / I_G ratio suggests that the sample also contains amorphous carbon, or that some of the tubes visible could be poorly graphitized MWNTs. The large I_D / I_G ratio at the start, which decreases with time suggests that, under these CVD conditions, the catalyst produces either badly graphitized tubes (SWNTs or MWNTs) or amorphous carbon first, before the growth of well–graphitized SWNTs starts to dominate.

Time / min	Mass % C	Average I_D / I_G ratio
0	0	–
5	2	1
15	5	0.29
30	9	0.09
45	18	0.25
60	11	0.23
90	8	0.26
120	5	0.65

Table 3.5. Characterization of samples produced at 900 °C, with flowrates of methane at 1.4 l min^{-1} and hydrogen at 0.8 l min^{-1}, but differing lengths of time that the methane is passed over the catalyst for the CVD.

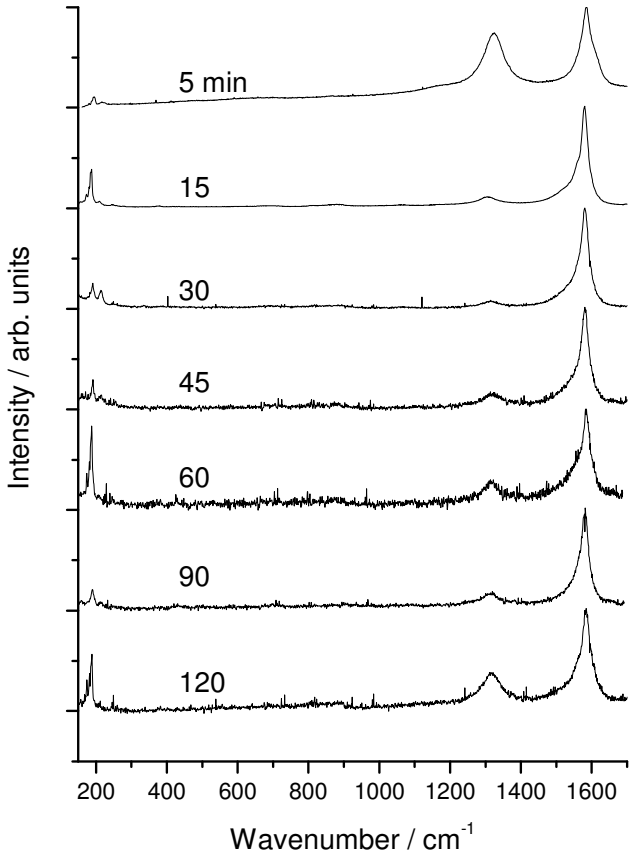

Figure 3.15. Raman spectra of samples produced by CVDs with the same conditions but different lengths of time. The highest quality tubes, with the lowest I_D / I_G ratio, were obtained after 30 minutes.

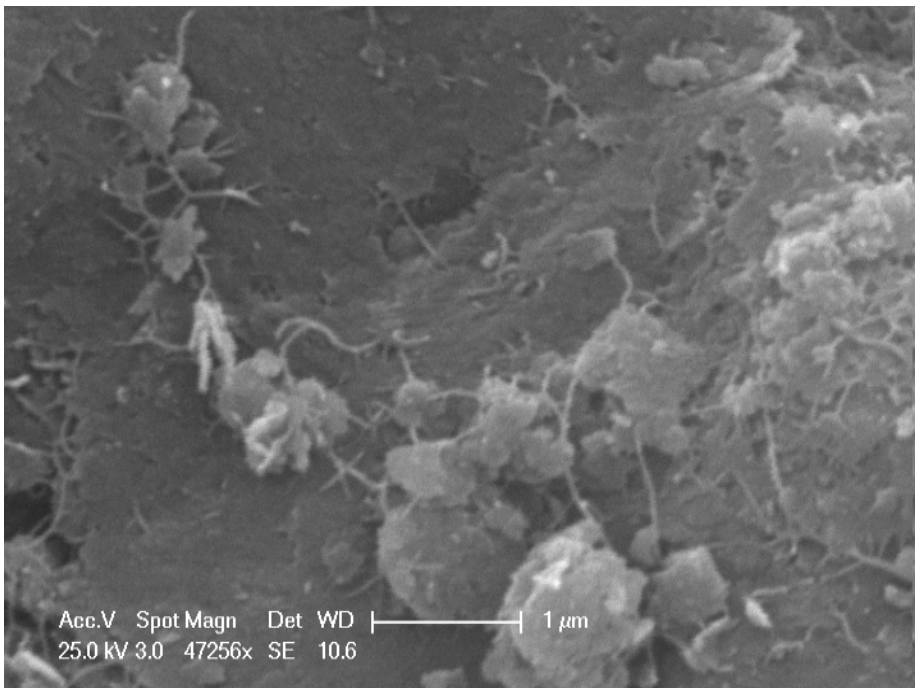

Figure 3.16. The sample with 5 minutes growth time can be seen to have tubes on some areas of the catalyst.

The mixture of gases in the furnace is constant over time, so the growth rate of SWNTs should be proportional to the number of nanoparticles actively growing nanotubes. As stated earlier, the observed rate of growth of SWNTs appears to be roughly constant at the beginning of the CVD. If the observed growth rate is dependent on the number of nanoparticles that are able to grow tubes, this suggests that the number of active particles is roughly constant during this initial (< 45 min) period. In the most widely accepted model of nanotube growth, the catalyst nanoparticles must be reduced to the metallic state.[2] For our experiments, where the constant growth rate is observed, the reduction process must be forming new active nanoparticles at around the same rate that any nanoparticles are being deactivated. There appears to be an abrupt change in the deposition of carbon between 45 and 60 minutes. This change in deposition suggests that at this point there are no nanoparticles left to replace those that are terminating. The cause of termination is not well understood, the most common hypothesis being that the nanoparticle becomes encapsulated with carbon so that it can no longer dissociate methane to add to the nascent nanotube.[1-3] As the number of active particles decreases, the rate of SWNT growth decreases, so after around 60 minutes the rate of etching is larger than

the rate of growth and the amount of carbon deposited on the catalyst decreases. During this period where etching dominates, the I_D / I_G ratio increases with time. This increase suggests that either the etching reaction reduces the quality of the tubes by causing defects to their structure, or that the SWNTs are preferentially removed during the etching so that a greater proportion of carbon impurities are left behind.

In the literature it has been reported that the rate of SWNT growth usually slows with time. This is most often ascribed to the formation of amorphous carbon around the support, which slows the diffusion of gas to the catalyst particles.[2,16,32] In our experiments, by comparison, the rate of growth is until there is the sudden change between 45 and 60 min. Etching throughout the entire duration of CVD could reduce build–up of amorphous carbon, allowing the tube growth to be constant. Conditions for growth of SWNTs in which carbon is etched are attractive in that the rate of growth remains high and amorphous carbon is removed. However, it should be noted that the growth of tubes still eventually ends, and that the etching does seem to damage the tubes that are formed. A time of 30 minutes was chosen for most of following CVD because it gave the tubes with lowest I_D / I_G ratio, i.e., the best quality, and the tubes are believed to be still growing at the time.

3.3.4.4 Methane experiments

The gases used during CVD are, of course, very important to the quality of the carbon nanotubes produced. As stated previously, the quality of the nanotubes produced can be improved by including a buffer gas, such as hydrogen and argon, to dilute the carbon–containing gas that forms the tubes. To understand the growth of nanotubes, the simplest system was explored: that is CVD with only the carbon–containing gas. Several CVD experiments were carried out at 900 °C for 30 minutes with different flowrates of methane only, and results are presented in Table 3.6.

Flowrate methane / l min^{-1}	Mass % C	Average I_D / I_G ratio
0.07	17	0.24
0.3	19	0.35
0.7	22	0.39
1.4	23	0.51
4.0	17	0.33
6.8	17	0.18

Table 3.6. Flowrates and characterisation for samples prepared at 900 °C for 30 min, with different flowrates of methane only.

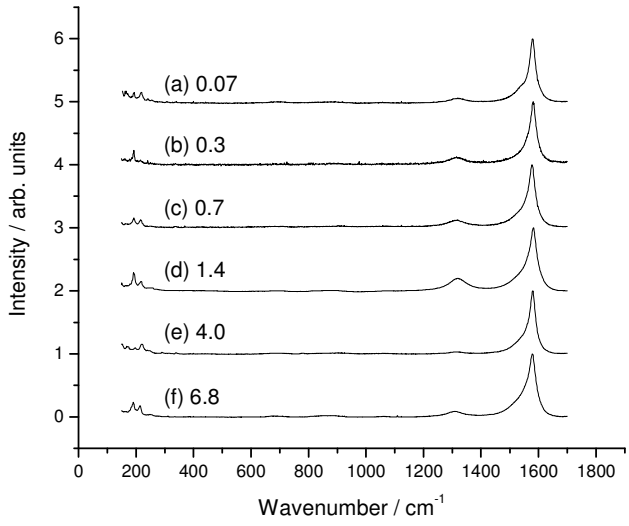

Figure 3.17. Raman spectra of products from CVDs with different flowrates of methane only. The spectra chosen for each sample were those with the lowest I_D / I_G ratios.

Representative Raman spectra for the samples are shown in Figure 3.17. All spectra showed RBMs, which indicate that SWNTs are present in the samples. Comparing all the spectra obtained, there was no evidence of different distributions of chiralities for each of the samples, because the same RBMs were present in all spectra, and the shapes of the G band were not significantly different. However, as Figure 3.18 shows, average I_D / I_G ratios for the samples did change with the methane flowrate, as did the amount of carbon deposited on each sample (mass % C) as shown in Figure 3.19.

There is a maximum in both of the plots at the same flowrate 1.4 l min^{-1}, which shows that a high quality of tubes (a small I_D / I_G ratio) can be obtained by using a very high flowrate of methane or a very low flowrate. In addition, it is observed that with the highest and lowest flowrates the least carbon is deposited on the catalyst during CVD. SEM images of the samples prepared with the lowest and highest flowrates are shown in Figure 3.20 and Figure 3.21 respectively. Both of the samples had much denser growth of tubes than the sample with the 1.4 l min^{-1} flowrate of methane, as shown in Figure 3.22.

We can explain the smaller amount of carbon deposited at low flowrates by assuming that if the supply of carbon is sufficiently small, it will control the amount of carbon deposited. The actual amount of carbon deposited compared to the amount passed as methane (around 1% for the lowest flowrate 0.07 l min^{-1}) is very small: this is likely due to the large volume through which the methane can pass without being exposed to the catalyst. However, it is difficult to predict how the furnace setup will affect the CVD. The modelling that would be required to understand the flow of gas through system, in particular the effect of the flowrate of methane, would be complicated by the shape of the boat and the catalyst. Such detailed calculations were outwith the scope of the present work. As for the quality of nanotubes formed at the low flowrates, the lower amount of carbon available to form tubes might favour the formation of SWNTs, as is discussed in Chapter 4 where a smaller flux of carbon is seen to improve the I_D / I_G ratio and formation of SWNTs. Similar trends in formation of SWNTs with a low vapour pressure of camphor has been observed previously.[33]

At very high flowrates, the amount of methane that is available to react is also small. The amount of carbon is reduced due to the short residence time of methane in the furnace compared with lower flowrates. As the methane is exposed to the heated catalyst for only a short time, it is less likely to react, which may also reduce the formation of amorphous carbon as has been suggested elsewhere.[15] The lower amount of carbon able to form tubes might favour the formation of SWNTs, as suggested for the low flowrate conditions. The plots of I_D / I_G both and % mass C

deposited both show maxima near 1.4 l min^{-1}: at this point the CVD is not limited by the amount of carbon being supplied, and the residence time is long, which encourages the deposition of carbon.

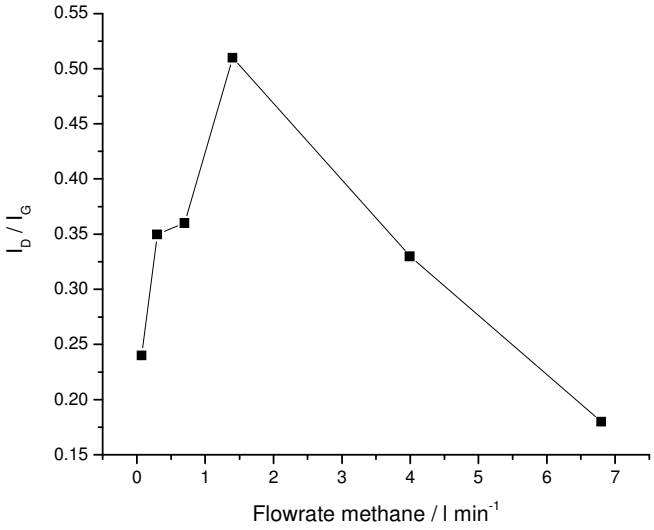

Figure 3.18. Plot of average I_D/I_G ratio against flowrate of methane shows a maximum at 1.4 l min^{-1}.

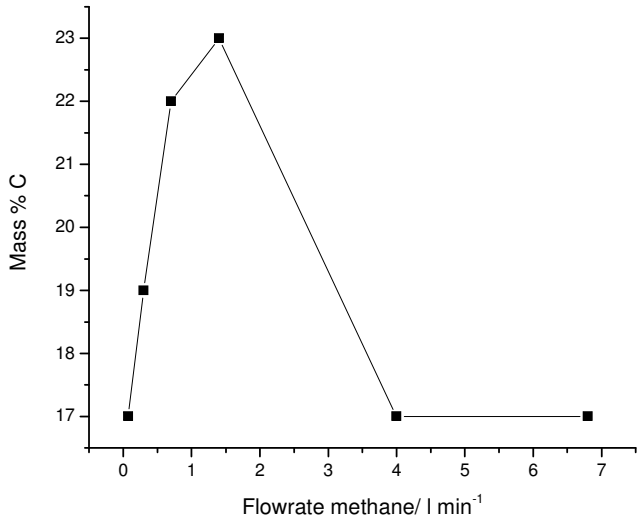

Figure 3.19. Plot of mass % C against methane flowrate shows that the poorest quality tubes were produced with a flowrate of 1.4 l min^{-1}.

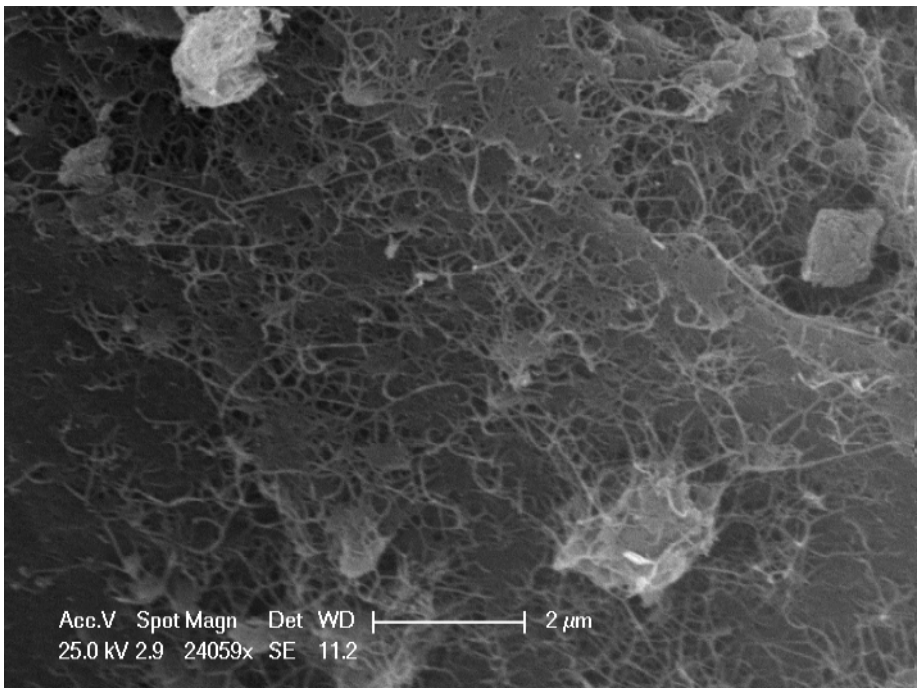

Figure 3.20. For the sample with a methane flowrate of 0.07 l min^{-1}, tubes were observed on the surface of the catalyst.

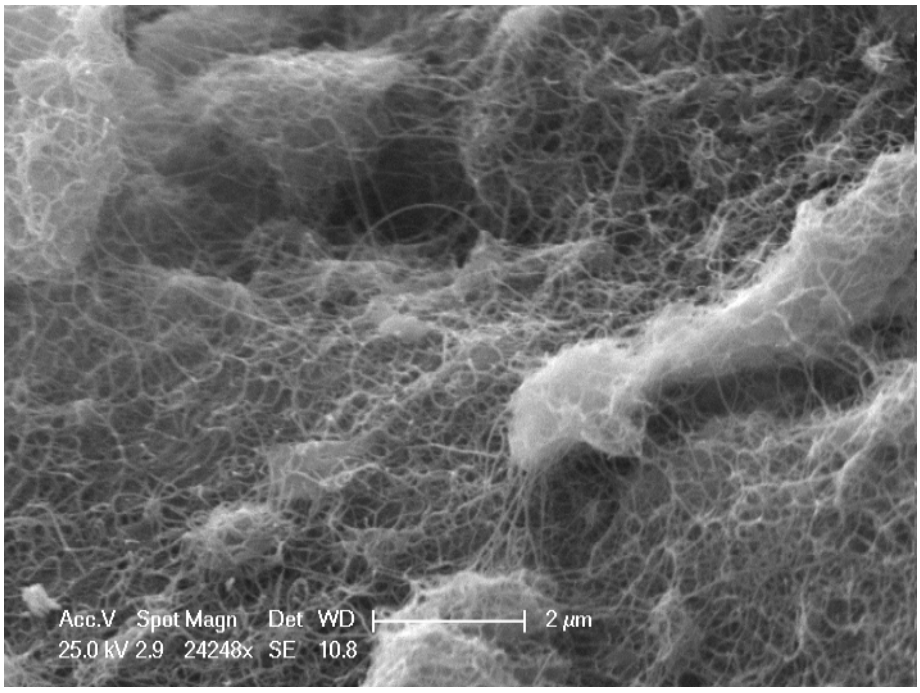

Figure 3.21. With highest flowrate of methane, 6.8 l min^{-1}, dense growth of nanotubes was observed.

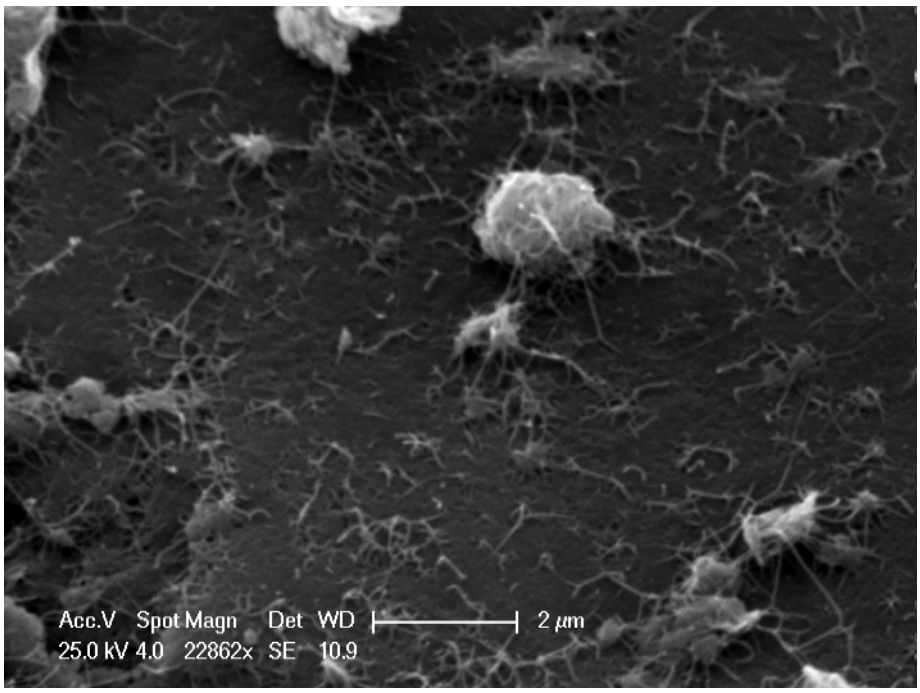

Figure 3.22. For the 1.4 l min^{-1}, poor growth of thick tubes that are possibly MWNTs can be seen on the surface of the catalyst.

3.3.4.5 CVDs with constant total flowrate of gas but varied flowrates of methane

In the experiments where the flowrate of methane was varied, it was not possible to vary both the concentration of methane and the residence time of the gas independently. To study the effect of the concentration of methane at nearly constant residence times, several CVDs were carried out with different component flowrates of methane and argon so that the total flowrate of the mixture for each experiment was the same (~ 1.4 l min^{-1}). The total flowrate was chosen to be equal to the flowrate of methane only that gave the largest amount of carbon deposited, as detailed in section 3.3.4.4.

Flowrate methane/ l min^{-1}	Flowrate argon/ l min^{-1}	Average I_D / I_G ratio	Mass % C
0.07	1.2	0.11	8
0.14	1.2	0.13	10
0.27	1.0	0.12	17
0.68	0.69	0.15	20
1.35	0	0.51	23

Table 3.7. Component flowrates of gases used in CVDs so that the total flowrates, and hence the residence times, are constant at around 1.4 l min^{-1} total flow of gas.

The CVD conditions for constant total flowrate are presented in Table 3.7, along with the average I_D / I_G ratio for the samples produced, and the mass % C deposited. Figure 3.23, shows increases in carbon deposited with increasing methane component flowrate. At low component flowrates (i.e., low methane concentrations) the amount of carbon deposited is very sensitive to the concentration of methane present, while at high concentrations there is less sensitivity. The differences in sensitivity to the methane concentration suggest that, at the low concentration, the nanoparticles can react faster than the carbon is supplied, so that termination of the growth is less likely. It might be possible to determine at what concentration the particles become saturated, that is the maximum concentration of methane at which particles can react without termination occurring. However, such experiments would be complicated by the possibility of other reactions that may deposit carbon but do not require the nanoparticles, such as gas phase reactions. Furthermore, it would be difficult to relate the concentration of methane in the reaction atmosphere to the actual rate of *decomposition* of methane.

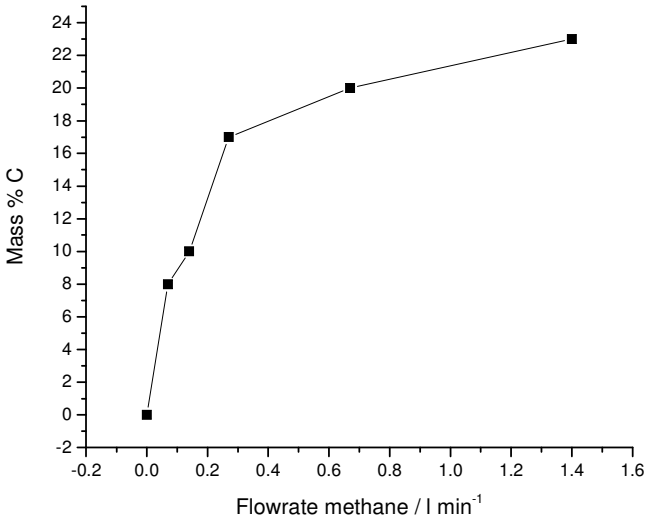

Figure 3.23. Plot of the mass % C of CVD samples produced with different component flowrates of methane that were diluted with argon to give the same total flowrate (1.4 l min^{-1}).

The Raman spectra shown in Figure 3.24 are representative spectra from each of the CVD samples. All samples show evidence of SWNTs being present. The plot of average I_D / I_G ratio with methane flowrate, shown in Figure 3.25, shows that the I_D / I_G ratio increases as the methane flowrate increases. This is direct evidence that high methane concentrations produce samples with high I_D / I_G ratios. It is difficult to say whether the high flowrate produces more carbon impurities, such as MWNTs and amorphous carbon, or if it actually produces SWNTs with more defects. It is interesting that the samples prepared with the lowest concentrations of methane do all have very similar I_D / I_G ratios. The similarity in the I_D / I_G ratios suggests that there might be an inherent limit to the quality of tubes that can be produced from this catalyst.

SEM images of the samples agree with the TGA results and Raman results in that the amount of tubes was fairly sparse on the samples with the lowest flowrate of methane, 0.07 l min^{-1}, as shown in Figure 3.26. The amount of growth can be seen to increase with the methane flowrate, so that very dense growth was observed on the sample with a methane flowrate of 0.7 l min^{-1}, as shown in Figure 3.27. However, less growth is seen on the sample prepared with a methane flowrate of 1.4 l min^{-1},

Figure 3.28, which, together with the large average I_D / I_G ratio, suggests that a lot of amorphous carbon has been deposited.

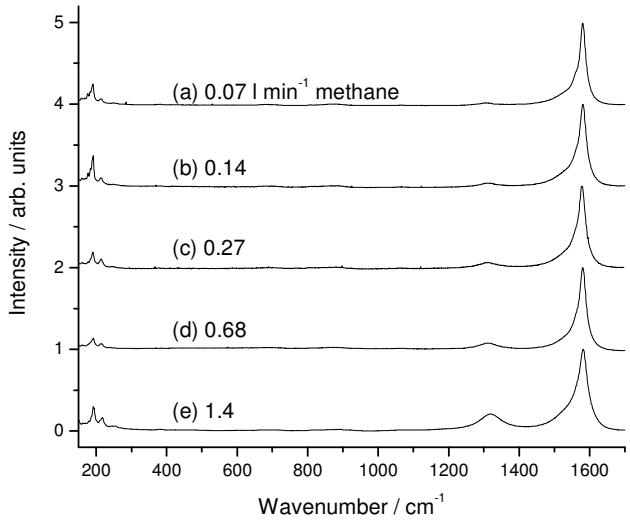

Figure 3.24. Raman spectra of products from CVDs where total flowrate was the same for all experiments (1.4 l min^{-1}) by varying the component flowrates of methane and argon gas.

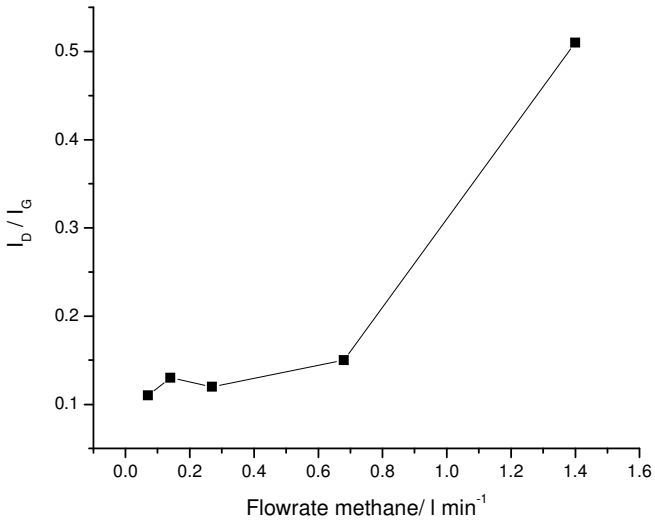

Figure 3.25. The average I_D / I_G ratio for samples produced by CVDs with a total flowrate of 1.4 l min^{-1} but differing component flowrates of methane and argon.

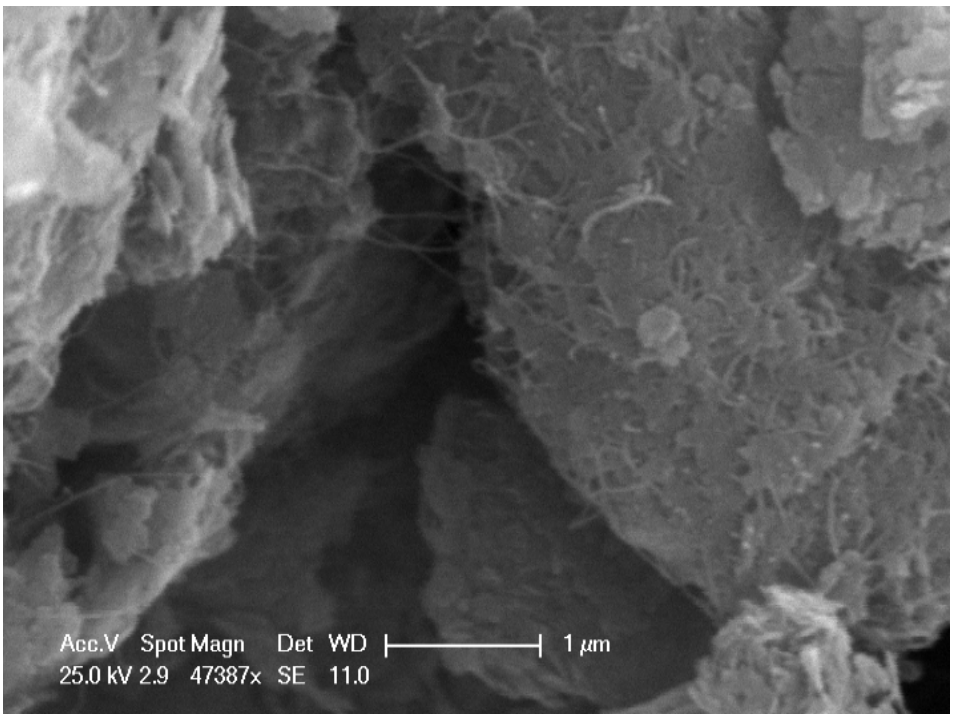

Figure 3.26. Sparse growth of nanotubes can be seen of the sample grown with the smallest flowrate of methane 0.07 l min^{-1}.

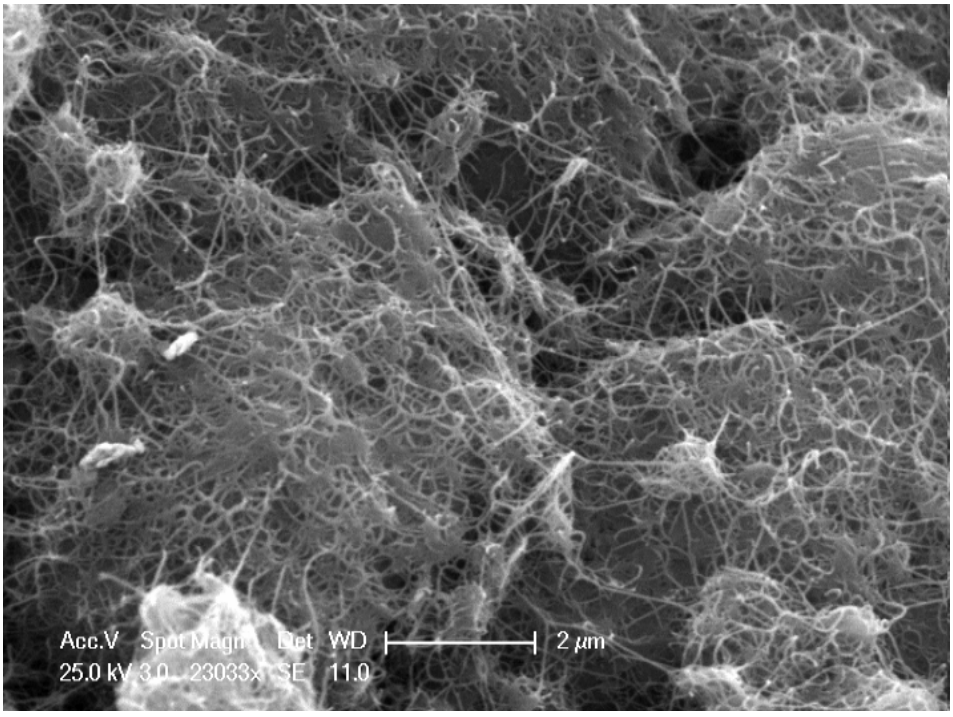

Figure 3.27. Dense growth of tubes can be seen on the sample with 0.7 l min^{-1} flowrate of methane.

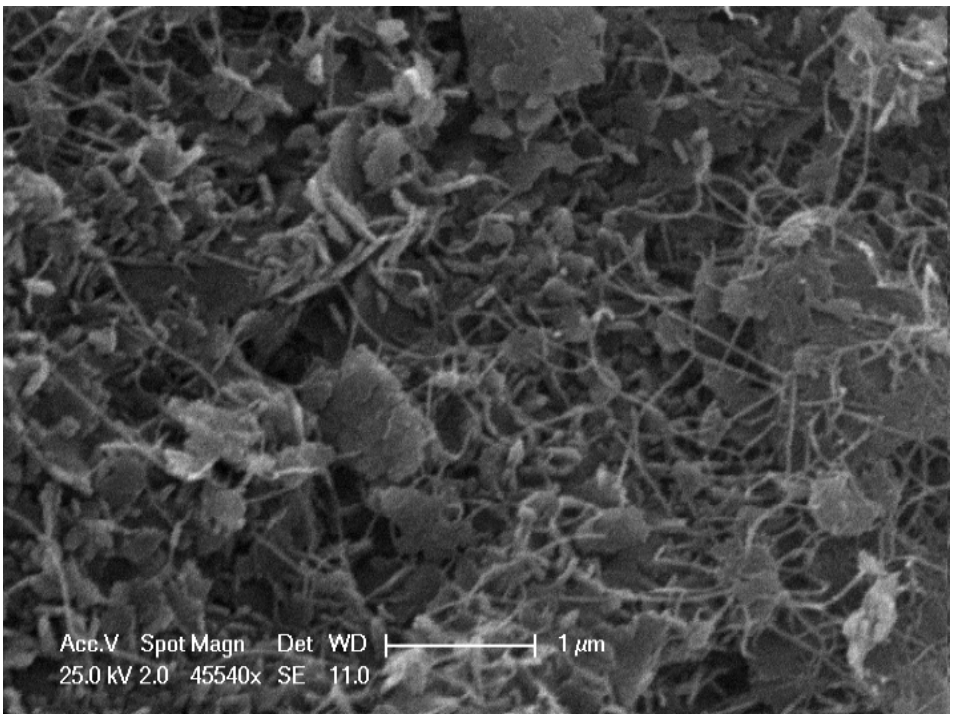

Figure 3.28. Poor growth of tubes seen on the sample with the highest flowrate of methane 1.4 l min^{-1} (no dilution with argon) suggests the deposition of a large amount of amorphous carbon due to the large I_D / I_G ratio and the large % mass of C for the sample.

By comparing the dependence of mass % C and average I_D / I_G ratio on methane concentration (Figure 1.24 and Figure 3.25) it can be seen that there is a balance between the amount of carbon deposited and the quality of the tubes produced. The shapes of the two graphs suggest that the best quality tubes are obtained when the growth of tubes is controlled by the concentration of carbon available. As the concentration increases, the amount of carbon deposited comes to a saturation point, and then perhaps non–tube forming reactions start to dominate, which increase the I_D / I_G ratio.

Closer inspection of the RBMs, as plotted in Figure 3.29, shows that there could be some variation in the diameters of the SWNTs present. The samples produced with the lowest flowrates of methane do seem to have more intense RBMs at lower frequencies (for example at 183, 176, 167, and 159 cm^{-1}). Care should be taken when interpreting the intensities of RBMs as they depend on many different factors such as the environment of the tubes. However, the systematic differences in the RBMs suggest that there is a difference in the distribution of chiralities and diameters of

SWNTs between the samples. This could be an indication that the amount of carbon available during the growth process has an effect on the chiralities produced. The variation in the chiralities of tubes with availability of the carbon precursors during growth has only very recently been noted in the literature.[34]

It is known that the frequency of a RBM is inversely proportional to the diameter of the SWNT from which it arises.[5] The increases in intensities of the low frequency RBMs could arise from a larger average diameter of the tubes. It has been mentioned earlier that it has been shown that in many cases, the diameter of a nanoparticle controls the size of the CNT that grows from it.[1,2] During a CVD with a low component flowrate of methane, it will take a longer time for the nanoparticles to be reduced as there is a smaller methane concentration. It is possible that the longer time needed for reduction to occur might promote the formation of larger particles, as they will have a longer time during which they can sinter or agglomerate. Once the nanoparticle has started grow a nanotube, it is assumed that is protected from sintering by the forming nanotube.[35] Conversely, it is also possible that at very low flowrates, larger particles that may have been likely to form MWNTs or to terminate growth, can actually produce single–walled tubes because of the restricted availability of carbon.

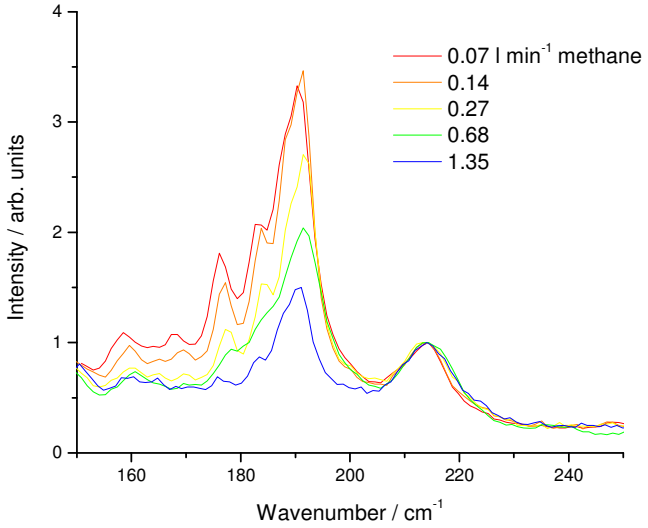

Figure 3.29. The RBMs of products from CVDs with different methane component flowrates at total flowrate 1.4 l min^{-1}. All spectra are normalised to the peak at 215 cm^{-1}. The samples with lower component flowrates of methane show more RBMs at lower frequencies.

3.3.4.6 Hydrogen reduction

The study of the nanotube growth process is complicated by the many reactions that are occurring during CVD. In particular, it is difficult to study independently the reduction of the iron oxide nanoparticles to the catalytically active iron. The reduction of the particles occurs at the very beginning of tube growth when it is thought the chirality of the tube may be determined.[36] Both reduction and growth–initiation processes occur soon after the carbon source is introduced. Both of the processes must depend on the amount of gaseous carbon precursor supplied. In order to establish a reaction mechanism, it would seem sensible that both the reduction process and the growth process would have to be unravelled.

It is generally accepted that the metal nanoparticles are the active form of the catalyst,[1-3,26,27] although there are some suggestions that substances such as iron oxide also play a part.[37,38] It has been found that some CVD processes have been improved by pre–reducing the catalyst, usually by passing hydrogen over the catalyst before the carbon–containing precursor is introduced. In the present work,

several attempts were carried out to reduce the catalyst fully before CVD. In this way it was hoped that it would be possible to study the growth of the carbon nanotubes having eliminated the effects of methane as an initial reducing agent. Unfortunately, most of the CVDs carried out with pre–reduction produced much less carbon and much higher I_D / I_G ratios than the corresponding non–reduction experiment: as can be seen from Table 3.8. It is interesting to note that where reduction increases the I_D / I_G ratio, it also seems to remove the RBMs. The lack of these low frequency peaks suggest that SWNTs are no longer being produced in these CVDs. The reduction process might promote the formation of larger particles that would produce MWNTs due to sintering of the metal particles formed. However, SEM of the samples that were reduced show no apparent growth of nanotubes, including MWNTs. An example is shown in Figure 3.30. The SEM images images are consistent with the high values of the I_D / I_G. If the catalyst particles are sintering then they must be forming particles that do not form MWNTs under these conditions, although the small amount of carbon deposited may make any tubes present difficult to observe.

Reduction conditions	CVD conditions	Mass % C	Average I_D / I_G ratio	RBMs present?
None	1.4 CH_4 / 0.8 H_2, 30 min, 900°C	9	0.09	Yes
1.4 H_2, 30 min	1.4 CH_4 / 0.8 H_2, 30min, 900°C	1	2.8	No
None	0.3 CH_4, 30 min, 900°C	19	0.35	Yes
0.2 Ar / 0.8 H_2, 10 min,	0.3 CH_4, 30 min, 900°C	10	1.3	No
None	1.4 CH_4 / 0.8 H_2, 30 min, 700 °C	3	0.24	Yes
0.2 Ar / 0.8 H_2, 10 min,	1.4 CH_4 / 0.8 H_2, 30 mins, 700 °C	1	1.2	No
None	0.03 CH_4 / 0.2 Ar, 20 min, 865°C	1	5.1	No
0.2 Ar / 0.8H_2, 10 min	0.03 CH_4 / 0.2 Ar, 20 min, 865°C	1	0.12	Yes

Table 3.8. In all cases, except for the pair in the bottom two rows, it can be seen that the reduction step reduces the amount of carbon deposited, increases the I_D / I_G ratio, and removes RBMs from the Raman spectrum. However, in the last pair the growth of SWNTs seems to be aided by the reduction step. This improvement in the growth suggests that the reduction step increases the activity of the catalyst. Note that this is seen with the lowest component flowrate of methane (0.03 l min^{-1}).

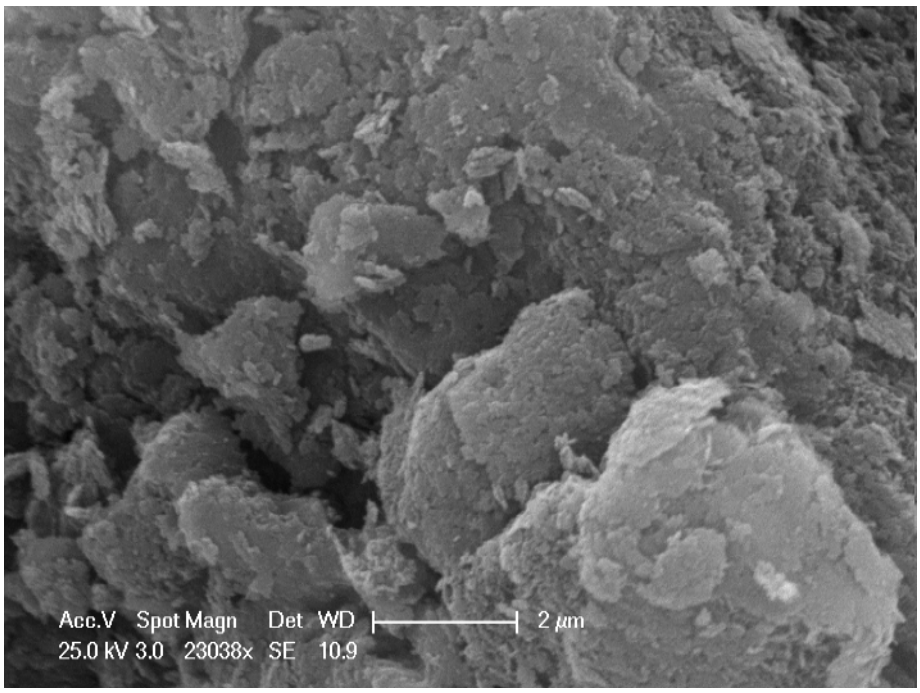

Figure 3.30. SEM of the sample that was reduced before CVD, with 1.4 l min^{-1} CH_4 and 0.8 l min^{-1} H_2 for 30 minutes at 900°C, shows no growth of nanotubes. None of the samples that were reduced before CVD showed any growth of nanotubes by SEM.

There is evidence that the introduction of hydrogen actually makes the catalyst more active. A CVD experiment was carried out with the MgO supported catalyst described in the other experiments, but using the CVD conditions described in Chapter 4. The CVD was carried out at the lower temperate of 865 °C and a very low flowrate of methane (0.03 l min^{-1}) which was diluted with a flow of argon (0.2 l min^{-1}). This CVD deposited very little carbon (~ 1% C by mass) and its Raman spectrum, Figure 3.31(a), shows that the carbon produced was very amorphous, as is evident from the very large D band present. However, when the catalyst was reduced with a mixture of 0.2 l min^{-1} argon and 0.8 l min^{-1} hydrogen for 10 min immediately before the methane was admitted, very different results were obtained. The amount of carbon deposited was around the same (~ 1% C by mass) as for the unreduced sample, but the Raman spectra collected were very different: as can be seen from the spectrum presented in Figure 3.31(b). The D band is much less intense indicating that much more graphitized carbon was produced. Moreover the intensity of the RBMs, particularly the very intense peak at 188 cm^{-1}, and the splitting of the G band, are very different to any Raman spectra produced with this particular catalyst. These

results suggest a different distribution of chiralities or diameters has been produced during the CVD. The improvement of the tubes produced suggests that the hydrogen actually activates the catalyst to produce SWNTs: without reduction the catalyst is not able to produce tubes under identical of conditions. If the hydrogen does make the catalyst more active, it is unusual that the CVD products from both the reduced and non–reduced experiments deposit around the same amount of carbon (~1% C by mass). It should be noted, however, that it is very difficult to measure if there is actually a difference in the amount of carbon in the two samples due to the limits of precision in the TGA. Due to the low amount of growth, SEM did not reveal visible tubes for either sample.

There are other features of this successful pre–reduction that are interesting. The presence of RBMs in the Raman spectra and the low I_D / I_G ratio indicate that the formation of MWNTs has not become dominant, which suggests that the reduction conditions used in this CVD did not promote the formation of larger nanoparticles as in the other pre–reduction experiments. Indeed, there are some RBMs at higher frequencies (i.e., smaller tubes) that are not observed in any other Raman spectra produced from this catalyst. The presence of SWNTs does call into question whether the all other pre–reduction results in Table 3.8 can be explained by nanoparticles coalescing to form larger particles. The decrease in the quality and yield of tubes produced in CVDs that include a reduction step can be explained by the increase in over–activity of the catalyst. The reduced metal nanoparticles may decompose methane more quickly: thus increasing the rate of termination so that overall there is a drop in the amount of carbon deposited. The poisoning of the catalytic nanoparticles that are necessary to form SWNTs, allows the formation of amorphous carbon to dominate, and the I_D / I_G ratio is seen to increase.

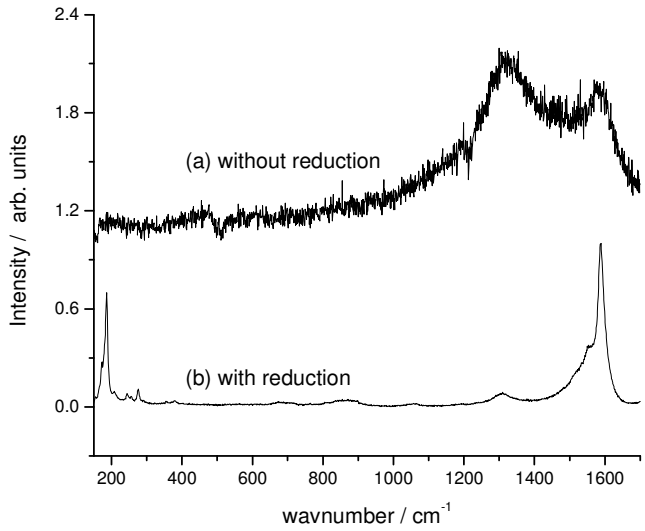

Figure 3.31. Raman spectra of products from CVDs with identical conditions (865 °C, 20 minutes, 0.03 l min^{-1} methane with 0.2 l min^{-1} argon) except (a) was not treated with hydrogen, and (b) was exposed to 0.8 l min^{-1} with 0.2 l min^{-1} argon for 10 minutes at 865 °C (pre–reduction) before the methane was introduced.

3.3.5 Summary

A catalyst system was devised in order to compare CVDs with different conditions, so that insight into the nanotube growth mechanism could be gained. The catalytic metal, iron, was added to the support as preformed metal oxide nanoparticles. Pre–formed particles were used in an effort to produce a catalyst that, when active, consists of nanoparticles with well–defined diameters that were able to produce SWNTs.

In the first set of experiments (section 3.3.4.2), several CVDs were carried out with the same reaction conditions, except the temperature was varied. As has been reported previously for similar iron / methane growth systems, the optimum temperature for SWNT growth was ~ 900 °C. The selection of temperature was found to affect the balance between rate of formation of tubes and the rate of decomposition of the methane to form carbon impurities. At 900 °C, the formation of SWNTs proceeded quickly, and the decomposition of the methane was slow enough

that CVD products with low I_D / I_G ratios were produced. SWNTs were formed in all the experiments, even those at low temperature (600 °C).

When the duration of the CVD was varied while keeping the same reaction conditions (section 3.3.4.3), it was found that at short CVD times (< 30 min), the growth rate of the nanotubes was constant. In previous studies it had been shown that the rate of growth of CNTs decreases with time until the amount of carbon deposited is constant with time. The decrease in rate is usually explained in terms of the particles becoming surrounded by amorphous carbon that slows the transport of the methane to the particle surface.[32] We found there was an abrupt change in the amount of carbon deposited with time (~ 45 min) after which carbon is actually etched away. As the flows of gases were kept the same throughout all the experiments, etching must happen during the entire duration of the CVD, as long as there is carbon present. The high rate of etching might explain the constant growth rate at short CVD times, as amorphous carbon is being quickly removed.

The simplest CVDs carried out, during which only methane was flowed over the catalyst at different rates, actually showed complicated trends that were explained in terms of several different processes. It was found that the quality of tubes was improved by growing with very high or very low flowrates of pure methane. The amount of carbon deposited was also found to be small at high and low flowrates. At some intermediate flowrate, the amount of carbon deposited was maximized: but, unfortunately, the quality of tubes was poor. The low carbon deposition and high quality of tubes at low flowrates of methane was explained in terms of the limited availability of carbon. The low growth of tubes at high flowrates, where there is a high quality of tubes produced, was also explained in terms of low availability of carbon. However, at high flowrate the amount of carbon deposited is not limited by the flowrate, but rather the small residence time of the methane in the furnace.

In order to separate the effects of residence time and total flowrate, several experiments were carried out using different fractional mixtures of methane and argon to give a fixed total flowrate (section 3.3.4.5). The variation of the average I_D /

I_G ratio and amount of carbon deposited showed that below some particular (undetermined) methane fraction, the nanoparticles can react with the amount of methane that is supplied without forming non–graphitic carbon side products. The Raman spectra of the samples also suggested that the lower component fractions (lower concentrations) of methane produced different distributions of nanotube chiralities or diameters. Up to now, the effect of carbon concentration on the chiralities of nanotubes produced has not been discussed in depth in the literature. Further experiments in this area may be useful to further understand the growth mechanism and perhaps gain some control over the chirality of nanotubes formed during CVD.

Several CVDs were carried out where the catalyst was exposed to hydrogen gas before the methane was introduced (section 3.3.4.6). The results showed that pre–reduction of the catalyst produces less tubes with higher I_D / I_G ratios. Several explanations have been put forward in the literature for similar observations, which mostly invoke some change in the size or availability of the nanoparticles in the catalyst. However, a CVD where a very low flow of methane was used did not produce SWNTs *unless the catalyst was reduced with hydrogen*. The production of SWNTs from a reduced catalyst suggests that the poorer yields of carbon from all the other pre–reduction CVDs are not due to changes in the size of the nanoparticles present. It is rather suggested that the hydrogen reduces the nanoparticles to metal, thereby increasing the activity of the catalyst to such an extent that it causes terminal amounts of carbon deposition, unless there is only a very small flow of methane available.

3.4 Conclusions and Future Work

This work has shown that iron oxide nanoparticles supported on a high surface area magnesium oxide can be used to grow high quality SWNTs under CVD conditions. The tubes produced were comparable, in terms of their I_D / I_G ratio, to tubes reported in the literature that were produced with similar iron on magnesium oxide catalysts.[11,15,22,24,25]

As has been noted previously, the temperature, the availability of methane and the length of time that the catalyst was exposed to methane were all found to be important factors that influenced both the quality of the tubes produced (I_D /I_G ratio) and the mass of carbon deposited on the catalyst.[33] It was also noted that both deposition and etching of carbon must have been occurring during the CVD process as the mass of carbon deposited actually decreased with time after a certain length of time. This decrease was attributed to the poisoning of the catalyst and the etching of the carbon by the gases in the furnace.

As stated previously, the availability of the carbon was found to be an important factor in nanotube growth. In CVDs, where the availability of carbon was large, large amounts of carbon were deposited but with few SWNTs. Samples with very low I_D / I_G ratios were obtained when the availability of carbon was low but only small amounts of carbon were depositied. The availability of carbon could be limited in CVD by using a low flowrate of methane gas or by decreasing the residence time of the methane in the furnace by increasing the total flowrate of the reaction gases.

Gas flows of methane and argon for best growth (in terms of greatest amount of carbon deposited and lowest I_D /I_G ratio) were explored for a 30 min CVD at 900°. Using methane gas only, the flowrate (and hence residence time) that deposited the greatest amount of carbon was found to be 1.4 L/min^{-1}. Several experiments were then carried out in which the total flowrate was held at 1.4 Lmin^{-1} but the concentration of methane in the argon buffer gas was varied. As the residence time of the gas was kept constant, it was clearly demonstrated that a lower concentration of methane produced higher quality tubes but a smaller mass of carbon. In future studies, it may be possible to investigate the mechanism of tube growth further by varying the availability of carbon to react. This data may be used to give an indication of relative rates of the different processes occurring nanotube growth by CVD (such as break down of the methane, the formation of tubes and the formation of amorphous carbon) and their dependences on the carbon concentration.

It was seen, for the first time, from the RBMs in the samples' Raman spectra, obtained in the experiments described above, that the availability of carbon to react also affected the diameter distribution of the SWNTs produced. This discovery opens up a new avenue of enquiry that may be very important for the growth of carbon nanotubes by CVD. The availability of carbon should be explored as a possible means of controlling the distribution of diameters and perhaps even the chiralities of a sample of tubes grown by CVD. However, the mechanism for the availability of carbon affecting on the diameter tubes that are grown during CVD has not been established. It is not clear whether the difference in diameters of nanotubes between CVDs can be explained in terms of the difference distribution of the diameters of the metal nanoparticles (perhaps produced by differences in the reduction process) or if the availability of carbon has an effect on the mechanism of tube growth so that different tubes are produced from the same size of particle. To explore this fully would require not only more comparative CVDs but also more in depth TEM and Raman spectroscopy.

It is clear that the reduction of the iron oxide to metal is an important step in the growth of carbon nanotubes. Preliminary experiments to study the reduction of the metal oxide with hydrogen gas before CVD showed that in most cases such a reduction was deleterious on the growth of tubes. It is difficult to ascribe a reason why this should be without a greater study of the catalyst before and after reduction with TEM. It does show that the growth of nanotubes using iron oxide on magnesium oxide catalysts is highly dependant on the way that the catalysts have been treated both thermally and chemically.

The catalyst and CVD conditions developed here have also been used in further work by Gavin Forrest of the School Chemistry at the University of Edinburgh. Single–walled nanotubes were synthesized and characterized so that the tubes could be used in toxicology studies by collaborators in Centre for Inflammation Research at the University of Edinburgh.[39] The catalyst was also used in a study on the inhibition of carbon nanotube growth on catalysts doped with alkali metal salts.[4]

Appendix A. Experimental details

A.1. Nanoparticle synthesis

Magnetite nanoparticles were prepared in a manner similar to the synthesis of Kang *et al.*[13] Typically, $FeCl_3.6H_2O$ (0.69 g, 2.6 mmol, Aldrich) and $FeCl_2.4H_2O$ (0.25 g, 1.3 mmol, Aldrich) were dissolved in 4 ml of 0.2 M hydrochloric acid which had been degassed by bubbling Ar gas through it. This solution of iron chlorides was then added quickly under argon to a degassed solution of 1.2 M ammonium hydroxide which was stirred magnetically. The solution went black immediately as the nanoparticles formed. The solution was left to stir for 30 min. The magnetic stirrer bar was removed and the black nanoparticles were induced to precipitate using a powerful magnet (3.8 cm × 3.8cm × 2.5 cm, ~ 1.3 T, $Nd_2Fe_{14}B$). The supernatant liquid was removed and 40 ml of degassed water was added. The particles were then re–suspended using an ultrasonic bath (Fisherbrand, FE 11002, Fisher Scientific, UK) and washed three more times in this way. Following this, the precipitated particles had 40 ml of degassed 0.01 M HCl solution added. The particles were then re–suspended and precipitated so that the supernatant could be removed and the particles could be dispersed in 40 ml degassed water to produce the final black dispersion of nanoparticles. A sample was removed and then dried in the oven so that the solid content could be determined. The solid content was then used to calculate how much of the dispersion would be required to be added to the support to prepare the desired catalyst (see Section A.2).

The nanoparticles were prepared for transmission electron microscopy (TEM) by diluting the as–prepared dispersion by a factor of 16. A small drop (2 μl) was then placed on a carbon coated 300 mesh TEM grid (Agar Scientific, UK) and was left to dry. TEM was carried out using a Philips CM120 Biotwin with an accelerating voltage of 100 kV.

A.2. Catalyst preparation

As the nanoparticles are known to settle out of the dispersion over time, catalysts were prepared by rotary evaporation so that the particles did not have a chance to

settle out. This allowed preparation of catalysts with evenly distributed nanoparticles through it. Catalysts were prepared by dispersing the supports, either Al_2O_3 (Aluminoxid C, Degussa) or MgO nanopowder (Aldrich), in water with sonication and then adding the required volume of nanoparticle dispersion. The catalysts were then sonicated for 10 min. The water was then removed using rotary evaporation and the catalyst was finally dried overnight in an oven at 80 °C. The dried catalyst was ground with a pestle and mortar to break up agglomerates, which resulted in a very fine powder. Surface area measurements were carried out with the assistance of Dr. Ronald Brown at the University of Edinburgh using Micrometrics Gemini 600 instrument with N_2 gas at 77 K.

A.3. Growth of carbon nanotubes by chemical vapour depostion

In all CVD experiments, 0.1 g of the catalyst was placed in an alumina boat in the centre of the alumina work tube (1 inch diameter) of a furnace (MTF 12/38/250, Carbolite, UK). Gas–tight ends were attached that were connected to the gas handling system. The furnace was then heated the sample to temperature (900 °C, unless otherwise stated) at a rate of 30 °C min^{-1} under a flow of 0.35 l min-1 of argon. Once the furnace had reached temperature the gas flows were changed to the required values. After a given time for the CVD, the gas flows were changed back and the catalyst was allowed to cool down under a flow of 0.35 l $min^{-1}$of argon. The samples were removed after the furnace had cooled to below 200 °C.

All CVD products were characterised by TGA (Stanton Redcroft Thermobalance TG762, heating from room temperature to 1000 °C at a rate of 10 °C min^{-1}) and Raman spectroscopy (Labram 300, 632.8 nm, 13 mW, with collections typically 100 seconds). Samples were prepared for TEM by dispersing some of the as–prepared products in ethanol with gentle sonication and dropping a little of the dispersed product onto carbon coated grids. The samples were viewed using a Philips CM120 Biotwin with an accelerating voltage of 100 kV. Samples for scanning electron microscopy (SEM) were prepared by scattering the powder onto a piece of carbon tape (a carbon sticky) that was affixed to a specimen stub. To ensure that the sample surfaces were conducting, they were covered with gold using a sputter coater.

Samples were imaged using a Philips XL30CP using the secondary electron detector with a typical working distance of 10 mm and a typical accelerating voltage of 30 kV.

3.5 References

1) A.-C. Depuis. The catalyst in the CCVD of carbon nanotubes—a review. *Prog. Mater. Sci.*, 2005, **50**, 929

2) A. Moisala, A. G. Nasibulin, E. I. Kauppinen. The role of metal nanoparticles in the catalytic production of single–walled carbon nanotubes—a review. *J. Phys.: Condens. Matter*, 2003, **15**, s3011.

3) R. B. Little. Mechanistic Aspects of Carbon Nanotube Nucleation. *J. Cluster Sci.*, 2003, **14**, 135.

4) H. Dai, A. G. Rinzler, P. Nikolaev, A. Thess, D. T. Colbert, R. E. Smalley. Single–wall nanotubes produced by metal–catalyzed disproportionation of carbon monoxide. *Chem. Phys. Lett*., 1996, **260**, 471.

5) P. E. Nolan, D. C. Lynch, A. Hall Cutler. Carbon Deposition and Hydrocarbon Formation on Group VIII Metal Catalysts. *J. Phys. Chem. B,* 1998, **102**, 4165.

6) M. S. Dresselhaus, G. Dresselhaus, R. Saito, A. Jorio. Raman spectroscopy of carbon nanotubes. *Phys. Rep.*, 2005, **409,** 47.

7) Y. Li, J. Liu. Preparation of Monodispersed Fe–Mo Nanoparticles as the Catalyst for CVD Synthesis of Carbon Nanotubes. *Chem. Mater.*, 2001, **13**, 1008.

8) M. Su, Y. Li, B. Maynor, A. Buldum, J. P. Lu, J. Liu. Lattice–Oriented Growth of Single–Walled Carbon Nanotubes. *J. Phys. Chem. B*, 2000, **104**, 6505.

9) Y. Zhang, Y. Li, W. Kim, D. Wang, H. Dai. Imaging as–grown single–walled carbon nanotubes originated from isolated catalytic nanoparticles. *Appl. Phys. A*, 2002, **74**, 325

10) Y. Li, W. Kim, Y. Zhang, M. Rolandi, D. Wang, H. Dai. Growth of Single–Walled Carbon Nanotubes from Discrete Catalytic Nanoparticles of Various Sizes. *J. Phys. Chem. B*, 2001, **105**, 11424.

11) H. Ago, K. Nakamura, N. Uehara, M. Tsuji. Roles of Metal–Support Interaction in Growth of Single– and Double–Walled Carbon Nanotubes Studied with Diameter–Controlled Iron Particles Supported on MgO. *J. Phys. Chem. B*, 2004, **108**, 18908.

12) D. Kondo, S. Sato, Y. Awano. Low–temperature synthesis of single–walled carbon nanotubes with a narrow diameter distribution using size–classified catalyst nanoparticles. *Chem. Phys. Lett.,* 2006, **422,** 481.

13) Y. S. Kang, S. Risbud, J. F. Rabolt, P. Stroeve. Synthesis and Characterization of Nanometer–Size Fe_3O_4 and γ-Fe_2O_3 Particles. *Chem. Mater.*, 1996, **8**, 2209.

14) J. Kong, A. M. Cassell, H. Dai. Chemical vapor deposition of methane for single–walled carbon nanotubes. *Chem. Phys. Lett*., 1998, **282**, 567.

15) L. Qingwen, Y. Hao, C. Yan, Z. Jin, L. Zhongfan. A scalable CVD synthesis of high–purity single–walled carbon nanotubes with porous MgO as support material. *J. Mater. Chem.*, 2002, **12**, 1179.

16) A. M. Cassell, J. A. Raymakers, J. Kong, H. Dai. Large Scale CVD Synthesis of Single–Walled Carbon Nanotubes. *J. Phys. Chem. B*, 1999, **103**, 6484.

17) N. N. Greenwood, A. Earnshaw. *The chemistry of the elements* (2^{nd} Ed.), 1998, Butterworth Heinemann.

18) M. T. Weller. *Inorganic Materials Chemistry*, 2001, Oxford University Press.

19) J. R. Smyth, T. C. McCormick. *Crystallographic Data for Minerals*. *in* Mineral Physics & Crystallography: A Handbook of Physical Constants. T.J. Ahrens (Editor), 1995, American Geophysical Union.

20) G. Attard, C. Barnes. *Surfaces*, 1998, Oxford University Press.

21) C. Sun, J. C. Berg. A review of the different techniques for solid surface acid–base characterization. *Adv. Colloid Interface Sci.*, 2003, **105**, 151.

22) G. Ning, F. Wei, Q. Wen, G. Luo, Y. Wang, Y. Jin. Improvement of Fe / MgO Catalysts by Calcination for the Growth of Single– and Double–Walled Carbon Nanotubes. *J. Phys. Chem. B*, 2006, **110**, 1201.

23) J.-F. Colomer, C. Stephan, S. Lefrant, G. Van Tendeloo, I. Willems, Z. Konya, A. Fonseca, Ch. Laurent, J. B. Nagy. Large–scale synthesis of single–wall carbon nanotubes by catalytic chemical vapor deposition (CCVD) method. *Chem. Phys. Lett.,* 2000, **317**, 83.

24) H. Ago, K. Nakamura, S. Imamura, M. Tsuji. Growth of double–wall carbon nanotubes with diameter–controlled iron oxide nanoparticles supported on MgO. *Chem. Phys. Lett.,* 2004, **391**, 308.

25) H. Ago, S. Imamura, T. Okazaki, T. Saito, M. Yumura, M. Tsuji. CVD growth of single–walled carbon nanotubes with narrow diameter distribution over Fe / MgO catalyst and their fluorescence spectroscopy. *J. Phys. Chem., B* 2005, **109**, 10035.

26) A. R. Harutyunyan, B. K. Pradhan, U. J. Kim, G. Chen, P. C. Eklund. CVD Synthesis of Single Wall Carbon Nanotubes under "Soft" Conditions. *Nano Lett.*, 2002, **2,** 525.

27) M. Lin, J. P. Y. Tan, C. Boothroyd, K. P. Loh, E. S. Tok, Y.-L. Foo. Direct Observation of Single–Walled Carbon Nanotube Growth at the Atomistic Scale. *Nano Lett.*, 2006, **6,** 449.

28) D. Mendoza, P. Santiago, E. R. Perez. Carbon nanotubes produced from hexane and ethanol. *Revista Mexicana De Fiscia*, 2006, **52,** 1–5.

29) G. Zhang, D. Mann, L. Zhang, A. Javey, Y. Li, E. Yenilmez, Q. Wang, J. P. McVittie, Y. Nishi, J. Gibbons, H. Dai. Ultra–high–yield growth of vertical single–walled carbon nanotubes: Hidden roles of hydrogen and oxygen. *Proc. Nat. Acad. Sci. USA*, 2006, **102**, 16141.

30) X. Zhao, M. Ohkohchi, S. Inoue, T. Suzuki, T. Kadoya, Y. Ando. Large–scale purification of single–wall carbon nanotubes prepared by electric arc discharge. *Diamond Rel. Mater.*, 2006, **15,** 1098.

31) A. R. Harutyunyana, T. Tokune, E. Mora. Liquid as a required catalyst phase for carbon single–walled nanotube growth. *Appl. Phys. Lett.*, 2005, **87**, 051919.

32) D. N. Futaba, K. Hata, T. Yamada, K. Mizuno, M. Yumura, S. Iijima. Kinetics of Water–Assisted Single–Walled Carbon Nanotube Synthesis Revealed by a Time–Evolution Analysis. *Phys. Rev. Lett.*, 2005, **95**, 056104.

33) M. Kumar, Y. Ando. Controlling the diameter distribution of carbon nanotubes grown from camphor on a zeolite support. *Carbon,* 2005, **43**, 533.

34) C. Lu, J. Liu. Controlling the Diameter of Carbon Nanotubes in Chemical Vapor Deposition Method by Carbon Feeding. *J. Phys. Chem. B,* ASAP Article 10.1021/jp0632283 S1520–6106(06)03228–7. Published on web on September 8, 2006.

35) Y.-L. Li, I. A. Kinloch, M. S. P. Shaffer, C. Singh, J. Geng, B. F. G. Johnson, A. H. Windle. Growth of Single–Walled Carbon Nanotubes by the Rapid Heating of a Supported Catalyst. *Chem. Mater.*, 2004, **16**, 5637,

36) S. Reich, L. Li, J. Robertson. Control the chirality of carbon nanotubes by epitaxial growth. *Chem. Phys. Lett.,* 2006, **421**, 469.

37) T. de los Arcos, M. G. Garnier, J. W. Seo, P. Oelhafen, V. Thommen, D. Mathys. The Influence of Catalyst Chemical State and Morphology on Carbon Nanotube Growth. *J. Phys. Chem. B*; 2004; **108**, 7728.

38) G. Eres, A. A. Kinkhabwala, H Cui, D. B Geohegan, A. A. Puretzky, D. H. Lowndes. Molecular Beam–Controlled Nucleation and Growth of Vertically Aligned Single–Wall Carbon Nanotube Arrays. *J. Phys. Chem. B*, 2005, **109**, 16684.

39) K. Donaldson, R. Aitken, L. Tran, V. Stone, R. Duffin, G. A. Forrest, A. Alexander. Carbon nanotubes: a review of their properties in relation to pulmonary toxicology and workplace safety. *Toxicol. Sci.*, 2006, **92**, 5.

40) G. A. Forrest, A. J. Alexander. Unpublished results.

4 Mechanism of carbon nanotube growth from camphor and its analogues by chemical vapour deposition

4.1 Introduction

4.1.1 Mechanism of carbon nanotube formation

It is known that the properties of a carbon nanotube (CNT) are controlled by its physical characteristics such as its chirality.[1,2] However, using current methods, samples of carbon nanotubes are usually produced as badly defined mixtures of SWNTs, MWNTs, and other impurities that are difficult to separate by length, diameter or any other characteristic.[3] To improve the feasibility of CNT–based electronics it would seem that the ability to adjust the reaction conditions so that a specific type of tube is favoured would be desirable. To this end, it is important to establish a detailed knowledge of the growth mechanism so that the growth of tubes can be controlled.[4,5]

Unfortunately, there is still great debate about the growth mechanism of CNTs,[6] which is partially due to the large number of conditions under which CNTs have been synthesised. Most of the reaction conditions for CNT formation are not conducive to detailed kinetic studies due to high temperatures and complex reaction environment, especially when considering processes occurring on the nanoscale.

Most syntheses of carbon nanotubes can be classified as either physical (high energy) or catalytic methods. The physical methods use a great deal of energy, for example by arc discharge, to form atomic carbon in the gas phase, which then condenses to form CNTs. The catalytic methods, such as chemical vapour deposition (CVD) use catalysts and—in general—quite high temperature (600 – 1000 ºC) to break down carbon–containing precursors, which then go on to react to form CNTs.[7,8] CVD is an important CNT production method as it offers many advantages over physical methods. The lower temperatures employed and less–specialised equipment necessary, makes CVD more attractive to industrial scale–up.[8,9] In addition, there are many parameters in CVD that can be explored as a way to control the tubes produced. For example, in addition to variables such as temperature and pressure, the choice of

catalyst support, and the carbon source can be studied. Using a CVD method, there has been some success in using preformed nanoparticles to produce nanotubes of specific size.[7] Surfaces can be patterned with catalyst,[10] and exposed to CVD conditions in order to make new nanoscale architectures with CNTs.[11] Growth of carbon nanotubes on surfaces is discussed in more detail in Chapter 6.

The formation of carbon nanotubes by CVD is a complex chain of reactions that involves many elementary steps.[12] Moreover, if good experimental evidence is available that supports a particular mechanism, then it is difficult to judge whether that mechanism only applies to those specific reaction conditions. Currently, from the literature, it is difficult to decide whether there are different reaction mechanisms occurring under different conditions, or if there should be one general mechanism that can explain all observed growths. In this work, we have focussed on one specific problem: the question of whether cyclic intermediates may be involved in growth of CNTs. We have looked specifically at growth using camphor as the carbon source.

4.1.2 Nano–structured carbon from camphor

The use of camphor as a precursor for chemical vapour deposition (CVD) of carbon nanostructures has been widely investigated. Fullerenes,[13] carbon fibers,[14] nanobeads,[15] and carbon nanotubes[16-19] have all been synthesized using camphor. Camphor is cheap and readily obtained from renewable resources, making it an ideal "green" bio–source for the production of nanotubes. In addition, it has been proposed by Kumar and Ando that the bicyclic structure of camphor (Figure 4.1) is key to the growth mechanism of CNTs.[16,19]

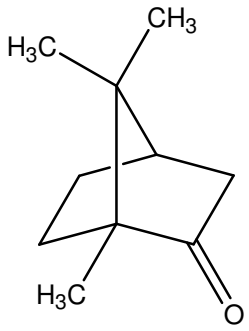

Figure 4.1. The structure of camphor. It has been proposed that the bicyclic structure of camphor is vital to the formation of carbon nanotubes in CVD using camphor as a carbon source.

4.1.3 Mechanism of nanotube growth from camphor

The suggested mechanism[16,19] of tube growth from camphor involves the addition of reactive pre–formed five– and six–membered rings or *cyclic radicals* formed by decomposition of the precursor: the bicyclic structure of camphor would, therefore, be vital to the production of tubes. The suggested growth mechanism is similar to the *ring addition mechanism* proposed for the formation of carbon nanotubes in CVD using benzene as the carbon source: [20,21] this mechanism, illustrated in Figure4.2, involves the adsorption of the benzene molecules onto the surface of the metallic nanoparticle in such a way that the graphitic structure can be formed by the elimination of H_2. Previous work has suggested that aromatic molecules are more likely to form single walled nanotubes (SWNTs) than aliphatic or cyclic hydrocarbons of a similar mass.[22] It has been argued that the camphoric hexagonal units are already "tilted" at advantage to form a curved graphitic sheet or CNT.[16] It has also been suggested that decomposition of camphor may produce a significant amount of five–member rings, which promote curvature in the forming graphene sheet. The propensity towards curvature is believed to promote growth of tubes with a "bamboo" (internally capped) structure from camphor.[16] An example of the "bamboo" structure is shown in Figure 4.3. The high graphitization of some of the samples grown from camphor has been attributed to oxygen atoms, present in the precursor, efficiently oxidizing amorphous carbon in situ.[19] The same argument has

been used to explain the high quality tubes produced from other oxygen containing precursors such as ethanol.[23]

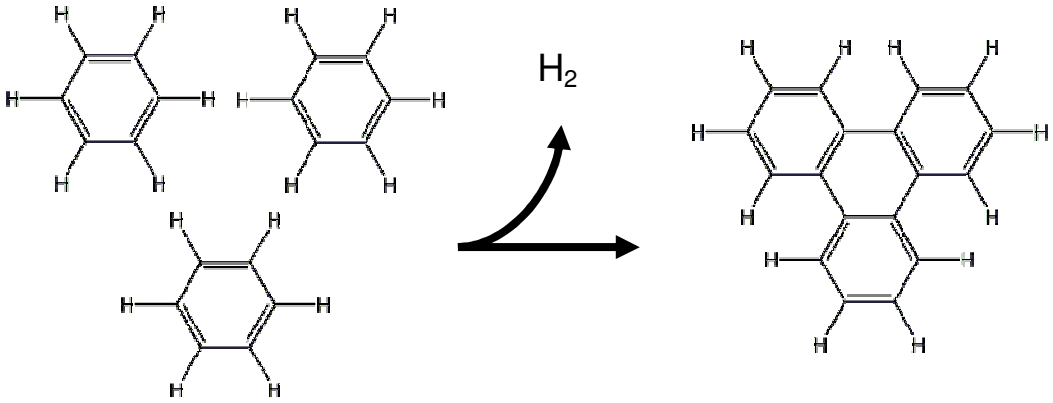

Figure 4.2. The *ring addition mechanism* suggested for the growth of carbon nanotubes from benzene.[20,21]

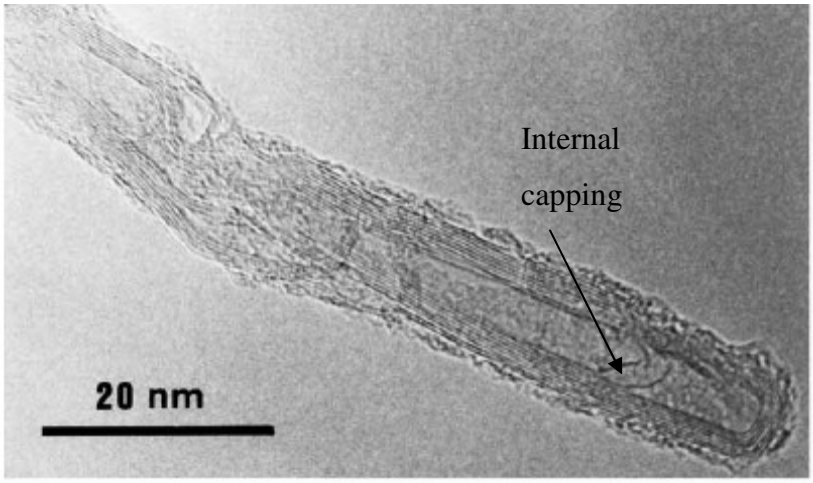

Figure 4.3. This TEM image, taken from the work of Kumar *et al.*,[19] shows the internal capping that has been reported in the literature as being common feature of tubes produced from camphor. Such internal capping is also referred to as the "bamboo" structure or morphology.

The ring addition mechanism is quite different from the popular *decomposition mechanism* as a model of single walled nanotube growth where a hydrocarbon such as methane is used. In such a mechanism of CVD, substantial evidence has been presented that the hydrocarbon is catalytically decomposed on the surface of the metal nanoparticle.[7] The carbon atoms produced then either dissolve into the nanoparticle until it becomes saturated, when the carbon then starts to precipitate out as a CNT, or the carbon atoms diffuse around the surface until they start to bond to each other.[24]

4.1.4 Determination of mechanism of nanotube growth from camphor

If molecules with certain structural features make better precursors for CVD growth of CNTs, then it would be of immense importance to rationalize which molecules would be good precursors for high quality growth. In this work, several precursors were used in a series of comparative CVD growths in order to establish links between precursor structure and as–produced CNT quality. The CVD syntheses of carbon nanotubes were carried out by passing different precursor compounds over a catalyst at elevated temperature. The well–studied Fe / Mo catalyst at 865 °C was used,[25] as it is known to favour production of single walled tubes, and therefore is of particular interest for understanding the formation of SWNTs from camphor. Information gained from comparative growths may also shed light on the type of mechanism by which the CNTs grow. If structure, and in particular the bicyclic structure of camphor, is important to tube growth, then there would be strong evidence for the postulated benzene–like *ring addition mechanism* for camphor. The precursors tested included camphor and several closely related analogues compounds, as well as benzene and methane.

4.2 Experimental

4.2.1 Catalyst preparation

The alumina–supported Fe / Mo catalyst was prepared by the metal–ion impregnation method.[25] $Fe_2(SO_4)_3$ (0.3 g, Aldrich, technical grade) and $(NH_3)_2MoO_4$ (0.04 g, Aldrich, 99.98%) were dissolved in ~150 cm^3 of deionised water, and approximately 2 g of alumina (Degussa Aluminoxid C) was added to the solution giving a Fe:Mo:alumina ratio of 1:0.13:13. The water was removed by rotary evaporation and the solid dried overnight in an oven at 100 °C. The resulting powder was ground thoroughly using a mortar and pestle.

4.2.2 Chemical vapour deposition

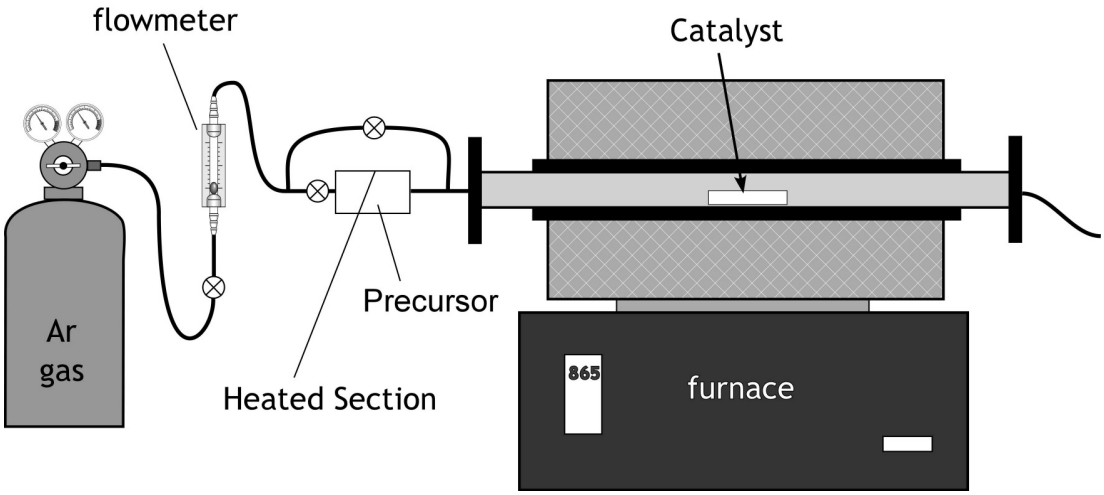

Figure 4.4. Diagram of CVD setup. The carbon precursor (e.g., camphor) is placed in the first heated zone on the left. The first zone temperature was < 200 °C. Precursor vapour was flowed over the catalyst by passing Ar towards the main furnace (at right), which was heated to 865 °C. See text for further details.

The CVD was carried out using a 2–stage heating setup similar to Kumar and Ando shown as Figure 4.4. [18] In a typical procedure, the precursor (e.g., camphor 0.53g, 3.5 mmol, Aldrich, 96%) was placed in the first heating zone, and 0.1 g of the alumina supported Fe / Mo catalyst was placed in a quartz boat in the centre of the second furnace. Ar gas was passed over the precursor and through the second furnace at a rate of 200 cm^3 min^{-1}. Once the catalyst had reached the working temperature of 865 °C, the precursor was heated to the required temperature and the vapour was allowed to pass into the second furnace. After 20 minutes, the furnace was allowed to cool under flowing Ar gas. The procedure was repeated with molar equivalents of camphorquinone, norcamphor, norbornane, camphene, fenchone, menthone, 2-decanone and benzene. All precursor compounds were purchased from Aldrich (except methane, from BOC Edwards) and used without further purification. The CVD procedure using methane was similar, except that once the furnace reached 865 °C, the gas flow was changed to 200 cm^3 min^{-1} of Ar gas and 34 cm^3 min^{-1} of methane. After 20 minutes, the furnace was allowed to cool under a flow of argon.

Two experiments were carried out, with methane and benzene, where the catalyst was exposed to hydrogen before the precursor was passed through the furnace, to study the effect of pre–reduction of the catalyst on the growth of tubes. These two CVDs were carried out as above, but with the additional first step of passing 800 cm^3 min^{-1} H_2 mixed with 200 cm^3 min^{-1} Ar for 10 minutes once the furnace had reached 865 °C.

4.2.3 Characterization

Product samples were characterized using thermogravimetric analysis (TGA, Stanton Redcroft Thermobalance TG762, heating from room temperature to 1000 °C at a rate of 10 °C min^{-1}) and Raman spectroscopy (Labram 300, 632.8 nm, 13 mW, with collections typically 100 seconds). Samples were prepared for transmission electron microscopy (TEM) by dispersing some of the as–prepared products in ethanol with gentle bath sonication and dropping a little of the dispersed product onto carbon coated grids. The samples were viewed using a Philips CM120 Biotwin with an accelerating voltage of 100 kV. Samples for scanning electron microscopy (SEM) were prepared by scattering the powder onto a piece of carbon tape (a carbon sticky) that was affixed to a specimen stub. To ensure that the sample surfaces were conducting, they were covered with gold using a sputter coater. Samples were imaged using a Philips XL30CP using the secondary electron detector with a typical working distance of 10 mm and a typical accelerating voltage of 30 kV.

4.3 Results and Discussion

4.3.1 Characterisation methods

As discussed in Chapter 2, Raman spectroscopy of carbon nanotubes gives a wealth of information about the CNTs.[26,27] Raman spectra of both MWNTs and SWNTs show two peaks which are characteristic for graphitic structure: the G band at around 1590 cm^{-1}, which is the main feature in well–ordered, highly graphitic samples, and the D band at around 1300 cm^{-1}, which is a disorder activated band. The ratio of the intensities (I_D / I_G ratio) of these bands is a commonly used measured of the graphization of samples as well as a measure of the quality of the sample.[27,28] Pure

pristine SWNTs have a very small I_D / I_G ratio. The spectra of SWNTs have extra features that are not present in the spectra of MWNTs.[28] Radial breathing modes (RBMs) are found at low frequencies between 150 – 350 cm^{-1}. The frequencies of these peaks are known to be inversely proportional to the diameter of the tube from which they originate. The Raman spectra of SWNTs also show a splitting in their G band, which is an indicator for their presence.

Scanning electron microscopy (SEM) is useful for identifying the growth of tubes, as they can be viewed directly. Unfortunately, the resolution of the microscope used does not allow the determination of whether the tube–like structures are bundles of SWNTs, MWNTs or perhaps carbon fibres. Transmission electron microscopy (TEM), however, can be used to study the internal structure of tubes, and so can be used to distinguish between carbon fibres, MWNTs, and bundles of SWNTs.

Thermogravimetric analysis (TGA) was used to determine the amount of carbon deposited on the catalyst during CVD. Yields were calculated as the fraction of carbon that was deposited during CVD compared to the mass of carbon that was contained in the precursors passed through the furnace.

4.3.2 Fixed precursor pre–heating

In preliminary experiments all of the precursors were heated to the same temperature (200 °C) to ensure that their vapours would definitely be passed through the furnace, over the catalyst.

4.3.3 Scanning electron microscope characterisation

SEM confirmed the growth of fibres for all the samples. However, there was great variation in the tubes produced by the different precursors. For example, camphorquinone (Figure 4.5) produced straight, thin fibres, which appear to be < 100 nm wide and several microns long. The smooth morphology of these fibres is consistent with nanotubes. In contrast the fibres from norbornane, shown in Figure 4.6, are larger around 200 nm in diameter and misshapen (“twisted”) suggesting that they are not carbon nanotubes but rather carbon fibres. The tubes produced from

norcamphor, camphor and camphene seemed to be intermediate between the samples produced from camphorquinone and norbornane. As the SEM images in Figure 4.7, 4.8, and 4.9 show, there is a wide variation in the thickness of the fibres produced from camphor, norcamphor and camphene.

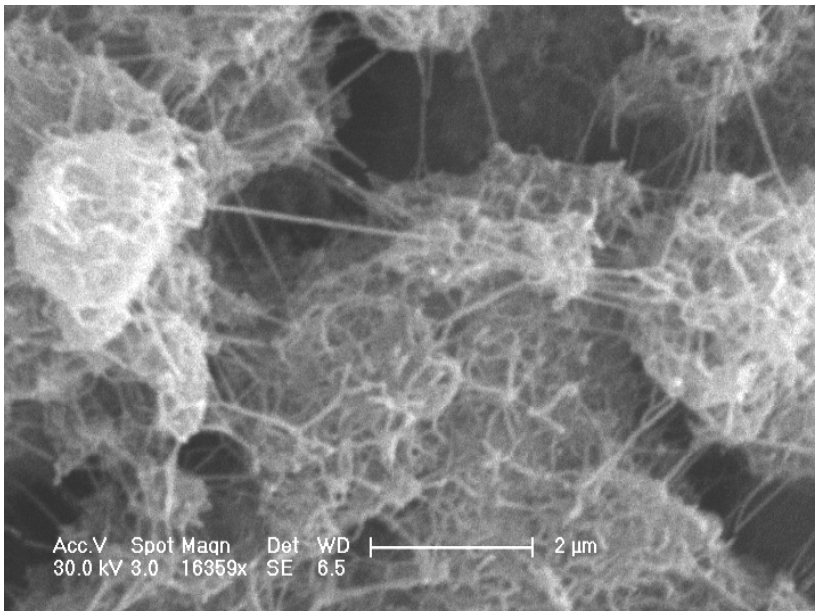

Figure 4.5. SEM image of CVD product produced from camphorquinone. Small fibres, < 100 nm in diameter, can be seen on the larger catalyst particles.

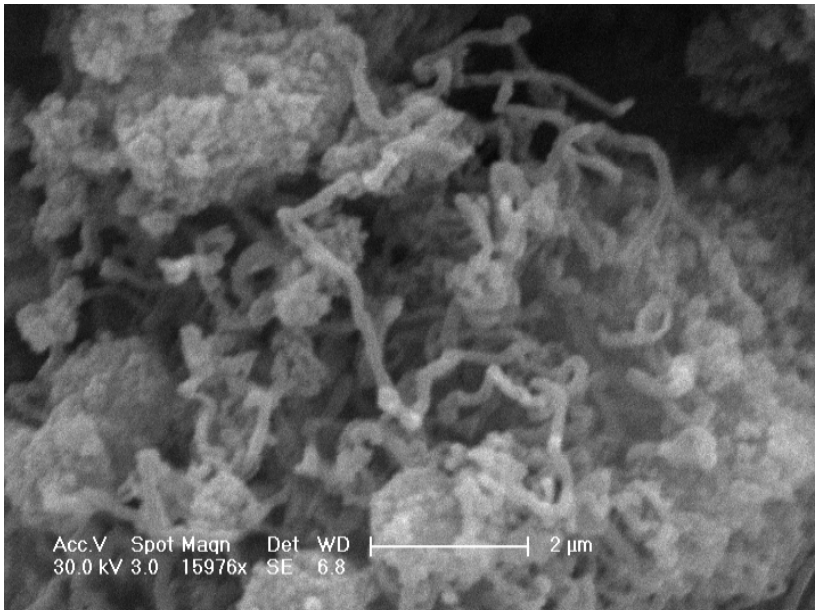

Figure 4.6. SEM image of CVD product produced from norbornane. Large fibres, > 200 nm in diameter, can seen on the larger catalyst particles. The size and morphology of the fibres suggested that they are not of high quality, and may possibly be carbon fibres rather than tubes.

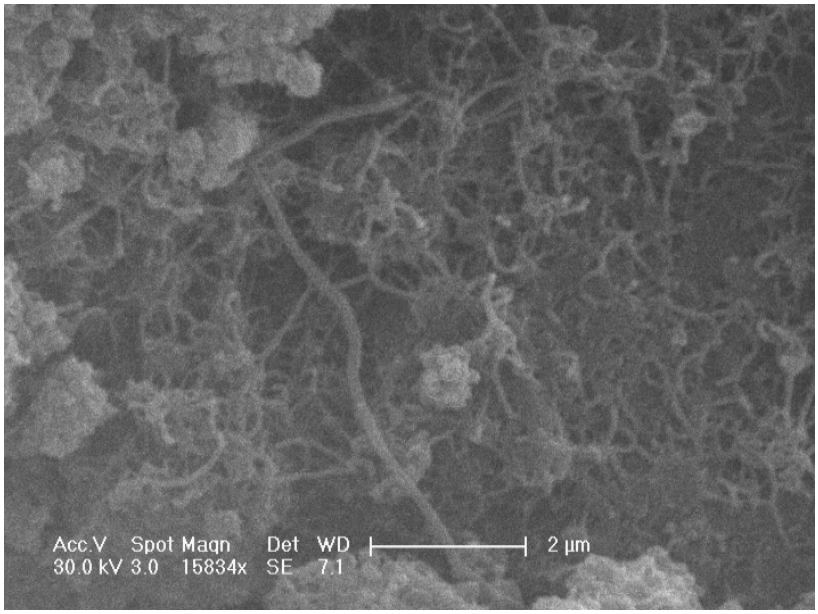

Figure 4.7. SEM image of CVD product produced from camphor. There is a wide variation in diameters of the fibres, which suggests the presence of different types of tubes (MWNTs and SWNTs) and fibres.

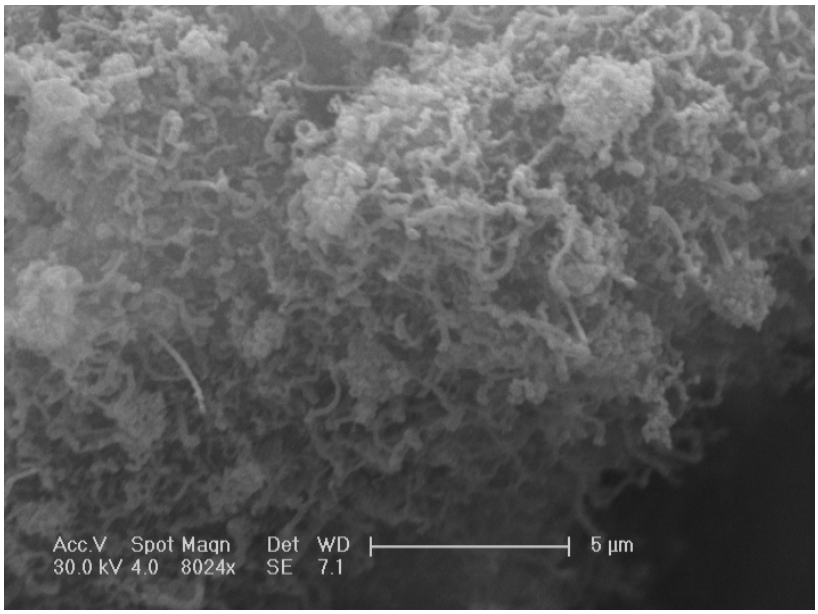

Figure 4.8. This SEM shows the tubes produced from norcamphor. The diameter and shape of the fibres suggests poor quality, and possibly that carbon fibres have been formed.

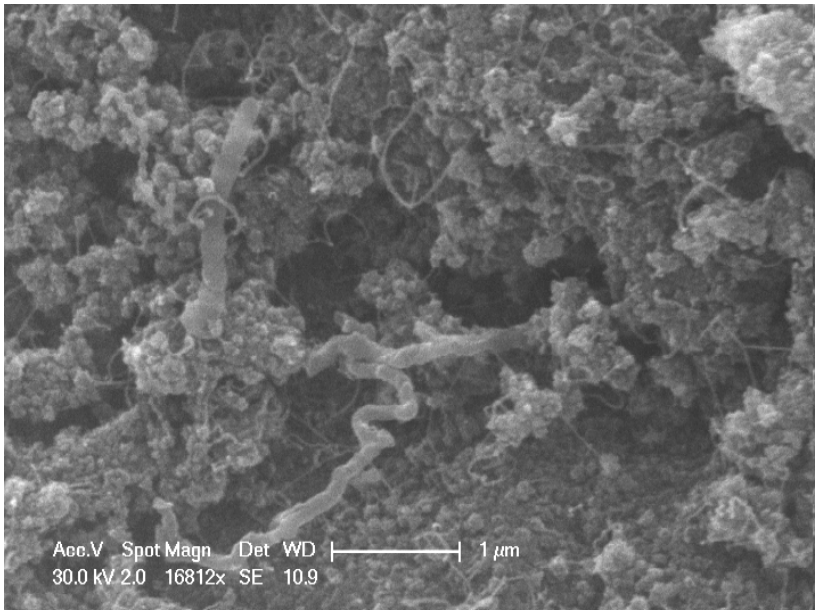

Figure 4.9. Camphene was used to produce the tubes shown in this SEM image. The very large fibres present have an irregular shape that suggests that they are carbon fibres rather than tubes.

4.3.4 Transmission electron microscope characterisation

The TEM image (Figure 4.10) of CVD product made from camphorquinone shows bundles of single–walled nanotubes. These can be identified as bundles due to low contrast of the smooth ribbon–shaped features, and in addition some individual tubes can be seen. It is difficult to estimate the diameters of the tubes, due to the magnification and resolution of the image, but the SWNTs visible seem to be around 1 nm diameter. There is also a misshapen carbon fibre in the image that seems to have several particles of high contrast, which is likely to be the metallic catalyst. The large amount of metal inside the fibre suggests that some large particles of metal just be formed from the catalyst during CVD.

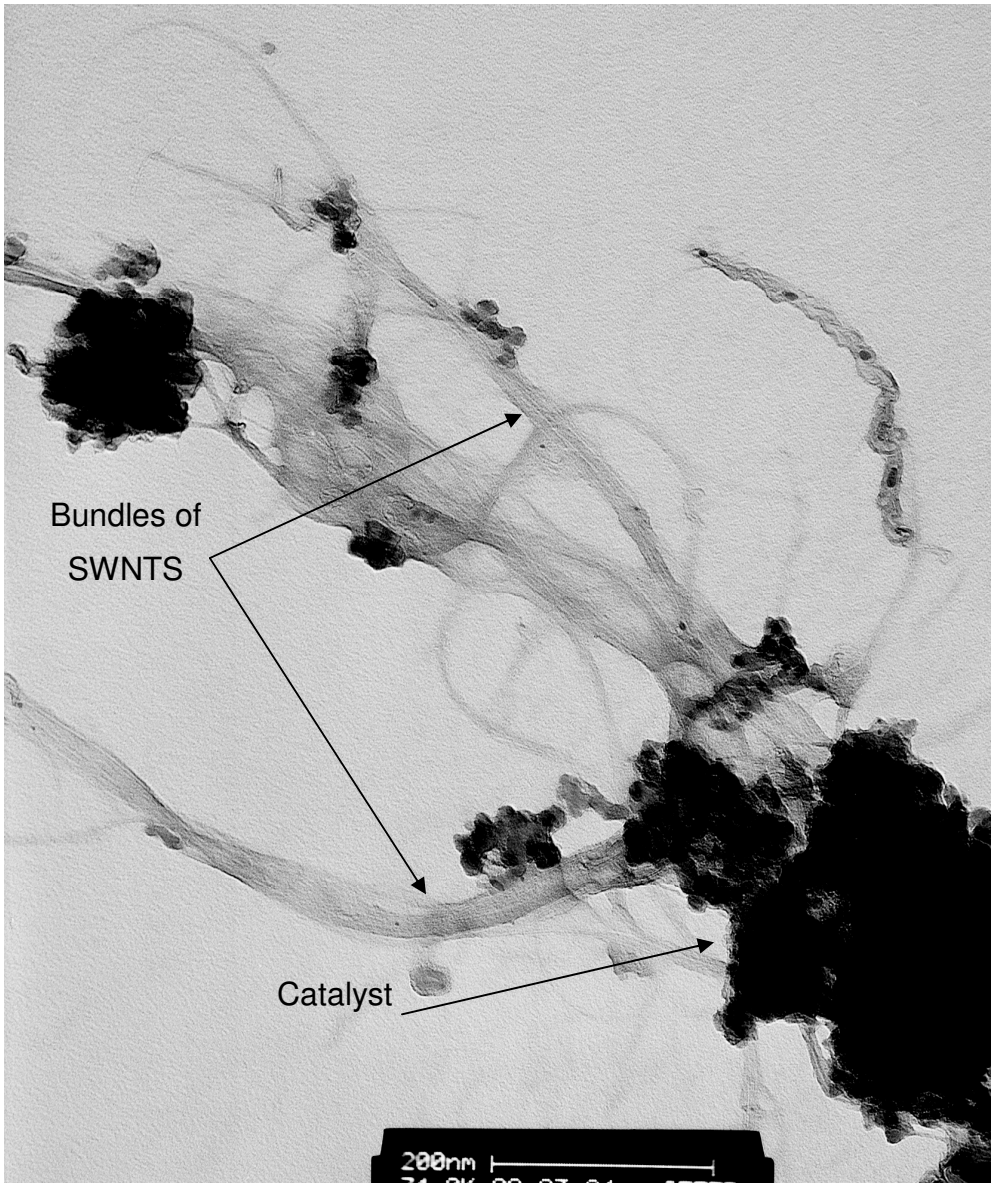

Figure 4.10. TEM image of sample prepared from camphorquininone.

Figure 4.11 shows the TEM image of the CVD produced from camphor. The most apparent feature is the large MWNT (~ 60 nm in diameter) which has the internally–capped "bamboo" structure, as has been found for other tubes produced from camphor.[16] There are also two isolated SWNTs visible in the image. This is further evidence of the camphor sample being made up of different types of tubes. The CVD product from norcamphor presented as Figure 4.12 shows a large misshapen carbon tube that is around 50 nm in diameter. All the observations noted from the TEM are consistent with those noted from the SEM.

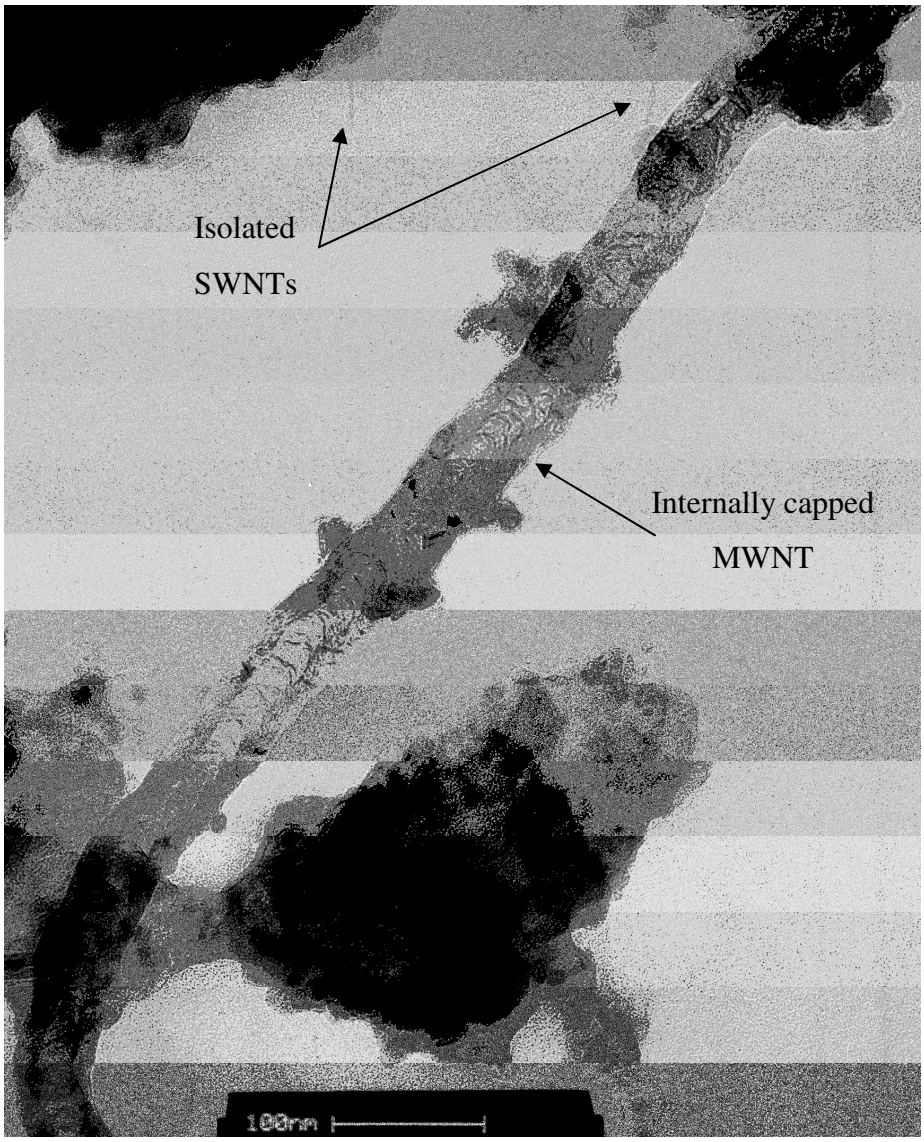

Figure 4.11. This TEM image shows that the camphor CVD product contains some internally capped MWNTs, and also some isolated SWNTs.

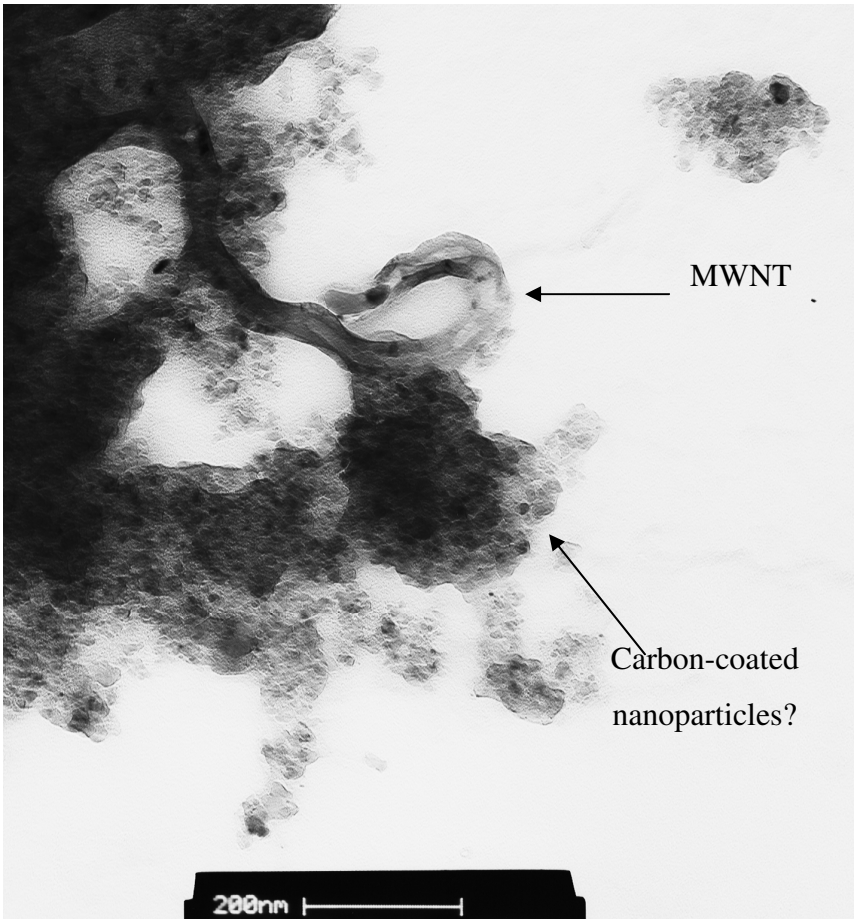

Figure 4.12. The CVD product from norcamphor contained large misshapen carbon tubes. There also appears to be some high contrast particles that are covered is less dense material that could be carbon-coated nanoparticles.

4.3.5 Raman spectroscopy

Raman spectra of each of the samples were consistent with SEM and TEM images. The spectrum of camphorquinone sample, Figure 4.13(a), shows a very small D band compared to the G band, which suggests the sample is highly graphitized, and the presence of the RBMs at lower frequency indicates that SWNTs are present. The norbornane spectrum, in Figure 4.13(b), shows a large D band and a smaller G band, indicating that the sample has a high content of sp^3 carbon, and is very disordered. The samples for the other precursors showed great variation in their Raman spectra taken at different spots on the sample powder. For example, some spectra for the camphor sample showed the presence of RBMs and a G band that was more intense

than the D band, as in Figure 4.13(c); whilst other spectra, such as Figure 4.13(d), had no RBMs, and D and G bands of around equal intensity. Unfortunately, it was not possible to relate a particular Raman spectrum to a particular position where the catalyst had been in the furnace, as the powder had already been mixed when it was removed from the reaction boat.

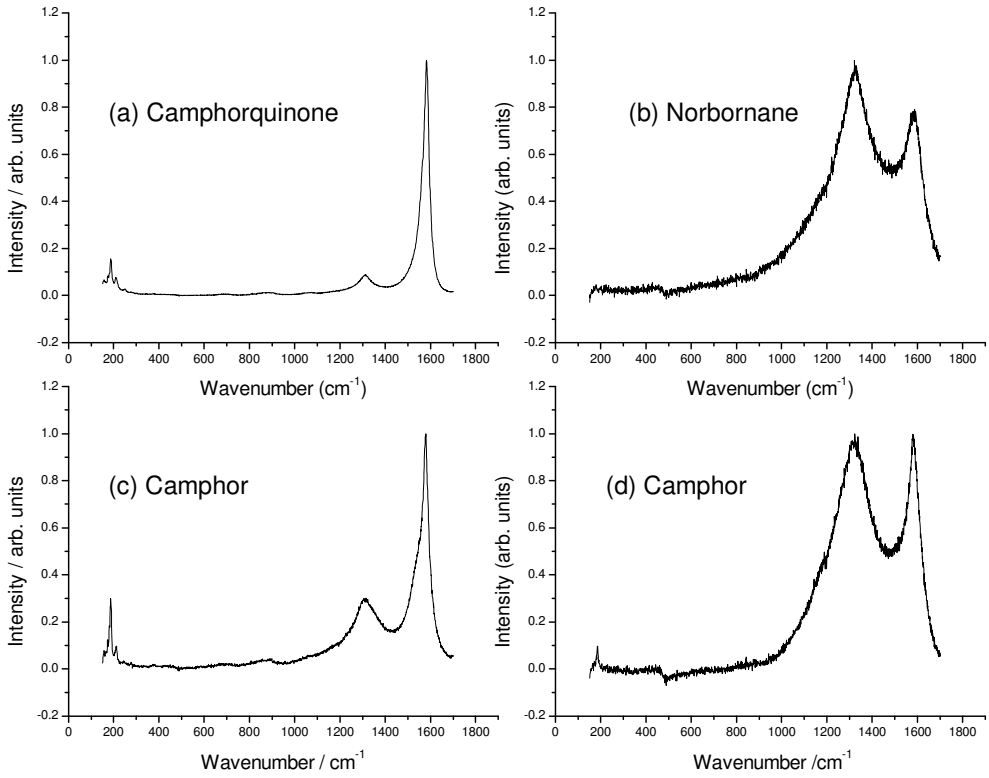

Figure 4.13. Raman spectra of CVD products from syntheses where precursors were heated to 200 °C. The product from camphorquinone (a) is well graphitized (small D band) and contains SWNTs (evident from RBMs). Norbornane (b) produced a sample with no SWNTs, and is not well graphitized, as is evident by the large D band. The spectra from the camphor sample varied greatly as the two examples (c) and (d) show.

Average I_D / I_G ratios, presented in Table 4.1, were calculated from six spectra for each sample. The results show that it is difficult to relate the quality (I_D / I_G ratio) and the type of tube produced (SWNTs or MWNTs) with the structure of the precursor

used. However, our observations can be explained in terms of the physical properties of the precursors: as is evident from Figure 4.14, which shows a plot of I_D / I_G ratio against the boiling points of the precursors. The precursors with the lowest boiling points produce the worst tubes. The precursors with the lower boiling points would have higher vapour pressures when they are heated to 200 °C. The high vapour pressure means that the precursor would pass through the furnace faster, giving a higher flux of carbon over the catalyst during CVD.

Precursor	**Melting point/ °C**	**Boiling point/ °C**	**Average I_D / I_G ratio**	**% yield**
Camphorquinone	199.0	226.5	0.23	8
Camphor	179.0	207.4	0.81	7
Norcamphor	95.0	170.0	1.84	9
Camphene	41.0	160.0	2.22	11
Norbornane	87.7	112.6	2.85	9

Table 4.1. Analysis of CVD products from syntheses where all precursors were heated to 200 °C. The I_D / I_G ratio shows no clear correlation with precursor molecule structure, but do show that worse tubes are produced for precursors with lower boiling points: see also Figure 4.14.

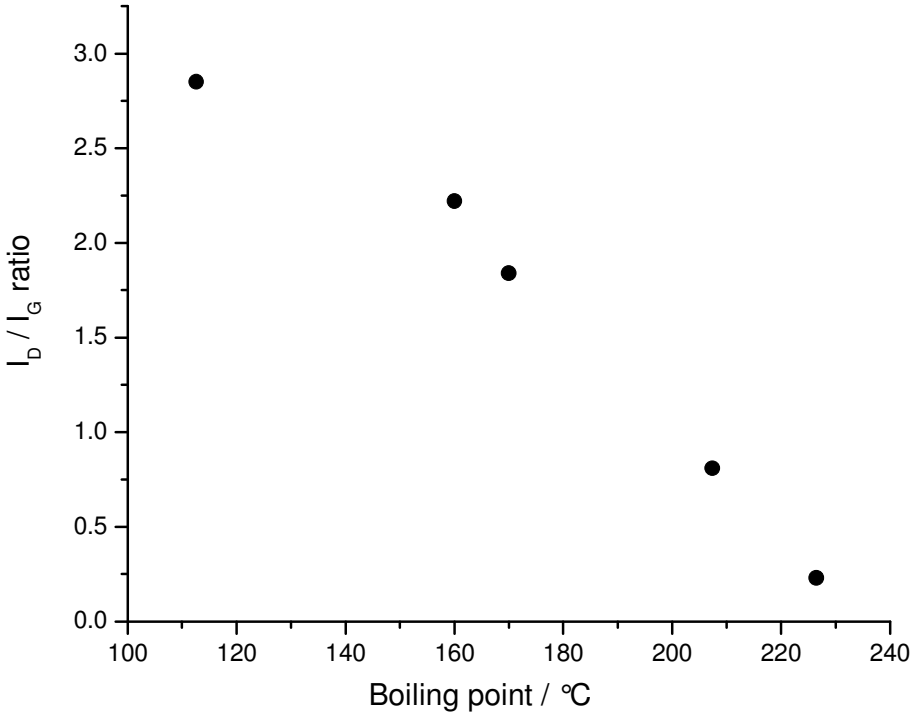

Figure 4.14. Plot of average I_D / I_G ratio against boiling point of the precursor. All precursors were heated to 200 °C. The decrease of I_D / I_G with increasing boiling point suggests that the vapour pressure of the precursor during CVD is critical to the quality of the tubes.

As has been seen previously (see Chapter 3),[19] the lower the flux of carbon over the catalyst, the better the quality of tubes produced and higher is the proportion of SWNTs formed. The improvement of quality with lower C fluxes can be ascribed to the reduced number—or density—of reactions in the gas phase that produce carbonaceous impurities. Our comparative CVD experiments also suggest that growth of SWNTs is promoted by smaller C fluxes. It would seem sensible to reason that the amount of carbon involved in forming a SWNT is much less than the amount for a MWNT, so under conditions of low carbon flux SWNTs may be favoured.[19] In Chapter 3, it was seen that when the residence time was kept constant but the concentration of methane in the gas phase was increased, the I_D / I_G also increased suggesting that poorer quality nanotubes were being produced for higher methane concentrations. Here a similar trend is observed in that the precursors with high vapour pressures produce samples with high I_D / I_G ratios. We assume that the

residence time was mainly determined by the flowrate of argon, which was the same for each experiment, and the vapour pressure of the precursor controlled its concentration in the gas phase. High fluxes of carbon have been shown to promote growth of other types of carbon structures, including the formation of carbon–coated iron particles.[7] The formation of these coated particles has been proposed as one of the main ways that the growth of CNTs is terminated. It is thought that with very large fluxes of carbon, the metal catalyst particles become covered with carbon and thus become inactive. Some carbon-coated particles are thought to be visible in the TEM image of the norcamphor sample,Figure 4.12. This low boiling point precursor would have produced a high carbon flux during CVD that may have promoted the formation of these particles.

In conclusion, to be able to compare the effect of the precursor's molecular structure on the CNTs produced during CVD, it is vital to equalize the flux of the precursor through the system.

4.3.6 Constant precursor vapour pressure

In the second set of experiments, each of the precursors were heated to a different temperature so that all the CVDs were carried out under approximately the same vapour pressure of precursor. The temperatures required were calculated using either the enthalpy of vapourisation or the Antoine constants of the precursor (see Appendix 4.A). Thermodynamic data were obtained from the DETHERM Database,[28] except for the enthalpy of vaporisation of camphorquinone, which was estimated with Trouton's rule.[30] The general rule that we employed was that the precursors were heated to around 20 to 30 °C below their boiling point. It should noted that it was difficult to heat the precursors to the required temperature accurately throughout the 20 minute CVD. There will have been, therefore, some error in the vapour pressure of the precursors during the CVD. The flowrate of methane (34 $cm^3 min^{-1}$) was chosen so that roughly the same amount of carbon (~ 0.2 g min^{-1}) was passed as for the other precursors. Apart from the first heating zone temperature, the general experimental procedure followed was otherwise the same, as described in Section 4.3.2.

The structures of the precursors (except methane) used are shown in Figure 4.15. Precursors were selected on the basis that their structure had some similarity to camphor so that, when CVD products were compared, the effect of differences in structure could be studied. For example, the effect of the bicyclic structure compared to a cyclic or a linear structure could be obtained by comparing camphor, menthone and 2-decanone. Benzene was used as it has been suggested that CNTs grow preferentially by the *ring addition* mechanism. Methane was used as it is most commonly used to grow SWNTs by our chosen conditions.

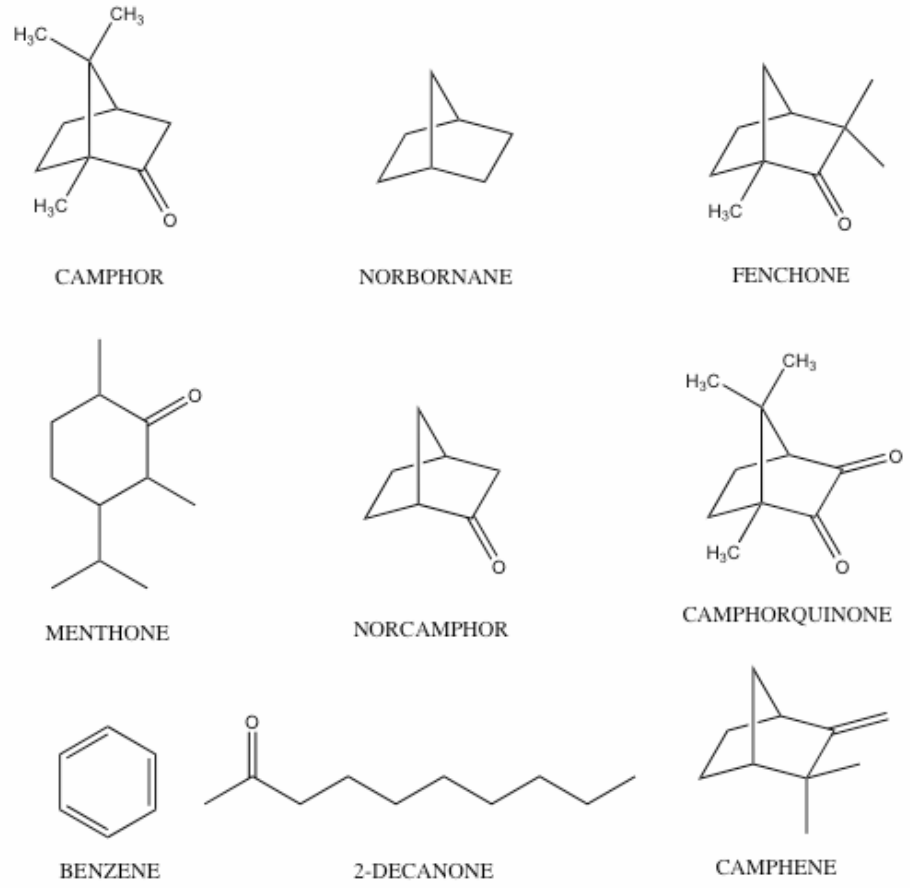

Figure 4.15. Structures of precursors (except methane) used in comparative CVDs.

4.3.7 Transmission electron microscopy

TEM of the CVD products showed that all precursors produced both MWNTs and SWNTs: a representative TEM image is shown in Figure 4.16. At the TEM

magnifications available, it is difficult to distinguish between bundles of single–walled tubes and thin multi–walled tubes. Determining which is which is made even harder by the height variation of the samples so that different parts of the sample appear with different amounts of defocus. It was not possible to estimate the relative amounts of SWNTs and MWNTs for each sample from TEM; however, it was noticed that methane did seem to produce more SWNTs than the other precursors: see Figure 4.17. It was also not possible to inspect the sample with high enough resolution to determine whether there were any catalyst particles at the ends of a tube. Therefore it was not possible to determine if the tubes were growing by the tip–growth or base–growth mechanism. It has been found previously for this sort of catalyst system that base growth mostly occurs.[25]

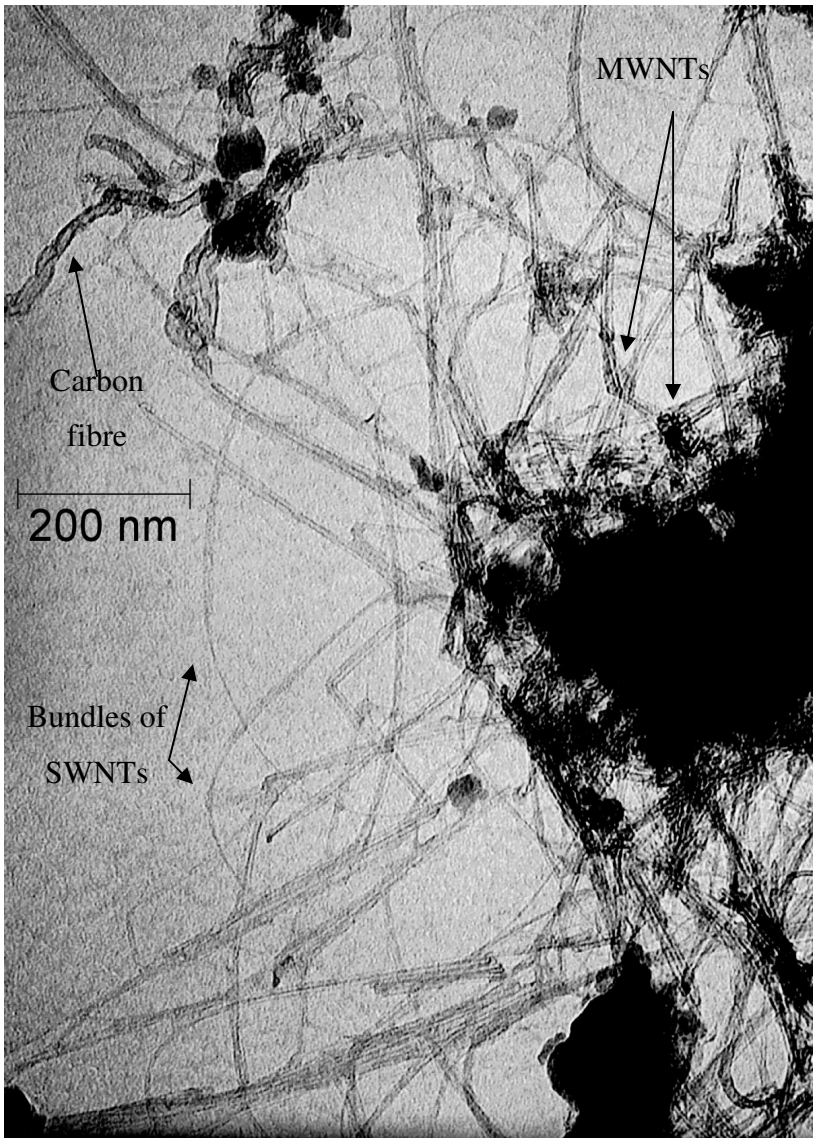

Figure 4.16. TEM image of MWNTs and SWNTs produced using benzene as precursor. The image is representative for what was found for all precursors except methane. Due to the relatively low magnification available, we assume that features with resolvable sidewalls are MWNTs.

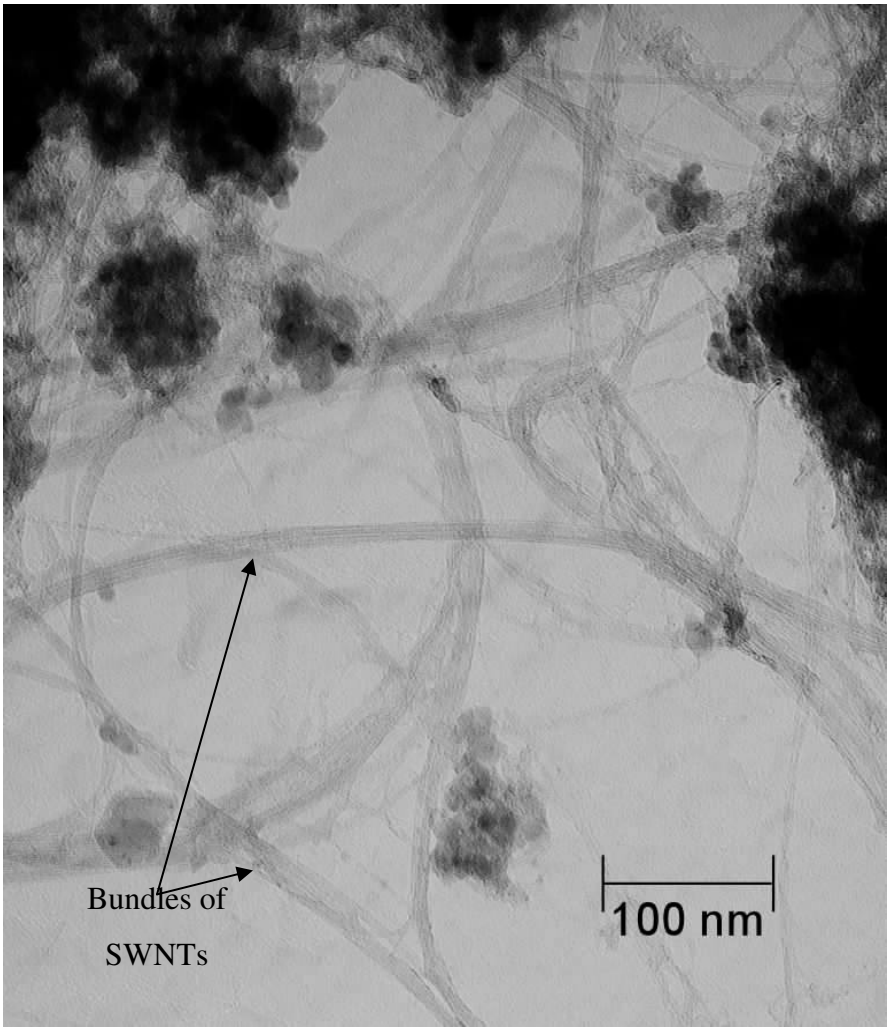

Figure 4.17. TEM images of tubes produced using methane as precursor. The bundles are thought to be SWNTs as they have no resolvable sidewalls at this magnification.

4.3.8 Raman spectroscopy

The Raman spectra for all samples are shown in Figure 4.18. All the spectra are remarkably similar in that all show strong RBMs and an asymmetric G band, which suggests the presence of SWNTs. The I_D / I_G ratios, and yields for all the samples, are presented in Table 4.2. There is very little difference between all the samples, in

either the I_D / I_G ratio or yield, except for methane and benzene. As several spectra were collected from each sample, the root mean square (rms) deviation of the I_D / I_G for each sample could be evaluated, and are shown in Figure 4.18. There is quite a large variation in the rms deviations of the I_D / I_G ratio of the samples. However, all the values of the rms deviations are smaller than that for the camphor sample (0.33) obtained previously, in Section 4.3.2. This suggests much less variation in the quality of tubes than for the previous camphor sample. Looking at Table 4.2, there appears to be no simple relationship between the structure of the precursor and the quality or yield of carbon deposited.

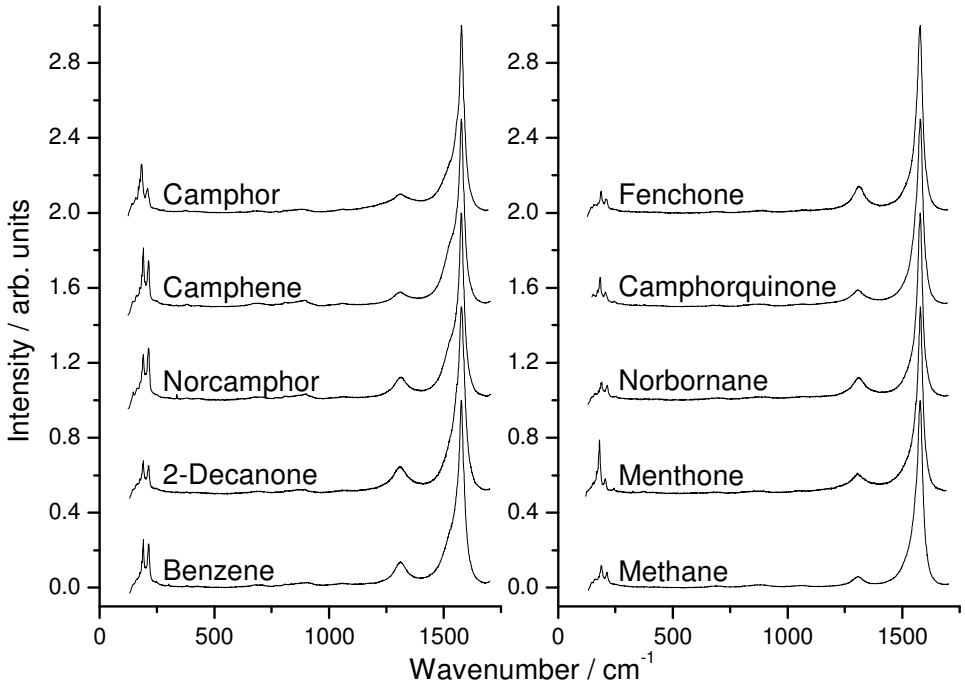

Figure 4.18. Raman spectra for CVD products. All shown similar I_D / I_G ratios (except methane), and the presence of RBMs and splitting of the G band suggest the presence of SWNTs in the samples.

Precursor	Average I_D / I_G ratio	Root mean square deviation of I_D / I_G ratio	% Yield
Camphor	0.21	0.08	14
Fenchone	0.18	0.03	12
Camphorquinone	0.23	0.03	14
Camphene	0.24	0.16	10
Norcamphor	0.27	0.15	14
Norbornane	0.26	0.08	15
Menthone	0.16	0.01	11
2-Decanone	0.16	0.04	12
Benzene	0.23	0.06	7
Methane	0.08	0.02	3

Table 4.2. Analysis of CVD products from syntheses where precursors were heated to ~ 30 °C below their boiling points. The I_D / I_G ratios and yields of these precursors (except methane) are very similar, suggesting that the quality of the tubes produced is not directly related to the structure of the precursors. The root mean square (rms) deviation of the I_D / I_G ratios, obtained from multiple Raman spectra of each sample, do show some variation. However, all of the rms deviations are much smaller than that of the camphor sample in the previous set of experiments (0.33). The lower yields for methane and benzene can be explained by their greater stability (see text for details).

4.3.9 Effect of oxygen on tube growth

One reason why camphor was suggested to be a good precursor for the CVD of CNTs was that its structure includes oxygen. It was suggested that the oxygen could form oxygen–containing radicals that would etch away amorphous carbon, and hence improve the quality of tubes.[4,7] Similar arguments have been made about using alcohols as precursors or adding reactive gases, such as water or hydrogen, to improve tube growth. There is little evidence of an improvement in tube quality in the results detailed here. Camphorquinone (two O atoms), camphor (one O atom), and both camphene and norbornane (no O atoms): all produce tubes of around the

same quality with the same yield. However, these molecules do have very much smaller O:C ratios than, for example, ethanol.

4.3.10 Mechanism of tube growth

Our results show no evidence for the formation of SWNTs by the *ring addition mechanism* under the conditions used. If the ring addition mechanism did operate for these precursors then, according to Kumar *et al.*,[16,19] we should be able to see some differences between the CNTs obtained from different precursors. Kumar *et al.* argued that according to the ring addition mechanism, structures that dissociate to form reactive six–membered ring radicals should be good at producing carbon nanotubes, as these would combine to form graphitic sheets, whereas molecules that produce five–membered ring radicals would introduce defects into the carbon nanotube.[19] It has been shown by Sato *et al.* that under flash pyrolysis conditions[31] (800 °C, 3 Torr) camphor produced no five–membered ring products. In contrast, fenchone produced both five and six–membered rings. In the work of Sato *et al.*,[31] gas chromatography was used to analyze the compounds from the pyrolysis. Comparing the reported areas of the peaks for each of the cyclic products in the chromatogram of fenchone, about 30 % were five–membered. According to the ring addition model of carbon nanotube growth, fenchone should therefore produce worse tubes than camphor, as it would introduce more five–membered rings into the tubes. It should be pointed out, however, that in the pyrolysis experiments, the reaction was thought to take place in the gas phase: whereas in the experiments presented here, a catalytic metal surface is likely to be involved. The low pressure also reduces the reaction rates, which may be important in the syntheses presented here. Critically, the importance of the bicyclic structure is ruled out from the results of growth with menthone and 2-decanone. Both of these precursors produced tubes with similar characteristics to all the others, although their decompositions are not likely to form cyclic fragments.

In the study where benzene was suggested to form carbon nanotubes through the *ring addition mechanism*,[20,21] the CVD was carried out at a lower temperature (~700 °C) and only MWNTs were produced. In the experiments presented here, we suggest that

the growth of the tubes from benzene occurs by the *decomposition mechanism*. The I_D / I_G ratios for all the precursors—including benzene—are similar, and high temperature growth conditions were chosen to promote SWNT growth with the specific catalyst we used.

4.3.11 Effect of precursor structure on nanotube quality and yield

We do find some evidence that the structure of the precursor affects both the quality and yield of carbon nanotubes produced. Both methane and benzene have lower yields than the other precursors, which might be explained by their greater kinetic stability. Methane and benzene are different from the other precursors as they do not contain any saturated C–C bonds. The first step in the decomposition of methane must be the breaking of a C–H bond: this requires much more energy than the C–C bonds, which is the weakest type of bond present in the other molecules.[32] Benzene only has C–H and aromatic C–C bonds to break, which are also stronger than the single C–C. As methane and benzene are more resistant to decomposition than the other precursors, less of the precursor reacts as it passes through the furnace, therefore producing a smaller yield of deposited carbon.

The flux of carbon has been shown to affect the quality of tubes, see Section 4.3.5. As only a small amount of methane actually reacts, the flux of reactive carbon during the CVD is smaller in comparison to the other precursors. Therefore methane, due to the stability of its structure, gives better SWNTs than the other precursors: as demonstrated by its low I_D / I_G ratio. It has also been argued that in other CVD conditions methane produces good tubes as, due to high kinetic stability, it will only decompose on the metal particles and not on other surfaces to produce amorphous carbon.[33] It is not clear why benzene does not show improved quality over the other precursors, since less of it is observed to react: giving a lower yield of carbon.

There are other differences between the product samples: close inspection of all samples' Raman spectra show differences in the shape of the G band and the intensities of the RBMs.

4.3.12 Different distributions of carbon nanotubes from different precursors

In Figure 4.19, it can be seen that the benzene sample has a much wider G band than the methane sample. From the Raman spectra of individual SWNTs it is known that the G band of SWNTs has two contributions.[26,27] The higher frequency G band, labelled ω^+, is usually fitted by a Lorentzian function and is centred around 1590 cm^{-1}, while the lower frequency band, ω^-, depends on the electronic properties of the tube. Semiconducting tubes have a ω^-_{semi} band best fitted by a Lorentzian, while metallic tubes have a band best fitted by a Breit–Wigner–Fano function. The frequency of the ω^-_{met} band for metallic and semiconducting tubes both depend, in different ways, on the diameter of the CNT from which they arise. For the methane and benzene samples, it was found that the semiconducting ω^- peak was ~ 50 cm^{-1} below ω^+, and the metallic ω^- peak was ~ 80 cm^{-1} below the ω^+. As the Raman spectroscopy of the samples was carried out using a large laser spot size (< 1 mm) and the samples contain a mixture of different tubes, the G band is always made up of three contributions. Fitting the Raman spectra (Figure 4.19) of the benzene and methane samples to the appropriate line shapes shows that the benzene tubes have a much larger contribution to the G band from metallic tubes. The integrated intensities for the different contributions are presented in Table 4.3, which shows that the ratio of ω^-_{met} to ω^-_{semi} is much larger for benzene. The difference in the ratios of the contributions to the G band suggests a different distribution of tube structures. It should be noted that there may be another contribution to the G band from other carbon materials such as MWNTs and amorphous carbon. However, reports state that these would have G bands at higher frequency than SWNTs:[27,28] it does not seem likely that the differences in the Raman spectra can be explained simply by different amounts of MWNTs and amorphous carbon.

It is necessary to point out that from these Raman spectra alone it is not possible to state whether either of the samples contain a greater ratio of metallic tubes to semiconducting tubes overall. The intensity of the Raman signal from a nanotube of a particular chirality is very sensitive to the wavelength of the laser excitation. This is due to the resonance enhancement that is unique to carbon nanotubes. The benzene

sample shows a bigger ratio of the intensity of ω^{-}_{met} to ω^{-}_{semi}, but that only means that it contains more metallic tubes that have resonance enhancement at this laser wavelength (633 nm). Different shapes of G band are to be expected when spectra are collected with different laser wavelengths, such changes in the spectrum of a sample have been documented before in the literature.[34]

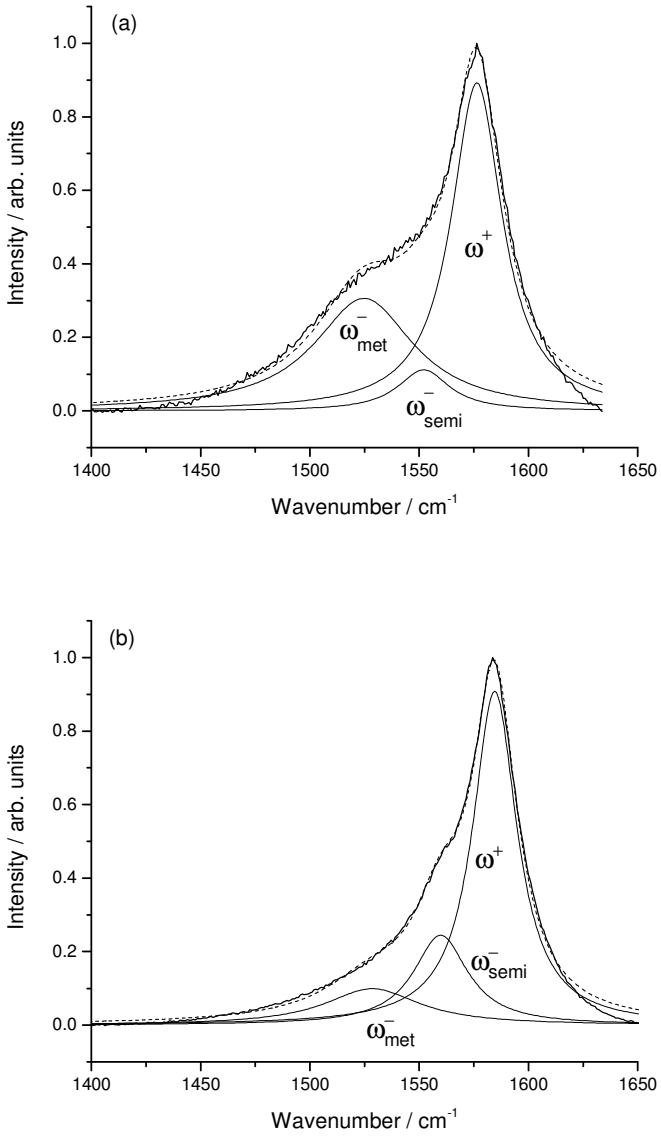

Figure 4.19. Raman spectra of samples from (a) benzene, and (b) methane, showing fits of two Lorentzian and one Breit–Wigner–Fano curves to the G band region. The larger area of the metallic ω^{-}_{met} peak in the benzene spectra (~ 1525 cm^{-1}) suggests the presence of more metallic tubes than the methane sample.

Precursor	Area of peaks (normalized to area of ω^+)		
	ω^-_{met}	ω^-_{semi}	$\omega^-_{met} / \omega^-_{semi}$
Methane	0.22	0.33	0.68
Benzene	0.68	0.13	5.22

Table 4.3. Integrated Raman G band intensities of ω^-_{met} and ω^-_{semi} peaks for CVD products grown from methane and benzene. The results indicate that the precursors produce different distributions of tube diameters, with a larger fraction of metallic tubes grown from benzene.

The benzene Raman spectrum has more intense RBMs (relative to the G band) than methane. As each RBM mode relates to tubes with different diameters, the difference in the intensities of the RBMs could be seen as evidence of different distributions of diameters or chiralities of tubes. However, it is difficult to interpret the intensities of the RBMs,[35] as their linestrengths are not simply dependent on the number of tubes, but on a number of other factors including the environment of the tubes in the samples and the wavelength of the laser excitation. If the energy of the laser is close to the difference in energy between two van Hove singularities in the electronic density of states of a tube, then there is a very large enhancement of the Raman signal.[27] The RBMs present in the sample spectrum will be those that have an energy gap close the laser excitation energy (1.96 eV at 633 nm). Although there are only a few RBMs visible in the Raman spectra for the samples, there will be other SWNTs with different diameters present that are not visible in the spectra. In fact, the strong Raman signal observed from SWNTs is in part due this resonance enhancement effect. For each SWNT, there are several transitions possible with different energies. So, typically for a SWNT there will be at least one transition that corresponds to an optical wavelength: most Raman excitation sources are visible wavelength lasers. However, the sharpness of the van Hove singularities means that only a few tubes will exhibit resonance enhancement for any given excitation wavelength: only a selection of those present in any given sample will have strong RBMs in the collected Raman spectrum.

Figure 4.20 shows the RBM region of the methane and benzene sample spectra. We might assign the RBM at 188 cm^{-1} as a (15,0) tube, which is a metallic zig–zag tube[35] with a transition energy between van Hove singularities of ~ 1.9 eV.[36] A greater number of (15,0) tubes in one sample compared to another would correspond to a stronger RBM at 188 cm^{-1} as well as a greater contribution of the metallic ω^- to the G band with an excitation at 633 nm (1.96 eV).

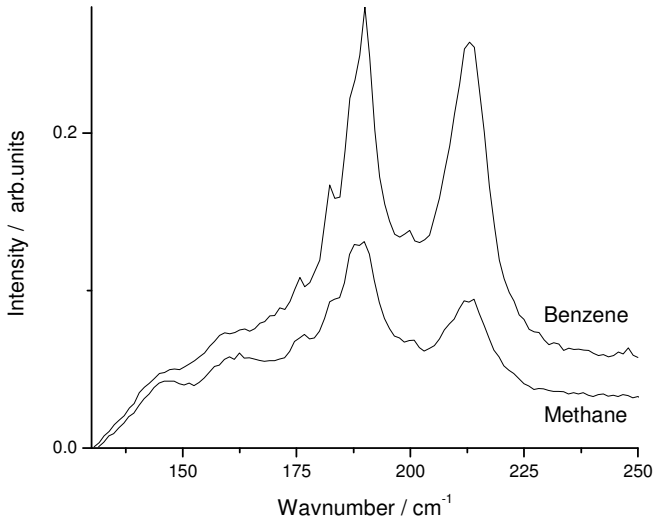

Figure 4.20. This plot shows the RBM region of the Raman spectra of the methane and benzene. The spectra have both been normalised to the ω^+ peak of the G bands. Both spectra have the same RBMs present, with differing intensity.

Other Raman spectra from the literature (using the same laser wavelength, 633nm), of CNT samples that were produced from methane and benzene using an iron on magnesium oxide catalyst, show similar differences in ω^- bands.[22] In this previous work, the differences in the spectra were not explained in terms of differences in the distributions of chiralities of tubes, however. Samples produced from naphthalene and anthracene were thought to produce more metallic tubes as they showed a greater splitting in their G bands compared to a sample produced from methane.[22]

The Raman spectra of the other samples presented here can be classified, approximately, into those which have Raman spectra like methane or like benzene. The spectra in Figure 4.18 have been presented so that those that are similar to benzene are on the left while those similar to methane are on the right. For example, the camphene sample Raman spectrum is similar to that of benzene as it has strong RBMs and a G band with a pronounced shoulder at lower wavenumbers. In contrast, camphorquinone's spectrum is similar to that of methane as the RBMs are slightly less intense and the G band is narrower than the benzene spectrum. There is no obvious way to correlate the members of either class to a shared feature of their molecular structure, or to a bulk property. The different members of each group could have very different distributions of chiralities. A Raman experiment with only one laser wavelength of excitation will only show a selection of the RBMs that correspond to the tubes whose signals are resonantly enhanced, even though there could be many other SWNTs present. It may be possible, by using multiple Raman excitation wavelengths, to further unravel the nature of the nanotube distribution: this will be explored below in Section 4.3.14.

4.3.13 Proposed mechanisms

In Section 4.3.12, we have presented evidence that different precursors produce different distributions of chiralities of tubes. There are two CVD reaction steps during which the precursors could affect the size of SWNTs. The first is the reduction of the metal salts to the active catalyst nanoparticle, and the second is the actual growth of the tubes from the nanoparticle.

The diameters of SWNTs have been related directly to the size of nanoparticles from which they are grown.[7,8] If the diameter of the nanoparticle can control the diameter of the SWNT produced, then the initial formation of the nanoparticles is vital in controlling the growth of the tubes. In the CVD experiments presented here it is assumed that the catalyst is reduced to the zero oxidation state by the precursor before growth of the tube starts (see Chapter 1). It is possible that the different precursors would reduce the metal salts to form different sizes of metal nanoparticles, and thus produce nanoparticles of different size. It is very difficult to rationalise

systematically how the structure of a molecule would affect the speed at which it would reduce the catalyst to metal or, more importantly, the size of nanoparticles produced.

As stated previously, the results of our experiments suggest that the tubes are formed by the *decomposition mechanism* rather than by *the ring addition mechanism*. The precise mechanism of CNT growth is still unresolved, but it can be assumed that catalytic breakdown of the precursor (or some other active species that is formed by reaction of the precursor in the gas phase[12]) produces atomic carbon that either dissolves into the particle and then precipitates out, or diffuses around the surface of particle, to form the carbon nanotube. The formation of SWNTs must be dependent on the kinetics of the reaction as it is known that both MWNTs and graphite are more thermodynamically stable than SWNTs.[5] The rate of growth of the nanotube must be dependent on the amount of carbon available from the nanoparticle, which is in turn dependent on the flux of precursors and the kinetics of breakdown of the precursor on the surface. The balance of the rates of these reactions must be important in the formation of carbon nanotubes. For example, it has been suggested that if the amount of carbon in a nanoparticle is too great, as would happen when the precursor arrives at the particle at a high rate and decomposes quickly, then the nanoparticle may become inactive due to the growth of a carbon layer of around the nanoparticle. These carbon–coated nanoparticles are often seen in TEM images of CVD products.[7]

It seems evident that the structure of the precursor affects the kinetics of decomposition on the catalyst surface (and in the gas phase), although it may be difficult to predict quantitatively. One of the most popular theories of tube growth is the "*yarmulke mechanism*".[37] In that theory, the end–cap of the nanotube forms first on the surface of the catalytic nanoparticle. Once the end–cap has formed the tube grows by the addition of carbon atoms at the edge of the cap where the dangling bonds are stabilised by the metal particle. Let us assume that the growth of the SWNT proceeds by the *yarmulke mechanism* under the conditions we have used. If the decomposition of the precursor occurs slowly at the beginning of tube growth, then the end–cap of the forming tube will have more time to organise itself into the

most stable structure that will define its chirality, perhaps with the size of the nanoparticle determining its diameter. However, if the decomposition occurs quickly, then the tube starts to grow whether it has the optimal structure or not: see Figure 4.21.

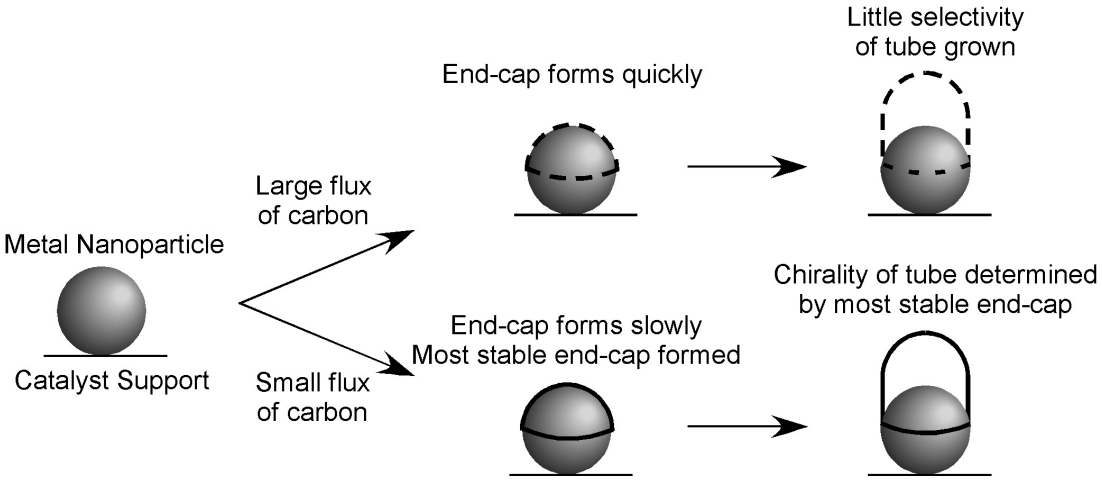

Figure 4.21. In the so–called yarmulke mechanism, the closed end–cap forms first on the nanoparticle, after which the tube grows from the particle by the addition of carbon to the edge of the end–cap. The dangling carbon bonds of the edge are stabilised by the metal particle. In the theory presented here, the rate at which the carbon precipitates to form the end–cap is thought to be vital. A small rate of carbon precipitation allows the formation of the most stable end–cap, whereas a large rate will cause less stable end–caps to form (shown by the dashed line). This theory suggests that tubes grown from methane should show a smaller distribution of chiralities.

Our theory of tube growth predicts that the part of the tube which forms first controls the chirality of the tube that grows. Recently, there have been several papers that have modelled the end–caps of carbon nanotubes and calculated their formation energies.[38-40] The work from the Robertson group[40] concludes that "*the structure and energetics of carbon caps on a catalytic particle will be key for chirality–selective growth of carbon nanotubes*". The basic assumption of these works is that the free energies of the formation of the end–caps will control the formation of the tubes. The theory that is presented here agrees with that conclusion of the calculations, but in addition we add that the *kinetics* of the formation of the end–cap, which in turn is controlled by the kinetics of the precursor decomposition, will also have an effect on the distribution of chiralities.

4.3.14 Multi–wavelength Raman spectroscopy

To investigate more fully, the distribution of the chiralities that form from different precursors, Raman spectroscopy at several different wavelengths was carried out on the samples produced from benzene and methane. As stated previously, each wavelength will enhance the Raman signal of a different selection of tubes according to their chiralities. So for each different wavelength used, a different selection of RBMs should be visible in the spectrum obtained. The benzene and methane samples were selected as they are the precursors with the simplest structures, which may make interpretation of the results easier. In addition, two more CVDs were carried out. Both of these CVDs included exposing the catalyst to hydrogen gas (at 865 °C) to reduce the metal particles to try to remove the effect of the precursor on the initial activation or size of the catalyst particles. One pre–reduced CVD used methane as the carbon source while the other used benzene. The % C of the CVD products, the yields and average I_D / I_G ratios (using 633 nm excitation) are presented in Table 4.4. The reduction conditions used can be seen to increase the amount of carbon deposited by methane with little effect on the I_D / I_G ratio. There is no great difference between the two benzene CVDs in terms of the amount of carbon deposited or the I_D / I_G ratio.

Carbon source	Catalyst reduced?	Average I_D / I_G ratio	Mass % C CVD product	% Yield of carbon
Methane	No	0.08	7	3
Methane	Yes	0.11	18	5
Benzene	No	0.23	16	7
Benzene	Yes	0.29	15	6

Table 4.4. Comparative CVDs were carried out using methane and benzene, as described in Section 4.3.6, with two additional experiments where the catalyst was exposed to hydrogen at 865 °C for 10 minutes before the precursor was passed through the furnace.

In addition to the Raman spectra collected using the 633 nm excitation laser, Raman spectra of the 4 samples were collected using 4 different excitation wavelengths: 531, 568, 647, and 676 nm (we are grateful to Hugh Vass in the School of Physics of the University of Edinburgh for help in collecting these spectra). Appendix B includes tables of all the RBMs identified. In addition (n,m) values have been assigned to the RBMs, where possible, using calculated values of the energy gap[41,42] between the van Hove singularties in the electronic density of states. This was limited to tubes with a chiral vector of between (6,0) and (20,0).

Figure 4.22 shows the radial breathing mode region of all of the spectra collected. Comparing the spectra for the methane and benzene samples, it can be seen that the methane sample has RBMs at higher frequencies, particularly in the spectra collected at 676 nm and 531 nm. As the frequency of a RBM is inversely proportional to the diameter of the tube from which it arises, the higher frequency RBMs suggests that the methane samples include SWNTs of smaller diameter than the benzene sample. An empirically derived relationship between the diameter (d_t) and the wavenumber of the observed RBM (ω_{RBM}) is stated in Equation 4.1:[43]

$$d_t / \mathrm{nm} \approx \frac{248}{\omega_{RBM} / \mathrm{cm}^{-1}} . \qquad (4.1)$$

Using this equation we can estimate the diameters of the tubes for the observed RBMs and the assigned tubes. A plot of the diameters of the tubes against the excitation energy for the methane and benzene samples is shown in Figure 4.23. The

plot shows clearly that the methane sample contains tubes of smaller diameter, down to ~ 0.7 nm, which are not found in the benzene. The methane and benzene samples produced with a pre–reduced catalyst have very similar plots (not shown) to the methane and benzene sample respectively: as is evident from the raw Raman spectra.

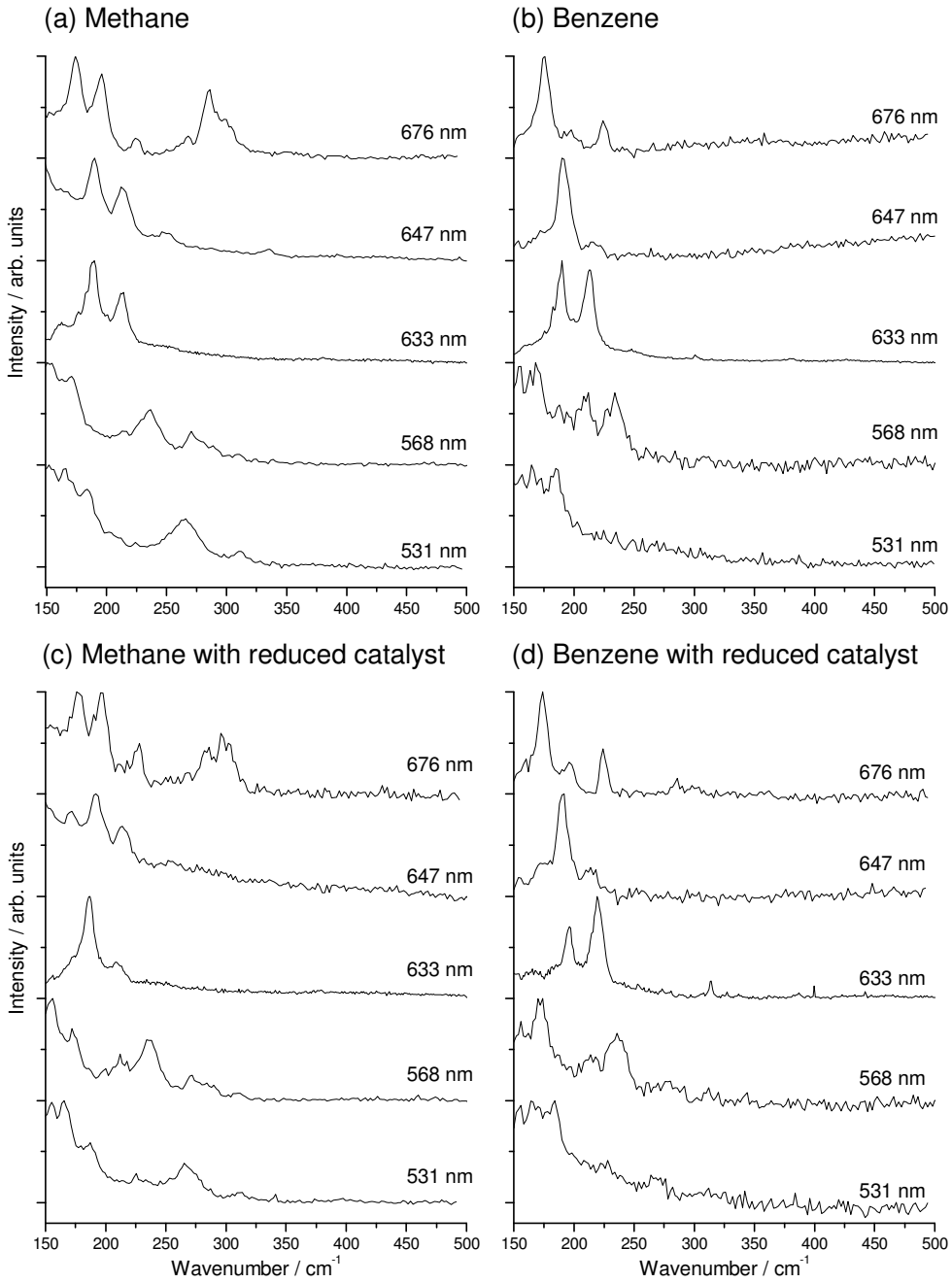

Figure 4.22. Raman spectra were collected at 5 different wavelengths for 4 different samples. Two of the CVD products were prepared as in Section 4.3.6 from (a) methane and (b) benzene. The other two samples were prepared in the same way but the catalyst was exposed to H_2 gas before the CVD so as to pre–reduce the catalyst. The samples prepared with the pre–reduced catalyst used (c) methane and (d) benzene as the carbon sources. Comparing the spectra it can

be seen that those from the methane samples have consistently different RBMs to the benzene samples.

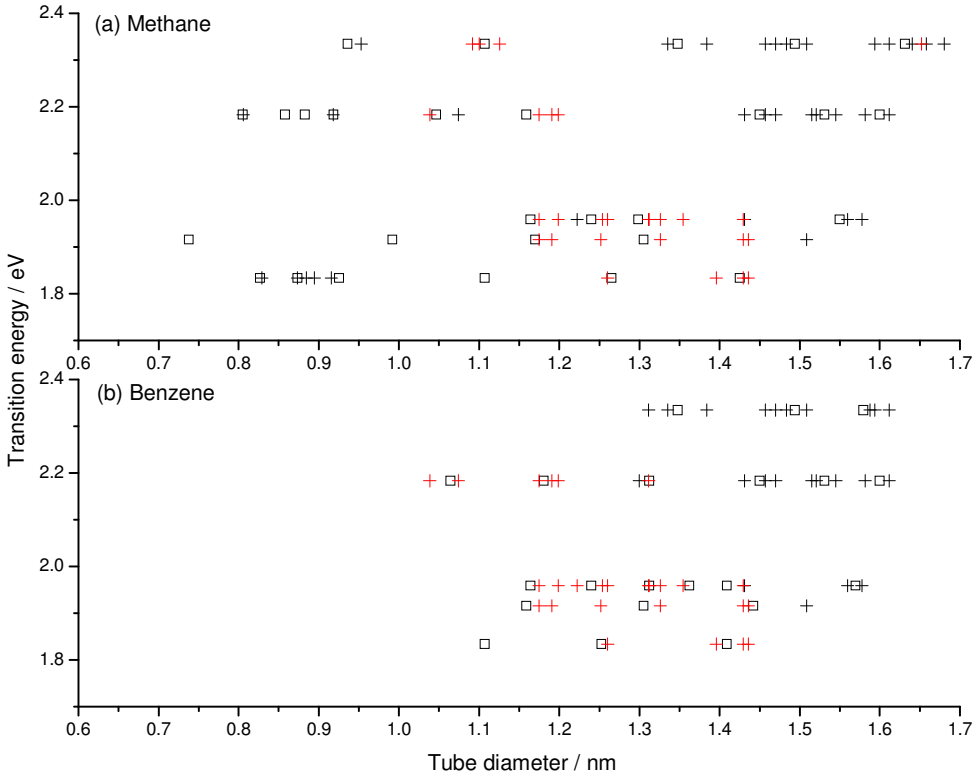

Figure 4.23. Plotted here are the calculated diameters of the nanotubes corresponding to the observed nanotubes (□) and the nanotubes with nearest theoretical (n,m) values (+) for the methane (a) and benzene (b). Red symbols are used for nearest theoretical (n,m) that are metallic tubes, while black is used for semiconducting tubes. The spectra of the methane sample contain RBMs corresponding to smaller diameters of tubes than those contained in the benzene sample.

More identifiable RBMs can be found in the methane Raman spectra than the benzene spectra. The methane has a total of 32 RBMs in its spectra whereas benzene has 21. The greater number of RBMs for methane goes against the mechanism proposed in section 4.3.13. The proposed mechanism suggests that benzene should have more visible radial breathing modes as it is less stable than methane and therefore the CVD conditions should be less selective in the tubes that grow. However, it should be noted that the even though the spectra were collected with

several different excitation wavelengths, it is likely that still only a small selection of the chiralities present have been detected. In addition, the spectra of the benzene samples, which have larger I_D / I_G ratios than their methane equivalents, tend to have smaller Raman signals due to their overall less graphitic nature. A smaller signal usually gives a greater level of noise in the Raman spectrum. The greater noise (Figure 4.22) in the benzene samples' spectra could possibly mask the presence of weak RBMs. As can be seen from the TEM images in Figure 4.16 and Figure 4.17, the sample produced from benzene contains more multi–walled tubes than the methane sample, which is consistent with the larger value of I_D / I_G.

It is notable that the reduction process does not significantly change the Raman spectra of the CVD products compared to spectra from samples produced with the unreduced catalyst. It is difficult to judge whether the H_2 gas has indeed reduced all the metal salts to active nanoparticles. In Chapter 3, similar reduction conditions were found to have a drastic effect on the tubes produced by CVD. Although the difference is less pronounced here, the increase in the amount of carbon deposited from methane is evidence that the catalyst has been changed by the reduction (see Table 4.4). Indeed, the very small effect of the hydrogen reduction on the RBMs present does suggest that the precursor controls chiralities of the tubes during the CVD in some way *other* than determining the size of nanoparticles formed. The differences in the structures of the precursors, methane and benzene, and their difference in reactivity do not seem to control the chiralities or diameters of the tubes by forming different sizes of nanoparticles during the reduction of the catalyst to its active form.

The Raman spectra collected with several different excitation lasers suggest that neither of the mechanisms proposed in Section 4.3.13 are valid (Figure 4.21). The pre–reduction results also suggest that the differences in the diameters of tubes present in each sample are not due to differences in the sizes of nanoparticles formed during the reduction. Therefore the different diameters of tubes must arise during the growth of the tubes. From the spectra, it appears that methane, although it is more stable, produces a wider variety of tubes than benzene. The spectra do also show that

methane produces thinner SWNTs, while benzene produces wide SWNTs and (from TEM) MWNTs. Here we propose a mechanism to explain this finding based on the relative stability of the methane and the benzene. As stated before, methane is more stable than benzene under the high temperature conditions, so we think that benzene produces a larger flux of available carbon than the more stable methane.[7] Larger fluxes of carbon may promote the formation of larger diameter tubes and, in the extreme case, MWNTs. If we consider the yarmulke mechanism, where the end–cap forms first and defines the diameter and chirality of the tube, there must be some point where the atomic carbon stops adding to the growing edge of the end–cap on the surface of particle and starts to form the sidewall of the nanotube. Once the sidewall is growing, the end–cap will be pushed off the surface of the nanoparticle and the nanotube continues to grow. Otherwise, if the end–cap did continue to grow without forming the sidewalls then the nanoparticle may become encapsulated with carbon. The driving force for the formation SWNTs over the formation of carbon coated nanoparticles in the yarmulke mechanism has been suggested to be the relaxation of strain in the end–cap.[8] We propose that the lower curvature of the sidewalls of the nanotubes makes their formation more energetically favourable (like graphite). However, it should be pointed out that there is evidence of particle encapsulation during CVD experiments under certain conditions that have also produced SWNTs.[44] It was observed that while nanoparticles with small diameters produced SWNTs, larger particles became encapsulated with carbon. These observations have been attributed to the curvature of the end–cap.[8,44] The small nanoparticles produce end–caps that are highly strained, and growth of the nanotube sidewalls becomes favourable to reduce the stress in the end–cap, whereas the larger particles produce less curved end–caps that can increase in size until the particle becomes encapsulated.[45]

Here once again, we suggest that consideration of the kinetics of growth of CNTs must be considered. As demonstrated in Section 4.3.5, large fluxes of carbon seem to promote the formation of MWNTs, which has also been reported in the literature.[8,46,47] If we assume that the sizes of the nanoparticles are not controlling the diameters of the tubes, then we might consider that the precipitation (or diffusion) of

the atomic carbon from the nanoparticle surface to form the end–cap and the nanotube is the controlling factor. A diagram of our suggested mechanism is shown in Figure 4.24. If the rate of precipitation is small, due to the low availability of carbon, then the end–cap forms slowly. The difference in the free energy change between a carbon atom adding to the highly curved end–cap or adding to the less curved sidewall, will promote the formation of sidewall under the slow growth conditions. An end–cap formed slowly will more likely start to form the sidewalls of the tube earlier, corresponding to a smaller nanotube. In this model, growth of SWNTs with a small rate of precipitation of carbon can be thought of as the CVD process being under kinetic control. Due to the small amount of carbon available to react, the reaction does not approach equilibrium and a less stable product is formed as it is energetically more favourable to form the sidewalls of the nanotube. This pushes the end–cap off the surface of the nanoparticle, rather than form a larger end–cap on the nanoparticle. In contrast, when there is a large amount of carbon available and a higher rate of precipitation, larger end–caps (perhaps even several of them) can form quickly. Under these conditions the difference in energy between adding to the end–cap and forming the sidewall is not so important. The greater amount of carbon reacting brings the process closer to equilibrium. Under these conditions, with higher fluxes of carbon, the process can be thought of as being under thermodynamic control as the more stable product is formed, e.g., MWNTs and large SWNTs.

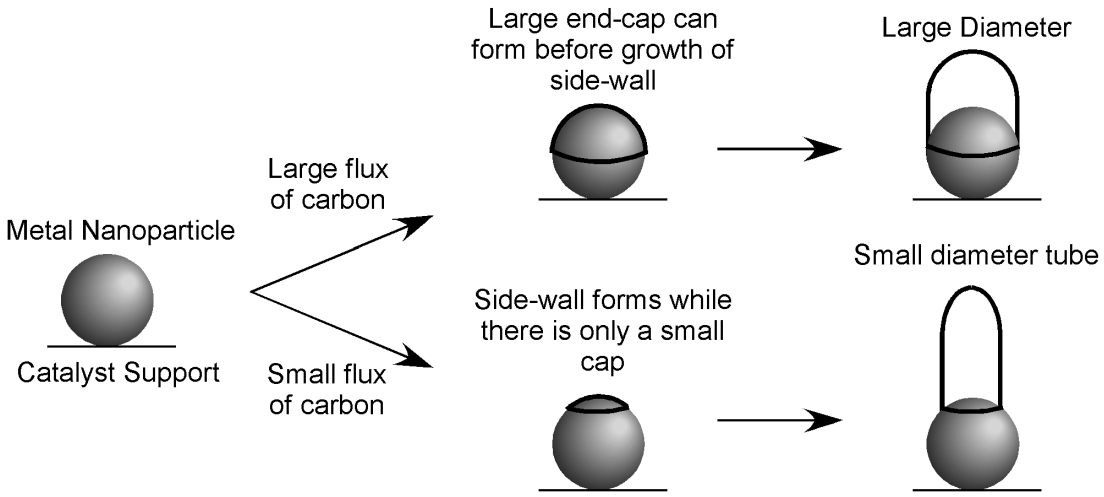

Figure 4.24. Diagram of the mechanism proposed in Section 4.3.14. Methane has been seen to produce smaller diameter SWNTs than benzene. This mechanism suggests that a nanoparticle may grow different sizes of tube depending on the flux of carbon. Under a small flux of carbon, the sidewall of the nanotube starts to form early to relieve strain, so that small diameter tubes are formed. Whereas with a large flux of carbon, the end–cap can become large before the sidewall starts to form, giving large diameter tubes.

4.4 Conclusions

In the literature, camphor has been proposed as a good precursor to grow carbon nanotubes by thermal CVD. It was suggested in work by Kumar *et al.*[19] that the bicyclic structure, and the O atom in the camphor molecule, contribute to its suitability as a carbon source. Comparative CVD experiments were carried out to test these assertions. The conditions used were archetypical for the synthesis of SWNTs: high temperatures (865 °C) and an alumina–supported Fe / Mo catalyst. Precursor vapour pressure was normalized by heating precursors to different temperatures so that they would have the same vapour pressures for CVD. Raman spectroscopy of the nanotube samples grown showed no obvious differences in quality with precursor structure. Some major differences in quality and yield would have been expected if the growth depended on formation and reaction of cyclic radicals formed by the precursors. Therefore, we put forward that the growth of SWNTs from camphor does not occur by addition of pre–formed rings as has been suggested previously.

The structure of the precursor was found to have more subtle effects on the tubes produced. Methane was found to produce better quality tubes than all the other precursors, and this was rationalised in terms of the greater kinetic stability of methane. Closer inspection of the Raman spectra of all the samples suggested differences in the distribution of the diameters or chiralities of the tubes. The differences in the distributions were rationalized by two explanations: (1) the different precursors reduce the metal salt in the catalyst to form nanoparticles of different sizes, which then template CNTs of different sizes to grow; (2) the tube diameter distribution is controlled by the kinetics of the tube growth, which is related to kinetics of precursor decomposition and the energies of the formation of end–cap of the SWNTs.

Further CVDs were carried out with benzene and methane where the catalyst was reduced with hydrogen gas to determine if the reduction process was controlling the size distribution of nanotubes. Raman spectra were collected with several different excitation laser wavelengths. The similarity of the pre–reduced and not pre–reduced sample spectra suggested that the distribution of tube sizes *is not controlled by the reduction of the catalyst by the different precursors*. However, there were clear differences between the samples produced by methane and benzene. The methane spectra contained more RBMs and also RBMs at higher frequencies, which is indicative of tubes with smaller diameter. These differences in size distribution suggest that the lower availability of carbon promotes the production of thinner tubes, which may be rationalised in terms of the kinetics of the formation of the end–cap versus the formation of the sidewalls.

Appendix A. Estimation of vapour pressure of precursors

In this work, it was necessary to estimate the vapour pressure of camphorquinone when heated to 200 °C. Once the this vapour pressure was known it would be possible then to calculate the temperatures required to heat the other precursors so that they would have the same vapour pressure. As no data about the vapour pressure

of camphorquinone was available, an approximate value of the enthalpy of vaporisation was found by using Trouton's rule,[30]

$$\Delta H_{vap} \approx T_b \times (85\,J\,K^{-1}mol^{-1}), \quad \textbf{(A.1)}$$

where ΔH_{vap} is the enthalpy of vaporisation and T_b is the boiling point of the camphorquinone (499.7 K). The rule gave a value of 42.5 kJ mol^{-1} for the enthalpy of vaporisation. The estimate from Trouton's rule is probably too low as the rule does not hold for liquids that are ordered due to intermolecular forces. The value of $\Delta H_{vap}/ T_b$ for similar compounds (see Table A.1) is larger than the 85 J K^{-1} mol^{-1} used in Trouton's rule.

Precursor	**ΔH_{vap} / J mol^{-1}**	**T_b / K**	**(ΔH_{vap} / T_b) / J mol^{-1} K^{-1}**
Norcamphor	50520	443	114
Camphene	40545	433	94
Norbornane	40628	386	105

Table A.1. The value of $\Delta H_{vap}/ T_b$ for these compounds is larger than the 85 J K^{-1} mol^{-1} that is assumed in Trouton's rule.

To calculate the vapour pressure of camphorquinione at 200 °C the integrated Clausius–Clayperion equation[30] was used,

$$p_1 = p_2 e^{-\chi}, \textbf{ where } \chi = \frac{\Delta H_{vap}}{R}\left(\frac{1}{T_1} - \frac{1}{T_2}\right), \qquad \textbf{(A.2)}$$

and where p_x is the vapour pressure of compound at temperature, T_x. Using the fact that under atmospheric pressure at 226.5 °C the vapour pressure of camphorquinone is equal to 760 Torr, the vapour pressure of camphorquinone can be calculated as 428 Torr at 200 °C. Unfortunately, when originally calculated this value was wrongly found to be ~ 350 Torr. The series of experiment in Section 4.3.6 required all the precursors used to be heated a temperature at which they would all have around the same vapour pressure. The pressure chosen was 350 Torr as it had (in error) been

calculated to be vapour pressure of camphorquinone at 200 °C. Therefore, this error caused us to use a vapor pressure of camphorquinone that was 18 % higher than the other precursor compounds. The error is not considered to be critical to the results and conclusions presented in this thesis.

Thermodynamic data were obtained from the DETHERM Database.[29] For three of the compounds (norcamphor, camphene and norbornane) only the enthalpies of vaporisation were available. The required temperatures were calculated using the integrated Clausius–Clayperion equation and assuming that the vapour pressure was equal to 760 Torr at their boiling point. The calculated values of the temperature required are presented in Table A.2.

Precursor	**$\Delta_{vap}H$ / J mol^{-1}**	**T_b / K**	**Required temperature / K**
Norcamphor	50520	443	425
Camphene	40545	433	412
Norbornane	40628	386	368

Table A.2. The information presented here was used with the Clausius–Clayperion equation to estimate the required temperature for the precursors to be heated so that each would have a vapour pressure of 350 Torr.

For all the other liquid and solid precursors, the Antoine Constants were obtained from the DETHERM Database. Antoine constants have empirically determined values that allow the calculation of the vapour pressure using the Antoine equation.[29]

$$\log_{10}(p/\text{Torr}) = A - B/((T/°C) + C) \qquad \textbf{(A.3)}$$

Again the pressure was chosen to be 350 Torr, and the required temperature was calculated. The values of the Antoine constants and calculated temperatures are presented in Table A.3.

Precursor	Antoine constants			Required temperature/ °C
	A	B	C	
Camphor	7.3849	1818.46	198.817	177
Benzene	6.87987	1196.76	219.161	57
Menthone	6.84888	1582.5	188.99	179
Fenchone	7.6227	2041.24	239.57	162
2-Decanone	7.04577	1657.888	183.669	185

Table A.3. The required temperature to produce a vapour pressure of 350 Torr was calculated using the Antoine equation and the constants obtained from the DETHERM Database.[29]

Appendix B. Assignment of chiral vectors to radial breathing modes

The Raman spectra of carbon nanotubes contain a great deal of information about the structure of the tubes. The frequency of a radial breathing mode (ω_{RBM}) that appears in the Raman spectrum of a carbon nanotube can be related to the diameter of the nanotube (d_t). The most commonly used relationship, which was empirically determined,[42] is given in Equation 4.1 (Section 4.3.14). The diameter of the tube is related to the chiral vector of the nanotube. However, it is not possible to assign a particular (n,m) value to a RBM on its frequency alone as there are many nanotubes which have similar diameters and therefore similar ω_{RBM}.

The strong Raman signals that can be observed for SWNTs are due to the resonance enhancement that often occurs with energies of the excitation lasers that are commonly used in Raman spectroscopy. These excitation energies can coincide with the energy gap between pairs of van Hove singularities in the electronic density of states of the SWNTs. When these energies do match, there is a dramatic enhancement of the Raman signal that allows even the spectra of *individual* nanotubes to be obtained.[43]

For the Raman signal to be resonance enhanced the excitation laser energy (E_L) must roughly to equal to transition of the energy between the singularities (E_{ii}). Each of the different chiralites of the nanotubes have several of these transitions, and the size of a particular E_{ii} can be calculated from the chiral vector (n,m). So, for any given energy of excitation laser, it is possible to deduce the (n,m) values of tubes that could be in resonance. Using the diameter of tube, which can be calculated from the frequency of the RBM, and knowing which tubes are in resonance with laser, it is possible to suggest chiral vectors for each radial breathing mode present in a spectrum.[48]

Although some empirically determined values of the transition energies and frequencies of the radial breathing modes of tubes of certain chiral vectors have been determined,[36,48,49] there are not enough to be used to assign chiral vectors to RBMs in a spectrum comprehensively, so here theoretically calculated values were used. Calculated diameters and the corresponding transition energies were obtained for tubes ranging from (6,0) to (20,0) from Professor Maruyama's group at the University of Tokyo. The calculations used the tight binding approximation and the zone folding approach based on the work of Kataura *et al.*,[49] and detailed description of the calculations is described in the work of Saito *et al.*[42] The ω_{RBM} for each tube was calculated using the relationship above (Equation 4.1).

Such an assignment of chiral vectors was carried out for 4 samples that are described in Section 4.3.14 and are presented in Tables B.1to B.4. A chiral vector was considered to be a likely match for a RBM if the calculated resonance energy was within 100 meV of the excitation energy (suggested as the width of the resonance window for bundled SWNTs[50]) and if the caculated ω_{RBM} was within 5 cm^{-1} of the observed RBM. Most RBMs have several possible chiral vectors and it is possible that some of the observed RBMs have contributions to its intensity from several different chiralities of tubes.

Table B.1. Observed radial breathing modes and (n,m) assignment for methane sample.

Excitation wavelength / nm	Excitation energy / eV	Observed RBM / cm^{-1}	Possible (n,m) values	Calculated RBM / cm^{-1}	Calculated transition energy / eV
676	1.834	174	(18,0)	173.5	1.832
			(13,7)	177.7	1.812
			(17,2)	172.7	1.816
		196	(12,6)	196.8	1.896
		224	?		
		268	(9,4)	270.9	1.744
			(11,1)	270.9	1.904
			(7,6)	277.2	1.848
		284	(11,0)	284	1.796
			(10,2)	280.5	1.782
		300	(7,5)	299.2	1.944
647	1.9163	168	(19,0)	164.4	2.056
			(18,0)	173.5	1.832
			(17,2)	172.7	1.816
		190	(15,3)	187	1.964
			(11,8)	198.1	1.904
		212	(15,0)	208.3	1.96
			(10,7)	211.1	2.052
		250	?		
		336	?		
633	1.959	160	(16,6)	159	2.016
			(12,11)	157.2	2.056
		176?	(18,0)	173.5	1.832
			(15,5)	173.3	2.18
		183?	(14,5)	183.1	1.896
		191	(11,8)	189.1	1.904

			(12,6)	196.8	2.012
	1.959	191	(15,3)	187	1.964
			(16,1)	189	2
			(12,6)	197.8	2.012
		200	(12,6)	197.8	2.012
			(13,4)	202.9	1.932/2.112
		213	(14,2)	206.9	1.956
			(10,7)	211.1	2.052
568	2.183	155	(18,4)	153.9	2.156
			(20,0)	156.8	2.216
		162	(15,7)	160.5	2.196
			(13,9)	163.1	2.108
			(12,10)	163.7	2.172
		171	(14,7)	168.7	2.148
			(13,8)	170.2	2.292
			(15,5)	173.3	2.18
		214	(10,7)	211.1	2.124
			(15,0)	208.3	2.216
			(14,2)	206.9	2.188
		237	(9,6)	238.8	2.296
			(13,1)	230.9	2.156
		270	(11,1)?	270.1	1.904
		281	?		
		289	?		
		308	(9,2)	307.8	2.156
531	2.335	152	(16,8)	147.6	2.336
			((14,10)	149.6	2.488
			(13,10)	150.1	2.424
			(17,6)	151.2	2.364
			(18,4)	153.9	2.384
			(19,2)	155.6	2.396

	2.335	166	(16,5)	164.4	2.284
			(17,3)	167.2	2.356
			(18,1)	168.7	2.396
			(13,8)	170.2	2.292
		184	(12,8)	179.2	2.296
			(11,9)	180.1	2.38
			(13,6)	185.7	2.344
		224	(11,5)	220.3	2.26
			(8,8)	225.4	2.22
			(12,3)	227.2	2.384
		265	(12,0)	260.3	2.4

Table B.2. Observed radial breathing modes and (n,m) assignment for benzene sample.

Excitation wavelength / nm	Excitation energy / eV	Observed RBM / cm^{-1}	Possible (n,m) values	Calculated RBM / cm^{-1}	Calculated transition energy / eV
676	1.834	176	(18,0)	173.5	1.832
			(13,7)	177.7	1.812
			(17,2)	172.7	1.816
		198	(12,6)	196.8	1.896
		224	?		
647	1.916	172	(19,0)	164.4	2.056
			(18,0)	173.5	1.832
			(17,2)	172.7	1.816
		190	(15,3)	187	1.964
			(11,8)	198.1	1.904
		214	(15,0)	208.3	1.96
			(10,7)	211.1	2.052
633	1.959	158	(16,6)	159	2.016
			(12,11)	157.2	2.056
		176	(18,0)	173.5	1.832
			(15,5)	173.3	2.18
		182	(14,5)	183.1	1.896
		189	(11,8)	189.1	1.904
			(12,6)	196.8	2.012
			(15,3)	187	1.964
			(16,1)	189	2
			(12,6)	197.8	2.012
		200	(12,6)	197.8	2.012
			(13,4)	202.9	1.932/ 2.112
		213	(14,2)	206.9	1.956

			(10,7)	211.1	2.052
568	2.183	155	(18,4)	153.9	2.156
			(20,0)	156.8	2.216
		162	(15,7)	160.5	2.196
			(13,9)	163.1	2.108
			(12,10)	163.7	2.172
		171	(14,7)	168.7	2.148
			(13,8)	170.2	2.292
			(15,5)	173.3	2.18
		189?	(16,1)	189.1	2.00
			(14,4)	190.8	2.376
		210	(10,7)	211.1	2.124
			(15,0)	208.3	2.216
			(14,2)	206.9	2.188
		233	(9,6)	238.8	2.296
			(13,1)	230.9	2.156
531	2.335	157	(18,4)	153.9	2.384
			(19,2)	155.6	2.396
			(20,0)	156.2	2.216
		166	(16,5)	164.4	2.284
			(17,3)	167.2	2.356
			(18,1)	168.7	2.396
			(13,8)	170.2	2.292
		184	(12,8)	179.2	2.296
			(11,9)	180.1	2.38
			(13,6)	185.7	2.344

Table B.3. Observed radial breathing modes and (n,m) assignment for methane sample with hydrogen reduction.

Excitation wavelength / nm	Excitation energy / eV	Observed RBM / cm^{-1}	Possible (n,m) values	Calculated RBM / cm^{-1}	Calculated transition energy / eV
676	1.834	176	(18,0)	173.5	1.832
			(13,7)	177.7	1.812
			(17,2)	172.7	1.816
		198	(12,6)	196.8	1.896
		228	?		
		286	(11,0)	284	1.796
			(10,2)	280.5	1.782
		302	(7,5)	299.2	1.944
647	1.9163	172	(19,0)	164.4	2.056
			(18,0)	173.5	1.832
			(17,2)	172.7	1.816
		192	(15,3)	187	1.964
			(11,8)	198.1	1.904
		213	(15,0)	208.3	1.96
			(10,7)	211.1	2.052
		252	?		
33	1.959	156	(16,6)	159	2.016
			(12,11)	157.2	2.056
		174	(18,0)	173.5	1.832
			(15,5)	173.3	2.18
		187	(11,8)	189.1	1.904
			(12,6)	196.8	2.012
			(15,3)	187	1.964
			(16,1)	189	2.00
			(12,6)	197.8	2.012

		196	(12,6)	197.8	2.012
			(13,4)	202.9	1.932/ 2.112
633	1.959	209	(14,2)	206.9	1.956
			(10,7)	211.1	2.052
568	2.183	156	(18,4)	153.9	2.156
			(20,0)	156.8	2.216
		172	(14,7)	168.7	2.148
			(13,8)	170.2	2.292
			(15,5)	173.3	2.18
		200	(12,6)	196.7	2.012
				202.9	2.112
		212	(10,7)	211.1	2.124
			(15,0)	208.3	2.216
			(14,2)	206.9	2.188
		235	(9,6)	238.8	2.296
			(13,1)	230.9	2.156
		272	(11,1)?	270.1	1.904
		289	?		
		310	(9,2)	307.8	2.156
531	2.335	156	(16,8)	147.6	2.336
			((14,10)	149.6	2.488
			(13,10)	150.1	2.424
			(17,6)	151.2	2.364
			(18,4)	153.9	2.384
			(19,2)	155.6	2.396
		165	(16,5)	164.4	2.284
			(17,3)	167.2	2.356
			(18,1)	168.7	2.396
			(13,8)	170.2	2.292
		187	(12,8)	179.2	2.296

			(11,9)	180.1	2.38
			(13,6)	185.7	2.344
531	2.335	225	(11,5)	220.3	2.26
			(8,8)	225.4	2.22
			(12,3)	227.2	2.384
		265	(12,0)	260.3	2.4

Table B.4. Observed radial breathing modes and (n,m) assignment for methane sample with hydrogen reduction.

Excitation wavelength / nm	Excitation energy / eV	Observed RBM / cm^{-1}	Possible (n,m) values	Calculated RBM / cm^{-1}	Calculated transition energy / eV
676	1.834	160?			
		174	(18,0)	173.5	1.832
			(13,7)	177.7	1.812
			(17,2)	172.7	1.816
		190?			
		196	(12,6)	196.8	1.896
		224	?		
		286	(11,0)	284.0	1.796
			(10,2)	280.5	1.782
647	1.9163	154	(13,11)	150.1	1.996
			(20,1)	152.2	1.916
		172	(19,0)	164.4	2.056
			(18,0)	173.5	1.832
			(17,2)	172.7	1.816
		180	(13,7)	177.7	1.812
			(14,5)	183.1	1.896
		192	(15,3)	187	1.964
			(11,8)	198.1	1.904
		214	(15,0)	208.3	1.96
			(10,7)	211.1	2.052
633	1.959	159	(16,6)	159	2.016
			(12,11)	157.2	2.056
		176	(18,0)	173.5	1.832
			(15,5)	173.3	2.18
		182	(14,5)	183.1	1.896

		190	(11,8)	189.1	1.904
			(12,6)	196.8	2.012
			(15,3)	187	1.964
			(16,1)	189	2
			(12,6)	197.8	2.012
		200	(12,6)	197.8	2.012
			(13,4)	202.9	1.932/2.112
633	1.959	212	(14,2)	206.9	1.956
		247	(10,7)	211.1	2.052
568	2.183	156	(18,4)	153.9	2.156
			(20,0)	156.8	2.216
		172	(14,7)	168.7	2.148
			(13,8)	170.2	2.292
			(15,5)	173.3	2.18
		214	(10,7)	211.1	2.124
			(15,0)	208.3	2.216
			(14,2)	206.9	2.188
		236	(9,6)	238.8	2.296
			(13,1)	230.9	2.156
531	2.335	156	(18,4)	153.9	2.384
			(19,2)	155.6	2.396
			(20,0)	156.2	2.216
		164	(16,5)	164.4	2.284
			(17,3)	167.2	2.356
			(18,1)	168.7	2.396
			(13,8)	170.2	2.292
		170	(16,5)	164.4	2.284
			(17,3)	167.2	2.356
			(18,1)	168.7	2.396
		178	(13,8)	170.2	2.292
			(11,10)	171.7	2.24

			(14,6)	175.7	2.412
		184	(12,8)	179.2	2.296
			(11,9)	180.1	2.38
			(13,6)	185.7	2.344
		228	(11,5)	220.3	2.26
			(8,8)	225.4	2.22
			(12,3)	227.2	2.384
		264	(12,0)	260.3	2.4

4.5 References

1) R. Saito, G. Dresselhaus, M. S. Dresselhaus. *Physical Properties of Carbon Nanotubes.* Imperial College Press, 1998.

2) H. Dai. Carbon nanotubes: opportunities and challenges. *Surf. Sci.*, 2002, **500**, 218.

3) R. Krupke, F. Hennrich. Separation Techniques for Carbon Nanotubes. *Adv. Eng. Mat.,* 2005, **7**, 111.

4) F. Beuneu. Nucleation and growth of single wall carbon nanotubes. *Solid State Comm.,* 2005, **136**, 62.

5) R. B. Little. Mechanistic Aspects of Carbon Nanotube Nucleation. *J. Cluster Sci.,* 2003, **14**, 135.

6) P. T. A. Reilly, W. B. Whitten. The role of free radical condensates in the production of carbon nanotubes during the hydrocarbon CVD process. *Carbon,* 2006, **44**, 1653.

7) A. Moisala, A. G. Nasibulin, E. I. Kauppinen. The role of metal nanoparticles in the catalytic production of single–walled carbon nanotubes — a review. *J. Phys: Condens. Matter.,* 2003, **15**, s3011.

8) A.-C. Depuis. The catalyst in the CCVD of carbon nanotubes—a review. *Prog. Mater. Sci.,* 2005, **50**, 929.

9) Y. Shibuta, S. Maruyama. Molecular dynamics simulation of formation process of single–walled carbon nanotubes by CCVD method. *Chem. Phys. Lett.,* 2003, **382**, 381.

10) P. Argyrakis, L. Teo, T. Stevenson, R. Cheung. Fabrication of PDMS stamps for the patterned growth of carbon nanotubes. *Microelec. Eng.,* 2005, **78–79**, 647

11) H. Dai. Carbon Nanotubes: Synthesis, Integration, and Properties. *Acc. Chem. Res*., 2002, **35**, 1035

12) G. Eres, A. A. Kinkhabwala, H. Cui, D. B. Geohegan, A. A. Puretzky, D. H. Lowndes. Molecular Beam–Controlled Nucleation and Growth of Vertically Aligned Single–Wall Carbon Nanotube Arrays. *J. Phys. Chem. B,* 2005, **109**, 16684.

13) K. Mukhopadhyay, K. M. Krishna, M. Sharon. Fullerenes from camphor: a natural source. *Phys. Rev. Lett.,* 1994, **72**, 3182.

14) M. Sharon, K. Mukhopadhyay, I. Mukhopadhyay, K. M. Krishna. Semiconducting mutlichannel–multilayer camphoric tubes. *Carbon,* 1996, **33**, 331.

15) M. Sharon, K. Mukhopadhyay, K. Yase, S. Iijima, Y. Ando, X. Zhao. Spongy carbon nanobeads a new material. *Carbon,* 1998, **36**, 507.

16) M. Kumar, Y. Ando. Single–wall and multi–wall carbon nanotubes from camphor – a botanical hydrocarbon. *Diam. Rel. Mater.* 2003, **12**, 1845.

17) M. Kumar, Y. Ando. A simple method of producing aligned carbon nanotubes from an unconventional precursor — Camphor. *Chem. Phys. Lett.,* 2003, **374**, 521.

18) M. Kumar, Y. Ando. Camphor — a botanical precursor producing garden of carbon nanotubes. *Diam. Rel. Mater.,* 2003, **12**, 998.

19) M. Kumar, Y. Ando. Controlling the diameter distribution of carbon nanotubes grown from camphor on a zeolite support. *Carbon,* 2005, **43**, 533.

20) Y. Tian, Z. Hu, Y. Yang, X. Wang, X. Chen, H. Xu. In situ TA–MS study of the six–membered–ring–based growth of carbon nanotubes with benzene precursor. *J. Am. Chem. Soc.,* 2004, **126**, 1180.

21) Y. Tian, Z. Hu, Y. Yang, X. Chen, W. Ji, Y. Chen. Thermal analysis–mass spectroscopy coupling as a powerful technique to study the growth of carbon nanotubes from benzene. *Chem. Phys. Lett.,* 2004, **388**, 259.

22) Q. Li, H.Yan, J. Zhang, J. Liu. Effect of hydrocarbons precursors on the formation of carbon nanotubes in chemical vapor deposition. *Carbon,* 2004, **42**, 829.

23) M. Shigeo, R. Kojima, Y. Miyauchi, S. Chiashi, M. Kohno. Low–temperature synthesis of high–purity single–walled carbon nanotubes from alcohol. *Chem. Phys. Lett.,* 2002, **360,** 229.

24) S. Maruyama, R. Kojima,Y. Miyauchi, S. Chiashi, M. Kohno. Low temperature synthesis of high–purity single–walled carbon nanotubes from alcohol. *Chem. Phys. Lett.,* 2002, **360**, 229.

25) A. M. Cassell, J. A. Raymakers, J. Kong, H. Dai. Large scale CVD synthesis of single–walled carbon nanotubes. *J. Phys. Chem. B,* 1999, **103**, 6484.

26) M. S. Dresselhaus, G. Dresselhaus, A. Jorio, A. G. Souza Filho, R. Saito. Raman spectroscopy on isolated single wall carbon nanotubes. *Carbon,* 2002, **40**, 2043.

27) M. S. Dresselhaus, G. Dresselhaus, R. Saito, A. Jorio. Raman spectroscopy of carbon nanotubes. *Physics Reports,* 2005, **409**, 47.

28) W. Qian, T. Liu, F. Wei, H. Yuan. Quantitative Raman characterization of the mixed samples of the single and multi–wall carbon nanotubes. *Carbon,* 2003, **41**, 1851–1864.

29) The Detherm Database (http://i–systems.dechema.de/detherm/) maintained by DECHEMA (Society for Chemical Engineering and Biotechnology) Theodor–Heuss–Allee 25, D-60486 Frankfurt am Main. http://www.dechema.de/

30) P. Atkins, J. de Paula. *Physical Chemistry* (7th Ed.), Oxford University Press. 2002.

31) T. Sato, K. Murata, A. Nishimura, T. Tsuchiya, N. Wasada. Pyrolysis of organic compounds — II : The flash pyrolysis of camphor and its related compounds. *Tetrahedron,* 1967, **23**, 1791.

32) D. R. Linde (ed). Bond strengths in polyatomic molecules. In: *Handbook of Chemistry and Physics*. Boca Raton CRC Press, 2005, 9–64.

33) J. Kong, A. M. Cassell, H. Dai. Chemical vapor deposition of methane for single–walled carbon nanotubes. *Chem. Phys. Lett.* 1998, **292**, 567.

34) A. M. Rao, E. Richter, S. Bandow, B. Chase, P. C. Eklund, K. A. Williams, S. Fang, K. R. Subbaswamy, M. Menon, A. Thess, R. E. Smalley, G. Dresselhaus, M. S. Dresselhaus. Diameter–Selective Raman Scattering from Vibrational Modes in Carbon Nanotubes. *Science,* 1997, **275**, 187.

35) M. Machon, S. Reich, H. Telg, J. Maultzsch, P. Ordejon, C. Thomsen. Strength of radial breathing mode in single–walled carbon nanotubes. *Phys. Rev. B,* 2005, **71**, 035416.

36) H. Telg, J. Maultzsch, S. Reich, F. Hennrich, C. Thomsen. Chirality Distribution and Transition Energies of Carbon Nanotubes. *Phys. Rev. Lett.,* 2004, **93**, 177401.

37) P. J. F. Harris. *Carbon Nanotubes and Related Structures.* Cambridge University Press, 1999.

38) S. L. Lair, W. C. Herndon, L. E. Murr, S. A. Quinones. End cap nucleation of carbon nanotubes. *Carbon,* 2006; **44**, 447.

39) S. Reich, L. Li, J. Robertson. Control the chirality of carbon nanotubes by epitaxial growth. *Chem. Phys. Lett.,* 2006, **421**, 469.

40) S. Reich, L. Li, J. Robertson. Structure and formation energy of carbon nanotube caps. *Phys. Rev., B* 2005, **72**, 165423.

41) H. Kataura, Y. Kumazawa, Y. Maniwa, I. Umezu, S. Suzuki, Y. Ohtsuka, Y. Achiba. Optical Properties of Single–Wall Carbon Nanotubes. *Synth. Met.,* 1999, **103**, 2555.

42) R. Saito, G. Dresselhaus, M. S. Dresselhaus. Trigonal warping effect of carbon nanotubes. *Phys. Rev.* B, 2000, **61**, 2981.

43) M. S. Dresselhaus, G. Dresselhaus, A. Jorio, A. G. Souza Filho, M. A. Pimenta, R. Saito. Single Nanotube Raman Spectroscopy. *Acc. Chem. Res.,* 2002, **35,** 1070.

44) M. Lin, J. P. Y. Tan, C. Boothroyd, K. P. Loh, E. S. Tok, Y.-L. Foo. Direct Observation of Single–Walled Carbon Nanotube Growth at the Atomistic Scale. *Nano Lett.,* 2006, **6**, 449.

45) J. H. Hafner, M. J. Bronikowski, B. R. Azamian, P. Nikolaev, A. G. Rinzler, D. T. Colbert, K. A. Smith, R. E. Smalley. Catalytic growth of single–wall carbon nanotubes from metal particles. *Chem. Phys. Lett.,* 1998, **296**, 195.

46) J. H. Hafner, M. J. Bronikowski, B. R. Azamian, P. Nikolaev, A. G. Rinzler, D. T. Colbert, K. A. Smith, R. E. Smalley. Catalytic growth of single–wall carbon nanotubes from metal particles. *Chem. Phys. Lett.,* 1998, **296**, 195.

47) C. L. Cheung, A. Kurtz, H. Park, C. M. Lieber. Diameter–Controlled Synthesis of Carbon Nanotubes. *J. Phys. Chem. B,* 2002, **106,** 2429.

48) R. B. Weisman, S. M. Bachilo. Dependence of Optical Transition Energies on Structure for Single–Walled Carbon Nanotubes in Aqueous Suspension: An Empirical Kataura Plot. *Nano Lett.,* **2003**, 3, 1235–1238.

49) H. Kataura, Y. Kumazawa, Y. Maniwa, I. Umezu, S. Suzuki, Y. Ohtsuka, Y. Achiba. Optical Properties of Single–Wall Carbon Nanotubes. *Synth. Met.,* 1999, **103**, 2555.

50) C. Fantini, A. Jorio, M. Souza, M. S. Strano, M. S. Dresselhaus, M. A. Pimenta. Optical Transition Energies for Carbon Nanotubes from Resonant Raman Spectroscopy: Environment and Temperature Effects. *Phys. Rev. Lett*., 2004, **93**, 47406.

5 Direct functionalization of carbon nanotubes with sulfur

5.1 Introduction

There are many barriers to taking full advantage of the remarkable intrinsic properties of carbon nanotubes (CNTs). For example, as carbon nanotubes tend to have high aspect ratios (typically in the millions), the large cooperative van der Waals forces between the tubes mean they tend to form bundles and have low solubilities.[1] The difficulty in dispersing carbon nanotubes makes it hard to include them in polymer composites in order to obtain the great improvement in properties that were predicted from the tubes' intrinsic characteristics.[2] The solubility of carbon nanotubes has been improved using traditional surfactants and other molecules that have strong non–covalent interactions such as π stacking.[3] However, there has also been great interest in covalent functionalization of nanotubes.[1,3] A great deal of research has been undertaken to find ways to functionalize carbon nanotubes with long alkyl chains to make them easier disperse in non–polar solvents.[4]

Functionalization has also been used as a strategy to position carbon nanotubes: usually through some sort of self assembly.[4-7] The positioning of tubes is vital to the production of electronic devices. In this chapter, the direct functionalization of carbon nanotubes with sulfur–containing groups using a plasma, followed by selective assembly on gold surfaces, is explored as a method of gaining control over carbon nanotubes.

5.1.1 Functionalization of carbon nanotubes with thiols

A great challenge lies in trying to position carbon nanotubes in a reliable fashion that could be used to fabricate reproducible electronic devices. One approach makes use of the self assembly of thiols (–SH) onto gold surfaces.[4-7] Tubes, in this approach, have been functionalized with sulfur–containing groups by a several–step process. The tubes are first oxidised, in solution, to introduce reactive carboxylic acid groups, which are then reacted with standard organic reagents to attach thiol substituted alkyl chains through amide or ester formation. The oxidation step is particularly

undesirable as it damages the tube structure and introduces defects that alter the properties of the tube. The end–caps of the tubes are also removed by the oxidation, which creates a high density of thiol groups at the open ends. The functionalized, shortened tubes tend to "stand on end" when they self assemble on a gold surface. An image of one of these surfaces is shown in Figure 5.1, which was obtained by atomic force microscopy.[6] The tubes attach to the surface in this way to maximise the amount of thiol–gold interaction, and to increase the van der Waals interaction between the sidewalls of the tubes. It would seem advantageous to be able to functionalize the outside of the tube without opening or shortening the tubes, so that the carbon nanotubes could bridge between electrodes rather than standing perpendicular to the surface.

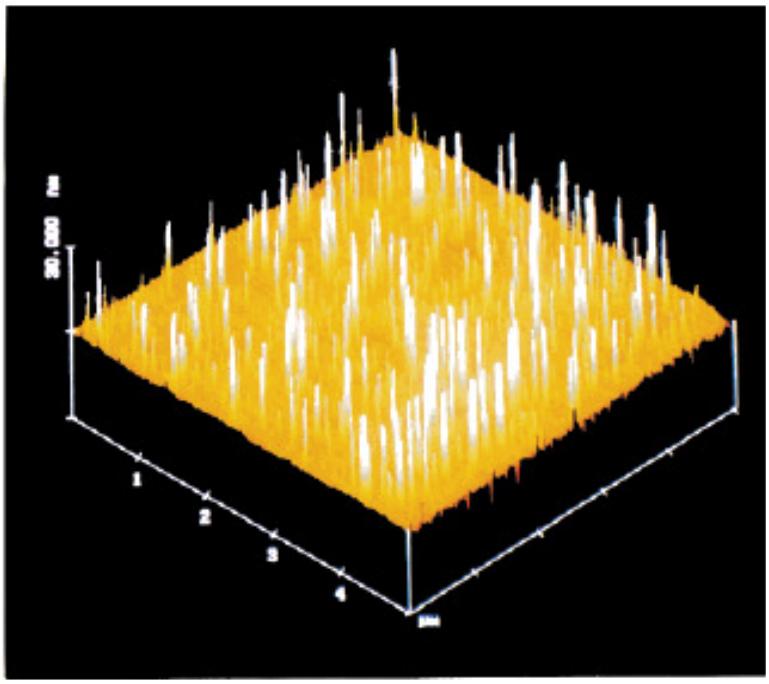

Figure 5.1. AFM image of thiol functionalized nanotubes, showing their self assembly onto a gold surface. The tubes "stand on end" to maximize the interaction of the thiols with the gold, and to maximize the van der Waal forces between the tubes. The figure is reproduced from the work of Z. Liu *et al*.[6]

5.1.2 Plasma functionalization

The term *plasma* refers to a gas that contains ions, neutral species, and high energy electrons that cause excitations and ionisations within the plasma. Plasmas are

commonly used to etch micron size features during microfabrication to produce, for example, integrated circuits. Recently, carbon nanotubes have been functionalized with fluorine by exposing them to reactive plasmas in a reactive ion etcher (RIE).[8,9] Glow discharge has been used to generate a hydrogen plasma that functionalized the surface of tubes with H atoms.[10,11]

Typically, weakly ionized plasmas are generated in etchers by applying an oscillating voltage between electrodes,[12] usually at 13.6 MHz, which excites the electrons of the gas in the etcher. Due to the electrons having a much smaller mass than the nuclei, the electric field between the electrodes accelerates them to much larger speeds. The overall effect is that the molecules and atoms of the gas become ionized as a result of high–energy collisions. As the electrons are accelerated to greater speeds, they move further from the interior towards the electrodes and the walls of the reactor. The movement of the electrons causes the plasma to become positively charged. Over time, a potential difference develops between the plasma and the sidewalls. Any sample that is placed in the reactor is going to be at a more negative potential than the plasma. The potential difference between the sample and the plasma causes the energetic ions from the plasma to strike the sample. In some plasma etchers the bias of the sample can be changed so that the energy of the ions hitting it can also be varied. As carbon nanotubes are covered with an extended electronic π system, their surfaces are electron rich: therefore it is desirable to try to react carbon nanotubes with positive ions.

5.1.3 Plasma advantages

In this work, plasmas have been used to functionalize carbon nanotubes because a plasma has several advantages over the usual solution–based procedure. Firstly, it is expected that positive sulfur–containing ions would be formed that would be likely to react with the π system of the CNTs. There is also no need to disperse the nanotubes fully in a solvent. This can be a difficult step that may require long periods of sonication,[13] which has been reported to harm tubes. If the tubes are not well dispersed in the solvent, and therefore still in bundles, it is also possible that the reagents would only have access to tubes on the outside of the bundles. In plasma

functionalization, the reactive molecules are in the gas phase and may be able to penetrate deeper into the bundles. In the solvent system they would not, especially if the reagents and solvent are polar, as the nanotubes are hydrophobic.

Functionalization of carbon nanotubes using gases such F_2 or HF at high temperature has been successful in covalently attaching large amounts of fluorine to CNTs: although long reaction times are required.[14,15] Plasma functionalization can also shorten reaction times[8,9] due to the enhancement of rate by the irradiation with ions and electrons, and the highly reactive species that form in the plasma.[16]

5.2 Results and Discussion

5.2.1 Preliminary experiments

Ongoing work by Plank *et al.* at the Scottish Microelectronic Centre (SMC) had functionalized CNTs with fluorine using both CF_4 and SF_6.[8] Closer inspection of the XPS data from the SF_6 treated sample had shown the presence of a sulfur peak, as shown in Figure 5.2. The presence of this S peak in the sample suggested that direct plasma functionalization of CNTs with sulfur was possible. Also the peak position in terms of binding energy at around 163.4 eV is closer to the binding energy observed for elemental sulfur[17] or thiols,[18] rather than for sulfur in a high oxidation state. The binding energy suggested that the sulphur was present in a low oxidation state. One of the aims of the work with the fluorine was to introduce reactive chemical groups onto the CNTs that could be converted to thiols. The thiols would then aid the positioning of the CNTs onto metal surfaces such as gold.

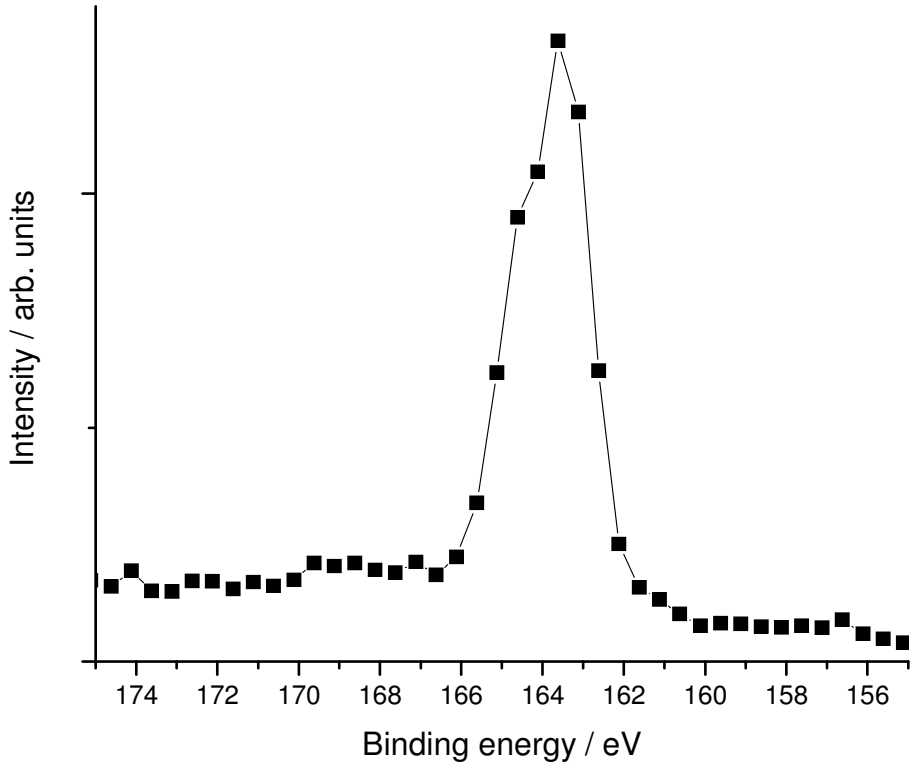

Figure 5.2. XPS spectrum of a sample of carbon nanotubes that has been exposed to an SF_6 plasma. A small sulfur peak with the S $2p_{3/2}$ peaks at around 163.4 eV shows that sulfur had been deposited onto the nanotubes. The binding energy for the S $2p_{3/2}$ is close to that of elemental sulfur, which has a value of 163.8 eV.[17]

The direct attachment of thiols in one plasma treatment would have advantage of reducing the amount of processing involved. Some consideration had to be given to the conditions that would produce an appropriate plasma for functionalizing the CNTs. Usually plasma etchers supply the reactants in the form of gases. Several gaseous sulfur compounds were considered. Sulfur dioxide and hydrogen sulfide are both commercially available, but they are both very toxic. Sulfur dioxide was also discounted, as the S atom is present in a very high oxidation state compared to the S atoms in a thiol, and also the gas may have damaged the tubes by oxidising them.

Fortunately, a plasma etcher in the School of Chemistry was available for experiments that could utilize reagents in vapour form. Plasmas can be produced from a vapour of elemental sulfur, although the sulfur is usually heated to melt it to increase its vapour pressure.[19] The electrodes of the plasma etcher can be heated to make this possible. The use of elemental sulfur to produce the plasma allowed the use of hydrogen gas in the plasma. The hydrogen gas was included with a view to reducing sulfur species, which may attach covalently to the tubes, to thiols. Argon was also included in the gas flow as it has been found to stabilize and homogenize the plasma.[20]

More detailed descriptions of the experimental procedure are presented in Appendix A.1. Briefly, at the first attempt, commercially purchased HiPco carbon nanotubes (Carbon Nanotechnologies, Inc.) were suspended in ethanol. The dispersion was then filtered and collected onto a poly(tetrafluoroethene) (PTFE) filter as a mat of tubes. The filter and tubes were suspended above an aluminium pan that contained elemental sulfur. A diagram of the setup is shown in Figure 5.3. Two samples used a piece of metal wire to support the filter, while another two used a shaped piece of glass. The pan was sitting on the electrode of the etcher, which had been heated 120 °C so that the sulfur would melt. When the argon / hydrogen plasma was struck, the distinctive blue colour of a sulfur plasma was observed over the heated sulfur. For each setup, two different flows of gas were used. In each case, the flow of argon was 75 sccm while the flowrate of H_2 was varied, being either 5 sccm or 25 sccm. The total pressure was around 0.2 Torr. Once exposed, the nanotubes on the filters were then studied with x–ray photoelectron spectroscopy.

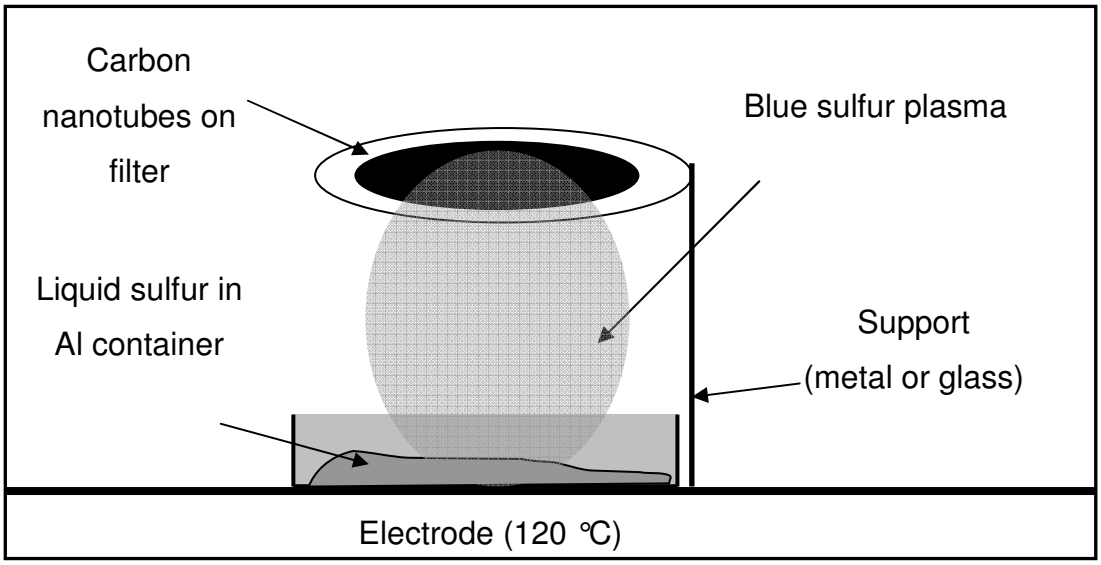

Figure 5.3. A mat of carbon nanotubes on a filter was suspended above molten sulfur in a plasma etcher. When the plasma was struck, the purple argon / hydrogen plasma could be seen in the etcher, with the blue sulfur plasma localised over the sulfur. It was observed that the nanotubes were exposed to the sulfur plasma. Two different supports were used in different experiments, *viz*, one of metal and one of glass.

5.2.1.1 X–ray photoelectron spectroscopy

X–ray photoelectron spectroscopy (XPS) was used to analyse the elemental contents of the plasma–treated carbon nanotubes. The atomic percentages of sulfur, carbon and oxygen were calculated using the software of the spectrometer (VG Scientific) and are presented in Table 5.1. Linear backgrounds were used for all the elements, and the atomic percentages were then calculated from the area of the peaks using Wagner coefficients.[21] The aluminium Wagner coefficients are used to take into account different atomic weights and different probabilities of the atoms interacting with the x–ray to produce a photoelectron. All except one of the samples was found to contain around the same sulfur to carbon ratio of (~ 0.1). There is no obvious reason why the sample at 5 sccm flowrate of hydrogen, using the metal support, should produce a sample with significantly less sulfur (see Table 5.1).

Sample	Setup	Flowrate H_2 / sccm	Atomic %			S / C	O / C
			S	C	O		
A	Metal support	5	0.9	97.5	1.6	0.009	0.016
B		25	8.9	87.6	3.4	0.102	0.039
C	Glass support	5	7.3	77.3	15.2	0.094	0.197
D		25	8.2	82.0	9.7	0.100	0.119

Table 5.1. The atomic percentages of sulfur, carbon and oxygen were determined by XPS of sulfur plasma–exposed tubes. Approximately the same atomic percentages of sulfur were found to be present in all of the samples, with exception of the first sample listed. It can be seen that the samples in which the filter was supported on glass appear to have higher percentage oxygen content.

The binding energy of a peak in the XPS spectrum can be used to indicate the chemical environment of the corresponding atom. In order to establish the chemistry of the sulfur atoms present in the samples, it was necessary to deconvolute the peaks found in the region of the S 2p peak in the spectrum, using XPS peak software.[22] The 2p peak of sulfur is composed of two peaks corresponding to the S $p_{3/2}$ and S $p_{1/2}$ states of the atom when the electron is removed. First, the binding energies of the samples were corrected by shifting all the values in each spectrum, so that the carbon peak was centred at 284.6 eV, which is the expected value for sp^2 hybridised carbon.[17] The energy difference between the S $p_{3/2}$ and S $p_{1/2}$ was fixed at 1.18 eV and the ratio of their intensities at 2:1 respectively (due to multiplicity of the $p_{3/2}$ being twice that of the $p_{1/2}$).[23] Both of the 2p peaks for sulfur were fitted,[18,23,24] to a 70:30 mixture of Lorentzian and Gaussian lineshapes. Figure 5.4 shows the S 2p region for the two samples (A and C) produced with a hydrogen flowrate of 5 sccm, and Figure 5.5 shows the same for the samples (B and D) produced with a hydrogen flowrate of 25 sccm. The samples with the metal support were fitted with one pair of

peaks, whereas the samples with the glass support were fitted with two pairs. The extra peaks at higher binding energies in the spectrum of the samples with the glass support (samples C and D) suggest the presence of sulfur atoms in very different environments to those found in the metal–supported samples (A and B).

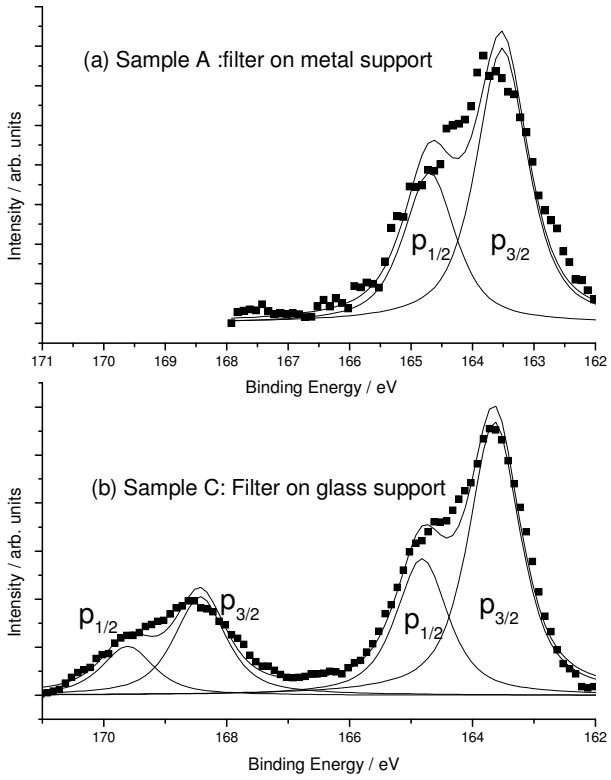

Figure 5.4. These plots show the sulfur region of the XPS spectra for the samples processed with a hydrogen flowrate of 5 sccm and argon flowrate of 75 sccm. The sample that had the tubes on a support made of glass (b) has additional peaks at higher binding energy. These extra peaks suggest the presence of sulfur in a higher oxidation state. The spectrum of the sample with the metal support (a) only shows one pair of peaks that relate to sulfur atoms in a low oxidation state, such as elemental sulfur or thiols.

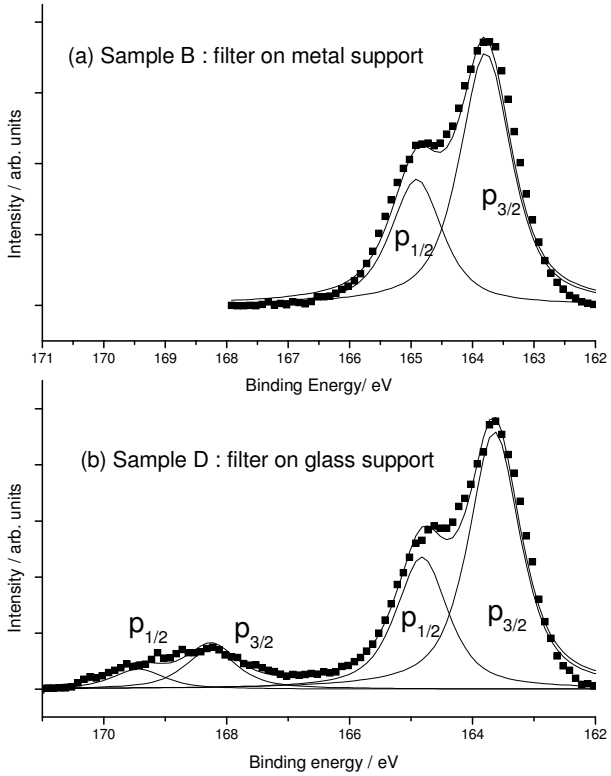

Figure 5.5. The XPS spectra at the sulfur region of the samples produced from a hydrogen flow of 25 sccm with 75 sccm of argon. Sample B, where the filter with the tubes was supported on a metal wire (a), has only one pair of peaks that can be assigned to sulfur with a low oxidation state (such as elemental sulfur, or thiol). In addition to these peaks, sample D (with glass support) had a pair of peaks at a higher binding energy. These peaks are thought to result from sulfur in a higher oxidation state.

The fitted binding energies of the $p_{3/2}$ peaks of the samples are presented in Table 5.2. Typical binding energies, taken from literature sources, for sulfur in different chemical environments are shown Table 5.3. The S $p_{3/2}$ with the lower binding energy was found to be between 163.5 – 163.8 eV. Comparing this range of values with those presented in Table 5.3, we see that the environments with the most similar value of binding energy are those for elemental sulfur and for thiols. The elemental sulfur might simply condense on the tubes from the vapour, while the thiol (or other S–containing functional groups) could have been formed by the reaction of sulfur–containing groups with the tubes. As can be seen from the table, the closeness of the binding energies of elemental sulfur and thiol groups prevents unequivocal

determination of the chemical identity of the sulfur type by XPS. Indeed, the samples could possibly contain S atoms in several different environments, all of which would contribute to the XPS spectrum. In the case of the elemental sulfur and thiol, the binding energies are so close that deconvolution does not seem possible. Attempts to fit the S 2p peaks to two pairs of peaks, rather than one, resulted in the area for one of the pairs disappearing to nothing. There are also a great number of environments in which the sulfur could be present that have sulfur atoms in similarly low oxidation states. For example, as well as reacting to form thiols, the sulfur could have formed organic sulfide (C–S–C) or disulfide groups (C–S–S–C). Unfortunately, it was not possible to obtain reference spectra of other sulfur containing substances using the same spectrometer, such as elemental sulfur, as these raw materials could have contaminated the spectrometer.

Sample	**Setup**	**Flowrate H_2 / sccm**	**Binding energy of S $2p_{3/2}$ / eV**
A	Metal support	5	163.5
B		25	163.8
C	Glass support	5	163.6, 168.4
D		25	163.6, 168.3

Table 5.2. The binding energies for the S $2p_{3/2}$ peak obtained from the fitting of the XPS spectra, shown in Figures 5.4 and 5.5, are tabulated here. All samples have a $2p_{3/2}$ peak (~ 163.6 eV) whose binding energy can be related to low oxidation state sulfur, such as elemental sulfur or thiol groups. The samples with the glass support also had a second $2p_{3/2}$ peak (~ 168.3 eV) that could be related to high oxidation state sulfur, such as the sulfate ion or an organic sulfonic acid (see Table 5.3).

Sulfur group	Binding energy of S $p_{3/2}$ peak / eV	Reference
R–S–H	163.7	18
R–S–Au	162	24
elemental sulfur	163.8	17
S–O	167	23, 25
organic sulfonic acid ($R–SO_3^-$)	168.1 168.2 168.0 – 168.3 167.0	26 27 28 29
sulfate / bisulfate (SO_4^{2-} / HSO_4^-)	168.9 168.9 168.1 – 168.6	28 29 30
sodium sulfide	166.50	31
$Fe(II)SO_4$	168.95	31
$Fe_2(III)(SO_4)_3$	169.00	31

Table 5.3. Values of binding energies for the $p_{3/2}$ peak of sulfur, taken from the literature.

The material of the support (metal or glass) for the filter seems to have had an effect on the functionalization of the tubes by the plasma. Samples C and D, the glass supported samples, have an extra pair of peaks in the S 2p region at higher binding energies. The higher value of the binding energy suggests that the sulfur present is in a higher oxidation state. The values of the binding energy obtained from fitting the peaks, at 168.3 and 168.4 eV, may be attributed to sulfate ions, or perhaps sulfonic acids: see Table 1.3. As there are different values in the literature reported for both organic sulphonic acids and sulphate ions, it is not possible to identify the form of sulfur present on the basis of XPS by itself. However, the binding energy of the peak does suggest that it arises from sulfoxy groups. Oxygen was not directly used in the experimental gas mixture, which would seem to preclude the reaction of the sulfur with oxygen in the plasma. As there were no plasma characterization techniques available on the plasma reactor, such as optical emission spectroscopy, the presence

of oxygen species during the plasma treatment could not be ruled out. Since the samples were exposed to air after plasma processing, it is possible that some reaction occurred before XPS analysis. In the literature, the presence of S 2p peaks with a large binding energy (> 167 eV) has been identified in the XPS spectra of carbon nanotubes that have been functionalized with thiols[6,7] and in other sulfur containing organic compounds.[23,25] These peaks have been attributed to the oxidation of sulfur compounds.

5.2.1.2 Differences in plasma reactivity

It is difficult to rationalise fully, the reasons why there should be a difference between the reactivities of the plasmas produced when the tubes on a PTFE filter are suspended on a metal support and when they are suspended on a glass support. The most obvious difference between the different setups was that the support for the filter was a conductor in one setup and an insulator in the other. One way to explain the difference in reactivity is to consider the potential difference between the sample and the plasma. As mentioned in Section 5.1.2, due to the greater mobility of the electrons compared with the positive ions in the plasma, the plasma tends to lose electrons to the walls of the etcher creating a potential difference that accelerates positive ions towards the sample. The greater the potential difference between the sample and the plasma, the more energetic is the bombardment of ions. We could perhaps expect that a greater potential difference, and therefore a more energetic bombardment, would be more likely to produce reactive sulfur fragments. The bombardment of ions is likely to produce defects and dangling bonds that could react with oxygen when the sample is removed from the reactor.

XPS results for the preliminary experiments showed that samples of carbon nanotubes that were exposed to a sulfur plasma, were found to contain sulfur. The sulfur contained in the processed samples could be elemental sulfur, which has simply condensed on the carbon nanotubes from the sulfur vapour, or sulfur species could have reacted with the tubes to form groups containing sulfur in low oxidation states, such as thiols. In addition, samples in which the nanotubes were supported by

glass showed XPS peaks that were attributed to sulfur in higher oxidation states, most likely as sulfoxy groups.

We found that it was not possible to study these samples further due to the difficulty of removing the intact samples from the PTFE filter. Only very small quantities could be functionalized, due to the need for homogeneous dispersal of the tubes onto a surface. In addition, the setup required for the sample exposure was very difficult to use. Such difficulties encouraged us to investigate a simpler method of sample preparation, in which the solid carbon nanotubes and sulfur were first mixed together.

5.2.2 Plasma exposure of carbon nanotubes and sulfur mixtures

Detailed descriptions of the experimental procedures can be found in Appendix A.2. Table 5.4 shows the reaction conditions that were used to investigate the functionalization of the CNTs in the sulfur plasma, along with sample numbers that will be used in the following sections. The samples were prepared by grinding, in a mortar and pestle, commercially obtained SWNTs (HiPco, Carbon Nanotechnologies, Inc.) with elemental powdered sulfur. The mixture was then transferred to an aluminium tray that was then placed in the etcher. The electrodes of the etcher had been heated to 120 °C to melt the sulfur. Once the sulfur had become liquid, the chamber was evacuated to less than 0.2 Torr. The hydrogen and argon gases were then introduced, and the plasma was struck for 60 seconds. It should be noted that sample 1 was heated in the etcher so that the sulfur melted, but neither the control nor sample 1 were exposed to a plasma.

Sample	**Mass sulfur / g**	**Mass CNTs / g**	**Flow Ar / sccm**	**Flow H_2 / sccm**
Control	0	0.002	0	0
1	0.02	0.002	0	0
2	0.02	0.002	75	25
3	0.02	0.002	50	50
4	0.02	0.002	25	75

Table 5.4. Reaction conditions of plasma sulfurization. The control and sample 1 were not exposed to the argon / hydrogen plasma. All plasma exposures were carried out for 60 s. The plasma exposure was carried using a plasma etcher in which the electrodes were heated to 120 ºC in order to melt the sulfur (see text for details).

The plasma observed had two different regions: the area directly over the liquid sulfur was the characteristic blue colour of a sulfur plasma, while in the rest of the etcher the purple of the argon plasma could be seen. After the plasma exposure, the samples were dispersed in toluene, filtered, and washed with more toluene to remove the excess sulfur. The tubes were re–dispersed in ethanol and drop coated onto a silicon wafer for characterization.

5.2.2.1 X–ray Photoelectron Spectroscopy

XPS was carried out on the final products. The atomic percentages of sulfur, carbon and oxygen were determined as outlined in Section 5.2.1.1, and are presented in Table 5.5. It was concluded from the XPS data that all samples except the control contained about the same amount of sulfur (< 5 % atomic). The control had no identifiable S 2p peaks in its XPS spectrum.

Sample	Flow Ar / sccm	Flow H_2 / sccm	Atomic percentage			Ratio of S / C
			S	C	O	
Control	–	–	–	98.8	1.2	–
1	0	0	4.8	92.1	3.0	0.053
2	75	25	4.0	92.3	3.6	0.043
3	50	50	4.1	92.8	3.1	0.044
4	25	75	4.2	93.3	2.5	0.045

Table 5.5. Atomic percentages of elements of interest, and the atomic ratio of sulfur to carbon as determined by XPS. Sample 1 was heated to 120 °C, but was not exposed to plasma. No identifiable S peak was found in the control sample.

The peaks found in the S 2p region of the XPS spectra of the samples were fitted as described in Section 5.2.1.1, and are presented in Figure 5.6. All the samples except the control, which was not exposed to sulfur, showed peaks in the sulfur region with binding energies 163.7 – 163.8 eV. The binding energies of the S $p_{3/2}$ peaks were compared against typical binding energies, shown in Table 5.3. As before, the closeness of the binding energies of elemental sulfur and thiol groups prevents the determination of the chemical identity of the sulfur as either of those groups unequivocally by XPS. The presence of oxidised sulfur groups can be discounted as there are no peaks in any of the spectra that have binding energies near to 167 eV.

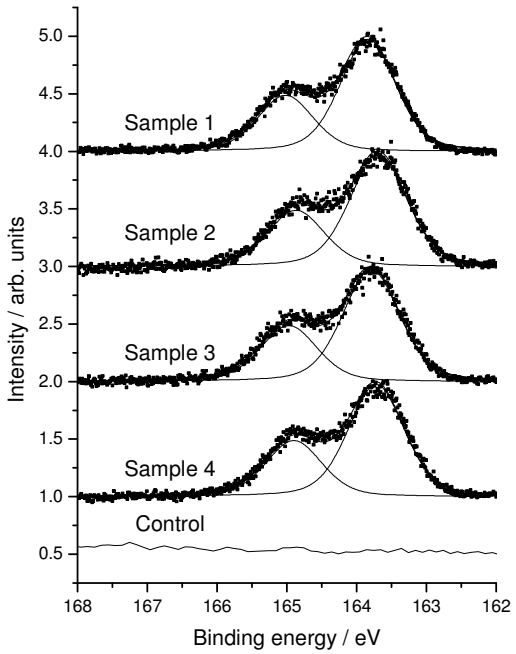

Figure 5.6. The sulfur region of the XPS spectra for all samples, including the control. The fitting of the peaks is described in Section 5.2.1.1. All samples show binding energies of the S $p_{3/2}$ around 167.3 eV, which is close in value to the binding energies of thiol and elemental sulfur.

5.2.2.2 Raman Spectroscopy

The Raman spectra for all the samples, shown in Figure 1.7, are remarkably similar. They all show a large G band (~ 1500 cm^{-1}) compared to the D band (~ 1300 cm^{-1}) which indicates that the tubes are still highly graphitized. The splitting of the G band and presence of radial breathing modes at low frequencies all confirm that the samples still contain single–walled nanotubes.[32] The peak at ~ 2600 cm^{-1} is also characteristic of carbon nanotubes, is known as the G' band and originates from the double excitation of the same vibration as the D band. The G' band is not disorder activated like the D band and can be seen in the spectra of all graphitic materials.[32] Table 5.6 shows the ratio of the D band to the G band for all of the samples. As discussed previously in Chapter 2, the I_D / I_G ratio is a very a common measure used to estimate the amount of defects in carbon nanotubes. The similarity, and the small values, of the I_D / I_G ratios suggest that the plasma treatment did not damage the tubes to any significant extent.

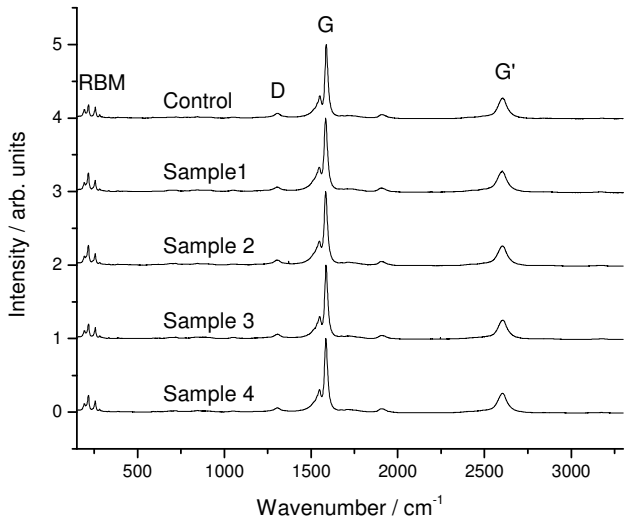

Figure 5.7. Raman spectra for all samples. Peaks labelled RBM are the radial breathing modes, which indicate the presence of SWNTs. The peak labelled G is related to the amount of well–ordered carbon while the peak labelled D relates to disorder. The small size of the D band for all the spectra compared to the G band shows that the plasma treatment does not increase the disorder in the tubes.

Sample	I_D / I_G ratio
Control	0.07
1	0.07
2	0.06
3	0.06
4	0.07

Table 5.6. The ratio of the intensity of the D band to that of the G band, a measure of the non–graphitic defects in the tubes, does not change with exposure to plasma.

No characteristic peaks for sulfur containing groups,[33] such as the S–C stretch at 600 – 720 cm^{-1}, the S=C peak at 1095 cm^{-1}, or the S–H stretch at 2500 – 2580 cm^{-1}, were observed in the plasma treated tubes. There was a peak in all spectra at 587 cm^{-1} that could have been attributed to the S–S bond (585 cm^{-1})[33]. However, as Figure 5.8 shows, all the samples including the control have the small peak at 587 cm^{-1}. The peak common to all the spectra could be assigned very tentatively as an intermediate frequency mode (IFM) of the SWNTs.[32] In contrast, the S=C and the S–S peaks were detected in the Raman spectra of the product from the chemical thiolation of CNTs by Liu *et al.*[7] The lack of observable sulfur peaks in the Raman spectra is attributed to the small amounts of sulfur present in our samples (~ 5 %). To support this assertion, we note that in other work, where carbon films and rods have been doped with similar atomic percentages of sulfur to those in this work, no Raman peaks attributable to sulfur functional groups were observed.[34-38]

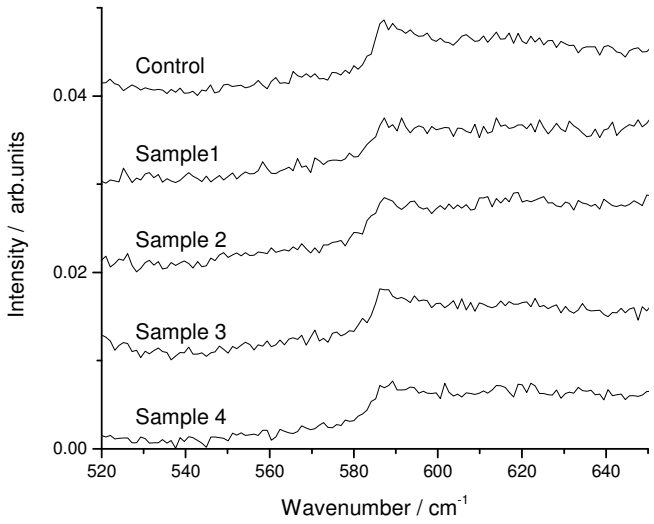

Figure 5.8. Close–up (520 – 650 cm^{-1}) of the Raman spectra of all product samples, including the control. This region shows a peak that could be attributed S–S bond, which has a characteristic vibration at 585 cm^{-1}. However, it is present in all the spectra, including that of the control, which was not exposed to any sulfur. The peak is more likely to be a weak feature of the Raman spectrum of SWNTs known as the Intermediate Frequency Mode (IFM).[32]

5.2.2.3 Selective deposition of sulfur plasma–exposed nanotubes onto gold surfaces

Gold surfaces were exposed to ethanolic solutions of the tubes in order to establish whether there would be any evidence of bonding between the gold surfaces and the tubes. Experimental details can be found in Appendix A.4. Briefly, SiO_2 wafers were first patterned with gold strips 2 μm wide, approximately 25 nm high, and with 2 μm trenches. Ethanolic dispersions of each of the samples including the control were made, and into each a patterned wafer was placed. After 12 hours the wafers were removed and then rinsed with copious volumes of ethanol. Scanning electron microscopy (Figure 5.9) showed the presence of bundles of SWNTs across the trenches between the gold electrodes. The bundles seem to be mostly under 100 nm thick. Very occasionally, small amounts of the carbon nanotubes were observed on the bare SiO_2 surface. It was found that selective deposition onto the gold *only occurred for samples that had been treated both with sulfur and hydrogen / argon*

plasma. The selective deposition of the plasma–treated tubes is strong corroborating evidence that the sulfur was strongly bonded to the CNTs, as we assume that the interaction between the gold surface and the tubes is most likely to occur through some type of sulfur group. In contrast, the tubes that were *not exposed to the plasma were found not to become deposited onto the gold features*. Presumably, these tubes must have been removed when the samples were rinsed in excess ethanol. To be consistent with the observations, it is suggested that if the tubes that were not subjected to plasma *did* have some sulfur chemically attached, it must not be present as functional group capable of bonding onto the gold surface.

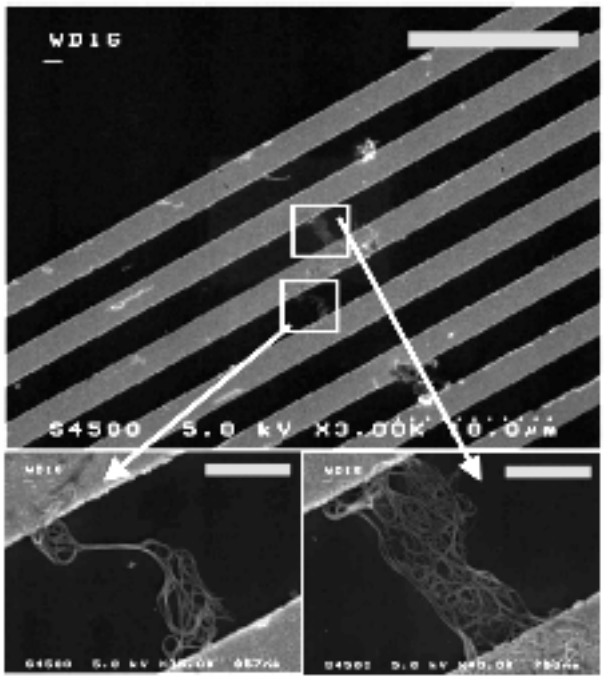

Figure 5.9. Bundles of SWNTs can be seen bridging the gaps between the gold features.[39]

Further evidence that exposure of nanotubes to the sulfur plasma changes how the tubes deposits themselves on to gold surfaces can be seen from attempts to produce electrical devices with them. As will be discussed in Section 5.2.3, sulfur plasma treated tubes were used to fabricate field effect transistors by Natalie Planck (School of Engineering and Electronics, University of Edinburgh). The yield of the devices was found to be higher, at 10 %, when the sulfur plasma treated tubes were used compared to pristine tubes, which gave a yield of only 1 %.

There are several different sulfur–containing groups that are known to form bonds onto gold metal surfaces, such as thiols, dialkyl disulfides, dialkyl sulfides, thiophenols,[40] polysulfides,[41] and sulfonic acids.[42] There are two ways that the sulfur groups can form bonds with a gold surface.[43] For instance, thiols lose the hydrogen atom attached to the sulfur atom and form a covalent bond between the sulfur and the gold surface. A similar bond forms for disulfides through the breaking of the S–S bond. In contrast, the sulfides (C–S–C) cannot form these covalent bonds, and are thought to form dative bonds to the gold surface that are less strong than the bonds

formed for the thiols and disulfides. From the analysis available it is not possible to determine which, if any, of these types of groups are present, although it is possible to exclude sulfonic acid groups from the XPS data. Indeed, from the XPS data and Raman data, it is not possible to determine whether there is a covalent bond between the sulfur group and the nanotubes. It is possible that there is some sort of physical interaction between the tubes and the sulfur–containing groups, which may go on to form bonds to the gold surface.

In the first instance, the driving force for the deposition of the tubes onto the gold is probably not the formation of S–Au bonds. Rather, it is the non–specific adsorption of the tubes as they fall out of the dispersion. If the tubes land upon the silicon surface they are washed away during the rinsing stage. Upon landing on the gold surface, strong covalent bonds are formed when the sulfur groups come in contact with gold. This covalent bonding to the surfaces makes such tubes less likely to be rinsed off in the cleaning stage. The tubes are therefore selectively positioned on the gold surfaces due to the strength of the bonding between the sulfur plasma–treated CNT and the gold surface.

That the tubes make connections between the gold areas is possibly useful in device fabrication, compatible with current lithographical techniques. In previous solution–phase methods of thiolisation of SWNTs, the very short—highly dispersed—thiolized tubes were found to stand up on the gold surface,[7] making the engineering of devices more difficult.

5.2.2.4 Characterization of sulfur–containing groups

Due to the small amount of sulfur present in the samples, and the closeness of the binding energies of elemental sulfur and thiols, it is difficult to determine the nature of the sulfur present in the different samples. X–ray photoelectron spectroscopy confirms that there is sulfur present in the samples of tubes after they have been exposed to sulfur and heated, but it cannot be used identify the groups present. Raman spectroscopy has revealed that the nanotubes are undamaged by the treatment

with plasma but there are no peaks corresponding to sulfur containing groups visible in the spectra of the samples. In Section 5.2.2.3, we studied the way that the tubes deposited themselves onto gold surfaces from a dispersion of the tubes in ethanol. The selective attachment of the tubes to the gold suggested the presence of sulfur groups that are strongly bound to the tubes, either physically (non–covalent, weak binding) or through a covalent bond. As mentioned above there are many sulfur functional groups that form bonds to gold surfaces[40-43], so there are multiple possible functional groups that could be present in the samples.

There appears to be few characterization techniques that could be used to investigate further the type of sulfur group present in the samples. For example, if mass spectrometry (MS) was used to study the tubes, it might be possible to confirm that carbon and sulfur are present, but due to fragmentation and rearrangements occurring in the MS, it would be difficult to identify the sulfur groups in the sample. Electrospray–MS of HiPco CNT has been found to be exceedingly cluttered.[45] The large infra–red (IR) absorbances of nanotubes, and the low concentration of functional groups, mean that the specialized diffuse IR reflectance technique is most appropriate. Due to constraints of available equipment, some of our previous attempts to study oxygen–containing groups on carbon nanotubes by reflectance IR spectroscopy were wholly unsuccessful. Also, the oxygen groups should have relatively strong IR signals compared to sulfur containing groups,[33] and therefore we shied away from attempting such analysis of the sulfur–CNTs.

5.2.2.5 Possible mechanism of sulfurization

Considering the empirical observation that only the tubes that were exposed to both sulfur and the hydrogen / argon plasma showed evidence of selective assembly, we suppose that the functional group responsible for the attachment of the bundles of the tubes is indeed the thiol group. As discussed in section 5.2.2.1, the presence of thiol is consistent with the XPS results, and it is well known that thiols groups efficiently attach themselves to gold surfaces.[46] The hydrogen plasma would contain reactive hydrogen species that could react with sulfur that had covalently attached to the

nanotubes, or indeed first react with the sulfur in the gas phase to produce species that then go on to react with the tubes.

An interesting feature of the XPS results, presented in Table 5.5, is that the sample that was not exposed to plasma (sample 1) contained around the same amount of sulfur as the other samples. Several test experiments, where nanotubes and sulfur were mixed and then heated to 120 °C, were carried out to investigate if more of the sulfur could be removed with more stringent washing of these samples. XPS showed that the sulfur content *could* be decreased by washing the sample in more toluene, and by refluxing the samples. However, the sulfur was never completely removed. It was found that the amount of sulfur compared to carbon was reduced to ~ 2% (S / C = 0.02) by refluxing the sample in 50 ml toluene for 1 hour and then washing with 100 ml toluene. The sulfur present might still be elemental sulfur not covalently bound to the CNTs. However, there is also the possibility that some of the sulfur may have become covalently attached to the carbon nanotubes during the refluxing. It is well known that, as elemental sulfur is heated, the S_8 rings becomes unstable at ~ 119 °C, and the single bonds between the atoms can break to form sulfur oligomers such as S_8.[47] In the vapour phase, there are several different sulfur species that are present (S_n with $2 \leq n \leq 10$): the relative amounts of these species depend on temperature and pressure. It is possible that these fragments actually react to form covalent bonds with the nanotubes. It is well known that elemental sulfur will react with alkenes, for example the cross–linking formed during vulcanistion of polyisoprene (natural rubber) where the rubber can be simply cross–linked by heating it with sulphur.[48] It is also interesting to note that the ends of tubes would have the chemistry most similar to alkenes, because the π electrons of the carbon atoms in the end–caps of the carbon nanotubes are known to be most localised, where the graphene curvature is greatest.[49] The end caps are thought to react like fullerenes, which have chemistry similar to alkenes rather than aromatic molecules.[50]

This leads us to a possible mechanism for the formation of thiols on the carbon nanotubes, which is shown in Figure 5.10. A two step reaction mechanism to the thiolization would account for the experimental observation that both the treatment

with sulfur and hydrogen plasma are required. In the first step, the sulfur vapour or even the liquid sulfur actually reacts with the tubes to attach sulfide groups (CNT–S_n). These are then reduced to thiol groups in a second step by the hydrogen in the plasma.

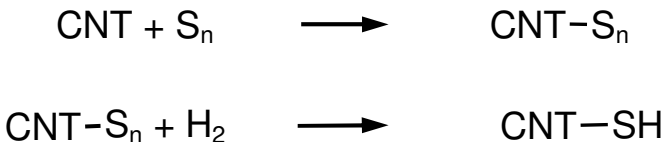

Figure 5.10. Reaction scheme of suggested reaction mechanism (see text for discussion). In this hypothesis, the carbon nanotube reacts with a sulfur oligomer in a first step, and then the sulfur group reacts with hydrogen to form a thiol. The hydrogen gas (H_2) in the second step could also be positively charged (H_2^+) or atomic hydrogen (H).

5.2.3 Device Fabrication

As part of the collaboration on this project, some prototype field effect transistors (FET) were fabricated by Natalie Plank (School of Engineering and Electronics, University of Edinburgh), using the techniques of nanotube plasma functionalization and directed assembly described in this thesis.[51] To put the present work into context, the results of the device fabrication and testing are briefly summarised here.

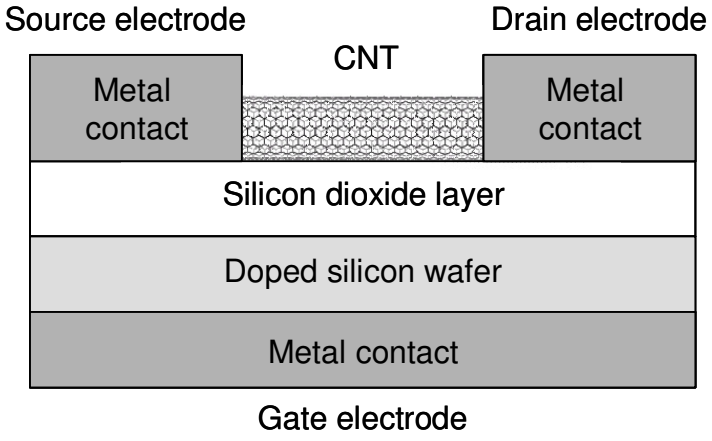

Figure 5.11. Schematic of a carbon nanotube field effect transistor (FET). A potential applied at the gate electrode creates an electric field that can vary the density of charge carriers in the

carbon nanotube. In this way the gate potential can be used to control the current between the source and drain electrodes.[52]

Nanotubes were produced by two different methods, being high pressure carbon monoxide HiPco (Carbon Nanotechnologies, Inc.) and laser ablation (produced in NEC, Japan). The carbon nanotubes were functionalized using the plasma conditions as for sample 4 in section 5.2.2, using similar characterisation techniques during processing. Devices were fabricated by e–beam lithography and evaporation of gold to produce electrodes on SiO_2 covered silicon wafers. For the self assembly, the tubes were dispersed in 1,2-dichloroethane, which is known to be one of the best solvents to disperse carbon nanotubes. Further details can be found elsewhere.[51]

As can be seen from the SEM images in Figures 5.12 and 5.13 the bundles of functionalized tubes bridge the electrodes in a similar manner to that described in section 5.2.2.3. As previously mentioned, it was found that the yield of devices was around 10 %, which is much larger than the 1% yield obtained when pristine tubes were used. However the devices formed were very sensitive to the degree of bundling. When large bundles formed devices, usually from higher concentration dispersions in dichloroethane, the dominating conduction was found to be metallic. In order to increase the field–dependent behaviour of the devices, a process known as "burn off" was attempted.[53] In the burn off process, high voltages were placed between the source and drain electrodes to try to remove metallic tubes preferentially. Due the large voltage, and therefore large currents, any metallic tubes will tend to heat resistively, and may eventually burn. The semiconducting tubes, which may only conduct when a sufficient gate voltage is applied, do not conduct during burn off, and therefore will not be removed. Overall, the relative amount of semiconducting tubes can be increased. Burn off was most successful for smaller bundles that were produced by lower concentration dispersions, and FET devices were produced that showed the p–type semiconducting behaviour that is expected for carbon nanotubes,[54] albeit with some metallic contributions.

The difference between the two of sources of tubes was found to rely on the way that they dispersed in the 1,2-dichloroethane. The HiPco tubes did not disperse as well as

the tubes obtained from laser ablation: the HiPco tubes formed larger bundles that made poorer devices. As the CNTs are not shortened in the plasma functionalization procedure, the carbon nanotubes are still quite difficult to disperse. The dispersion of the functionalized tubes is a highly important problem for this type of work, especially if this method of functionalizing CNTs is to be used to produce devices.

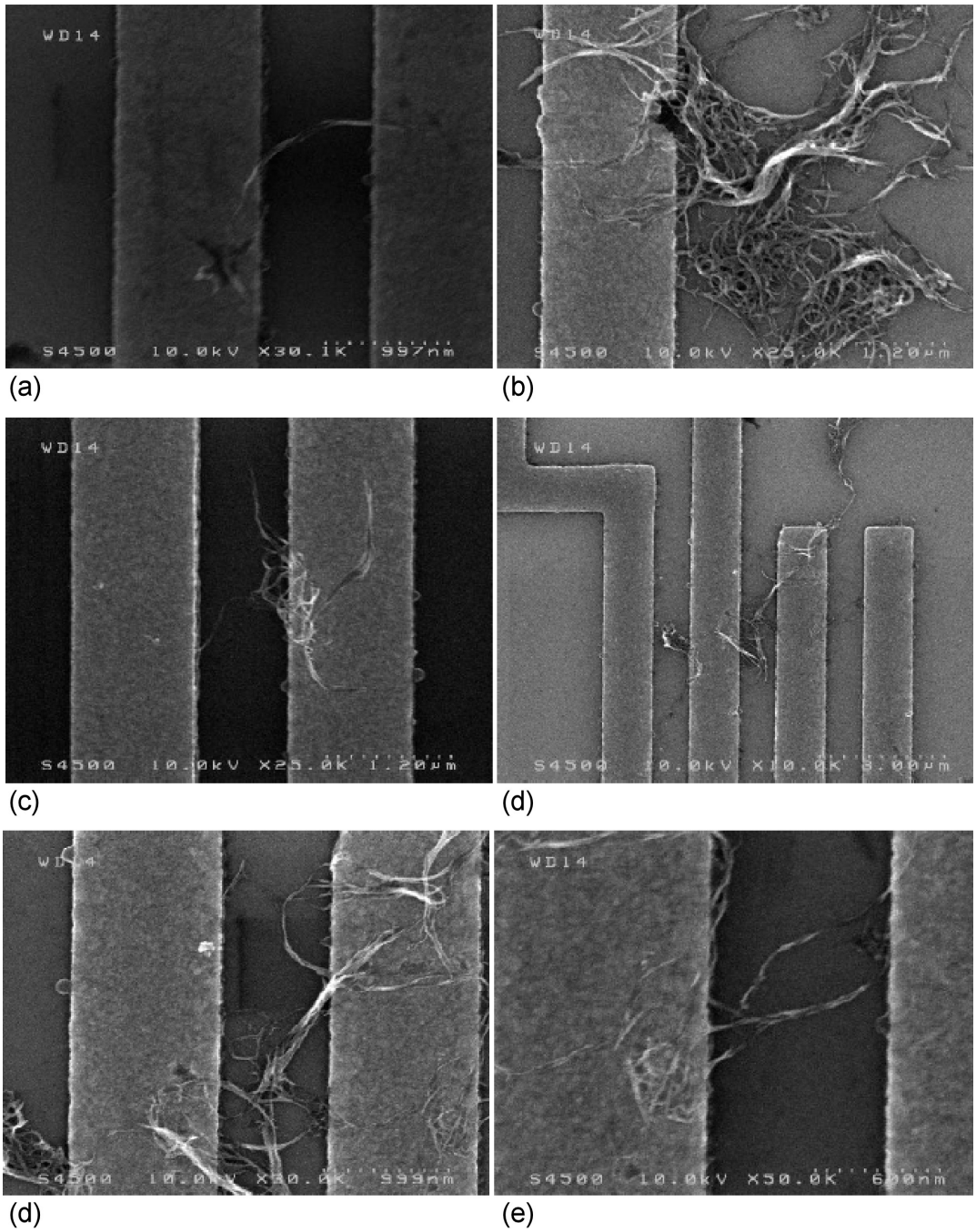

Figure 5.12. Six SEM images of bundles of sulfur–plasma functionalized HiPco tubes (a) – (f) bridging the gold electrodes.

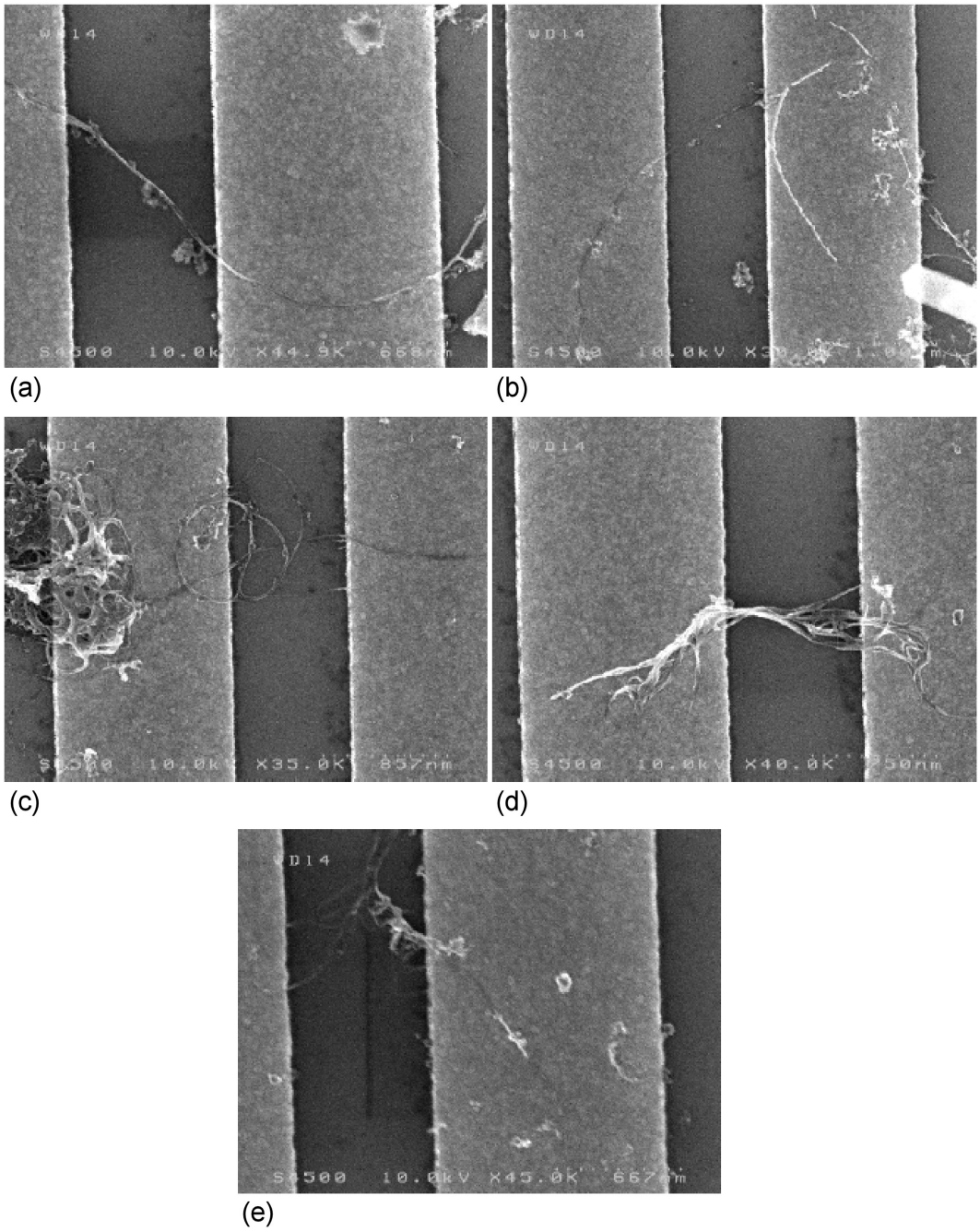

Figure 5.13. Five SEM images of bundles of sulfur–plasma functionalized laser ablation tubes (a) – (f) bridging the gold electrodes.

5.3 Summary

In summary, SWNTs were functionalized by mixing commercially obtained pristine tubes with elemental sulfur. This mixture was heated to 120 °C to melt the sulfur,

and then exposed to a radiofrequency Ar / H_2 plasma. The excess sulfur was then removed by washing with toluene. Raman spectroscopy showed that little or no damage had been done to the structural integrity of the nanotubes. Evidence for the functionalization of the tubes with sulfur was found from both XPS and directed assembly of the tubes onto gold surfaces. XPS showed that amount of sulfur attached was around 5 % atomic. The XPS binding energy of the sulfur was consistent with thiol, although the binding energies of elemental sulfur and other sulfur groups were too close to conclusively prove the presence of thiol groups. The functionalized tubes were observed to adhere onto gold surfaces, whereas the unfunctionalized tubes did not, further supporting the presence of covalently bonded or physically absorbed sulfur groups. The sulfur–plasma functionalized tubes have been used to fabricate simple field effect transistors by colleagues at the School of Engineering and Electronics. The plasma functionalized tubes gave a high yield of devices.

5.4 Conclusions

The deposition of SWNTs selectively on to gold surfaces from their dispersion was shown to be possible by using SWNT that had been previously treated with a sulfur/ hydrogen/ argon plasma in a simple single step process. Although the XPS data of the sulfur plasma treated samples did contain peaks with binding energies consistent with functional groups such as thiols, it was not possible to determine unequivocally the chemical nature of the sulfur present. Only further characterization with techniques such as High resolution electron loss spectroscopy (HREELS) might be able to elucidate the nature of the sulfur present.[55]

When used to fabricate FETs, the sulfur plasma treated tubes showed an increase in the yield of devices compared with untreated SWNTs. Although, this method of functionalization does have some advantages over some of the previous chemical approaches used, for example, it does not require a destructive oxidation step.[1,4-6] The device fabricated from this selective deposition were composed of bundles of tubes rather than individual tubes due to the difficultly of dispersion the tubes in a

solvent and the yield of devices was still very low compared to the level that would be required for industrial fabrication of devices.

Appendix A. Experimental procedures for direct functionalisaton of carbon nanotubes with sulfur

A.1. Suspension of carbon nanotube films in S plasma

Single wall carbon nanotubes (5 mg, HiPCO, Carbon Nanotechnologies Inc) were were dispersed in isopropanol (15 ml) using a magnetic stirrer for 2 hours resulting in the formation of a thick black paste. The dispersion was then filtered through a 2 μm polytetrafluoroethylene (PTFE) filter membrane (Millipore) under vacuum, and left to dry for 24 hours at room temperature resulting in the formation of films of nanotubes on top of the PTFE membranes.

A small aluminium container with around 0.2 g sulfur (Aldrich) was placed on the heated electrode of the etcher (Plasma Etch Inc., PE-200). To expose each filter to the sulfur plasma, the filter was suspended above the electrode of the plasma etcher so that the filter was parallel to the electrode and above the heated sulfur: see Figure 5.3. In two of the experiments, the filter was supported on a piece of the metal wire, while in the other two the filters were supported on a shaped piece of the glass. Once the samples were positioned, the chamber was evacuated to around 0.2 Torr and the argon gas was introduced at a flowrate of 75 sccm, along with hydrogen gas at either 5 or 25 sccm. When the plasma was struck the samples were exposed for 2.5 min with a radiofrequency (RF) power of 250 W. Once the plasma exposure had been carried out, there was still sulfur present in the container showing that it had not all evaporated. The samples were then characterized with XPS

A.2. Plasma Exposure of sulfur and nanotube mixtures

An amount of 2 mg single–walled carbon nanotubes (Carbon Nanotechnologies, Inc.) were mixed with 0.02 g elemental sulfur powder (Aldrich). All but one sample

(sample 1) and the control were exposed to an argon and hydrogen plasma in a plasma reactor (Plasma Etch Inc. Etcher PE-200, USA). Argon was used to facilitate the generation of the plasma while the hydrogen was included to provide a reducing atmosphere to try to promote the formation of thiols. The electrodes of the reactor were heated to 120 ºC to melt the sulfur. The different gas flows for each sample are outlined in Table 5.4 above; the total pressure was around 0.2 Torr. The samples were exposed for 1 minute with a RF power of 250 W. A blue plasma (characteristic of sulfur) could be seen above the sample, with a purple plasma (characteristic of argon) in the rest of the reactor. All samples were removed, placed in 2 ml of toluene, filtered through a 2 µm PTFE filter, and then rinsed with a further 5 ml of toluene to try to remove any excess elemental sulfur. The CNTs were then re–dispersed in 2 ml of ethanol and drop–coated onto silicon wafers for characterisation.

A.3. Characterization

The CNTs were characterised with XPS (PG Scientific Sigma Probe) to measure the amount of sulfur in each sample using Al K (α) X–rays (148.6 eV) and a spot size of around 100 µm diameter. Raman spectroscopy was undertaken to establish whether there were defects in the tubes (Labram 300, 633 nm, 10 mW).

A.4. Deposition of plasma–exposed nanotubes on gold surfaces

A pattern of 2 µm wide lines of Au with 2 µm spacings on a silicon wafer was created using standard lithography techniques and gold evaporation by Natalie Plank at the School of Engineering and Electronics at University of Edinburgh. A 0.5 mg sample of functionalised nanotubes was placed in 2 ml of ethanol and sonicated (Fisherbrand, FE 11002) for 10 mins. The patterned wafer was left in the ethanolic dispersion for 12 hours before being removed and rinsed thoroughly with excess ethanol. The samples were then viewed using a Hitachi S4500 scanning electron microscope, which was operated by Natalie Plank.

5.5 References

1) C. A. Dyke, J. M. Tour. Covalent Functionalization of Single–Walled Carbon Nanotubes for Materials Applications. *J. Phys. Chem. A,* 2004, **108,** 11151.

2) X. L. Xiea, Y.-W. Maia, X.-P. Zhou. Dispersion and alignment of carbon nanotubes in polymer matrix: A review. *Mater. Sci. Eng.,* 2005, **R 49,** 89.

3) D. Tasis, N. Tagmatarchis, A. Bianco, M. Prato. Chemistry of Carbon Nanotubes. *Chem. Rev.,* 2006, **106,** 1105.

4) J. Chen, M. A. Hamon, H. Hu, Y. Chen, A. M. Rao, P. C. Eklund, R. C. Haddon. Solution properties of single–walled carbon nanotubes. *Science,* 1998, **282**, 95.

5) J. Liu, A. G. Rinzler, H. Dai, J. H. Hafner, R. K. Bradley, P. J. Boul, A. Lu, T. Iverson, K. Shelimov, C. B. Huffman, F. Rodriguez-Macias, Y.-S. Shon, T. R. Lee, D. T. Colbert, R. E. Smalley. Fullerene pipes. *Science,* 1998, **280**, 1253.

6) Z. Liu, Z. Shen, T. Zhu, S. Hou, L. Ying, Z. Shi, Z. Gu. Organizing Single–Walled Carbon Nanotubes on Gold Using a Wet Chemical Self–Assembling Technique. *Langmuir,* 2000, **16,** 3569.

7) J. K. Lim, W. S. Yun, M. H. Yoon, S. K. Lee, C. H. Kim, K. Kim, S. K. Kim. Selective thiolation of single–walled carbon nanotubes. *Synth. Met.,* 2003, **139**, 521.

8) N. O. V. Plank, R. Cheung. Functionalization of carbon nanotubes for molecular electronics. *Microelec. Eng.,* 2004, **73–74**, 578.

9) N. O. V. Plank, L. Jiang, R. Cheung. Fluorination of carbon nanotubes in CF_4 plasma. *Appl. Phys. Lett.,* 2003, **83**, 2426.

10) B. N. Khare, M. Meyyappan, A. M. Cassell, C. V. Nguyen, J. Han. Functionalization of carbon nanotubes using atomic hydrogen from a glow discharge. *Nano Lett.,* 2002, **2**, 73.

11) B. N. Khare, M. Meyyappan, J. Kralj, P. White, M. Sisay, H. Imanaka, J. Koehne, J. C. W. Baushchlicher. A glow discharge approach for functionalization of carbon nanotubes. *Appl. Phys. Lett.,* 2002, **81**, 5237.

12) M. J. Madou. *Fundamentals of microfabrication : the science of miniaturization* (2nd ed.) Boca Raton CRC Press, 2002.

13) K. L. Lur, M. Lago, Y. K. Chen, M. L. H. Green, P. J. F. Harris, S. C. Tsang. Mechanical damage of carbon nanotubes by ultrasound. *Carbon,* 1996, **34**, 814.

14) T. Hayashi, M. Terrones, C. Scheu, Y. A. Kim, M. Rühle, T. Nakajima, M. Endo. NanoTeflons: Structure and EELS Characterization of Fluorinated Carbon Nanotubes and Nanofibers. *Nano Lett.,* 2002, **2**, 491.

15) E. T. Mickelsona, C. B. Huffmana, A. G. Rinzlera, R. E. Smalley, R. H. Haugea, J. L. Margravea. Fluorination of single–wall carbon nanotubes. *Chem. Phys. Lett.,* 1998, **296**, 188.

16) J. W. Coburn, H. F. Winters. Ion– and electron–assisted gas–surface chemistry—An important effect in plasma etching. *J. Appl. Phys.*, 1979, **50**, 3189.

17) C. J. Powell. Elemental binding energies for X–ray photoelectron spectroscopy. *Appl. Surf. Sci.,* 1995, **89,** 141.

18) Y. Joseph, N. Krasteva, I. Besnard, B. Guse, M. Rosenberger, U. Wild, A. Knop-Gericke, R. Schlogl, R. Krustev, A. Yasuda, T. Vossmeyer. Gold nanoparticle / organic linker films: self–assembly, electronic and structural characterisation, composition and vapour sensitivity. *Faraday Discuss.,* 2004, **125**, 77.

19) S. Bausch, B. Sailer, H. Keppner, G. Willeke, E. Bucher, G. Frommeyer. Preparation of pyrite films by plasma–assisted sulfurization of thin iron films *Appl. Phys. Lett.,* 1990, **57,** 25.

20) D. L. Flamm, V. M. Donnelly. The design of plasma etchants. *Plasma Chem. Plasma Process.,* 1981, **1**, 317.

21) D. Briggs, M. P. Seah. *Practical Surface Analysis by Auger and X–Ray photoelectron spectroscopy*. John Wiley and Sons Ltd., 1987.

22) XPS Peak is freely available software, written by Raymond Kwok.

23) J. C. Love, D. B. Wolfe, R. Haasch, M. L. Chabinyc, K. E. Paul, G. M. Whitesides, R. G. Nuzzo. Formation and Structure of Self–Assembled Monolayers of Alkanethiolates on Palladium. *J. Am. Chem. Soc.,* 2003, **125**, 2597.

24) C. Vericat, M. E. Vela, G. Andreasen, R. C. Salvarezza. Sulfur–substrate interactions in spontaneously formed sulfur adlayers on Au(111). *Langmuir,* 2001, **17**, 4919.

25) J. Heeg, C. Kramer, M. Wolter, S. Michaelis, W. Plieth, W.-J. Fischer. Polythiophene — O_3 surface reactions studied by XPS. *Appl. Surf. Sci*., 2001, **180**, 36.

26) P. Kappena, N. Bracka, P. S. Halea, W. Prissanaroon, E. Welterb, P. J. Pigram. Radiation and storage–induced ageing of polypyrrole doped with dodecylbenzene sulfonic acid. *Appl. Surf. Sci.,* 2005, **243**, 287.

27) W. Prissanaroon, N. Brack, P. J. Pigram, J. Liesegang. Electropolymerization of DBSA–doped polypyrrole films on PTFE via an electroless copper interlayer. *Surf. Interface Anal*., 2003, **35,** 974.

28) J. P. Lens, J. G. A. Terlingen, G. H. M. Engbers, J. Feijen. Introduction of sulfate groups on poly(ethylene) surfaces by argon plasma immobilization of sodium alkyl sulfates. *Polymer,* 1998, **39**, 3437.

29) A. A. Audi, P. M. A. Sherwood. X–ray photoelectron spectroscopic studies of sulfates and bisulfates interpreted by Xα and band structure calculations. *Surf. Interface Anal.,* 2000, **29**, 265.

30) L. Ruangchuaya, J. Schwank, A. Sirivat. Surface degradation of α-naphthalene sulfonate–doped polypyrrole during XPS characterization. *Appl. Surf. Sci.,* 2002, **199**, 128.

31) M. Descostes, F. Mercier, N. Thromat, C. Beaucaire, M. Gautier-Soyer. Use of XPS in the determination of chemical environment and oxidation state of iron and sulfur samples: constitution of a data basis in binding energies for Fe and S reference compounds and applications to the evidence of surface species of an oxidized pyrite in a carbonate medium. *Appl. Surf. Sci.,* 2000, **165**, 288.

32) M. S. Dresselhaus, G. Dresselhaus, R. Saito, A. Jorio. Raman spectroscopy of carbon nanotubes. *Phys. Rep.,* 2005, **409**, 47.

33) J. B. Lambert, H. F. Shurvell, D. A. Lightner, R. G. Cooks. Structural *Analysis. In: Organic Structural Spectroscopy*. Prentice–Hall, 1998, 232.

34) A. Gonzalez-Berrios, D. Huang, N. M. Medina-Emmanuelli, K. E. Kristian, O. O. Ortiz, J. A. Gonzalez, J. De Jesus, I. M. Vargas, B. R. Weiner, G. Morell. Effects of heavy-ion radiation on the electron field emission properties of sulfur-doped nanocomposite carbon films. *Diamond Relat. Mater.,* 2004, **13**, 221.

35) S. Glenis, A. J. Nelson, M. M. Labes. Sulfur doped graphite prepared via arc discharge of carbon rods in the presence of thiophenes. *J. Appl. Phys.,* 1999, **86**, 4464.

36) R. Kalish, C. Uzan-Saguy, R. Walker, S. Prawer. Electrically active sulfur–defect complexes in sulfur implanted diamond. *J. Appl. Phys.,* 2003, **94**, 3923.

37) S. Gupta, B. R. Weiner, G. Morell. Investigations of the electron field emission properties and microstructure correlation in sulfur–incorporated nanocrystalline carbon thin films. *J. Appl. Phys.,* 2002, **91**, 10088.

38) S. Gupta, B. R. Weiner, G. Morell. Ex situ spectroscopic ellipsometry and Raman spectroscopy investigations of chemical vapor deposited sulfur incorporated nanocrystalline carbon thin films *J. Appl. Phys.,* 2002, **92**, 5457.

39) N. O. V. Plank, R. Chenug. R. J. Andrews. Thiolation of single–wall carbon nanotubes and their self–assembly Appl. Phys. Lett., 2004, 85, 3229.

40) A. Ulman. Formation and Structure of Self–Assembled Monolayers. *Chem. Rev.,* 1996, **96**, 1533.

41) G. Ciccarellaa, A. Maffeia, G. Vasapolloa, L. Blasib, D. Pisignanob, R. Rinaldib. Use of cholesteryl polysulfides in self–assembly and soft lithography on Au (111) and ITO. *Appl. Surf. Sci*., 2005, **246**, 313.

42) J. E. Chadwick, D. C. Myles, R. L. Garrell. Self–assembly of sulfinate monolayers on gold: new membrane mimetics. *J. Am. Chem. Soc*., 1993, **115**, 10364.

43) Y. Xia, G. M. Whitesides. Soft Lithography. *Angew. Chem. Int. Ed*., 1998, **37**, 550.

44) S. Niyogi, M. A. Hamon, H. Hu, B. Zhao, P. Bhowmik, R. Sen, M. E. Itkis, R. C. Haddon. Chemistry of Single–Walled Carbon Nanotubes. *Acc. Chem. Res.,* 2002, **35,** 1105.

45) G. A. Forrest, University of Edinburgh. Unpublished results.

46) J. C. Love, L. A. Estroff, J. K. Kriebel, R. G. Nuzzo, G. M. Whitesides. Self–Assembled Monolayers of Thiolates on Metals as a Form of Nanotechnology. *Chem. Rev.,* 2005,**105**, 1103.

47) N. N. Greenwood, A. Earnshaw. *Allotropes of Sulfur*. In: *Chemistry of the Elements* (2nd Ed.) Butterworth Heinemann 1998, 652 – 661.

48) M. Akiba, A. S. Hashim. Vulcanization and crosslinking in elastomers. *Prog. Poly. Sci.,* 1997, **22**, 475.

49) .S. Niyogi, M. A. Hamon, H. Hu, B. Zhao, P. Bhowmik, R. Sen, M. E. Itkis, R. C. Haddon. Chemistry of Single–Walled Carbon Nanotubes. *Acc. Chem. Res.,* 2002, **35**, 1105.

50) R. Taylor, D. R. M. Walton. The chemistry of fullerenes. *Nature,* 1993, **363**, 685.

51) N. O. V. Plank. Functionalisation and characterisation of carbon nanotubes for molecular electronics. Thesis (PhD), University of Edinburgh, 2005.

52) S. J. Tans, A. R. M. Verschueren, C. Dekker, *Nature,* 1998, **393**, 49.

53) R. Seidel, A. P. Graham, E. Unger, G. S. Duesberg, M. Liebau, W. Steinhoegl, F. Kreupl, W. Hoenlein. High–current nanotube transistors. *Nano. Lett.,* 2004, **4**, 831.

54) P. Avouris, R. Martel, V. Derycke, J. Appenzeller. Carbon nanotube transistors and logic circuits. *Physica B,* 2002, **323**, 6. 85, 3229.

55) P. Atkins, J. de Paula. *Physical Chemistry* (7^{th} Ed.), 2002, Oxford University Press, UK

6 Growth of carbon nanotubes on surfaces

6.1 Introduction

The growth of carbon nanotubes on surfaces is an active area of research as it is seen as an effective approach to produce devices such as field effect transistors and field emission devices.[1-3] Most of the approaches have used chemical vapour deposition (CVD) methods to grow the tubes. A metal catalyst (usually Fe, Ni, Co, Mo, or their alloys) is deposited onto a surface and then the surface is exposed to a carbon–containing gas at high temperature. The catalyst metal is usually dispersed on the surface in such a way so as to aid the formation of nanoparticles: either during pre–treatment of the surfaces, for example with hydrogen, or during the actual the CVD itself. The metal catalysts can be deposited in many different forms. Common examples are thin layers of the metal, which are evaporated onto the surface,[4] or solutions of metal salts that can be applied to the surface.[5] There is also interest in using pre–formed nanoparticles that may control the diameter of the nanotubes produced.[6]

In some cases, the metal is not deposited by itself but rather is deposited with some support for the catalyst particles.[7] The role of the support in the growth of nanotubes, as in CVD on powdered catalysts, is to provide a large surface area to reduce the sintering of the catalyst particles. It has also been suggested that electronic interactions between the support and the catalyst metal can positively affect the growth of tubes.[8] There are some surfaces that are unsuitable for the growth of nanotubes. The growth of carbon nanotubes on silicon surfaces from metal nanoparticles has been found to be terminated by the formation of the metal silicides, which are inactive as nanotube catalysts.[9] Catalysts, in particular metal nanoparticles, are mostly dispersed on silicon surfaces that have a surface layer of SiO_2, which prevents diffusion of the Si atoms to the metal and the resultant poisoning of the catalyst.[9]

Of course, control of the exact position of the growth of carbon nanotubes is highly desirable as, for example, it would allow an increased yield of electronic devices.

The deposition of the catalytic material has been patterned in several ways including traditional photolithography[10] as well as soft lithography techniques.[5,7]

6.1.1 Magnesium oxide as a catalyst support

Magnesium oxide has been shown to be a good support for carbon nanotube growth.[11-15] Magnesium oxide's suitability as a support has been attributed to the strong interaction of the MgO with the metal catalyst particles.[16] There is also some evidence that the growth of tubes is improved by the MgO and the Fe in the catalyst forming the $MgFe_2O_4$ alloy when they are heated.[17] The improvement is thought to be due to the formation of very small (< 5 nm), well–dispersed nanoparticles on the MgO surface. The formation of these particles has been explained in terms of a reduction in the size of the metal nanoparticles present, effectively by soaking–up excess iron oxide like a sponge.[17] Once the catalyst has been annealed to form a homogeneous solid solution of $MgFe_2O_4$ in MgO, reduction by the carbon–containing gas (e.g., methane) precipitates out very small particles of iron.[10]

Despite magnesium oxide being a good support for carbon nanotube growth, there has been little research focussed on using it as a support for growth on surfaces.[18-20] Patterned growth has been achieved through micro–contact printing.[19] One of the attempts to grow carbon nanotubes on a surface resulted, in actual fact, from trying to produce thin–film composite materials of MgO and CNTs to explore ion–induced secondary electron emission characteristics.[20] The composite formed has properties that would make it suited to use in, for example, plasma display panels.

6.1.2 Magnesium oxide precursors

The present work had two aims. The first aim was to develop a simple catalyst system that could be used to pattern growth of carbon nanotubes on surfaces using simple soft lithography techniques. Soft lithography is a technique that uses a patterned elastomer as a mask, a stamp or a mould stamps to pattern surfaces.[21] The soft lithography requires some sort of "liquid catalyst" that can be dispersed on the surface to take the shape of the mould. We investigated different magnesium compounds, such as magnesium nitrate, that could be dispersed with iron nitrate onto

a surface so that, when the sample was heated, an Fe / MgO catalyst would be formed. The carbon nanotubes would then grow on the catalyst when the sample is exposed to CVD conditions. From the point of view of having good patterning, the catalyst needs to produce well–ordered and well–defined areas of growth. To produce good growth of tubes it is known that a catalyst with high surface area is desirable.[22] The catalyst systems that have appeared in the literature to–date[18-20] all use polymer additives, probably to increase the surface area of the MgO formed as structure–directing agents. Here the magnesium compounds were used without any polymer additives, in order to establish their primary characteristics.

Another aim of the present work was to explore the use of calcination of different magnesium compounds, to improve the growth of nanotubes on surfaces. It has been reported that the quality of tubes grown from Fe / MgO can be improved by calcining the catalysts in air for 10 hours.[17] Extended calcination is believed to allow formation of a solid solution of the $MgFe_2O_4$ in MgO. The solid solution is thought to ensure that the Fe is well dispersed, and when exposed to CVD conditions it forms small nanoparticles that are ideal for forming nanotubes. A diagram of the suggested process is shown in Figure 6.1.

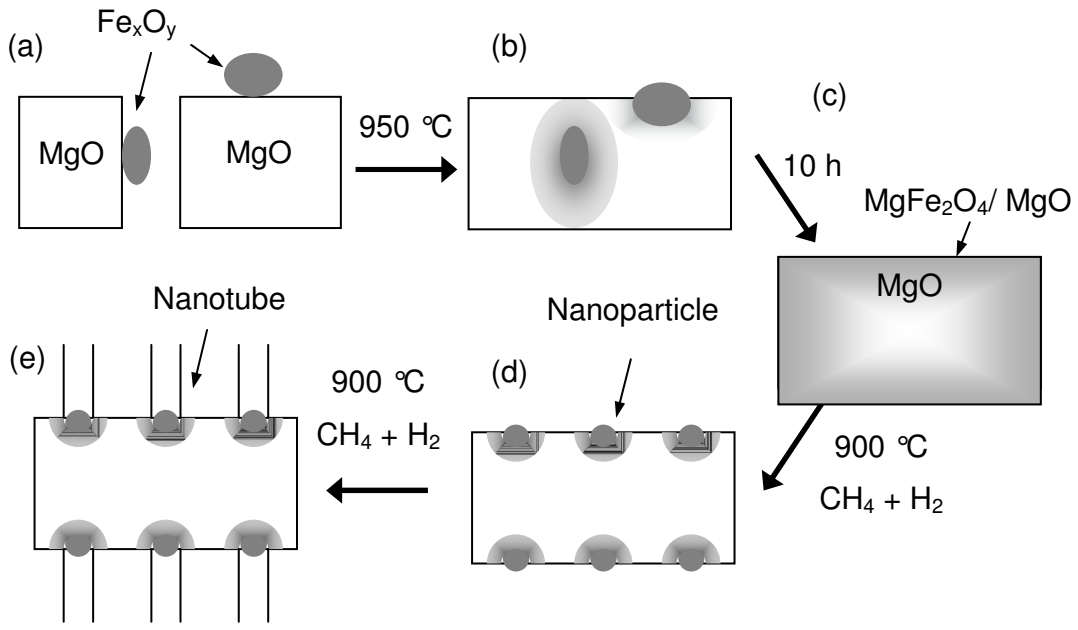

Figure 6.1. In a catalyst composed of iron oxide and magnesium oxide, the iron may be in the form of large particles (a). When heated to 950 °C in air, the iron oxide diffuses into the

magnesium oxide (b) to form a solid solution of $MgFeO_4$ in MgO (c). When exposed to CVD conditions, the $MgFe_2O_4$ reacts with the reaction gases to form small, well–dispersed iron nanoparticles (d) that then can go on to form nanotubes (e).

6.2 Growth of nanotubes on silicon wafers

The patterning of catalyst relies on having a solution or dispersion that can be deposited onto a surface. In the present approach, different magnesium compounds that are known to form magnesium oxide when heated, were used to make CNT catalysts with iron nitrate. For detailed experimental procedures, see the Appendix A.1. The compounds chosen were magnesium nitrate, carbonate, acetate, and stearate. The results were compared against the nanopowder MgO that was used as the catalyst support in Chapter 3. Ethanolic solutions or dispersions of the different magnesium compounds were prepared to include iron nitrate so that the Fe % w/w of the final catalyst would be 1%. Silicon wafers ($1 \times 1 \times 0.1$ cm) with 1 μm thick layer of thermally–grown SiO_2, were dipped into the ethanolic catalyst solution so that a thin layer of the solution covered the surface. For each sample, two wafers were prepared (except for MgO). One of the two wafers was calcined in air at 600 °C so that the magnesium compound used would be converted to MgO, and the iron nitrate to iron oxide. The other wafer had no further treatment. The wafers were then exposed to CVD at 900 °C to form CNTs. The MgO sample was used without calcination.

The most striking difference between the samples after CVD was their shade. As can be seen in Figure 6.2, the samples grown with magnesium carbonate and magnesium oxide were much darker, and appeared to be more–even in shade across the surface than the other samples. The differences in the shades of the samples suggest that magnesium carbonate and magnesium oxide catalysts were the best at depositing carbon.

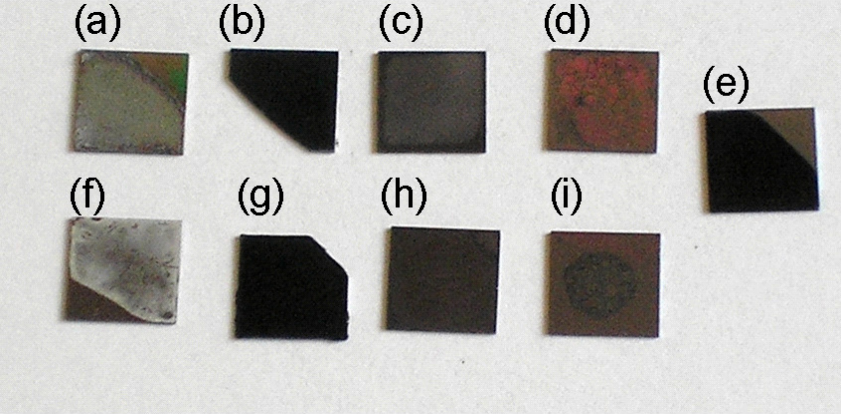

Figure 6.2. Photograph of the wafers after CVD. Samples (a) – (e) were not calcined before CVD, while samples (f) – (i) were. Magnesium nitrate was used in samples (a) and (f), carbonate in (b) and (g), acetate in (c) and (h), stearate in (d) and (i), and the MgO nanopowder was used in (e). The samples made with magnesium carbonate, (b) and (g), had a lot of carbon deposited on them during CVD: as can be seen by their black appearance. The MgO sample (e) also turned black. All the other samples were much lighter in shade. The pink colour in samples (d) and (i) is due to the SiO_2 coated wafer. Note that the points where the wafers were held during dipping into catalyst solution is seen as an uncoated triangular patch in the corners.

6.2.1 Raman Spectroscopy

Raman spectra for the samples are presented in Figure6.3. Raman spectra were collected from six randomly selected points on the catalyst surface of each sample. All the spectra show the characteristic G and D bands for carbon structures.[23,24] The G band (~ 1590 cm^{-1}) is associated with bonding of sp^2 hybridized carbon. The D band (1330 cm^{-1}) is a disorder–activated band that is intense in spectra of poorly graphitized samples. A large D band can indicate the presence of MWNTs and other less–graphitized carbon impurities. As discussed in detail in Chapter 2, the ratio of the intensities of the D and G band (I_D / I_G ratio) is often used in the literature as a measure of the "quality" of SWNTs produced in a synthesis.[23] In Figure 6.3, the spectrum with the smallest D band is shown for each sample. All of the samples, except the uncalcined stearate sample, also exhibited radial breathing modes (RBMs), which are characteristic of single–walled nanotubes.

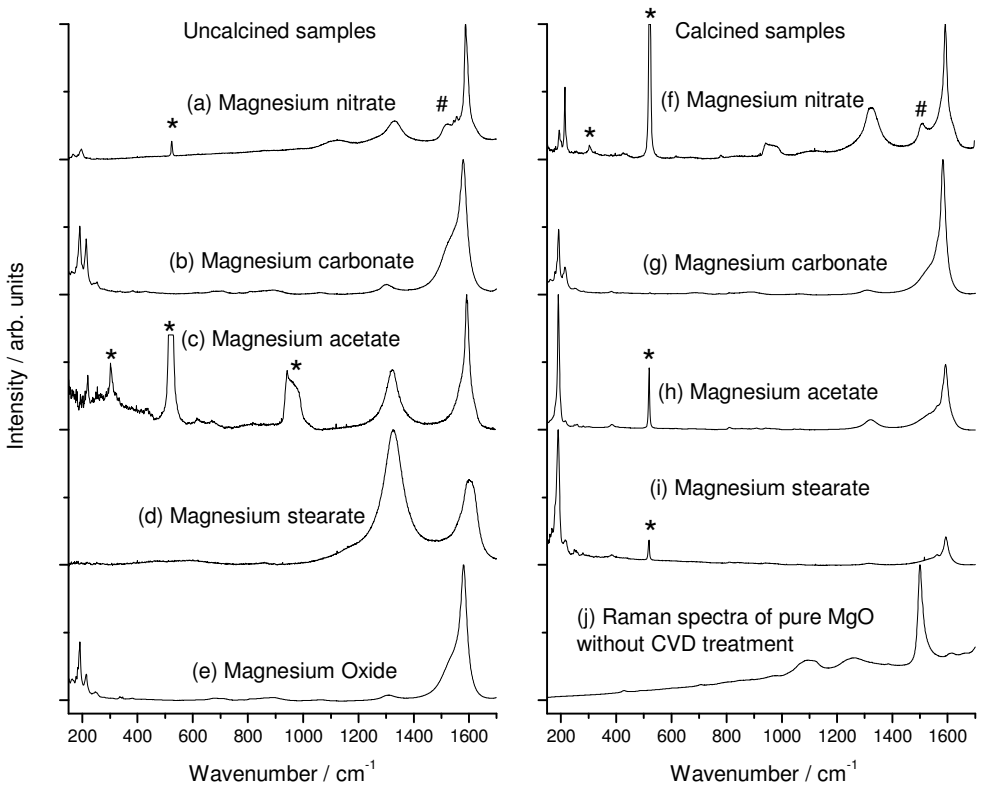

Figure 6.3. The Raman spectra with the smallest D bands for each sample are presented here. Each of the spectra has been normalised to its largest peak, to aid comparison. The samples that were not calcined are presented in the left hand column, (a) – (e), while the right hand column (f) – (i) corresponds to samples that were first heated to 600 °C for 30 minutes in air. Plot (j) shows the spectrum of a sample of pure magnesium oxide. There is a peak that can be attributed to MgO in the nitrate sample that is marked with the number symbol (#). Peaks that arise from the SiO_2 / Si wafer have been marked with an asterisk (*), and the peak at 520 cm^{-1} in plot (c) has been truncated for clarity.

In some spectra, typically on the samples that were less dark in shade, some peaks are attributed to MgO. A spectrum of a sample of fused MgO (Sigma Aldrich, UK) is shown in Figure 6.3(j). MgO is known to exhibit no first order Raman lines due to the inversion centre in its unit cell, although it has been claimed that some peaks of the first order spectrum have been seen in fine powder samples due to the abundance of ions at the surfaces.[25] The most intense peaks of the hypothetical first order

spectrum, which should occur at around 280 and 446 cm^{-1}, are not observed in our MgO spectrum. The second order spectrum of MgO, which involves the absorption or emission of two phonons instead of one, has been previously recorded.[26] Our spectrum for MgO does not agree with the expected second order spectrum. The peaks seen in our MgO spectrum also cannot be related to emission lines of either Ne or He discharge, ruling out the Raman laser as the cause.[27] The spectrum is not consistent with magnesium hydroxide ($Mg(OH)_2$),[28] which is known to form by the reaction of magnesium oxide with water, nor is it consistent with the spectrum of magnesium carbonate.[29] The spectrum of MgO is known to exhibit fluorescence, which appears as the rising baseline over the region 200 to 1600 cm^{-1} in Figure 6.3(j).[26] The fluorescence of the MgO is also apparent in the spectra of the samples that show the MgO peaks. A spectrum for MgO similar to ours has been reported in the literature:[11] that spectrum was recorded for a sample of a Fe / MgO catalyst that had undergone CVD, but no growth of tubes had occurred due to the low temperature used. A full investigation of the Raman spectroscopy of MgO was deemed to lie too far outside the remit of the present work, and we simply ascribe the peaks observed to be characteristic of MgO. Peaks that can be attributed to MgO have been marked with the number symbol (#) throughout the discussion. There are also several peaks due to the SiO_2 / Si wafer,[24] which are marked with asterisks (*).

Raman spectroscopy confirmed the better graphitic growth on the oxide and the carbonate, as identified qualitatively by the shade of the samples. Table 6.1 shows the mean I_D / I_G ratio for the six Raman spectra taken for each of the samples. The values of the mean I_D / I_G are much smaller for the carbonate and oxide than for any of the other compounds, suggesting good graphitic growth. In contrast, the other three magnesium compounds' spectra all showed large D bands, suggesting poor growth.

Magnesium compound	Formula	Dispersion or solution?	Pre–treatment	Shade after CVD	Average I_D / I_G
Magnesium carbonate	$Mg(CO_3)_4$. $Mg(OH)_2$. $5H_2O$	Dispersion	None	Black	0.09
			Calcined	Black	0.15
Magnesium oxide nanopowder	MgO	Dispersion	None	Black	0.11
Magnesium nitrate	$Mg(NO_3)_2$. $6H_2O$	Solution	None	Light grey	0.45
			Calcined	Light grey	0.88
Magnesium acetate	$Mg(C_2H_3O_2)$. $4H_2O$	Solution	None	Light grey	0.99
			Calcined	Light grey	0.46
Magnesium stearate	$Mg(O_2C(CH_2)_{16}CH_3)_2$	Dispersion	None	Speckled	1.43
			Calcined	Speckled	0.35

Table 6.1. The average I_D / I_G ratios for the samples presented here show that the best quality tubes were grown on the wafers that were coated with the magnesium carbonate or magnesium oxide catalysts. The magnesium compounds have different solubilities in ethanol. Only the nitrate and the acetate formed solutions, while the other compounds were dispersed as fine particulates in the ethanol.

It is interesting to note that the samples that have small I_D / I_G ratios have smaller variation in the RBMs compared to those with large I_D / I_G ratios. For the example, the low wavenumber region of the carbonate sample spectra, shown in Figure 6.4(a), show very little difference in the RBMs present compared to the nitrate sample spectra, shown in Figure 6.4(b). The spectra of the acetate and stearate samples also

exhibit big variations in the RBMs: these show fewer RBMs and some spectra actually have no identifiable RBMs. Greater variation in RBMs is consistent with poor growth of SWNTs on the samples. In the samples with good growth, the laser spot (> 20 μm) excites a region that covers many tubes. The better the growth, the better is the sample homogeneity: therefore, each of the spots will excite roughly the same distribution of tubes. In contrast, the laser only excites a few tubes in the samples with poorer growth (higher I_D / I_G). Excitation of spots containing a smaller selection tubes gives rise to more variation between the spectra. The nitrate, acetate, and stearate samples, in general had much lower Raman signals than the carbonate and oxide samples, which suggests that the former samples had less carbon deposited on them, and therefore fewer tubes. The differences in the tube density are confirmed by SEM as discussed in the next section. We also note that in general, the samples with larger I_D / I_G ratios gave smaller experimental signals compared the samples with small I_D / I_G ratios.

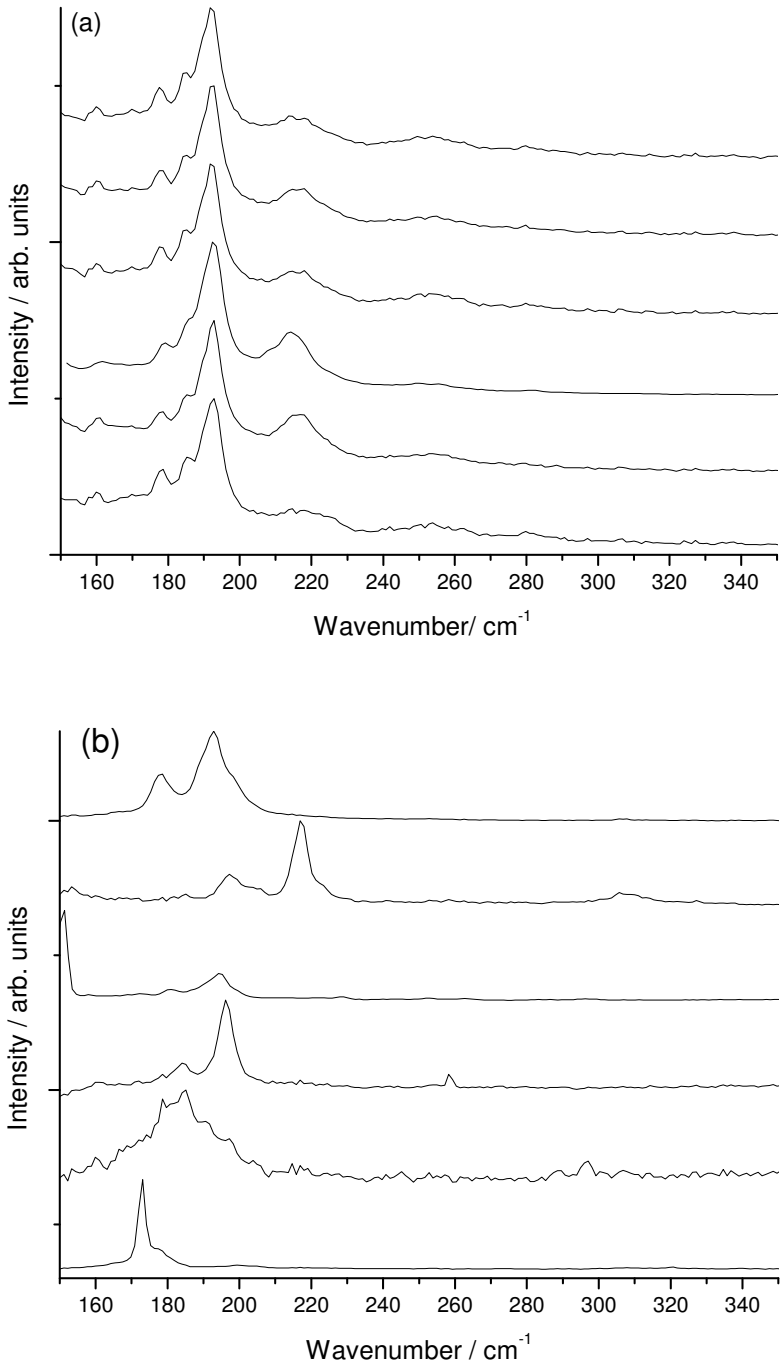

Figure 6.4. All the Raman spectra for the products of the calcined carbonate (a) and calcined nitrate (b) catalysts are shown here for the low wavenumber region, where the RBMs for SWNTs are observed. All the spectra have been normalised to the intensity of the most intense RBM. The carbonate spectra are all very similar, while the nitrate samples show great variations in the RBMs present: this is due to low nanotube growth density—see text for details.

6.2.2 Scanning electron microscopy

Magnesium carbonate and oxide samples

As is consistent with their Raman spectra and their physical appearances, the magnesium carbonate and magnesium oxide samples appeared similar by SEM as shown in Figure 6.5 and Figure 6.6. The surfaces of catalyst, in all the samples prepared from the carbonate and oxides, had cracks in it. These cracks appear similar to patterns that are formed by differential shrinkage of a material that is adhered onto a surface. We suggest that these cracks are caused by drying of the samples. Similar patterns can be seen in work where drying of a slurry of alumina particles was studied.[30] In the carbonate samples, the surface was continuous with isolated cracks in it, whereas in the MgO samples the catalyst had broken up into individual islands. At higher magnifications, the surface of the catalysts could be seen to be made up of many tubes. The tubes visible at high magnification are probably SWNTs in bundles, consistent with the Raman spectroscopy, although the presence of MWNTs cannot be excluded. Tubes can be seen bridging across the cracks, with lengths up to 10 μm.

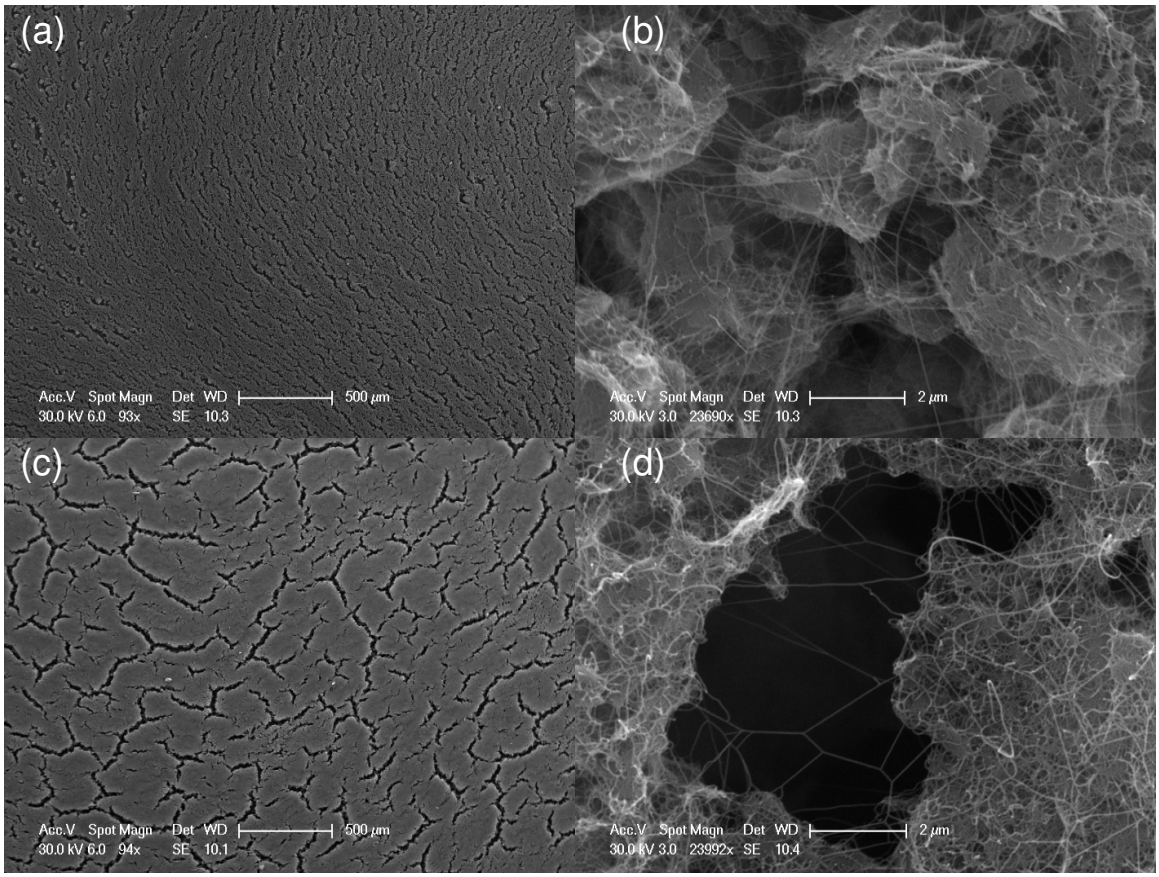

Figure 6.5. Samples grown from magnesium carbonate, including uncalcined (a) and (b), and the calcined (c) and (d). The surface of the catalyst, in both samples, appears covered in fissures which vary in size across the surface. At high magnifications it was possible to see the high density of tubes grown. The actual tubes in the images are most likely to be bundles of SWNTs, although there are also possibly MWNTs.

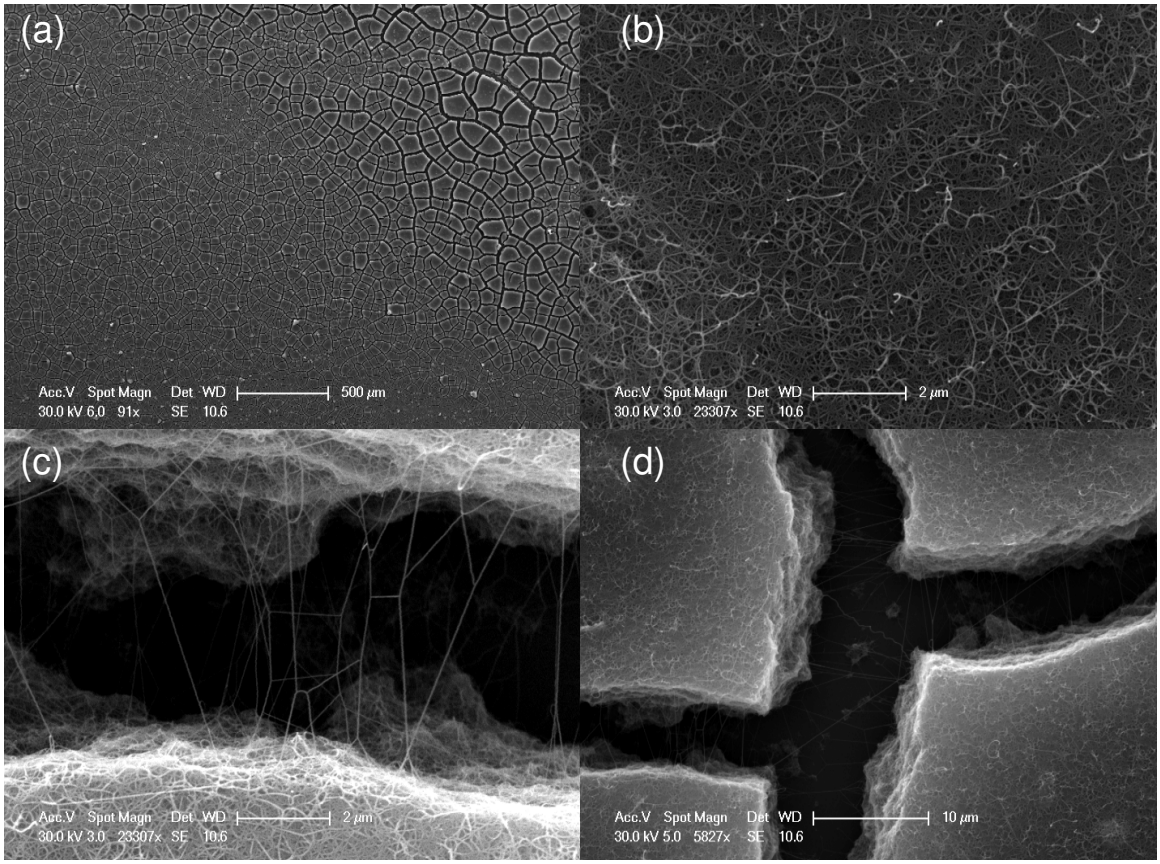

Figure 6.6. The MgO catalyst uncalcined appeared to have been broken up into islands of different sizes (a). The surface of these islands was covered in a dense mat of tubes (b). The gaps between the islands of catalyst seemed to extend down to the surface of the wafer and were decorated with tubes that bridged the gaps (c).

Magnesium nitrate samples

The magnesium nitrate sample showed very different morphology to that of the carbonate and oxide samples. The uncalcined sample after CVD, Figure 6.7, showed that the surface of the wafer was covered in needle–like objects. These objects could have formed from the crystallization of the magnesium nitrate from solution during drying. Sparse growth of tubes can be seen on the areas around the needles, Figure 6.7 (c), as well as on them, Figure 6.7(d). The appearance of the magnesium nitrate sample that was calcined in air before CVD is quite different, Figure 6.7, to the non–calcined sample. The catalyst can be seen to have formed a layer on top of the wafer that has cracked and been deformed, Figure 6.8(a). Again, only sparse growth of tubes can be seen either across the cracks in the surface, Figure 6.8(b), or on the surface itself, Figure 6.8(c).

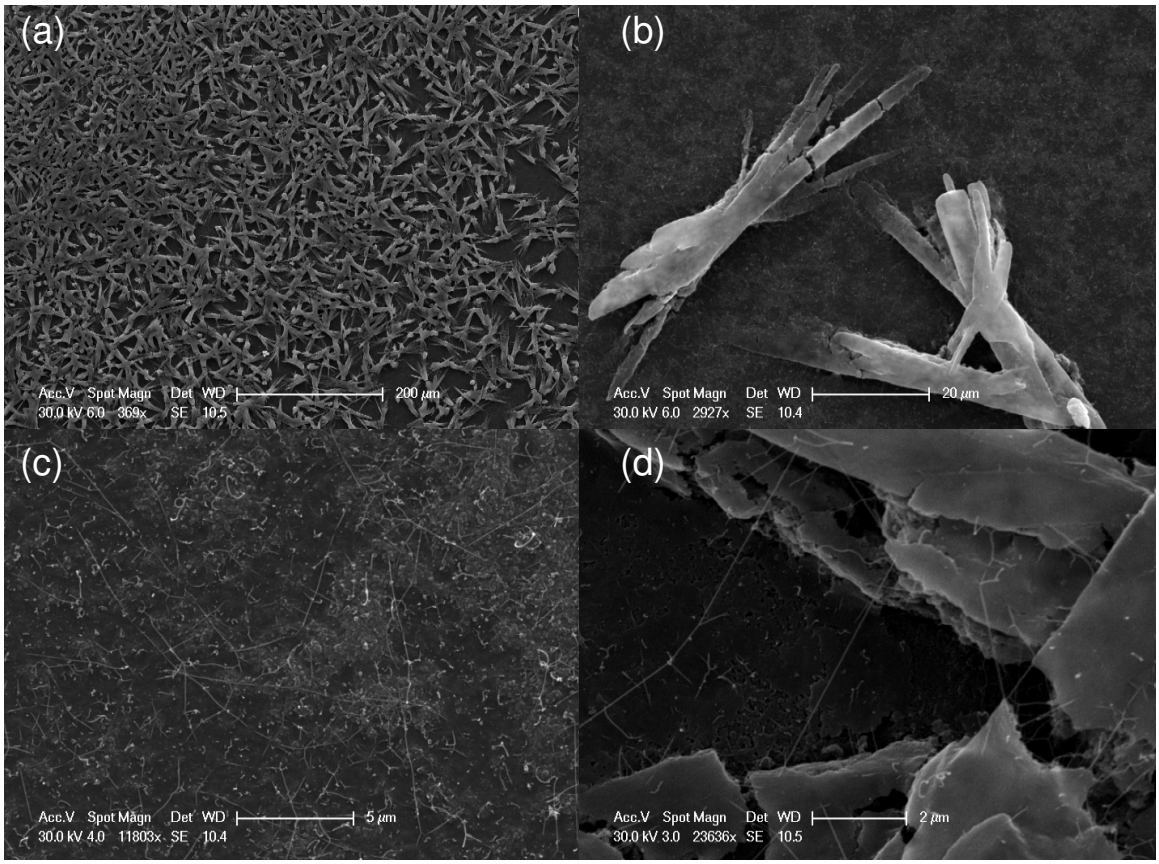

Figure 6.7. The uncalcined magnesium nitrate sample formed needle–like structures on the surface of the wafer. Only sparse growth of tubes can be seen either on the needles or around them.

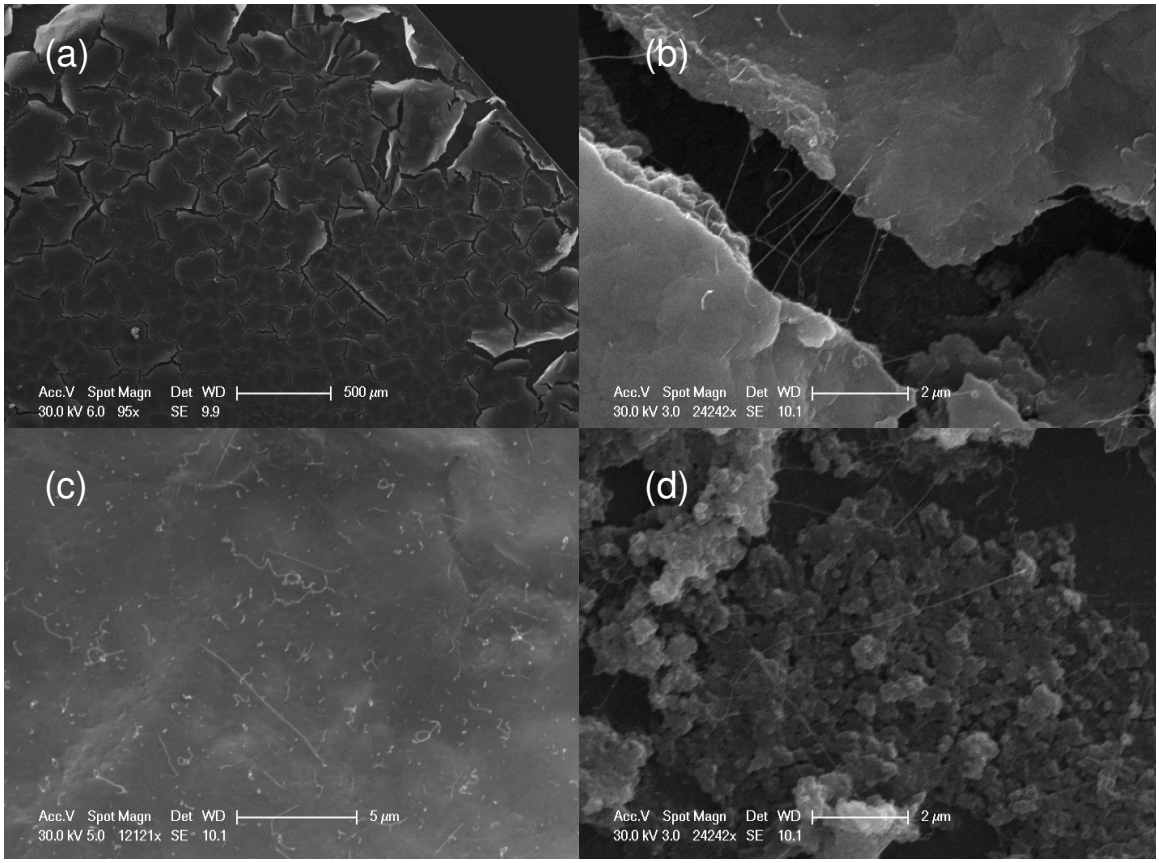

Figure 6.8. The magnesium nitrate that was calcined before CVD shows a very different surface compared to the uncalcined sample (*cf,* Figure 6.7). On the surface of the calcined sample, the catalyst has formed a layer of MgO that has cracked. Sparse growth of tubes can be seen on the surface of the catalyst or spanning the cracks. Some growth could be observed on the catalyst between the cracks.

Magnesium acetate samples

At low magnification, Figure 6.9(a), the uncalcined acetate sample was seen to have an interesting "crazy paving" pattern on the surface. Similarly to the calcined nitrate sample, the catalyst had formed a surface with many cracks. At low magnification, the slabs of the paving appear to be flat, Figure 6.9(a). However, at higher magnifications, Figure 6.9(b) it can be seen that the slabs are cracked and irregular, and are bounded by unbroken regions of the catalyst that appear to form straight lines. Very little growth of tubes can be seen on the fairly flat surface of the catalyst, Figure 6.9 (c), while there were more tubes visible around the cracked areas, Figure 6.9(d).

The calcined acetate sample appeared quite similar to the uncalcined sample in that the catalyst had formed a layer on top of the wafer as can be seen in Figure 6.10(a). However, it appears that the surface of the catalyst has more cracks and is less flat. Figure 6.10(b) and Figure 6.10(c) show the irregular shape of the catalyst that forms, especially around the cracks in the surfaces. The surface of the calcined catalyst is covered in plate–like or perhaps tube–like structures that are reminiscent of the surface of magnesium oxide prepared from the calcination of magnesium hydroxide.[31] The greater number of cracks and the less–flat surface seems to promote the growth of tubes. There even appears to be more growth of tubes on the flat areas, Figure 6.10(d).

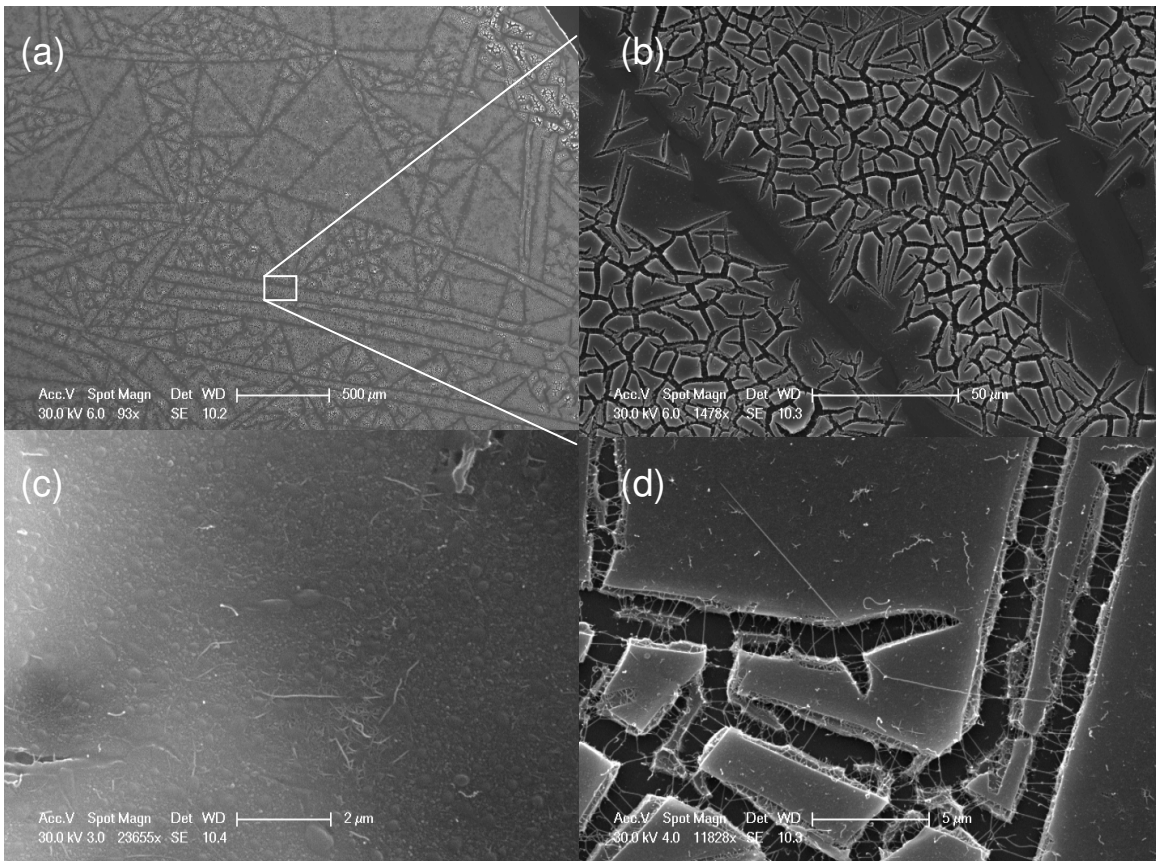

Figure 6.9. From the SEM images of the uncalcined acetate sample, it can be seen that the wafer is covered by a layer of catalyst. The surface of this catalyst layer is broken up by cracks (b,d). The flat unbroken areas between the cracked regions (b) resemble lines giving the surface of the sample a "tiled" appearance (a). Sparse growth of tubes is found in the flat unbroken region (c) with more growth visible at the crack areas (d).

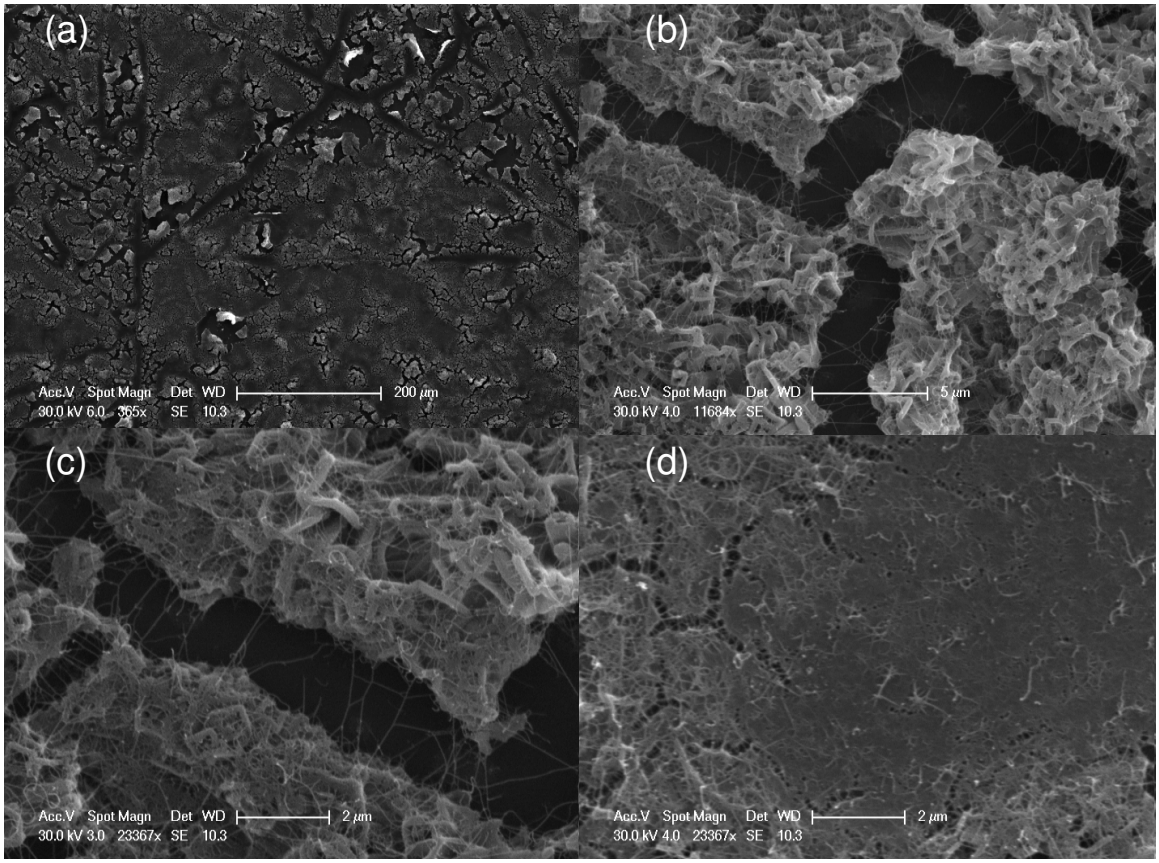

Figure 6.10. The calcined acetate sample appears in some ways similar to the uncalcined sample (*cf,* Figure 6.9): the calcined sample is covered by a layer catalyst that is broken up by cracks (a). However, the calcined sample seems to have more cracks. Also, the calcined sample appears to have a more irregular and a less flat surface (b), especially in the areas near cracks. This sample appears to have better growth of tubes at the cracks (c), and at the flat areas (d).

Magnesium stearate samples

The SEM images in Figure 6.11 show that the surface of the uncalcined stearate sample is irregular and made up of larger fragments of catalyst on the wafer. Tubes can be mostly seen on the edges of the smooth pieces, with a few tubes visible on the surface of the catalyst. The calcined sample, shown in Figure 6.12 is very similar to the uncalcined sample.

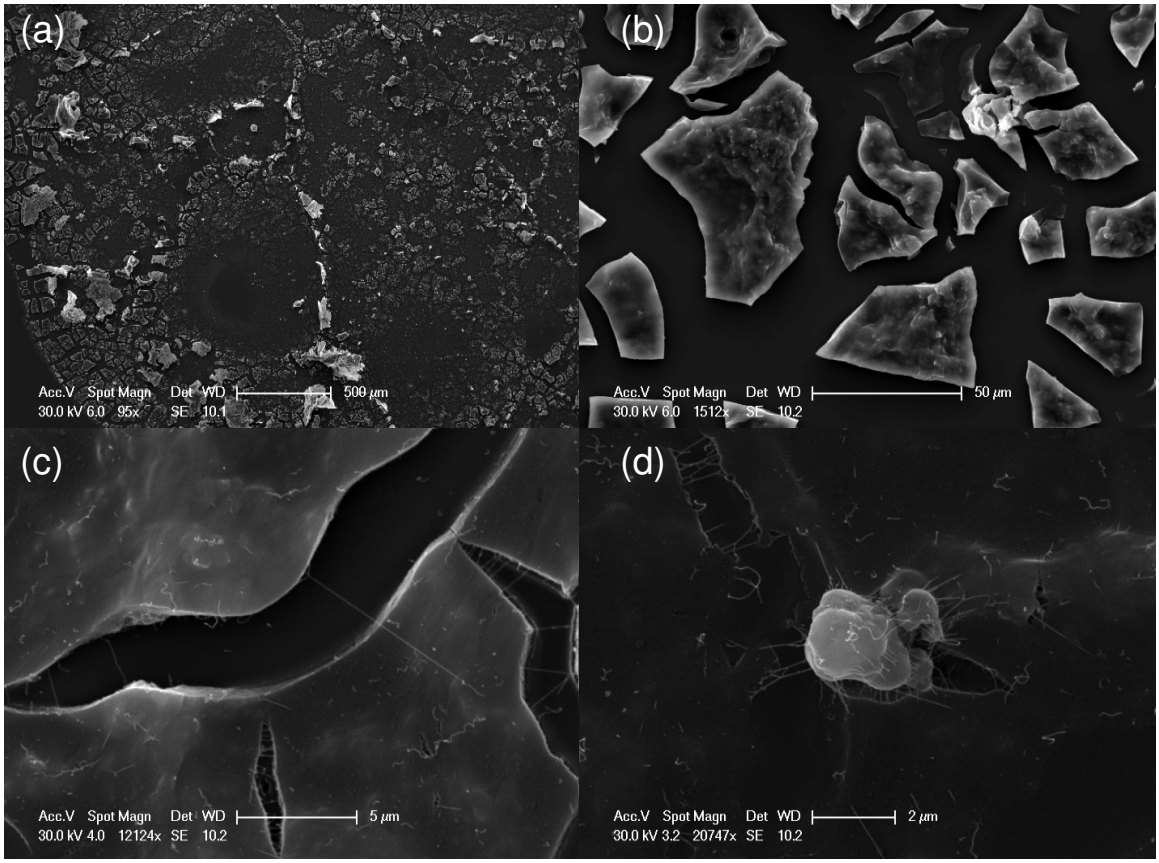

Figure 6.11. The sample prepared from the unclacined magnesium stearate is seen to have a rough surface (a) that is made up of large and fairly smooth pieces of catalyst (b). Growth of the tubes is mostly observed at the edges of the pieces (c), although some tubes can be seen on the surface of the catalyst (d).

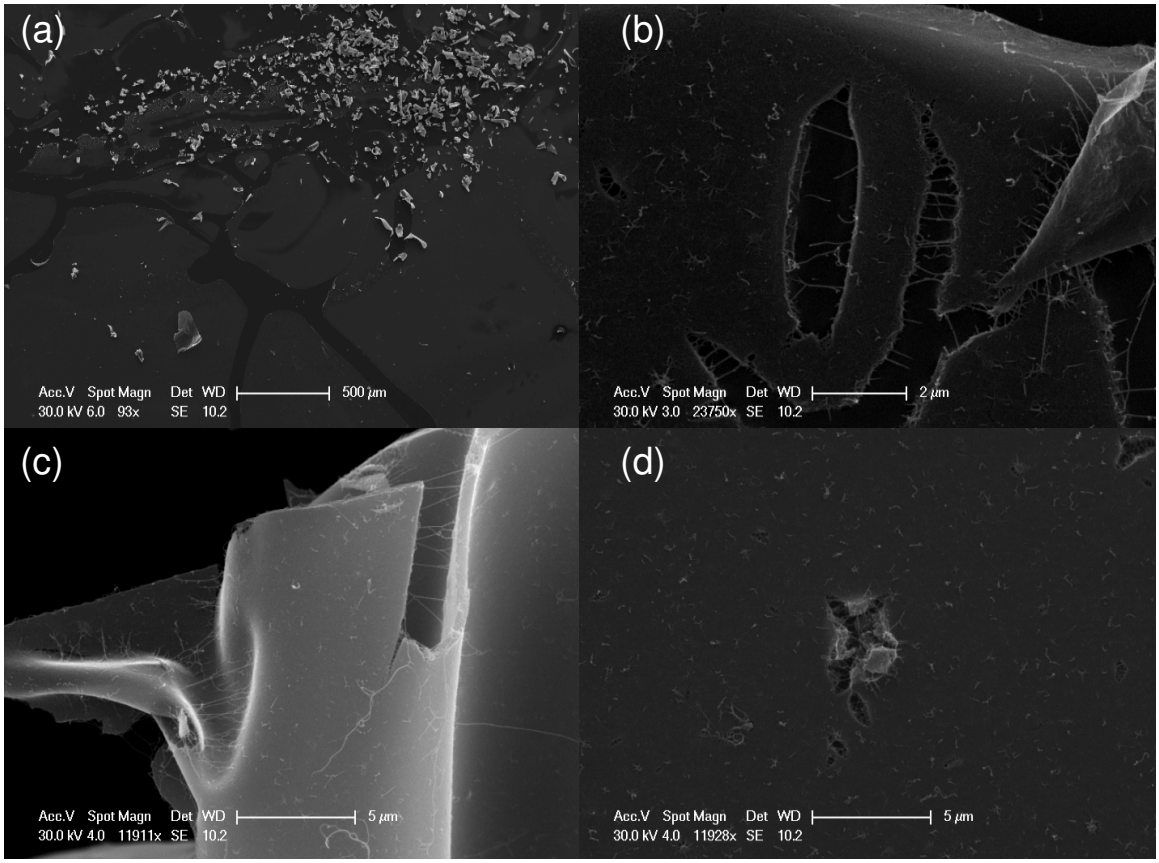

Figure 6.12. By SEM, the calcined stearate sample appears similar to the uncalcined sample (*cf,* Figure 6.11) in that the surface is covered in pieces of the catalyst (a). Likewise, tubes are mostly seen at the edges of pieces (c) with some visible on the surface of the catalyst (d).

Summary of SEM

Considering the SEM images of the samples overall, it seems that most of the tubes that were observed were found at the edges of the catalyst. It is tempting to suggest that, in general, the tubes grow better in places where they are free from obstructions, in such places as the surface of the catalyst. However, it is important to remember that the tubes at the edges, or that are suspended over a trench, are going to be easier to image in the SEM than a tube lying flat on a surface.[19] The SEM images show that the samples with most growth of tubes were those prepared with the magnesium oxide and the carbonate. In the other samples, the nitrate, the acetate and the stearate, the formation of large, smooth layers of catalyst seems to be detrimental to growth of tubes. The greater growth on the catalysts with more cracks can be qualitatively explained in terms of the surface of the catalyst. Usually, the need for a high surface area for nanotube growth is explained in terms of keeping the catalytic nanoparticles

well dispersed,[8,16] and allowing the diffusion of precursor gas to the nanoparticles as the tubes grow.[33,34] It is difficult to judge from the SEM images whether the samples with the smoother surfaces have a greater proportion of MWNTs, but large I_D / I_G ratios for these samples are consistent with this hypothesis. Clearly, the morphology of the catalyst *does* have an effect on the growth of tubes. In general it can be said that tubes grow best from edges where they are not obstructed. This would seem to bode well for situations where the catalyst can be patterned in well–defined areas with well–defined voids: e.g., as in conventional wiring between electrodes.

6.2.3 Effect of calcination on nanotube growth

By comparing the Raman spectroscopy and SEM results, it is possible to study how the calcination step affects the growth of the tubes on the catalyst. The results show that the effect of calcination on nanotube growth seems to vary with the magnesium compound used. For the carbonate, there is little difference in the growth between the calcined and uncalcined samples. For the nitrate sample, however, calcination under these conditions seems to have formed a smooth layer of catalyst on top of the wafer, which is not conducive to tube growth. In contrast, for the acetate and stearate, the calcined wafers actually showed an improvement in the I_D / I_G ratio. As discussed above, this could be due to the different morphology of the calcined catalyst. But there is also evidence that the decomposition of stearate and acetate to form the active catalyst for the uncalcined samples is hampered by the lack of oxygen during the heating of the catalyst. The carbonate and nitrate can decompose to the oxide by releasing carbon dioxide[35] or nitrogen dioxide and oxygen,[36] according to Equations 6.1 and 6.2.

$$Mg(CO_3)_{(s)} \rightarrow MgO_{(s)} + CO_{2(g)} \qquad \textbf{(6.1)}$$

$$2Mg(NO_3)_{2(s)} \rightarrow 2MgO_{(s)} + 4NO_{2(g)} + O_{2(g)} \qquad \textbf{(6.2)}$$

For the acetate and the stearate, oxygen will aid the removal of the carbon–containing anion through oxidation. For example, the improvement in growth seen when the stearate sample is calcined does not seem to be due simply to differences in the morphology of the catalyst. The calcined and uncalcined samples appear very similar by SEM. It was discovered that if a dried powder sample of the stearate catalyst was heated to 900 °C for 30 minutes under a flow of argon, a black, waxy

solid formed, which had a similar Raman spectrum to that of the growth on the uncalcined stearate sample shown in Figure 6.3(d). The dark shade of this solid is probably due to the pyrolysis of the carbon–rich stearate, which forms carbonaceous impurities: this is consistent with presence of a large D band in the Raman spectrum. The iron in the catalyst probably gets poisoned by this reaction: so, when the wafer is exposed to methane, it can not react. The calcination in air is necessary to form the active catalyst, which does not happen when the catalyst is heated in argon.

From the SEM images, it is apparent that the catalyst in the calcined stearate samples has a tendency to crack and actually break off the surface of the wafer, as can be seen in Figure 6.12(a). This tendency is possibly due to tension and stress that the formation of MgO produces. As the magnesium stearate decomposes, each mole of stearate forms a mole of the oxide. An estimate of the change in volume can be calculated from the ratio of the molar volume of the stearate to that of the oxide. Estimations for the molar volumes of the magnesium compounds, at room temperature, are shown in Table 6.2. It can be seen from the table that the stearate has the biggest ratio of molar volume to that of MgO. If we assume that the stress in the material is proportional to the decrease in volume then it can be seen that the stearate will suffer the largest stress. As the MgO formed is a brittle ionic solid, the stress can be relieved by fracturing. Shrinkage fracture–patterns are commonly found in systems where a material that is adhered to a surface contracts.[30] In the case of the stearate, the stress in the material becomes greater than the adhesion to the SiO_2 surface, and so pieces of the catalyst become detached from the surface. The curled–up pieces of catalyst, Figure 6.12(c), may have been caused by shrinkage due to the MgO oxide forming at the surfaces first. Contraction at the surface, surrounding a more flexible organic core, could cause the catalyst layer to curl–up.

Magnesium compound	Molar mass / g mol^{-1}	Density / g cm^{-3}	Molar volume / cm^3	Molar volume ratio to MgO
Magnesium oxide	40.3	3.6	11.3	1.0
Magnesium carbonate	84.3	3.0	28.5	2.5
Magnesium acetate	214.5	1.4	147.5	13.1
Magnesium nitrate	256.4	1.5	175.6	15.6
Magnesium stearate	591.2	1.0	579.6	51.5

Table 6.2. The change in volume of a magnesium compound upon decomposition is estimated by calculating the ratio of the molar volume of the compound to that of the oxide (using data available at room temperature[37]). Magnesium stearate is the compound that has the biggest change in volume: which may explain why the catalyst formed from it was seen to break away from the surface of the wafer.

6.2.4 Surface area measurements

Catalysts with large surface areas are thought to be good at growing tubes.[33] Due to the small amounts of catalyst on each of the wafers, it would be difficult to measure the surface area of the samples as they are prepared in Section 6.2. Therefore, it was necessary to prepare larger amounts of powdered catalyst. The powdered catalyst samples were prepared from identical solutions and dispersions, by allowing the solvent to evaporate. The dry residues were scraped out, and then ground in a mortar and pestle, before they were calcined 900 ºC in air for 30 minutes to ensure that the MgO precursors would have all decomposed. The resulting solids were scraped out of the boat and were not ground again. Some of the compounds gave free flowing powders while others had fused to leave a thin coating on the interior of the boat. These observations are summarized in Table 6.3, as are the surface areas of the

resulting solids as determined from adsorption measurements using the Brunauer, Emmett and Teller (BET) isotherm.[38]

Compound	Description after calcination	BET surface area / $m^2\ g^{-1}$	Melting point / °C (lit.)	Average I_D / I_G	
				Uncalcined	Calcined
Magnesium acetate	fused solid	6.0	72 – 75	0.99	0.46
Magnesium nitrate	fused solid	8.6	89 – 95	0.45	0.88
Magnesium stearate	fused solid	20.2	200	1.43	0.35
Magnesium carbonate	powder	59.0	662 (decomp.)	0.09	0.15
Magnesium oxide nanopowder	powder	77.2	2852	0.11	–

Table 6.3. Powdered samples of the catalysts were prepared and calcined so that their surface areas could be measured. The catalysts that grew the best the tubes, which had the smallest I_D / I_G ratios, were found to have the highest surface areas. The melting point of the magnesium compound was found to be important. If the compound becomes liquid as the catalyst is heated, then the catalyst formed at the CVD temperature will have a low surface area.

It is apparent that the magnesium compounds that gave the best tubes, the oxide and the carbonate, are those with highest surface areas. Figure 6.13 shows the trend of the I_D / I_G ratio for the calcined samples with the surface area measured for the equivalent powder sample. Figure 6.13 shows that as the surface area increases, so the quality of the tubes increases (the I_D / I_G ratio decreases).

Literature melting points for the magnesium compounds are also presented in Table 6.3. The actual melting point of our MgO nanopowder may be slightly reduced due to the small size of the particles.[39] The compounds with the low melting points—

lower than the CVD temperature—are the nitrate, acetate, and stearate. Unsurprisingly, these were also the compounds that produced fused solids when calcined, and had very low surface areas. When the catalysts prepared with these compounds are used in CVD, or are being calcined prior to CVD, the magnesium compounds melt. The liquid catalyst formed will then go on to make a low surface area catalyst, which will be less conducive for tube growth.

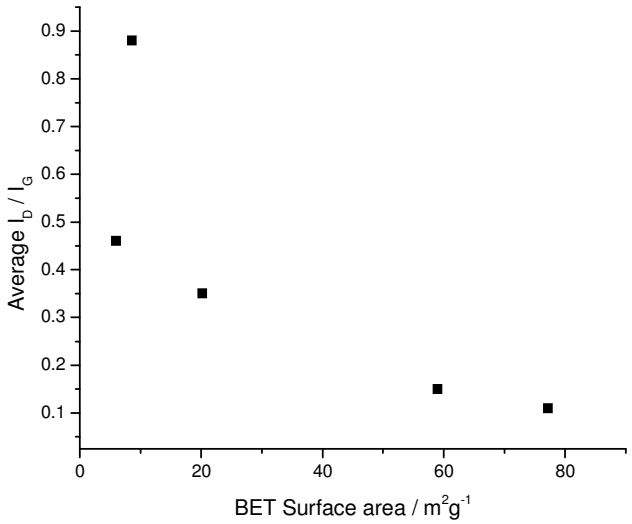

Figure 6.13. The quality of the tubes that can be grown on a catalyst appears to be related to the surface area of the catalyst. The catalysts with highest surface areas, the oxide and carbonate, produce the samples with lowest I_D / I_G ratios, and therefore the best tubes.

6.3 Embossing catalysts for patterned growth of CNTs

As shown in the preceding sections, the most effective catalysts were found to be the carbonate and oxide systems. As these compounds produced high quality tubes on the wafers, they were then used in further experiments in an attempt to pattern the catalyst, and therefore the growth, of the CNTs. Our motivation to produce the patterned catalyst, in the first instance, was to study the localised growth of nanotubes on a surface and to understand the role of the MgO support rather than to develop a protocol for positioning nanotubes to fabricate devices. Also, we are interested in establishing if these catalysts, which are dispersions of powders, could

be patterned at all. As stated previously, for patterned growth, a catalyst that is a true solution would seem to be desirable. Otherwise, the size of the features to be patterned would have to bigger than the size of particles used. However, as has been shown previously, these catalyst dispersions seem to give better growth due to the fact that the particles from which they are composed produce a high surface area and arguably a morphology that allows tubes to grow.

Here, due to its simplicity, we used soft lithography to pattern the nanotube catalyst on Si wafers. This form of patterning uses stamps made out of elastomers.[21,40] The first attempts were carried using micro–contact printing. In this technique, the catalyst solution is applied to the patterned stamp, which is then simply pressed onto the surface to transfer the catalyst to the surface. No pattering was seen from any of the attempts using micro–contact printing. The major problem seemed to be that once the catalyst had dried on the stamp, it would not be transferred to the wafer when they were brought into contact. If the catalyst was not allowed to dry on the stamp, the contact printing would produce a smudged film of catalyst over entire the surface of the wafer. It should be said that this is a difficulty requiring some careful re–engineering, rather than an unsolvable problem with micro–contact printing.

An alternative, simple approach to patterning the catalyst is embossing. In this technique, shown schematically in Figure 6.14, a small amount of the catalyst dispersion (iron nitrate, and either magnesium carbonate or magnesium oxide) is placed on the wafer surface. Then, a patterned poly(dimethylsiloxane) (PDMS) stamp is placed on top so that the liquid catalyst is forced to take up the void spaces in the pattern. Once dry, the stamp is removed and the patterned catalyst is exposed. Stamps with 100 μm wide lines and 100 μm wide gaps were used. It was found that if ethanol was used as the solvent, it dried too fast and it was difficult to pattern, so the catalysts were dispersed in water instead. Once the wafer was patterned with catalyst, it was used in CVD with the same conditions as before (Section 6.2) without calcination.

The PDMS stamp used was prepared by Iris Coe from the School of Physics in the University of Edinburgh (for details see Reference 40). The PDMS stamp was made by replica moulding of a master that was patterned with the desired. Briefly, a silicon wafer was covered in photoresist and patterned using traditional lithography to form the master for the stamp. Then, a PDMS pre–polymer was poured over the surface of the master. Once the polymer had been cured and become solid, it was simply peeled off the master to give the PDMS stamp.

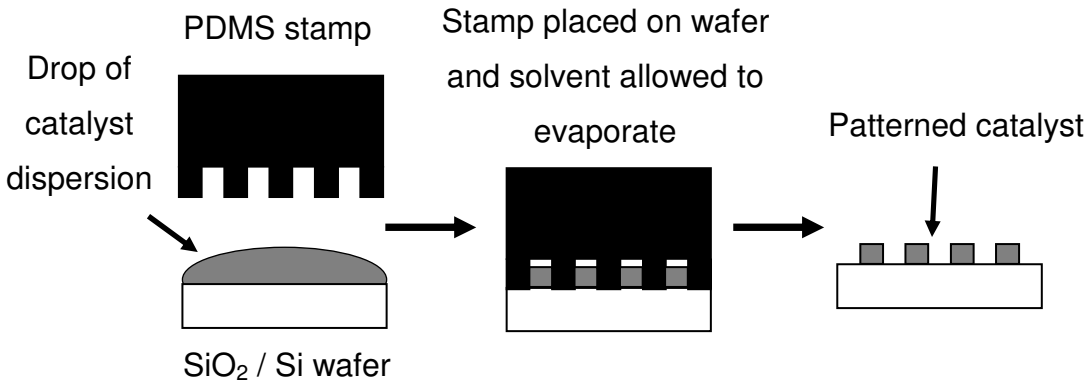

Figure 6.14. Schematic diagram of patterning of the catalyst using embossing with a PDMS stamp. A drop of the catalyst dispersion is placed on the wafer. The PDMS stamp is then placed on top so that the dispersion is forced into the voids of the stamp's pattern. The solvent is allowed to evaporate so that the catalyst is deposited on the surface of the wafer. The stamp can then be removed to leave the patterned catalyst.

6.3.1 Raman spectroscopy

Figure 6.15 shows the Raman spectra collected for the carbon deposited on the patterned magnesium carbonate catalyst. The presence of the D and G bands indicates the growth of some carbon, although the large D bands indicate that it is not well graphitized, and the lone RBM suggests that *some* SWNTs are present on the catalyst. Calculation of the I_D / I_G was made impossible by the presence of peaks attributed to the MgO support, and the large background to the spectra attributed to fluorescence of the sample. Comparison with the spectra of the patterned MgO nanopowder catalyst, shown in Figure 6.16, suggests that the MgO catalyst produced better tube growth. These spectra show that the tubes formed are well graphitized and, although not all the spectra have RBMs, their presence suggests the presence of

SWNTs on the catalyst surface. The average I_D / I_G calculated for the patterned MgO catalyst was 0.17, which is larger than the tubes grown on the dip–coated wafer (I_D / I_G = 0.11). The spectra collected do show much greater variation in the RBMs present, compared to with MgO catalyst in Section 6.2. The greater variation is probably due to the smaller amount of catalyst on the embossed wafer, giving a less dense growth of CNTs. By a similar argument to that in Section 6.2.1, each Raman spectrum will sample a different collection of tubes. The smaller amount of catalyst used also explains the greater intensity of the silicon peaks compared to the dip–coated MgO catalyst sample. There are several spectra of the patterned catalyst that show the presence of MgO peaks, which are found in the spectrum of pure MgO.

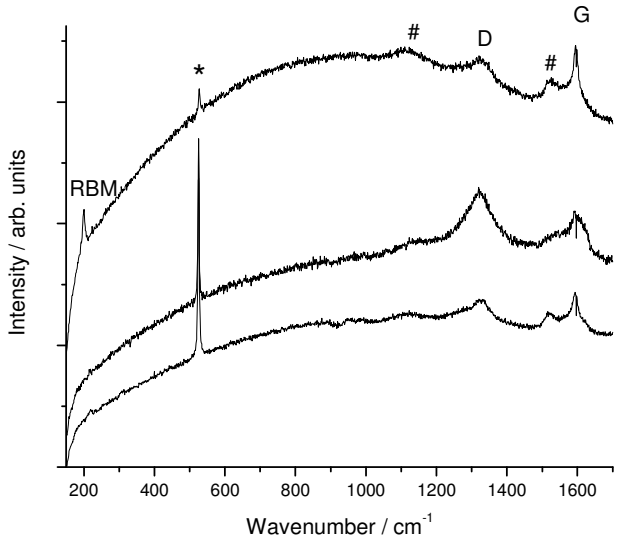

Figure 6.15. The spectra collected from different areas of the growth on the patterned $Mg(CO_3)_2$ catalyst suggest poor quality tube growth due to the large D bands observed and large fluorescence (broad background). The presence of a radial breathing mode (labelled RBM) does at least indicate that there are *some* SWNTs grown on the sample. Note that (#) is assigned to MgO, and (*) to SiO_2.

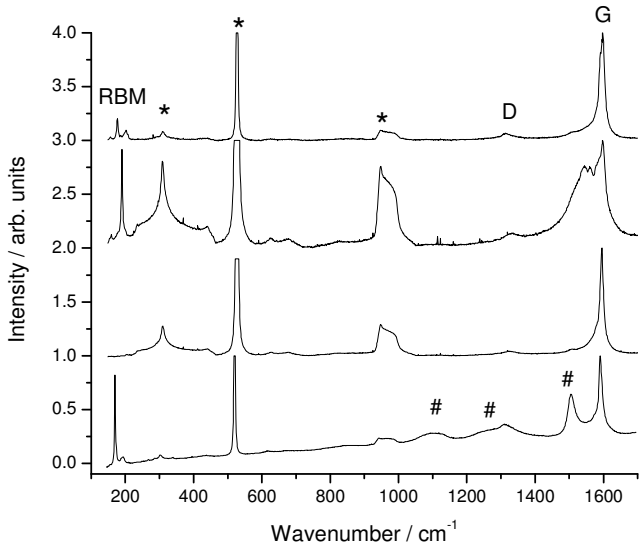

Figure 6.16. Raman spectra from patterned MgO catalyst on SiO_2 wafer. The small D bands in all spectra show that well graphitized, high quality tubes were produced. Some RBM peaks are also very intense. Note that (#) is assigned to MgO, and (*) to SiO_2.

In general the patterned samples grew fewer tubes than the dip–coated samples. It is difficult to judge whether the difference in growth is simply proportional to the amount of catalyst dispersed on the surface, or whether there are other factors. For example, it has been suggested that the catalyst, in addition to being the site for tube growth, also plays a part in "conditioning" the precursor gas.[41] This conditioning is described as catalytically forming different species, e.g., radicals, in the precursor gas that in some way improves the nanotube formation. For example, the growth of tubes during CVD has been seen to improve when the precursor gas was first passed over a heated Fe / Mo catalyst supported on Al_2O_3, before it went on to deposit carbon on a second Fe / Mo / Al_2O_3–supported catalyst that had been prepared by a sol–gel method.[41] It was suggested that the formation of benzene from the methane precursor gas was responsible for the improved growth.[41] If the catalyst used here performs this secondary function of conditioning, then it would be expected that the amount of C deposited would not simply depend on the amount of catalyst on the surface: the growth of the tubes could also be affected by the way the precursor gas flows over the catalyst.

6.3.2 Scanning electron microscopy

Magnesium carbonate sample

Scanning electron microscope images from the patterned carbonate catalyst are shown in Figure 6.17. At low magnification, it appears that the surface of the sample is patterned in lines of catalyst that are less than 100 μm wide. However, on closer inspection it can be seen that the apparent lines are made up of isolated aggregates of catalyst. As the magnesium carbonate, or any MgO formed from it, cannot melt at the temperatures used in the CVD, we conclude that the carbonate particles from the dispersion aggregate together to form these lines during drying. Even though the lumps are arranged in apparent lines, there are also areas where the distribution of lumps appears random. In addition, the thickness of the lines (the size of the aggregates) varies from line to line, and along the lines. This variation is probably to due to differences in the concentration of catalyst in the dispersion across the sample.

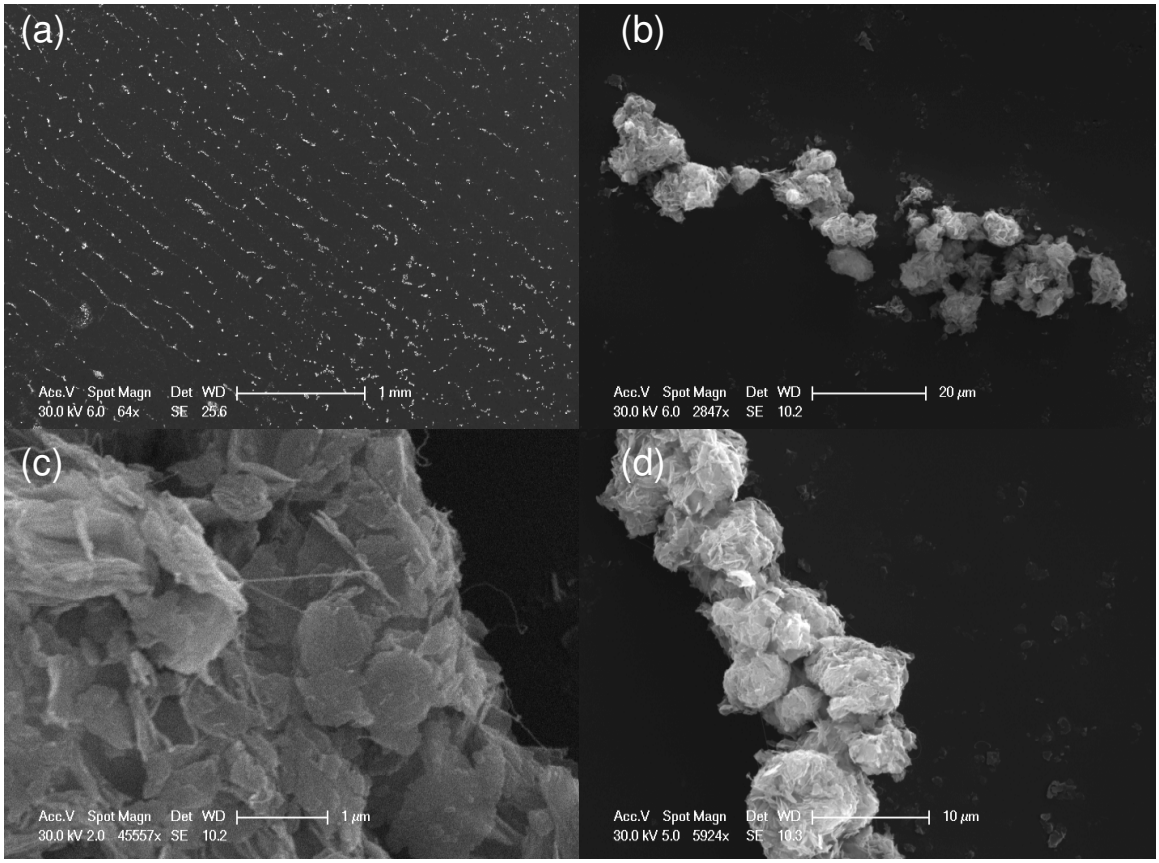

Figure 6.17. Lines of catalyst can be seen in (a) which have been formed by the embossing technique. However it can be seen that the apparent lines are made up of lumps of catalyst (b). These clumps have sparse growth of CNTs on them (c).

Higher magnification images of the patterned magnesium carbonate catalyst agree with the conclusion drawn from the Raman spectroscopy: that few nanotubes had grown on the catalyst. As can be seen in Figure 6.17 (c) only very few tubes are visible on the surface of the catalyst.

Magnesium oxide sample

Inspection of the patterned MgO catalyst after CVD, showed there were some areas of the wafer that appeared to have the 100 μm wide stripes of catalyst, shown in Figure 6.18 (a), corresponding to the pattern of the PDMS stamp used. However, as can be seen at the right of Figure 6.18 (a), the patterning is not continuous over the surface. The stripes of catalyst in the patterned areas show variations in the amounts of catalyst along their lengths. As discussed above for magnesium carbonate, this is probably due to the variation in concentration of MgO in the dispersion across the surface. At greater magnification, Figure 6.18 (c) and (d), it is possible to see that the rough surface of the catalyst areas is made up of agglomerates of the catalyst. Some growth of tubes is visible in the areas with small amounts of catalyst, Figure 6.18 (c). Areas with more catalyst have more visible tubes on the surface.

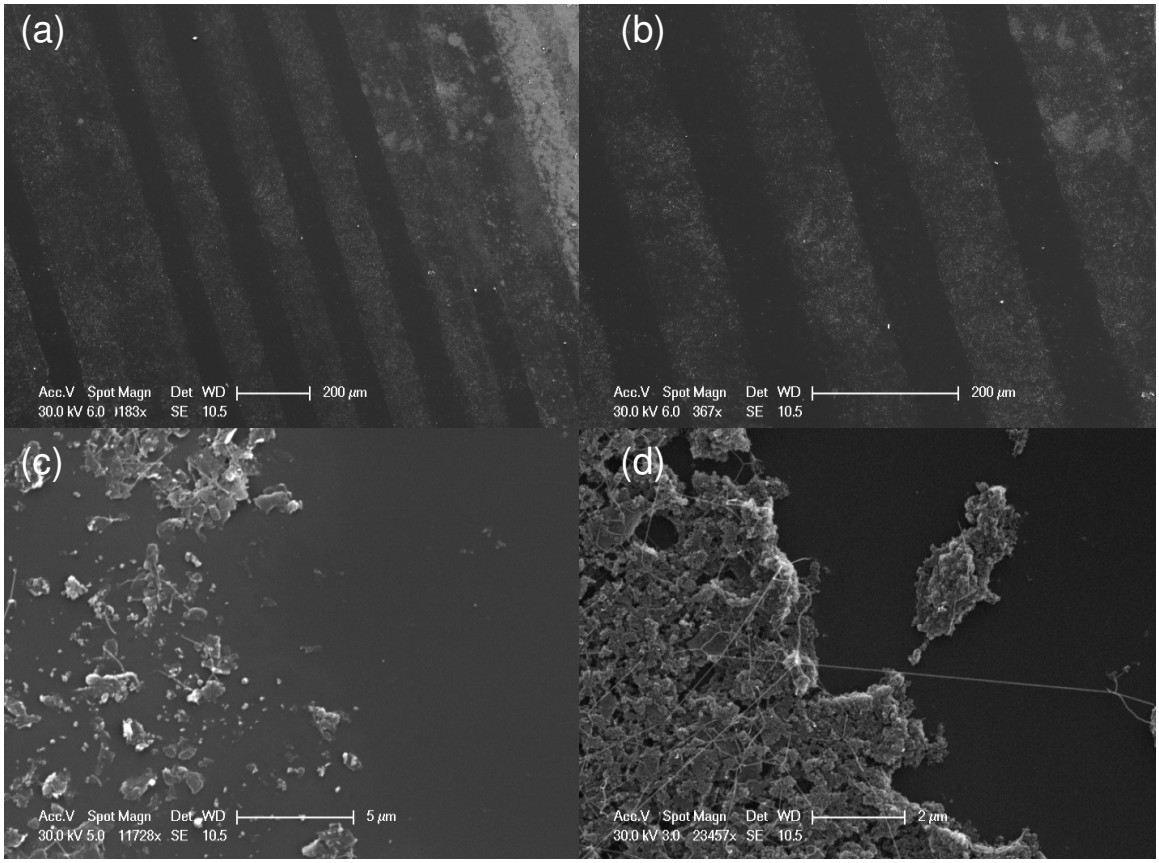

Figure 6.18. MgO patterned catalysts. Areas of patterning of the catalyst could be observed on the wafer (a). In the void areas between the lines of catalyst there was some spots of MgO observed (b). There was also variation in the amount of MgO deposited in the lines (c) and (d). As might be expected, there was greater growth of tubes on the areas with more catalyst.

6.3.3 Comparision of embossed catalyst samples

From the Raman spectroscopy, and the SEM images of the growth on the two patterned catalyst samples, it seems clear that the magnesium oxide catalyst gives better growth of tubes. In fact, the small D bands of the Raman spectra of the sample with the MgO catalyst show that the SWNTs produced are very well graphitized. The growth of tubes on the carbonate catalyst has been adversely affected by the patterning compared to the sample prepared by dip–coating. This difference is either due to the morphology of the catalyst produced, or that there is only a small amount of catalyst present on the surface, which may have lowered the "conditioning" of the precursor gas. The SEM images of the patterned samples show that the carbonate catalyst has formed compact aggregates, while the MgO nanopowder has formed

extended flat areas of catalyst. The better growth could be related to the greater surface area of the MgO nanopowder catalyst, as shown in Table 6.3.

Although, the SEM images suggest that carbonate showed patterning over a greater area than the MgO, it also showed the pattern formed was irregular, and was a less–faithful copy of the stamp than the patterned areas of the MgO nanopowder. We suggest that there is still scope for optimising the MgO nanopowder system. The embossing approach was very basic indeed, with the samples being prepared by hand. A more sophisticated setup in which, for example, the pressure applied to stamp could be controlled, would likely improve the patterning. Also the use of different solvents and additives such as polymers or surfactants, which could be used to direct the formation of the catalyst areas, could also be explored.

6.4 Extended calcinations to improve nanotube growth

It has been reported in the literature that the growth of nanotubes on catalysts, composed of Fe on MgO, can be improved by calcining the catalysts in air for extended periods of time (*e.g.*, 10 hours at 950 °C).[17] The long calcination is thought to produce a solid solution of the inverse spinel $MgFe_2O_4$ in the MgO. Under the CVD conditions, the $MgFe_2O_4$ is reduced by the methane precursor to form well–dispersed metal particles on the surface, which can go on to the form the SWNTs: see Figure 6.1.

The formation of $MgFe_2O_4$ in the MgO solid solution has not been previously used in the rational design of catalyst systems.[17] In order to see if the calcination step could be used to enhance the growth of tubes on catalysts dispersed on surfaces, dip–coated wafers as described in Section 6.2 were calcined in air at 950 °C for 10 hours. The wafers were then exposed to the same CVD conditions as previously described (Section 6.2). After the CVD, the samples, Figure 6.19, were seen to be less blackened compared to the samples prepared in Section 6.2, shown in Figure 6.2. The lighter shades suggest that less carbon has been deposited.

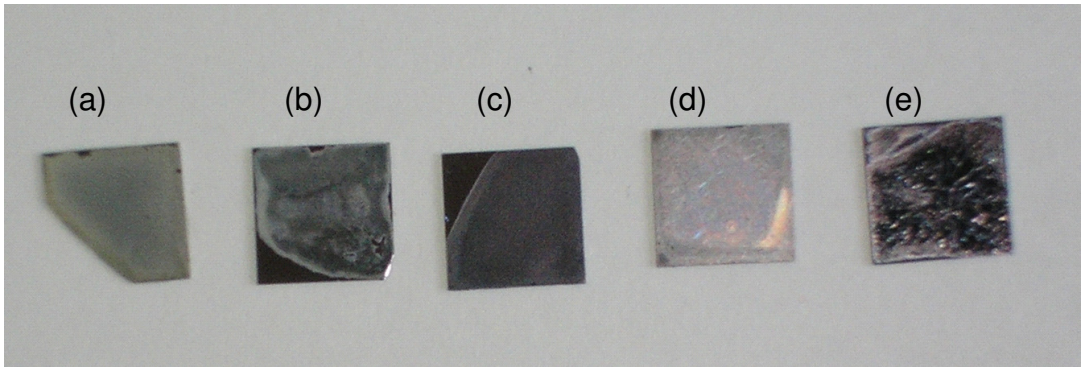

Figure 6.19. Wafers were prepared by dipping them into a solution or dispersion of a magnesium compound with iron nitrate. The wafers were then calcined for 10 hours in air at 950 °C before CVD. The magnesium compounds used were the same as in Section 6.2: these were carbonate (a), nitrate (b), oxide nanopowder (c), acetate (d), and stearate (e). Comparing the samples shown in Figure 6.2 and those shown here, it seems that the samples shown here are less black. The lighter shades, especially for the carbonate and oxide samples, suggest that extended calcination has reduced the amount of tube growth.

6.4.1 Raman Spectroscopy

As can be seen from the Raman spectra presented in Figure 6.20 all the samples showed growth of well graphitized carbon, and the presence of the RBMs at low wavenumbers indicates the presence of single–walled nanotubes. The average I_D / I_G ratios, presented in Table 6.4, all have around the same value, which indicates that the same quality of tubes is being produced by each catalyst. Not all the spectra collected could be used to calculate the average I_D / I_G ratio, as some of them had large fluorescence backgrounds as well as interfering peaks attributed to the MgO. The acetate and stearate samples showed MgO peaks and fluorescence more often than for the other samples.

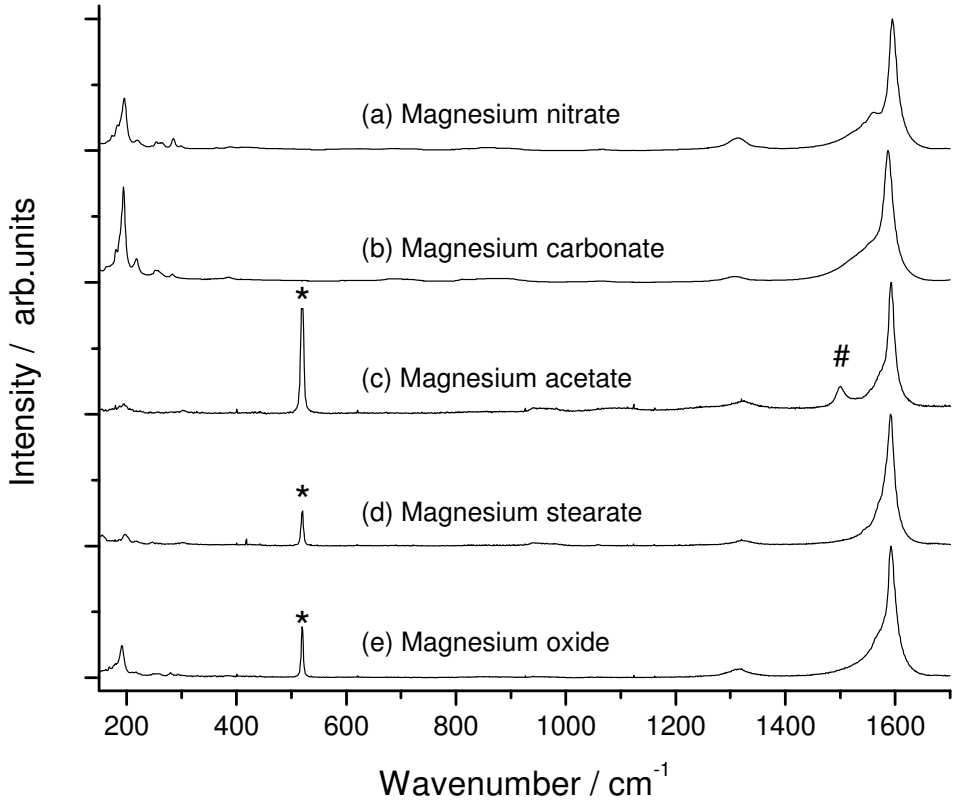

Figure 6.20. All the samples that were calcined for 10 hours show very well graphitized tubes. Here the spectra with smallest D bands are presented, and all are normalized to the G band.

Magnesium compound	Average I_D / I_G ratio		
	Calcined 10 hours	Calcined 30 minutes	Uncalcined
Magnesium carbonate	0.07	0.15	0.09
Magnesium acetate	0.11	0.46	0.99
Magnesium oxide nanopowder	0.14	–	0.06
Magnesium nitrate	0.14	0.88	0.45
Magnesium stearate	0.15	0.35	1.43

Table 6.4. The average I_D / I_G ratios for the samples show that well graphitized carbon has been deposited on the samples during the CVD. Some of the spectra had large peaks, attributed to the MgO, and fluorescence that made the estimation of the I_D / I_G ratio for the spectrum inaccurate. Such spectra were ignored for the purposes of calculating the average I_D / I_G ratio.

It is interesting to note that the RBM region of the spectra of the 10 hour calcined magnesium nitrate sample, shown in Figure 6.21, were much more similar to each other than the spectra for the 30 minutes calcined samples, shown in Figure 6.4(b). This greater consistency in the RBMs observed in the Raman spectra suggests much improved growth of SWNTs on the nitrate sample (for the rationale, see Section 6.2.1). This is in spite of the lighter shade of the sample compared to the uncalcined and 30 minute calcined samples, which suggest that less carbon was deposited in total. The spectra from the oxide and carbonate samples also show consistency in the RBMs present, while the acetate and stearate show greater variations.

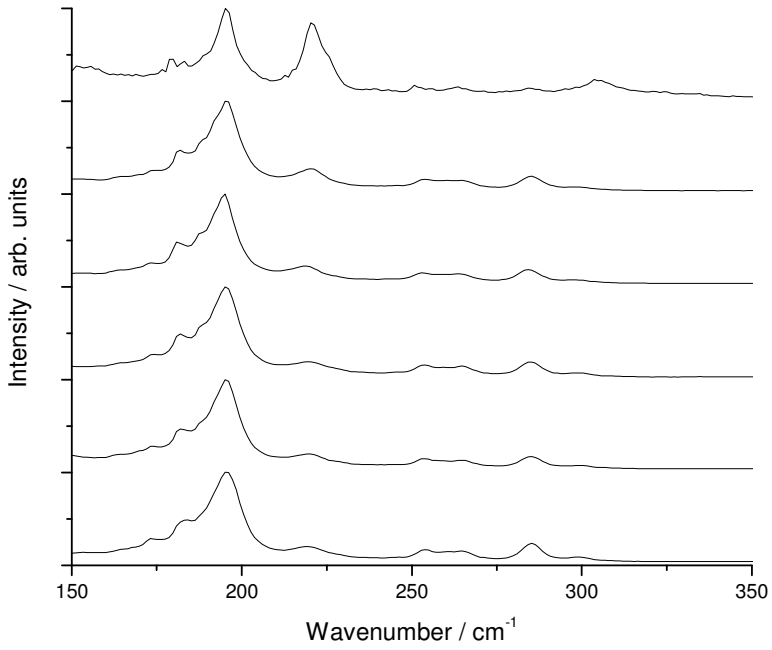

Figure 6.21. RBMs present in the spectra collected at different points across the 10 hour calcined nitrate sample show more consistency than for the previous nitrate samples, shown in Figure 6.4 (b).

It was observed that longer calcination times changes the diameters of tubes present in the sample. Figure 6.22 shows the low wavenumber region of the Raman spectrum of the 10 hour calcined sample and the uncalcined sample for the magnesium oxide nanoparticle catalyst. It can be seen that there are RBMs with higher wavenumbers present in the spectrum of 10 hour calcined sample. Similar peaks are seen in the 10 hour calcined samples of the nitrate and the carbonate (not shown). As the wavenumber of a RBM (ω_{RBM}) is related to the diameter of the tube (d_t) from which arises, we can estimate the range of diameters present in a sample using the empirically derived relation shown in Equation 6.3.[24]

$$d_t / \mathrm{nm} \approx \frac{248}{\omega_{RBM} / \mathrm{cm}^{-1}} \qquad \textbf{(6.3)}$$

Table 6.5 shows RBMs observed, and the corresponding range of diameters calculated using Equation 6.3. Although, it is reasonable to assume that only some of

the tubes present are in resonance with the excitation laser,[23] the relative changes in the spectra for a given catalyst are likely to be indicative of the changes in the overall distribution of tube diameters. It can be seen that all the 10 hour calcined samples have ranges that extend to smaller diameters of tubes. Similar findings by other groups[16,17] have been explained in terms of diffusion of Fe atoms into the MgO support to form $MgFe_2O_4$, leaving smaller surface iron nanoparticles. It has been largely established in the literature that the size of the nanoparticle determines the diameter of the nanotube formed form it.[6,8] Variations in the RBMs present in the Raman spectra of the stearate and acetate samples meant that it was not possible to confirm the trend for these samples.

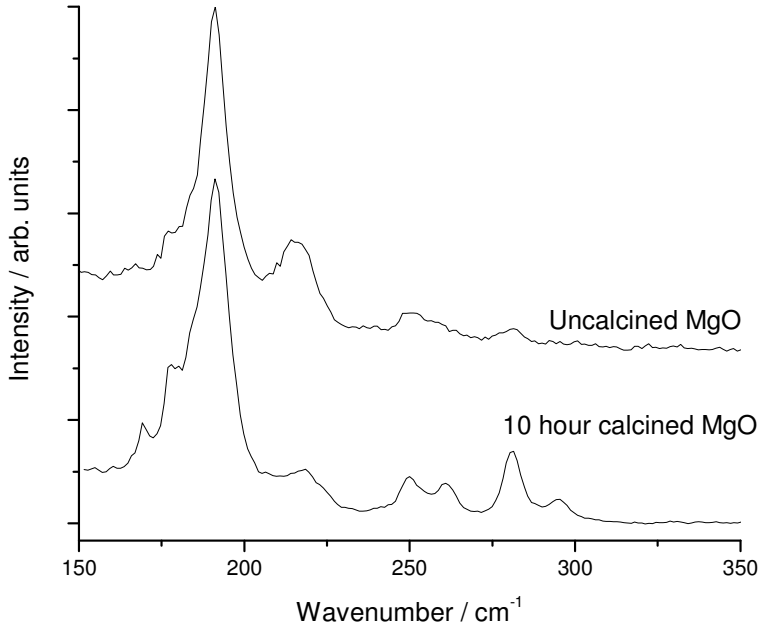

Figure 6.22. The 10 hour calcined MgO sample can be seen to have higher wavenumber RBMs than the uncalicined sample. These RBMs suggest the presence of thinner tubes. The long calcination may have promoted the formation of smaller nanoparticles than the uncalcined sample.

Magnesium compound	Calcination time	RBMs / cm^{-1}	Diameter range / nm
Magnesium nitrate	30 mins	148, 169, 174, 178, 180, 188, 192, 212	1.2 – 1.7
	10 hours	173, 181, 187, 185, 219, 253, 264, 284	0.9 – 1.4
Magnesium carbonate	30 mins	160, 178, 186, 192, 215, 253	1.0 – 1.6
	10 hours	179,186, 193, 215, 252, 256, 282	0.9 – 1.4
Magnesium oxide nanopowder	Uncalcined	167, 177, 191, 215, 250, 280	0.9 – 1.5
	10 hours	178, 191, 217, 250, 260, 281, 295	0.8 – 1.4

Table 6.5. The wavenumbers of the radial breathing modes that are present in the spectra of each sample are shown. The ranges of diameters present in the sample were calculated using Equation 6.3. It can be seen that the 10 hours calcined samples all have small diameter tubes that are not present in the other samples. The formation of the small tubes suggests that smaller nanoparticles have been formed on the 10 hour calcined catalyst, perhaps due the formation of $MgFe_2O_4$.

6.4.2 Scanning electron microscopy

Magnesium oxide sample

The surface of the magnesium oxide sample, Figure 6.23(a), appears similar to the uncalcined sample (*c.f.* Figure 6.6) in that the surface of the catalyst has broken up into islands: it appears that the long calcination has made the catalyst contract more. The catalyst islands in Figure 6.23 (b) have become rounded at the edges, with the sides of the island rising up off the wafer. These effects could have been caused by the sintering of the catalyst. Several very long bundles of tubes were observed bridging the islands of catalyst. One of these bundles, shown in Figure 6.24, was found to be around 150 μm in length. The length of the bundles may be related to the

morphology of the catalyst. Large gaps between the islands of catalyst may allow the uninterrupted growth of tubes between areas of catalyst. It could also be argued that bundles of this length are present in other samples, and it is the morphology of the catalyst that allows these long bundles to be seen in the image because they can grow straight rather than being coiled. As shown in Figure 6.23 (d), the surfaces of the catalyst islands are covered in tubes, as was observed for other MgO samples (Figure 6.6).

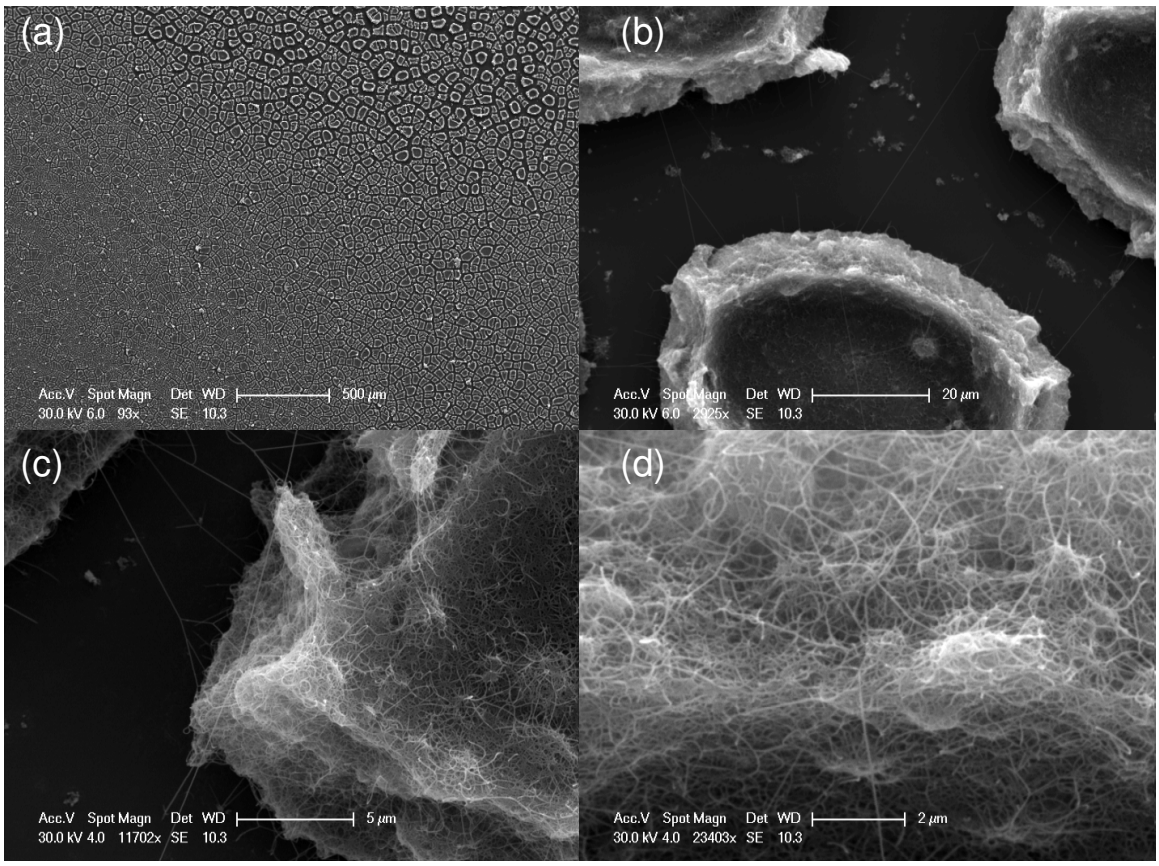

Figure 6.23. SEM images of the 10 hour calcined MgO nanopowder sample shows the catalyst broken up into islands (a). Bundles of tubes can be seen bridging between the islands (b). The surface of the catalyst islands can be seen to be thickly covered in tubes, (c) and (d).

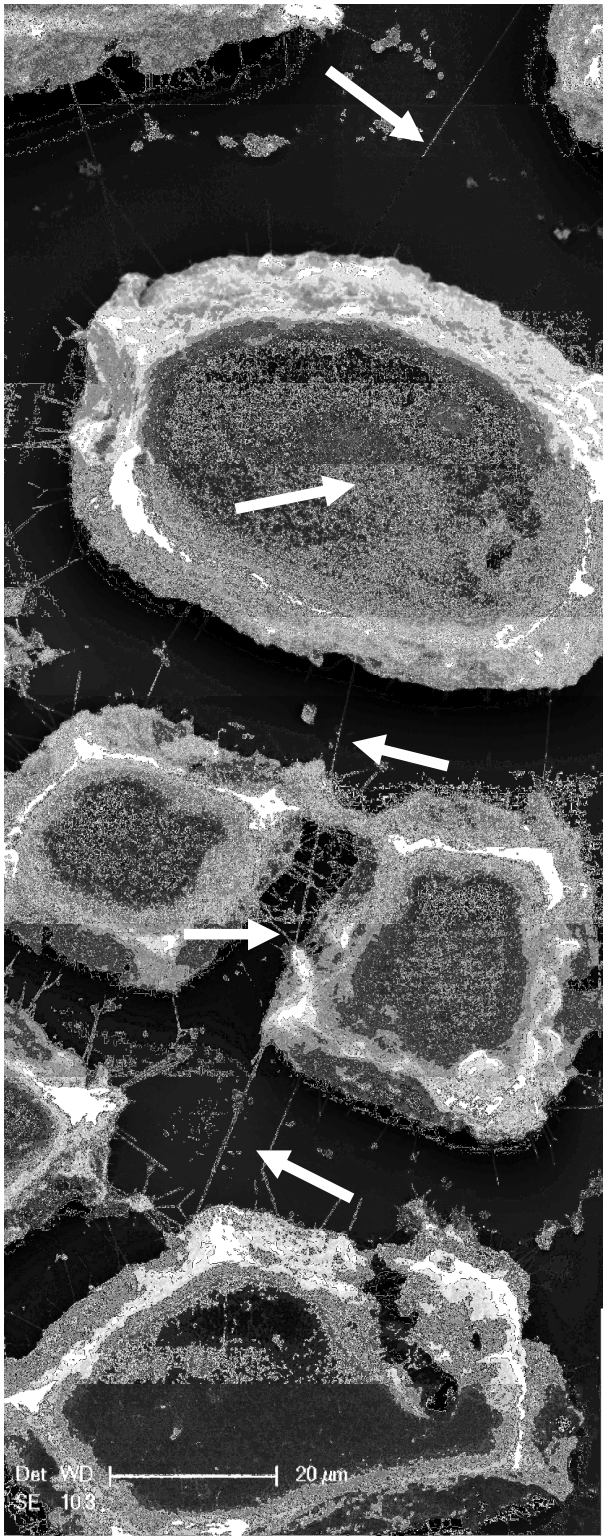

Figure 6.24. A very long bundle of tubes can be seen growing on the 10 hour calcined MgO catalyst. The formation of the long bundles may have been aided by the morphology of the catalyst or it may simply be easier to image them, as they can grow straight and alone rather than coiled as part of a mat of tubes.

Magnesium carbonate sample

The surface of the magnesium carbonate catalyst is also seen to be covered in cracks, Figure 6.25 (a); however, it has not formed in well separated islands like the MgO. Particles like these were not observed in either of the previous magnesium carbonate samples (Figure 6.5). We suggest that these particles are encouraged to form by the long calcination, which allows the sintering of smaller particles to form larger particles.

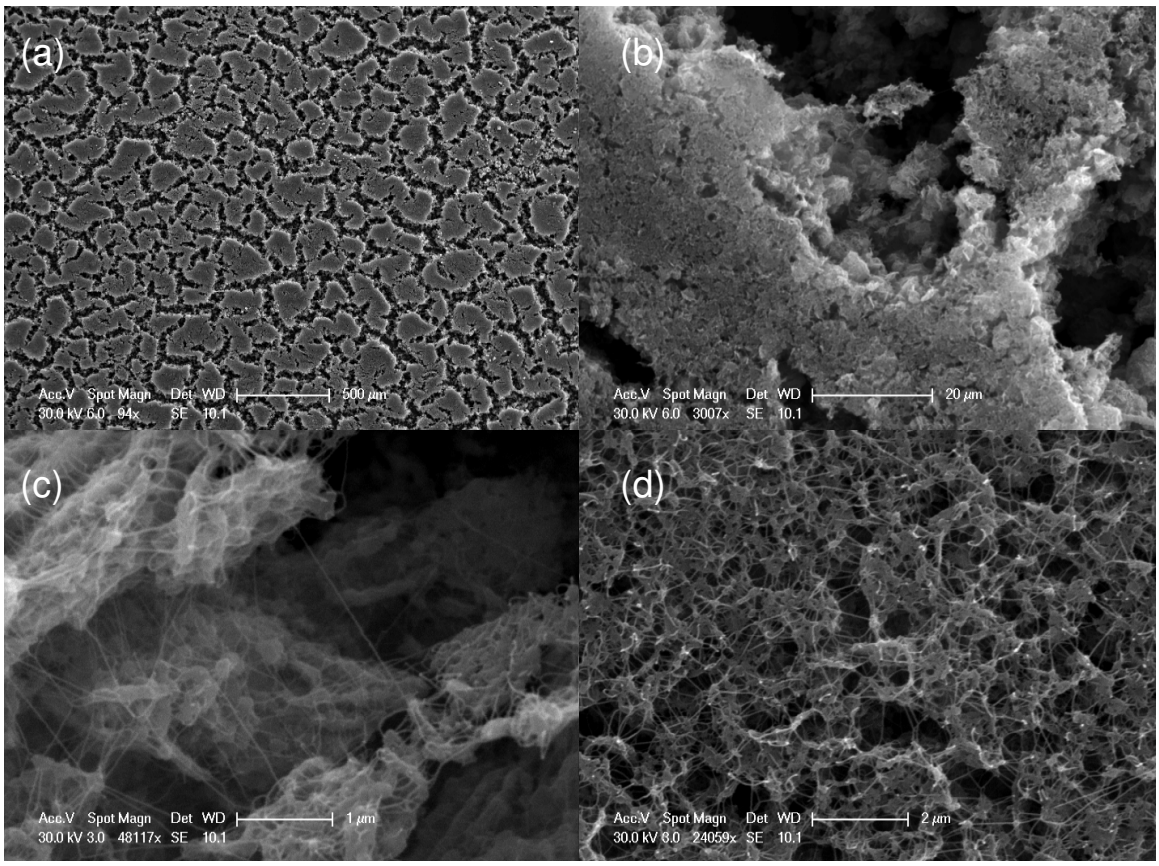

Figure 6.25. SEM shows the surface of the 10 hour calcined carbonate catalyst to be covered in cracks (a). Bundles of tubes can be seen growing over particles of the support (c). The surface of the catalyst is covered in bundles of tubes (d).

Magnesium nitrate sample

The nitrate sample that was calcined for 10 hours, Figure 6.26(a), appears to be similar by SEM to the sample that was calcined for 30 minutes (Figure 6.8(a)) in that the surface is covered by a layer of the catalyst. However, the sample that was calcined for longer appears to have smaller cracks in the surface. This sample has

several areas with different amounts of growth on it. Dense growth can be seen in Figure 8.26(b), while few tubes can be seen in Figure 8.26(d). As in most of the samples, more tubes can be seen around cracks in the surface of the catalyst.

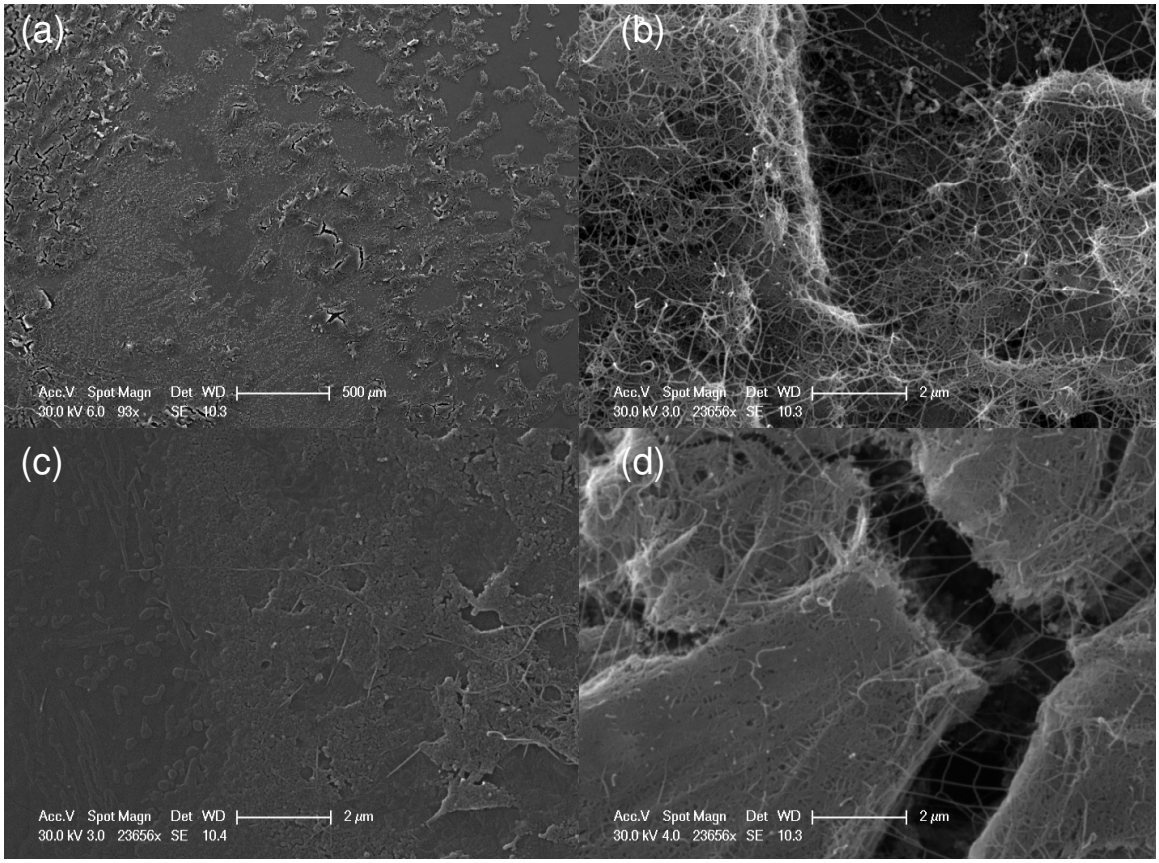

Figure 6.26. SEM images of the 10 hour calcined nitrate samples revealed that the surface of the catalyst was composed of different areas, some of which showed dense growth of tubes (b) while others showed fewer tubes on a smooth surface (c). Better growth of tubes was observed around cracks in the catalyst surface.

Magnesium acetate and stearate samples

The acetate and stearate samples appear to be similar to the samples with shorter or no calcination. The 10 h calcined acetate sample exhibits the distinctive straight lines on the surface, Figure 6.27 (a) and (b), that were seen in the SEM of the previous samples, Figures 6.9 and 6.10. In contrast, however, it can be seen that these lines are *trenches* between areas of catalyst. It is not immediately obvious how these—quite striking—structures were formed. As discussed in Section 6.2.2, the trenches do appear similar to shrinkage fracture patterns that could form while the catalyst is contracting: either due to the acetate changing to the oxide, or thermally as the

sample cools. There are several examples of trenches meeting at right angles that are visible in 6.27(b). When a crack forms, the stress in the solid perpendicular to the crack is decreased, so that new cracks tend to form in a different direction. Cracks meeting at right angles are commonly found in shrinkage fracture patterns in homogenous materials.[30] A crack will continue to grow in a straight line until it meets another crack or an area of the material with higher strength. The edges of the trenches, shown in Figure 6.27(c), have more structure that seems somewhat similar to the edges of the catalyst islands in the MgO nanopwder sample shown in Figure 6.23. Good growth of tubes for the 10 hour calcined acetate sample is observed across the catalyst, possibly aided by the greater number of cracks in the catalyst.

SEM showed the 10 hour calcined stearate sample to be very similar to the damaged structure seen for all the stearate samples (Figures 6.11 and 6.12).

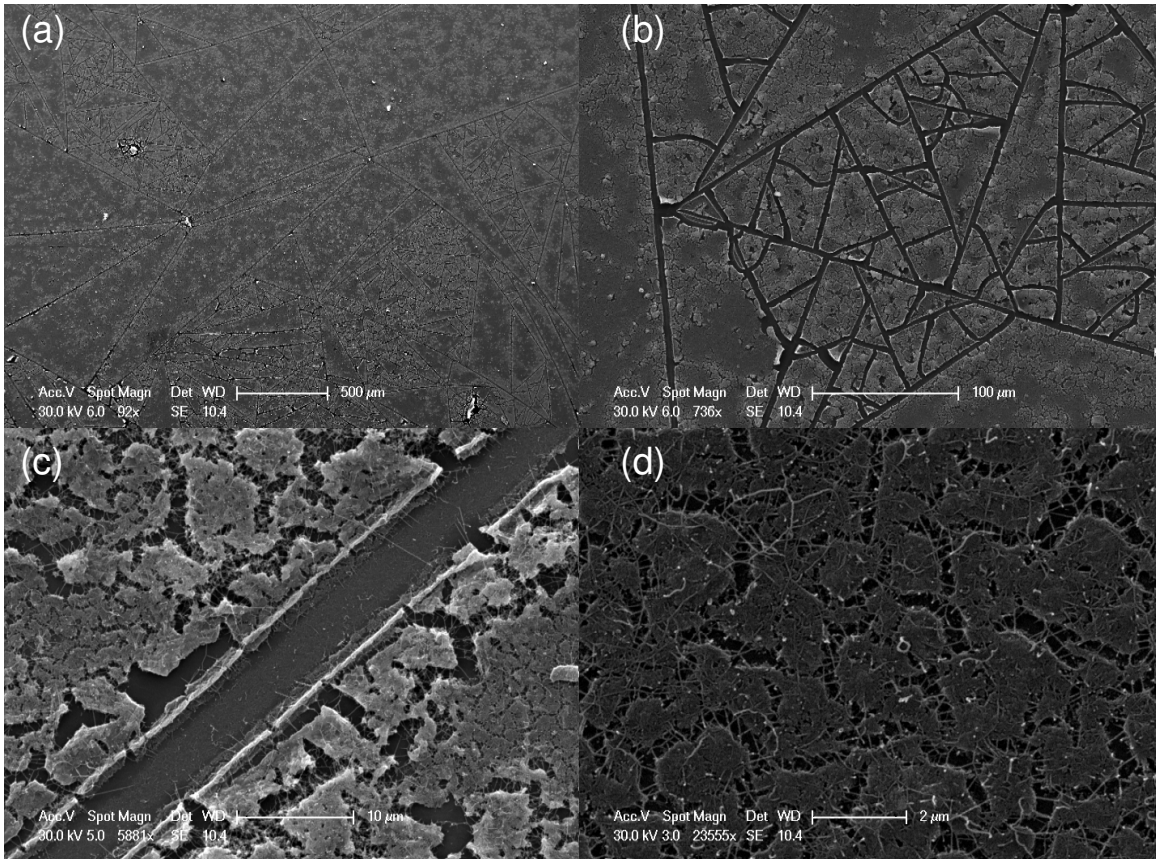

Figure 6.27. SEM images of the 10 hour calcined acetate sample show features similar to those shown in the SEM images of the other acetate samples (Figures 6.9 and 6.10). The long lines that divide up the surface of the wafer can be clearly seen (a). However, in the 10 hour calcined acetate sample, these lines are clearly seen to be cracks between the areas of catalyst. The surface of the catalyst is covered in tubes, which is perhaps due to the greater number of cracks on the surface of the catalyst.

Summary of SEM of 10 h calcined samples

In general, the SEM images of the 10 hour calcined samples show greater growth of nanotubes for the compounds that gave poor growth in Section 6.2: the nitrate, acetate and stearate. Growths on the carbonate and oxide samples appear similar to those obtained with shorter calcining time. Comparing the SEM images for samples of a particular compound, it appears that the samples that underwent the 10 hour calcination have the "roughest" surfaces. The surfaces of these samples appear most cracked.

6.4.3 Formation of $MgFe_2O_4$

The I_D / I_G ratios of the all samples (Table 6.4) show that the long calcination step appears to improve the quality of SWNTs grown on all the catalysts except for the MgO nanopowder, which does not change a great deal. This improvement in the quality of the tubes may be due to the formation of the $MgFe_2O_4$ / MgO solid solution, but it may also be due to physical differences in the morphology of the catalyst formed. The SEM images do show that the surfaces of samples that were calcined for 10 hours appear rougher, with more cracks than the samples prepared in Section 6.2.

Before the samples underwent CVD, Raman spectroscopy was used to try to identify if $MgFe_2O_4$ was present in the catalyst. Raman spectroscopy has been used to identify $MgFe_2O_4$ in MgO previously, as Fe and MgO have several uses in heterogeneous catalysis such as ammonia synthesis.[42,43] All the spectra that we obtained were similar to our spectrum of pure MgO. No peaks expected for $MgFe_2O_4$ were found in any of the calcined samples' spectra. However, the literature suggests that $MgFe_2O_4$ may not be detectable by Raman or x–ray diffraction for samples where the % w/w Fe was less than 3%:[43] therefore, the presence of the $MgFe_2O_4$ in our samples can not be excluded. As discussed in 6.2, the formation of smaller diameter tubes in the 10 hours–calcined samples may be explained by the formation of $MgFe_2O_4$.

To establish if the formation of the $MgFe_2O_4$ phase could be identified in samples exposed to the long calcination step, several wafers were prepared with the magnesium nitrate, carbonate, and oxide in the same way as those in Section 6.2, but with larger amounts of iron nitrate added. The amount of iron nitrate in the dispersion or solution was increased to give 3% Fe w/w for the final catalyst. All spectra appear similar to that of the pure MgO. Some of the magnesium nitrate spectra, however, do show peaks that are known for $MgFe_2O_4$.[43] Figure 6.28 shows an expanded section of Raman spectrum for the magnesium nitrate sample. The top spectrum shows the characteristic peaks for $MgFe_2O_4$ at 219, 334, 486 and 711 cm^{-1} as compared to the values of 217, 333, 486, 715 cm^{-1} that were taken from the literature.[42] The presence of peaks attributable to $MgFe_2O_4$ shows that this mixed metal oxide *can* form during the calcination of the catalysts.

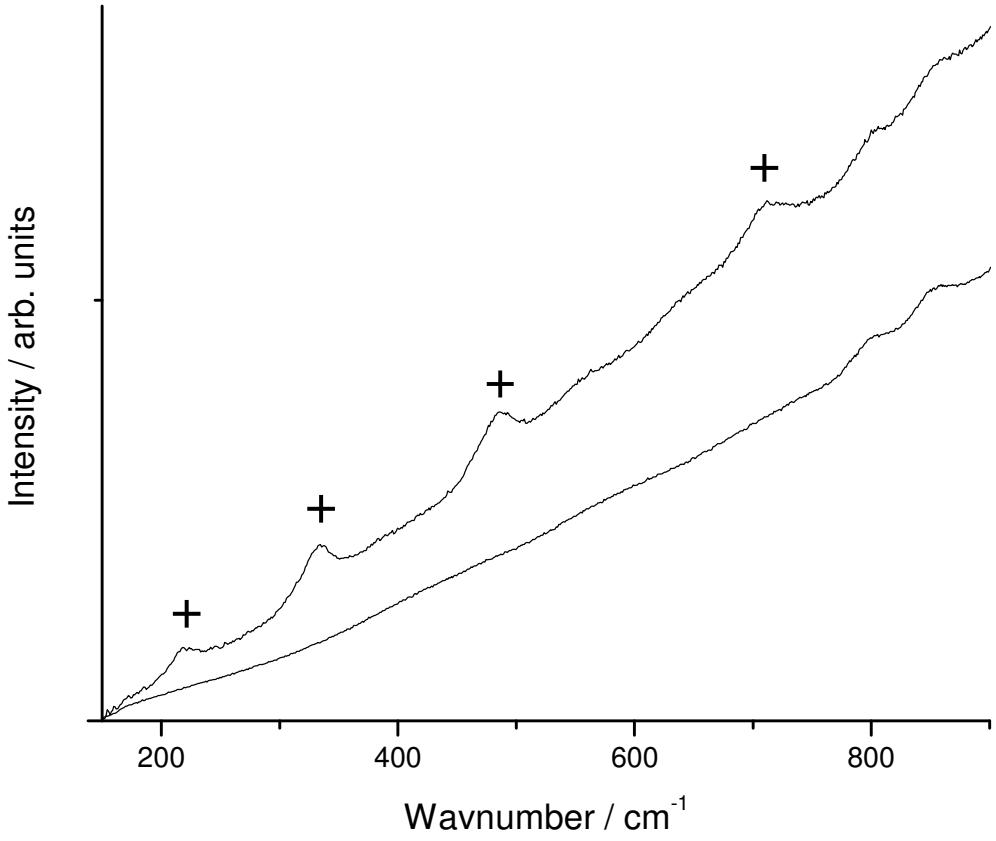

Figure 6.28. The plus symbols (+) show the peaks that are known for $MgFe_2O_4$. Their presence indicates the formation of $MgFe_2O_4$ in the magnesium nitrate sample during the 10 hour calcination. The lower spectrum was collected from the same sample, but in a different region, and shows no evidence for the peaks.

6.5 Conclusions

There were two aims in this work. The first was to investigate the use of different magnesium compounds in catalysts for carbon nanotube growth that could be dispersed onto a surfaces as liquids. The second was to investigate whether long calcination of such catalysts, which are thought to produce solid solutions of $MgFe_2O_4$ in MgO, could be used to improve the quality of the tubes formed.

The growth of carbon nanotubes onto catalysts, formed from iron nitrate and different magnesium compounds dispersed on SiO_2 surfaces, was studied by Raman spectroscopy and SEM. Tube growth was observed to improve with surface area as determined by surface adsorption measurements. From the SEM, it appears that rough surfaces with lots of edges also appear to increase growth compared to flat, smooth surfaces. The melting point of the magnesium compound was found to be vital. If the melting point is lower than the CVD temperature, the particles of the liquid catalyst can flow together to form a smoother, low surface–area catalyst, which is less suitable for growth. The magnesium compounds that were found to produce the best growth of nanotubes were the magnesium carbonate and the magnesium oxide nanopowder.

The carbonate and oxide catalysts were both used to produce surfaces patterned with catalyst by embossing. Both surfaces produced nanotubes in pre–defined places when exposed to CVD. Raman spectroscopy showed that the magnesium oxide sample grew highly graphitized tubes that were of better quality than those produced on the magnesium carbonate sample.

To investigate the effect of long calcinations on the growth of tubes on a surface, samples were prepared as previously, but calcined for 10 hours in air. Most of the samples that were calcined for 10 hours did show an improvement in the quality of growth by Raman spectroscopy. The formation of $MgFe_2O_4$ during the 10 hour calcination is suggested by the growth of tubes with smaller diameters that were not present in the samples that had been calcined for shorter time. In addition, peaks relating to $MgFe_2O_4$ could be seen in the Raman spectrum of the magnesium nitrate sample with 3% w/w Fe that was calcined for 10 hours. However, it is difficult to judge whether the improvement in growth was due entirely to the presence of the $MgFe_2O_4$, or if the changes in the morphology of the catalyst on the micron scale also improved the growth.

Appendix A. Experimental

A.1. Dip Coated Wafers

Ethanolic solution or dispersions of the magnesium compounds were prepared with the aid of an ultrasonic bath (Fisherbrand, FE 11002, Fisher Scientific, UK). The magnesium compounds were all obtained from Aldrich and used without further purification. Once the compounds had been dissolved or dispersed, the iron nitrate ($Fe(NO_3)_2$. $9H_2O$, Acros) was dissolved in a few ml of ethanol and added to the solution or dispersion of the magnesium compound while it was stirred magnetically. The details of the solutions and dispersions used are presented in Table A.1. The amount of ethanol added was determined either by the amount needed to dissolve the magnesium compound or to disperse it.

Sample	% Fe w/w of final catalyst	Mass of iron nitrate / g	Mass of magnesium compound / g	Volume of ethanol / ml
Magnesium nitrate	1	0.1	7.9	10
Magnesium carbonate	1	0.1	3.0	10
Magnesium stearate	1	0.025	4.6	35
Magnesium acetate	1	0.1	6.627	35
Magnesium oxide nanopowder	1	0.1	1.2	13
Magnesium nitrate	3	0.1	3.0	5
Magnesium carbonate	3	0.1	1.1	5
Magnesium oxide nanopowder	3	0.1	0.5	7

Table A.1. Details of the solutions or dispersions used for dip coating the samples.

Silicon wafer pieces 1 cm^2 with a 1 μm thick thermally grown oxide surface layer were rinsed in acetone (Fisher) and isopropanol (Fisher). They were then exposed to a mixed oxygen / argon plasma to ensure the removal of all organic residue from the surface (Plasma Etch Inc. Etcher PE-200, USA). Once clean, the wafers were simply dipped into a solution or dispersion of the magnesium compound and the iron nitrate. The excess liquid was removed by touching the wafer against the side of the beaker and then the wafer was allowed to dry in an oven 80 °C. The mass increase of a

wafer was too small to be measured using a standard analytical balance, indicating that less than 0.0001 g of catalyst mixture was deposited on the wafer.

Some wafers were used as prepared, while others were calcined. Two different calcinations were used. In one the wafers were kept at 600 °C for 30 minutes in air, while in the other they were kept at 950 °C for 10 hours in air.

A.2. Patterning of catalyst on wafer

Silicon wafer pieces, 1 cm^2, with a 1 μm thick thermally grown oxide surface layer were patterned with catalyst. The wafers were rinsed in acetone and isopropanol before use. Dispersions of the catalyst mixture were prepared as before with the carbonate and the oxide but with water instead of ethanol. Table A.2 shows the details of the dispersions used.

For the embossing, a PDMS stamp with 100 μm wide lines with 100 μm spaces was the used. The stamp had been fabricated by Iris Coe from the School of Physics at the University of Edinburgh. To pattern the wafers, 2 μl of the dispersion was pipetted onto the surface of the wafer then the PDMS was placed onto top pushed down. The wafer and stamp were placed in an oven at 80 °C to aid the evaporation of the water. Once the catalyst mixture was dry, the stamp was removed to reveal the patterned surface. The wafers then underwent CVD as for the dip–coated samples.

Sample	Mass of iron nitrate / g	Mass of magnesium compound / g	Volume of water / ml
Magnesium carbonate	0.015	0.45	3
Magnesium oxide nanopowder	0.016	0.21	14

Table A.2. Details of dispersions used for the patterning of the catalyst on the surface.

A.3. Chemical vapour deposition

CVD was carried out using the same setup as in Chapter 3 The wafers were placed in an alumina boat in the centre of the alumina work tube (1 inch diameter) of a furnace (MTF 12/38/250, Carbolite, UK). Gas–tight ends were attached that were connected to the gas handling system. The furnace then heated the wafers to 900 °C at a rate of 30 °C min^{-1} under a flow of 0.35 l min^{-1} of argon. Once the furnace had reached temperature the gas flows were changed to 1.35 l min^{-1} methane and 0.8 l min^{-1} hydrogen. After 30 minutes the gas flow was changed back to 0.35 l min^{-1} of argon, and the setup was allowed to cool to room temperature. The samples were removed after the furnace had cooled to below 200 °C. The wafers were then characterized with Raman spectroscopy and scanning electron microscopy (SEM).

A.4. Characterization

All samples were characterized with Raman spectroscopy (Labram 300, 632.8 nm, 13 mW, with collections typically 100 seconds) and SEM. Samples were prepared for scanning electron microscopy (SEM) by placing them onto a piece of carbon tape (a carbon sticky) that was affixed to a specimen stub. To ensure that the sample surfaces were conductive, they were covered with gold using a sputter coater.

Samples were imaged using a Philips XL30CP using the secondary electron detector with a typical working distance of 10 mm and a typical accelerating voltage of 30 kV.

Surface area measurements were carried out by Dr. Ronald Brown at the University of Edinburgh using Micrometrics Gemini 2360 (V5.00) instrument with N_2 gas at 77 K.

6.6 References

1) H. Dai. Carbon Nanotubes: Synthesis, Integration, and Properties. *Acc. Chem. Res*. 2002, **35**, 1035

2) C. Zhou, J. Kong, H. Dai. Electrical measurements of individual semiconducting single–walled carbon nanotubes of various diameters. *Appl. Phys. Lett.,* 2000, **76**, 1597.

3) S. Fan, M. G. Chapline, N. R. Franklin, T. W. Tombler, A. M. Cassell, H. Dai. Self–Oriented Regular Arrays of Carbon Nanotubes and Their Field Emission Properties. *Science,* 1999, **283**, 512.

4) D. N. Futaba, K. Hata, T. Yamada, K. Mizuno, M. Yumura, S. Iijima. Kinetics of Water–Assisted Single–Walled Carbon Nanotube Synthesis Revealed by a Time–Evolution Analysis. *Phys. Rev. Lett.*, 2005, **95**, 056104.

5) H. Kind, J.-M. Bonard, L. Forro, K. Kern. Printing Gel–like Catalysts for the Directed Growth of Multiwall Carbon Nanotubes. *Langmuir*, 2000, 16, 6877.

6) Y. Zhang, Y. Li, W Kim, D Wang, H Dai. Imaging as–grown single–walled carbon nanotubes originated from isolated catalytic nanoparticles. *Appl. Phys. A,* 2002, **74**, 325.

7) A. M. Cassell, N. R. Franklin, T. W. Tombler, E. M. Chan, J. Han, H. Dai. Directed growth of free–standing single–walled carbon nanotubes. *J. Am. Chem. Soc*., 1999, **121**, 7975.

8) A.-C. Depuis. The catalyst in the CCVD of carbon nanotubes—a review. *Prog. Mater. Sci.*, 2005, **50**, 929.

9) Y. J. Jung, B. Wei, R. Vajtai, P. M. Ajayan. Mechanism of Selective Growth of Carbon Nanotubes on SiO_2 / Si Patterns. *Nano Lett.,* 2003, **3**, 561.

10) N. R. Franklin, Y. Li, R. J. Chen, A. Javey, H. Dai. Patterned growth of single–walled carbon nanotubes on full 4–inch wafers. *Appl. Phys. Lett.,* 2001, **79**, 4571.

11) L. Qingwen, Y. Hao, C. Yan, Z. Jin, L. Zhongfan. A scalable CVD synthesis of high–purity single–walled carbon nanotubes with porous MgO as support material. *J. Mater. Chem.*, 2002, **12**, 1179.

12) H. Ago, S. Imamura, T. Okazaki, T. Saito, M. Yumura, M. Tsuji. CVD Growth of Single–Walled Carbon Nanotubes with Narrow Diameter Distribution over Fe / MgO Catalyst and Their Fluorescence Spectroscopy. *J. Phys. Chem. B*, 2005, **109,** 10035.

13) H. Ago, K. Nakamura, S. Imamura, M. Tsuji. Growth of double–wall carbon nanotubes with diameter–controlled iron oxide nanoparticles supported on MgO. *Chem. Phys. Lett.*, 2004, **391**, 308.

14) E. Flahaut, A. Peigney, C. Laurent, A. Rousset. Synthesis of single–walled carbon nanotube–Co–MgO composite powders and extraction of the nanotubes. *J. Mater. Chem.*, 2000, **10**, 249.

15) J.-F. Colomer, C. Stephan, S. Lefrant, G. van Tendeloo, I. Willems, Z. Konya, A. Fonseca, C. Laurent , J. B. Nagy. Large–scale synthesis of single–wall carbon nanotubes by catalytic chemical vapor deposition (CCVD) method. *Chem. Phys. Lett.*, 2000, **317**, 83.

16) H. Ago, K. Nakamura, N. Uehara, M. Tsuji. Roles of Metal–Support Interaction in Growth of Single– and Double–Walled Carbon Nanotubes Studied with Diameter–Controlled Iron Particles Supported on MgO. *J. Phys. Chem. B*, 2004, **108**, 18908.

17) G. Ning, F. Wei, Q. Wen, G. Luo, Y. Wang, Y. Jin. Improvement of Fe / MgO Catalysts by Calcination for the Growth of Single– and Double–Walled Carbon Nanotubes. *J. Phys. Chem. B*, 2006, **110**, 1201.

18) Q. Li, Y. Hao, X. Li, J. Zhang, Z. Liu. High–Density Growth of Single–Wall Carbon Nanotubes on Silicon by Fabrication of Nanosized Catalyst Thin Films. *Chem. Mater*. 2002, **14**, 4262.

19) S. Casimirius, E. Flahaut, C. Laberty-Robert, L. Malaquin, F. Carcenac, C. Laurent, C. Vieu. Microcontact printing process for the patterned growth of individual CNTs. *Microelec. Engin.* 2004,**73–74**, 564.

20) C. Du, N. Pan. Preparation of single–walled carbon nanotube reinforced magnesia films. *Nanotechnology,* 2004, **15**, 227.

21) Y. Xia, G. M. Whitesides. Soft Lithography. *Angew. Chem. Int. Ed*., 1998, **37**, 550.

22) A. M. Cassell, J. A. Raymakers, J. Kong, H. Dai. Large Scale CVD Synthesis of Single–Walled Carbon Nanotubes. *J. Phys. Chem. B*, 1999, **103**, 6484.

23) M. S. Dresselhaus, G. Dresselhaus, R. Saito, A. Jorio. Raman spectroscopy of carbon nanotubes. *Physics Reports,* 2005, **409**, 47.

24) M. S. Dresselhaus, G. Dresselhaus, A. Jorio, A. G. Souza Filho, M. A. Pimenta, R. Saito. Single Nanotube Raman Spectroscopy. *Acc. Chem. Res.,* 2002, **35**,1070.

25) K. Ishikawa, N. Fujima, H. Komura. First–order Raman scattering in MgO microcrystals. *J. Appl. Phys.,* 1985, **57**, 973.

26) N. B. Mason, W. Von der Ohe, S. L. Chodos. Second order spectrum of MgO. *Phys. Rev. B,* 1971, **3,** 1968.

27) D. R. Linde (Ed). *Bond strengths in polyatomic molecules*, in: *Handbook of Chemistry and Physics*. Boca Raton CRC Press, 2005, 9–64.

28) T. S. Duffy, C. Meade, Y. Fei, H.-K. Mao, R. J. Hemley. High–pressure phase transition in brucite, $Mg(OH)_2$. *American Mineralogist*, 1995, **80**, 222.

29) H. G. M. Edwards, S. E. Jorge Villar, J. Jehlicka, T. Munshi. FT–Raman spectroscopic study of calcium–rich and magnesium–rich carbonate minerals. *Spectrochim. Acta Part A,* 2005, **61**, 2273.

30) K.A. Shorlin, J.R. de Bruyn, M.Graham, S.W. Morris. Development and geometry of isotropic and directional shrinkage–crack patterns. *Physical Review E* 2000, **61**, 6950.

31) E. Alvarado, L. M. Torres-Martinez, A. F. Fuentes, P. Quintana. Preparation and characterization of MgO powders obtained from different magnesium salts and the mineral dolomite. *Polyhedron*, 2000, **19,** 2345.

32) A. M. Cassell, N. R. Franklin, T. W. Tombler, E. M. Chan, J. Han, H. Dai. Directed Growth of Free–Standing Single–Walled Carbon Nanotubes. *J. Am. Chem. Soc.,* 1999, **121**, 7975.

33) A. M. Cassell, J. A. Raymakers, J. Kong, H. Dai. Large Scale CVD Synthesis of Single–Walled Carbon Nanotubes. *J. Phys. Chem., B* 1999, **103**, 6484.

34) S. Fan, W. Liang, H. Dang, N. Franklin, T. Tombler, M. Chapline, H. Dai. Carbon nanotube arrays on silicon substrates and their possible application. *Physica E*, 2000, **8**, 179.

35) M. A. Aramendia, V. Borau, C. Jimenez, J. M. Marinas, J. R. Ruiz, F. J. Urbano. Influence of the preparation method on the structural and surface properties of various magnesium oxides and their catalytic activity in the Meerwein–Ponndorf–Verley reaction. *Appl. Catal. A,* 2003, **244**, 207.

36) N. N. Greenwood, A. Earnshaw. *Nitric acid and nitrates*, in *Chemistry of the Elements* (2nd Ed.) Butterworth Heinemann, 1998, 465.

37) Data obtained from Material data safety sheets supplied by Sigma–Aldrich UK.

38) G. Attard, C. Barnes. *Surfaces*, 1998, Oxford University Press.

39) A. Moisala, A. G. Nasibulin , E. I. Kauppinen. The role of metal nanoparticles in the catalytic production of single–walled carbon nanotubes — a review. *J. Phys: Condens. Matter*, 2003, **15**, s3011.

40) PhD Thesis (in preparation), Iris Coe, 2006, University of Edinburgh.

41) N. R. Franklin, H. Dai. An Enhanced CVD Approach to Extensive Nanotube Networks with Directionality. *Adv. Mater.,* 2000, **12**, 890.

42) Z. Wang, P. Lazor, S. K. Saxena, H. St. C. O'Neill. High pressure Raman spectroscopy of ferrite $MgFe_2O_4$. *Mater. Res. Bull.,* 2002, **37**, 1589.

43) S. G. Marchetti, R. Spretz, M. A. Ulla, E. A. Lombardo. Identification of the species formed in the Fe / MgO system: A Raman and Mössbauer study. *Hyperfine Interact.* 2000, **128**, 453.

7 Conclusions

7.1 Introduction

In this thesis, two areas of carbon nanotube research have been explored. The first area was the mechanism of nanotube growth under Chemical Vapour Deposition (CVD) conditions (Chapters 3 and 4) while the second was positioning nanotubes on surfaces (Chapter 5 and 6).

7.2 Growth mechanism of carbon nanotubes by CVD

In Chapter 3, a new iron oxide and magnesium oxide catalyst was developed that has been shown to be effective in producing SWNTs under CVD conditions with methane. Some conditions for tube growth were found that were then used as the basis of a series of comparative CVDs to investigate the mechanism of tube formation.

As has been shown previously, the temperature and the length of time that the catalyst was exposed to methane during the CVD were found to be important factors in the growth.[1-3] In addition to these factors, the availability of carbon to react was also found to be a useful concept to explain differences in quality of tubes and amount of carbon deposited. It was found that CVDs with a low availabilities of carbon produced samples with small I_D / I_G ratios suggesting growth of high-quality SWNTs with little unwanted carbon by-products. However, the amount of carbon deposited was small under these condition was also small. As availability of carbon increased, the amount of carbon deposited would also increase but the I_D / I_G ratio would increase. Hence the key to optimisation was seen to be the balancing of the amount of carbon (SWNTs) deposited with quality of sample produced in terms of the amount of unwanted carbon by-products. These experiments also showed, for the first time, that the availability of carbon in a CVD had an effect on the distribution of diameters of tubes produced.

In Chapter 4, the validity of the ring addition model of SWNTs growth was investigated. In this model of growth that has been proposed for the growth of

SWNTs from camphor,[4] nanotubes are formed by the reaction of preformed carbon-containing rings that are produced from the decomposition of the carbon feedstock molecule. Several comparative CVDs were carried out with different molecules as the carbon source to determine whether there was any relationship between the structural features of the molecule (such as being bicyclic, cyclic or acyclic) and the carbon nanotubes deposited. No evidence for the ring addition model was found as no relationship could be found between structure of the molecule and the I_D / I_G ratio or the yield of carbon of the CVD sample produced from it. Inspection of the Raman spectra of samples did indicate that different molecules had produced different distributions of diameters of SWNTs.

7.3 Postioning of carbon nanotubes on surfaces

Two very different approaches were used to position nanotubes. In the first approach described in Chapter 5, SWNTs were treated with a sulfur/argon/hydrogen plasma. X-ray photoeletron spectroscopy of the plasma treated nanotubes confirmed the presence of sulfur atoms in the sample but it could not indicate the nature (or the functional groups) of that sulfur.

These tubes were found to selective attach onto gold surfaces when these surfaces were exposed to a dispersion of the plasma treated tubes. When this selective attachment was used to a fabricate Field Effect Transistors, the sulfur-plasma treated gave a higher yield of devices compared with untreated nanotubes. The FETs, produced from the plasma treated nanotubes, did not show ideal properties due to the bundling of the tubes that were making up the devices. The bundling of the tubes results from the difficulties posed in dispersing nanotubes in such a way that no bundling would occur.

In Chapter 6, the approach adopted to achieve positioned nanotubes was to grow nanotubes in preordained positions by patterning a surface with a catalyst and then exposing the patterned catalyst to CVD conditions. An iron oxide/magnesium oxide was chosen as although magnesium oxide is known as a good support material for

nanotube catalysts,[5-7] it has not been widely used in the patterning surface for the growth of nanotubes. In order to establish which might be the most suitable for producing an effective catalyst, several different magnesium compounds were tested as possible precursors that could be applied to a surface and then would decompose to form the catalyst support. Silicon wafers with a silicon dioxide layer were simply dip coated in an ethanolic solution/dispersion of the magnesium compound which also had iron nirate added. These wafers were then exposed to CVD conditions. The catalyst precursors that had a melting point higher than the temperature, to which the samples were heated, during the CVD process, were found to be produce a high density of nanotube growth and low I_D / I_G ratios. The compounds with lower melting points are thought to produce a low surface area catalyst (high surface areas are known to promote growth of tubes[5]) due to them melting while being heated. It was also notes form SEM that the smooth surfaces produced by the compounds that melting may have produced a catalyst surface on the micron scale that was not conducive to the growth of tubes.

It was found the compounds that were most suitable were magnesium carbonate and magnesium oxide itself. Both of these were then used in further experiments where the catalyst was patterned using embossing. In this technique, a drop of the catalyst precursor dispersion is placed on a wafer and a patterned PDMS stamp is placed on top so that a pattern is formed while the solvent evaporated. It was found that the magnesium oxide precursor produced more accurate patterning, perhaps due to the very fine nature of the MgO powder used, and it also shown the most growth of tubes when compared with the magnesium carbonate.

The effect on the growth of nanotubes of calcining the wafers dip-coated for 10 hours was also studied. The calcination step was shown to improve the quality of the tubes in terms of the samples' I_D / I_G ratios. It is suggested, as other works have found,[8] that the improvement was explained by the formation $MgFe_2O_4$. The formation of $MgFe_2O_4$ is thought to produce smaller and better dispersed catalyst particles than were present in the uncalcined samples which then produces better growth of smaller nanotubes in turn. Indeed, there is evidence from the radial

breathing modes that the calcined samples did produce nanotubes with smaller diameter. Other evidence of the presence of $MgFe_2O_4$ came from calcined catalysts' Raman spectra which showed peaks attributable to the compound. These finding again show the importance of the thermal and chemical treatments that a nanotube catalyst undergoes on its behaviour.

7.4 Future Work

Looking at the thesis as a whole, it is clear that some common themes have appeared in the chapters concerned with the growth of tubes under CVD conditions. In particular both Chapters 3 and 6 have shown that the catalyst used in CVD are very much affected by the way that they are treated before CVD. In future research, more effort is needed in characterizing the catalysts involved but only as they are produced but after the particular treatment that they undergo before they are used in CVD. In addition, it is not simply a case of understanding the chemical composition of the catalyst or its structure at the nanometre scale, it is also important to consider the catalyst on the micron length scale, and perhaps even on the macroscopic scale, in hope of understanding how the structure of the catalyst on these length scales affects the growth of tubes.

In both Chapters 3 and 4, the concept of the availability of the carbon and its importance in the formation of tubes, in terms of both the quality of tubes and the distribution of the diameters, has been demonstrated. In Chapter 3, the availability was controlled by flowrate of the methane and the residence time of the gas whereas in Chapter 4, the availability is rationalized in terms of the stability of the molecules. It is assumed that fewer stable molecules decompose as they pass over the catayst compared to less stable molecules and therefore produce conditions where carbon is less available to form nanotubes.

One strand of research, which could be followed from the work in this thesis, is the investigation of how this availability of carbon affects the distribution of diameters in

the product of a CVD. It would be important to establish whether it is possible to affect the distribution of chiralities of the tubes or if it is only possible to influence the diameters of the tubes. Such an investigation would require detailed analysis with Raman spectroscopy (carried out with several excitation wavelengths)[9] and TEM[10] so that the diameters and chiralites of tubes present in different samples could be analyzed.

Controlling the availability of carbon may be a valuable means of gaining control over the synthesis of nanotubes. A vital step in the research would be to establish the mechanism of how the availability of carbon affects the diameters. Two mechanisms for this effect have been proposed in this work. In one mechanism, the size distribution of the nanoparticles in a catalyst is affected by the supply of the carbon feedstock; in turn this difference of size has an influence on the diameter of tubes produced. In the other mechanism, the rate at which the carbon is supplied to the nanoparticle favours tubes of different diameters or perhaps chiralities due to differences in the rates of processes involved in nanotube growth such as formation of the end-cap and the formation of the sidewall of a tube. As state previously, it is clear that further work in this area would require both detailed TEM analysis of the nanoparticles at different stages of the CVD process and the carbon nanotubes produced.

7.5 References

1) A.-C. Depuis. The catalyst in the CCVD of carbon nanotubes—a review. *Prog. Mater. Sci.*, 2005, **50**, 929
2) A. Moisala, A. G. Nasibulin, E. I. Kauppinen. The role of metal nanoparticles in the catalytic production of single–walled carbon nanotubes—a review. *J. Phys.: Condens. Matter*, 2003, **15**, s3011.
3) R. B. Little. Mechanistic Aspects of Carbon Nanotube Nucleation. *J. Cluster Sci.*, 2003, **14**, 135.
4) M. Kumar, Y. Ando. Controlling the diameter distribution of carbon nanotubes grown from camphor on a zeolite support. *Carbon,* 2005, **43**, 533.

5) L. Qingwen, Y. Hao, C. Yan, Z. Jin, L. Zhongfan. A scalable CVD synthesis of high–purity single–walled carbon nanotubes with porous MgO as support material. *J. Mater. Chem.*, 2002, **12**, 1179.

6) H. Ago, S. Imamura, T. Okazaki, T. Saito, M. Yumura, M. Tsuji. CVD Growth of Single–Walled Carbon Nanotubes with Narrow Diameter Distribution over Fe / MgO Catalyst and Their Fluorescence Spectroscopy. *J. Phys. Chem. B*, 2005, **109,** 10035.

7) H. Ago, K. Nakamura, S. Imamura, M. Tsuji. Growth of double–wall carbon nanotubes with diameter–controlled iron oxide nanoparticles supported on MgO. *Chem. Phys. Lett.*, 2004, **391**, 308.

8) G. Ning, F. Wei, Q. Wen, G. Luo, Y. Wang, Y. Jin. Improvement of Fe / MgO Catalysts by Calcination for the Growth of Single– and Double–Walled Carbon Nanotubes. *J. Phys. Chem. B*, 2006, **110**, 1201.

9) M. S. Dresselhaus, G. Dresselhaus, R. Saito, A. Jorio. Raman spectroscopy of carbon nanotubes. *Physics Reports*, 2005, **409**, 47

10) Ph. Lambin, A. Loiseau, C. Culot, L. P. Biro. Structure of carbon nanotubes by local and global probes. *Carbon*, 2002, 1635–1645.

8 Lectures and conferences

Postgraduate lectures and courses

Data Handling and Statistics (5 lectures)
Principles of Sampling/ Analysis (5 lectures)
Laser Spectroscopy (5 lectures)
Mass Spectroscopy (5 lectures)
Microscopy and Imaging (10 lectures)
Computational Methods (5 lectures)
Diffraction Methods (7 lectures)

Physical Chemistry Section Seminars
School Colloquia

Communicating Research to Non-Specialists
Unix 1: Introduction to UNIX
Unix 2 Enhancing your UNIX skills
Introduction to Computer Programming Using Fortran 90

Conferences

NT05: Sixth International Conference on the Science and Application of Nanotubes, Gothenburg, Sweden, June 2005.

RSC International Materials Chemistry Conference, Edinburgh, UK, July 2005.

9 Reprint of Publications

1) N. O. V. Plank, R. Chenug. R. J. Andrews. Thiolation of single–wall carbon nanotubes and their self–assembly *Appl. Phys. Lett.*, 2004, **85**, 3229.
2) R. J. Andrews, C. F. Smith, A. J. Alexander, Mechanism of carbon nanotube growth from camphor and camphor analogs by chemical vapor deposition. *Carbon*, 2006, **44,** 341

Thiolation of single-wall carbon nanotubes and their self-assembly

N. O. V. Plank[a] and R. Cheung
School of Engineering and Electronics, University of Edinburgh, Scottish Microelectronics Centre, West Mains Road, King's Buildings, EH9 3JF, Scotland, United Kingdom

R. J. Andrews
School of Chemistry, University of Edinburgh, Joseph Black Building, West Mains Road, King's Buildings, EH9 3JL, Scotland, United Kingdom

(Received 12 May 2004; accepted 10 August 2004)

A method for the thiolation of single-wall carbon nanotubes has been developed by exposing a sulfur/carbon nanotubes mixture to an argon/hydrogen gaseous plasma. X-ray photoelectron spectroscopy provides evidence of the existence of sulfur attached to carbon on the carbon nanotubes samples and Raman spectroscopy results show that the carbon nanotubes' structure has been preserved after the treatment. One added advantage of the reported method is that excess oxygen is not present on the nanotubes. The thiolated carbon nanotubes are shown to self-assemble onto gold electrodes. Our method for thiolating carbon nanotubes provides a reliable and simple way for preparing functionalized tubes for nanoelectronic circuits based on carbon nanotubes. © *2004 American Institute of Physics*. [DOI: 10.1063/1.1805702]

Carbon nanotubes (CNTs) offer the electronic device community a promising candidate for future electronic needs. The nanotubes themselves have shown excellent conduction properties with the ability to behave as semiconducting or metallic conducting tubes depending on how the tubes have formed.[1,2] The inherently small size of the nanotubes also allow for instant nanometer scale device production.[3] However, there are problems remaining in the field regarding how to selectively position the tubes for accurate, reproducible and high volume device production. One method to enable selective positioning for the production of CNT devices is to functionalize the nanotubes. Thiols are known to bond selectively to gold and other reports have demonstrated thiol functionalization techniques using long and short chain alkanethiols respectively.[4–6] Here, we report on the direct thiolation of single-walled CNTs, without any long chain carbon groups, by first physically mixing elemental sulfur with CNTs and then exposing the sulfur/CNT mixture to an Ar/H_2 plasma. The advantage of this method has been to allow CNTs to attach selectively to gold electrodes with a short functionalization time.

Single-wall CNTs from Carbon Nanotechnologies Inc. were used in our experiments. The sulfur/CNTs were prepared by physical mixing with elemental sulfur from Aldrich. The nontreated sample, sample 1, is referred to as the control sample throughout the text. Other samples were exposed to an argon and hydrogen based plasma mixture within a plasma etch reactor with the electrodes heated to 120 °C to allow the sulfur to melt, the reactor conditions and mixing ratios are outlined in Table I. After, the control CNT sample, nonplasma exposed and plasma exposed sulfur/CNT samples were immediately placed in 2 ml of toluene and rinsed through with 5 ml of toluene to rid of any excess sulfur before being drop coated onto a silicon wafer for characterization. For the self-assembly experiments, a drop of the functionalized nanotubes solution was placed in 2 ml of ethanol and sonicated for 10 min. A lithographically patterned clean gold sample was then left in the solution and covered for 12 h, after which the sample was cleaned in ethanol and viewed in the Hitachi S4500 scanning electron microscope. To characterize the extent of sulfur attachment to the nanotubes before self-assembly, x-ray photoelectron spectroscopy (XPS) and Raman spectroscopy have been used. In addition, we demonstrate the self-assembly of the thiolated tubes onto patterned gold electrodes.

Figure 1 shows the S $2p$ peaks for the control CNTs, CNTs that have been mixed with sulfur (sulfur/CNTs) and sulfur/CNTs mixture exposed to Ar/H_2 plasma. The peaks have been fitted using XPS peak software, with $\Delta E = 1.18$ eV between the S $p_{3/2}$ and S $p_{1/2}$ and fixed intensity ratio of 2:1 respectively. A mixture of Lorentz:Gaussian peaks were required at 70:30, with full width at half maximum of 1 as in the literature.[7,8] It has been observed in our experiments, that for all CNT samples exposed to sulfur treatment, a binding energy of 163.7–163.8 eV is found. According to the literature, S–H is present at 163.7 eV while S–S occurs at 163.8 eV and S–Au bond is known to occur at 162 eV.[7–9] Multilayer thiols have also been observed at 164.4 eV.[10] Due to the closeness of the energy peaks for sulfur-containing compounds, we conclude that some form of sulfur is bonded to the CNTs after sulfur treatment within the thiol region.

Figure 2 shows the influence of the flow rate of H_2 in the Ar/H_2 gas mixture during plasma exposure on (a) the S/C ratio and (b) the position of the S $2p$ energy peak. The amount of S/C (around 5%) does not appear to be affected

TABLE I. The weight of carbon nanotubes and sulfur and the reactor conditions. rf power was held at 250 W and exposure time was 60 s throughout.

Sample	Weight of sulfur/CNT (g)	Ar flow (sccm)	H_2 flow (sccm)
Control	0/0.002	No plasma	No plasma
1	0.02/0.002	No plasma	No plasma
2	0.02/0.002	75	25
3	0.02/0.002	50	50
4	0.02/0.002	25	75

[a]Electronic mail: natalie.plank@ee.ed.ac.uk

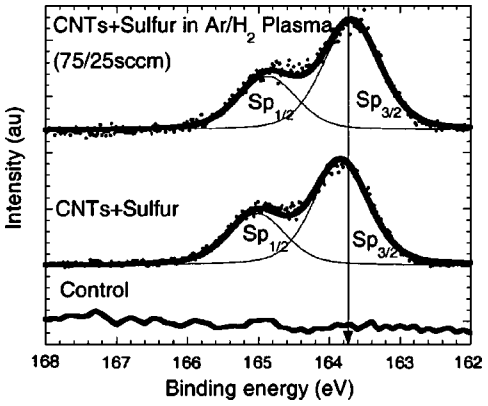

FIG. 1. X-ray photoelectron spectra of *S* 2*p* peak for control CNTs, sulfur/CNTs, and sulfur/CNTs exposed to Ar/H_2 plasma.

significantly by the presence of the plasma or by the rate of H_2 flow, yet the presence of the plasma does shift the S 2*p* peaks to slightly lower binding energies. Therefore, we see that the exposure to the Ar/H_2 plasma is not essential for sulfur to attach to the CNTs but does help to provide an excess H_2 environment for thiolation to take place. Plasma functionalization of graphite and glassy carbon using SO_2 plasma have shown similar sulfur atomic percentages and position of the S 2*p* peaks, at dc bias voltages and exposure times close to those used in our experiments.[11] Moreover, the adhesion of sulfur in the thiol region without the presence of additional S–O peaks is demonstrated in our thiolation method, even after 4 weeks exposure to atmosphere. The SO_2 bonding, often found in different methods of treating the tubes[4,5] and other forms of carbon,[6,12,13] is observed by others usually at ~167 eV. In addition, the oxygen peak component has not been seen to increase in our thiolated tubes after 4 weeks exposure to atmosphere, as has been the case in our previous studies on the fluorine functionalization process.[14,15] Experimental evidence suggests that the lack of oxygen incorporation into the tubes is inherent to our thiolization process.

The Raman spectra for the control CNTs, sulfur/CNTs, and sulfur/CNTs exposed to Ar/H_2 plasma are shown in Fig. 3. The presence of *D* and *G* bands and the RBM modes indicate that the tubular structure of the nanotubes have not been destroyed by our treatments, Fig. 3(a), and that the average tube diameter distribution ranges from 0.8 to 1.3 nm.[16] Many low intensity peaks inherent to the Raman

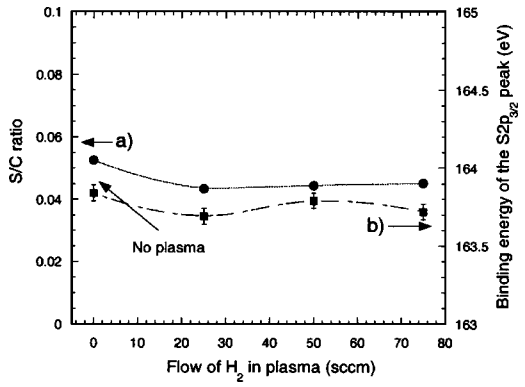

FIG. 2. Influence of H_2 flow rate in the Ar/H_2 plasma exposure (total flow =100 sccm) on (a) the S/C ratio and (b) the position of the *S* 2*p* energy peak, of the sulfur/CNTs. At H_2=0 sccm, no plasma has been struck.

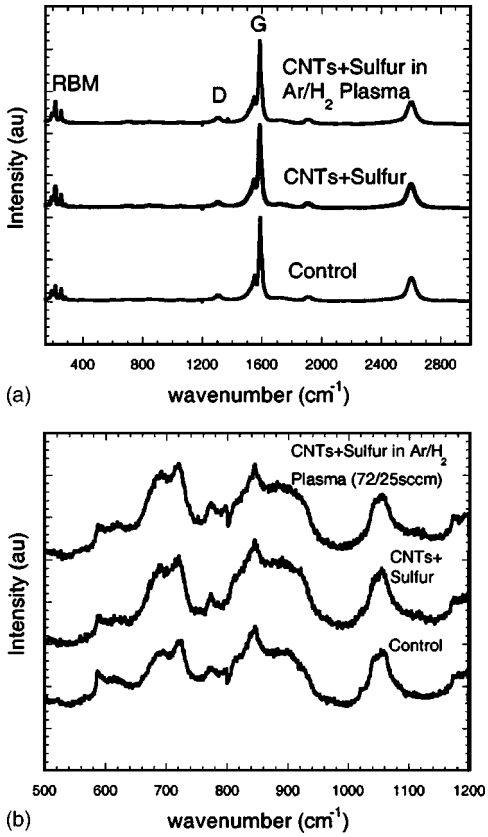

FIG. 3. Raman spectra of control CNTs, sulfur/CNTs, and sulfur/CNTs exposed to Ar/H_2 plasma, (a) over the whole spectra and (b) zoomed in over 500–1200 cm^{-1}.

spectra of carbon nanotubes[17,18] are evident in all three samples, Fig. 3(b). Neither the S=C peak at 1095 cm^{-1} nor S–S peak at 585 cm^{-1} have been observed after our thiolization treatment, in contrast to results reported by Liu *et al.*[5] The lack of S as indicated by Raman in our experiments could be due to the small sulfur atomic concentration measured, around 5% by XPS experiments, whereas in the method used by Liu *et al*. the sulfur content is expected to be higher. Other work where carbon films and carbon rods have been doped with sulfur resulting in atomic percentages similar to those observed in our experiments also show no sulfur-related peaks in the Raman spectra.[19–23]

We have used the thiolated tubes in the self-assembly process and Fig. 4 shows both low and high resolution scanning electron micrographs of the functionalized tubes lying across the gold electrodes after self-assembly. The success of the self-assembly indicates the existence of thiols in our tubes. The CNT bundles are seen to align across the electrodes as opposed to along the electrodes, probably due to the sulfur bonding preferentially to the ends of the nanotubes. Several authors have indicated the end groups of CNTs to be the most reactive part of the tubes.[1,2,4,5] The low stochiometries shown in Fig. 2 support the hypothesis that the sulfur will not have bonded along the entire length of the CNTs. In comparison, the sulfur/CNT nonplasma exposed sample has shown no sign of self-assembly to the gold electrodes or any surface physisorption effects after the self-assembly stage.

Thiolation of single-walled CNTs has been demonstrated whereby the ends of the nanotube bundles have been selectively functionalized making it favorable for the nanotubes to

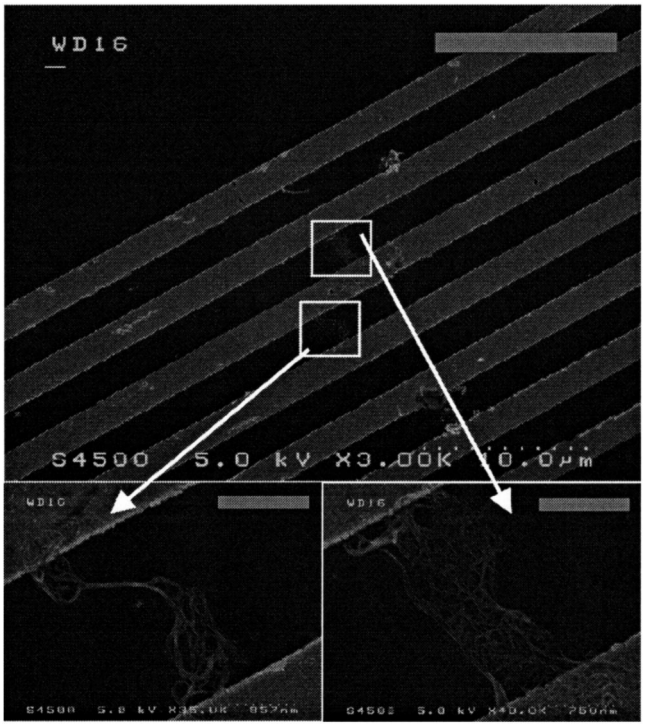

FIG. 4. Scanning electron micrographs for self-assembled thiolated tubes onto gold electrodes. The tubes shown are from sample 2.

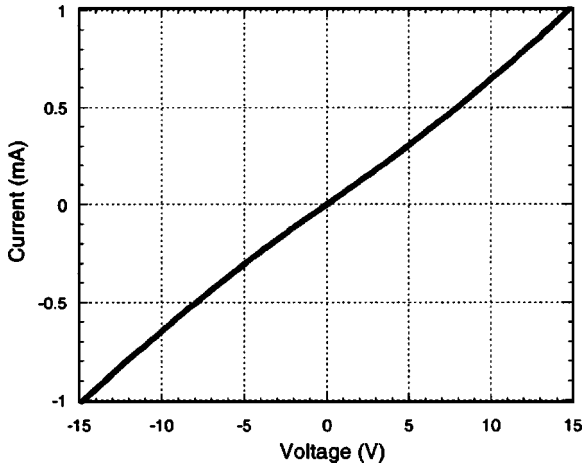

FIG. 5. The average current–voltage characteristics at room temperature of a CNT film produced onto gold electrodes after sulfur plasma exposure.

self-assemble across the gold electrodes. Similarly prepared carbon nanotube films have been assembled over gold electrodes on SiO_2 and have shown an average resistance of 15 454 Ω at 10 V (Fig. 5). The current is higher than that observed for single CNTs bridging electrodes by electric field alignment methods.[24] Work is currently under way to measure the electrical properties of the connected tubes after selective alignment of the tubes specific for nanoelectronic circuit fabrication.

The authors would like to thank Ronald Brown for assistance in the XPS measurements, Gavin Whittaker for use of the Plasma Etch reactor and discussions, Sara Falconi for use of the Raman spectroscopy equipment and Andrew Alexander.

[1]R. Saito, G. Dresselhaus, and M. S. Dresselhaus, *Physical Properties of Carbon Nanotubes* (Imperial College Press, London, 2001).
[2]H. Dai, Surf. Sci. **500**, 218 (2002).
[3]S. J. Tans, A. R. M. Verschueren, and C. Dekker, Nature (London) **393**, 49 (1998).
[4]Z. Liu, Z. Shen, T. Zhu, S. Hou, and L. Ying, Langmuir **16**, 3569 (2000).
[5]J. K. Lim, W. S. Yun, M.-h. Yoon, S. K. Lee, C. H. Kim, K. Kim, and S. K. Kim, Synth. Met. **139**, 521 (2003).
[6]M. Zharnikov and M. Grunze, J. Phys.: Condens. Matter **13**, 11333 (2001).
[7]Y. Joseph, N. Krasteva, I. Besnard, B. Guse, M. Rosenberger, U. Wild, A. Knop-Gericke, R. Schlogl, R. Krustev, A. Yasuda, and T. Vossmeyer, Faraday Discuss. **125**, 77 (2003).
[8]C. Vericat, M. E. Vela, G. Andreasen, and R. C. Salvarezza, Langmuir **17**, 4919 (2001).
[9]C. M. Whelan, M. R. Smyth, C. J. Barnes, N. M. D. Brown, and C. A. Anderson, Appl. Surf. Sci. **134**, 144 (1998).
[10]S. M. Kane and J. L. Gland, Surf. Sci. **468**, 101 (2000).
[11]M. Collaud Coen, B. Keller, P. Groening, and L. Schlapbach, J. Appl. Phys. **92**, 5077 (2002).
[12]J. Heeg, C. Kramer, M. Wolter, S. Michaelis, W. Plieth, and W. -J. Fischer, Appl. Surf. Sci. **180**, 36 (2001).
[13]J. C. Love, D. B. Wolfe, R. Haasch, M. L. Chabinyc, K. E. Paul, G. M. Whitesides, and R. G. Nuzzo, J. Am. Chem. Soc. **125**, 2597 (2003).
[14]N. O. V. Plank, L. Jiang, and R. Cheung, Appl. Phys. Lett. **83**, 2426 (2003).
[15]N. O. V. Plank and R. Cheung, Microelectron. Eng. **73–74**, 578 (2004).
[16]M. S. Dresselhaus, G. Dresselhaus, A. Jorio, A. G. Souza Filho, M. A. Pimenta, and R. Saito, Acc. Chem. Res. **35**, 1070 (2002).
[17]H. Kuzmany, B. Burger, A. Thess, and R. E. Smalley, Carbon **36**, 709 (1998).
[18]A. M. Rao, E. Richter, S. Bandow, B. Chase, P. C. Eklund, K. A. Williams, S. Fang, K. R. Subbaswamy, M. Menon, A. Thess, R. E. Smalley, G. Dresselhaus, and M. S. Dresselhaus, Science **275**, 187 (1997).
[19]A. Gonzalez-Berrios, D. Huang, N. M. Medina-Emmanuelli, K. E. Kristian, O. O. Ortiz, J. A. Gonzalez, J. De Jesus, I. M. Vargas, B. R. Weiner, and G. Morell, Diamond Relat. Mater. **13**, 221 (2004).
[20]S. Glenis, A. J. Nelson, and M. M. Labes, J. Appl. Phys. **86**, 4464 (1999).
[21]R. Kalish, C. Uzan-Saguy, R. Walker, and S. Prawer, J. Appl. Phys. **94**, 3923 (2003).
[22]S. Gupta, B. R. Weiner, and G. Morell, J. Appl. Phys. **91**, 10088 (2002).
[23]S. Gupta, B. R. Weiner, and G. Morell, J. Appl. Phys. **92**, 5457 (2002).
[24]M. S. Kumar, T. H. Kim, S. H. Lee, S. M. Song, J. W. Yang, K. S. Nahm, and E.-K. Suh, Chem. Phys. Lett. **383**, 235 (2004).

Available online at www.sciencedirect.com
SCIENCE DIRECT®
Carbon 44 (2006) 341–347
CARBON
www.elsevier.com/locate/carbon

Mechanism of carbon nanotube growth from camphor and camphor analogs by chemical vapor deposition

Robert J. Andrews, Catriona F. Smith, Andrew J. Alexander *

School of Chemistry, University of Edinburgh, West Mains Road, Edinburgh EH9 3JJ, UK

Received 7 June 2005; accepted 19 July 2005
Available online 1 September 2005

Abstract

Single walled nanotubes have been synthesized by chemical vapor deposition from camphor, camphor analogs (camphorquinone, norcamphor, norbornane, camphene, fenchone), and various other precursors (menthone, 2-decanone, benzene, methane). The high temperature conditions (865 °C) and Fe/Mo alumina catalyst used in the syntheses are archetypal conditions for the production of single walled carbon nanotubes. It has been shown that the mechanism of tube growth is unlikely to depend upon the production of reactive five- and six-member rings, as has been previously suggested. The results suggest that the presence of oxygen in the precursor does not significantly improve the quality of tubes by etching amorphous carbon: it is suggested that the control of the flux of the precursor to the catalyst is more important in the production of high quality tubes. There is, however, evidence for different distributions of tube diameter being produced from different precursors.

Keywords: Carbon nanotubes; Chemical vapor deposition

1. Introduction

The use of camphor as a precursor for chemical vapor deposition (CVD) of carbon nanostructures has been widely investigated. Fullerenes [1], carbon fibers [2], nanobeads [3], and carbon nanotubes (CNTs) [4–7] have all been synthesized using camphor. Camphor is cheap and readily obtained from renewable resources, making it an ideal ''green'' biosource for the production of nanotubes. Kumar and Ando have proposed that the bicyclic structure of camphor is key to the growth mechanism of CNTs [4,7]. The suggested mechanism of tube growth involves the addition of reactive pre-formed five- and six-member rings or *cyclic radicals* formed by decomposition of the precursor; the bicyclic structure of camphor would, therefore, be vital to the production of tubes. The suggested growth mechanism is similar to the one proposed for the formation of carbon nanotubes in CVD using benzene as the carbon source [8,9]: this *ring addition mechanism* involves the adsorption of the benzene molecules onto the surface of the metallic nanoparticle in such a way that the graphitic structure can be formed by the elimination of H_2 [8,9]. Previous work has suggested that aromatic molecules are more likely to form single walled nanotubes (SWNTs) than aliphatic or cyclic hydrocarbons of a similar mass [10]. It has been argued that the camphoric hexagonal units are already ''tilted'' at advantage to form a curved graphitic sheet or CNT [4]. It has also been suggested that decomposition of camphor may produce a significant amount of five-member rings, which promote curvature and are believed to promote formation of the bamboo (internally capped) structure of the tubes grown [4]. The high graphitization of some of the samples grown from camphor has been attributed to oxygen atoms (from the precursor) efficiently oxidizing amorphous carbon in situ

* Corresponding author. Tel.: +44 131 650 4741; fax: +44 131 650 4743.
E-mail address: andrew.alexander@ed.ac.uk (A.J. Alexander).

0008-6223/$ - see front matter © 2005 Elsevier Ltd. All rights reserved.
doi:10.1016/j.carbon.2005.07.025

[7]. The ring addition mechanism is quite different from the popular model of single walled nanotube growth where a hydrocarbon such as methane is used: in the *decomposition mechanism* of CVD, substantial evidence has been presented that the hydrocarbon is catalytically decomposed on the surface of the metal nanoparticle [11]. The carbon atoms produced are then dissolved in the nanoparticle until it becomes saturated, when it then starts to precipitate out as a CNT.

The theory that molecules with certain structural features may make better precursors for the CVD of CNTs is interesting. It would be of value to rationalize which molecules would be good precursors for high quality CNTs. In this work, several precursors were used in a series of comparative CVD growths in order to establish links between precursor structure and as-produced CNT quality. This information may also shed light on the type of mechanism by which the CNTs grow. If structure, and in particular the bicyclic structure, are important to tube growth, then there would be strong evidence for the postulated benzene-like *ring addition mechanism* for camphor. The precursors tested included camphor and several closely-related analog compounds, as well as benzene and methane. The CVD syntheses of carbon nanotubes were carried out by passing different precursor compounds over a catalyst at elevated temperature. The well-studied Fe/Mo catalyst at 865 °C was used, as it is known to favor production of single walled tubes and therefore is of particular interest for understanding the formation of SWNTs from camphor.

2. Experimental

The alumina supported Fe/Mo catalyst was prepared by the metal ion impregnation method [12]. $Fe_2(SO_4)_3$ (0.3 g, Aldrich, technical grade) and $(NH_3)_2MoO_4$ (0.04 g, Aldrich, 99.98%) were dissolved in ~150 cm^3 of deionised water, and approximately 2 g of alumina (Degussa Aluminoxid C) was added to the solution giving a Fe:Mo:alumina ratio of 1:0.13:13. The water was removed by rotary evaporation, and the solid dried overnight in an oven at 100 °C. The resulting powder was ground thoroughly using a mortar and pestle.

The CVD was carried out using a 2-stage heating set-up similar to Kumar and Ando [7]. In a typical procedure, the precursor (e.g., camphor 0.53 g (3.5 mmol) Aldrich, 96%) was placed in the first heating zone, and 0.1 g of the alumina supported Fe/Mo catalyst was placed in a quartz boat in the centre of the second furnace. Ar gas was passed over the precursor and through the second furnace at a rate of 200 $cm^3\ min^{-1}$. Once the catalyst had reached the working temperature of 865 °C, the precursor was heated to the required temperature and the vapor was allowed to pass into the second furnace. After 20 min, the furnace was allowed to cool under flowing Ar gas. The procedure was repeated with molar equivalents of camphorquinone, norcamphor, norbornane, camphene, fenchone, menthone, 2-decanone and benzene. All precursor compounds were purchased from Aldrich (except methane, from BOC Edwards) and used without further purification. The CVD procedure using methane was similar, except that once the furnace reached 865 °C, the gas flow was changed to 200 $cm^3\ min^{-1}$ of Ar gas and 34 $cm^3\ min^{-1}$ of methane. After 20 min, the furnace cooled under a flow of argon.

Product samples were characterized using thermogravimetric analysis (TGA, Stanton Redcroft Thermobalance TG762, heating from room temperature to 1000 °C at a rate of 10 °C min^{-1}) and Raman spectroscopy (Labram 300, 632.8 nm, 13 mW, with collections typically 100 s). Samples were prepared for transmission electron microscopy (TEM) by dispersing some of the as-prepared products in ethanol with sonication, and dropping a little of the dispersed product onto carbon coated grids. The samples were viewed using a Philips CM120 Biotwin with an accelerating voltage of 100 kV.

3. Results and discussion

Raman spectra of CNTs show the G and D bands that are characteristic for graphitic structures. As has been discussed in detail elsewhere [13], the G band (at ~1590 cm^{-1}) originates from ordered, well-graphitized carbon, while the D band (at ~1330 cm^{-1}) is the disorder-activated band. The Raman spectra of SWNTs show low-frequency peaks (~150–250 cm^{-1}) that result from radial breathing modes of the tubes (RBMs). The frequencies of the RBMs are inversely proportional to the diameters of the tubes. The shoulder to the low-frequency side of the G band (at ~1550 cm^{-1}) is also indicative of the presence of SWNTs [14]. The ratio of the area of the D band and G band (I_D/I_G ratio) in the Raman spectra has been used extensively as a measure of the graphitization of a sample, and as a measure of the quality of the tubes produced: a smaller I_D/I_G ratio corresponds to fewer defects. Thermal analysis of the CVD product revealed the relative amount of carbon present in our samples. The % yield was calculated by comparing the mass of carbon in the precursor that passed over the catalyst, with the mass deposited on the catalyst.

In a first set of experiments each precursor was heated to 200 °C to volatilize it so as to pass it through the furnace over the catalyst. As can be seen from Table 1, the yields are similar but the trend in I_D/I_G ratios cannot be explained easily in terms of the structure of the precursors. However, as Fig. 1 shows, there is a relationship between the boiling point of the precursor and the quality of the tube: a higher boiling point reduces the

Table 1
Analysis of CVD products from syntheses where all precursors were heated to 200 °C

Precursors	Melting point/°C	Boiling Point/°C	I_D/I_G ratio	% Yield
Camphorquinone	199.0	226.5	0.23	8
Camphor	179.0	207.4	0.81	7
Norcamphor	95.0	170.0	1.84	9
Camphene	41.0	160.0	2.22	11
Norbornane	87.7	112.6	2.85	9

The I_D/I_G ratio is an indicator of the quality of the tubes, the lower the value, the smaller the amount of disorder in the CNT structure: the results show that camphorquinone produced the highest quality tubes in these experiments. The % yield was calculated by comparing the mass of carbon passed over the catalyst with the mass of carbon deposited on the catalyst. The trend in I_D/I_G ratio with boiling point shows that the higher boiling points produced better quality of tubes.

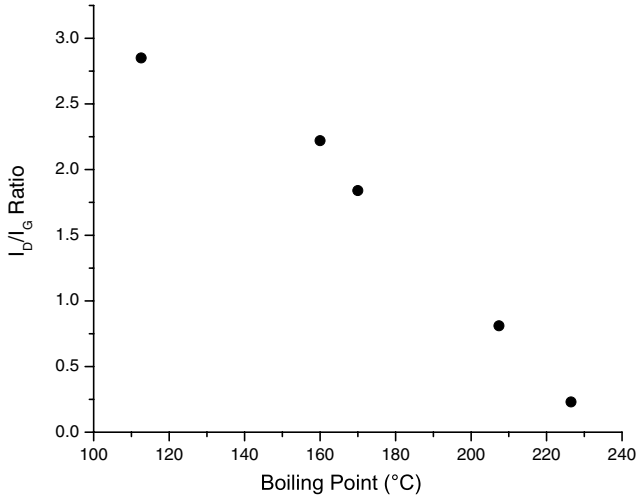

Fig. 1. Plot of I_D/I_G ratio against boiling point of precursor. All precursors in these experiments were heated to 200 °C. The plot shows that precursors with higher boiling points, and therefore lower vapor pressures, produced tubes with fewer defects.

I_D/I_G ratio, and therefore improves the quality of the tubes produced. The improved quality can be explained in terms of the vapor pressure of the precursors as they are being volatilized: precursors with higher boiling points will have lower vapor pressures at 200 °C. The lower vapor pressure will cause a lower flux of carbon source to pass over the catalyst. As has been observed previously, the quality of tubes produced from camphor can be improved by slowing the rate at which the camphor passes into the heated zone where CVD takes place [7]. Too high a concentration of precursor is thought to lead to the production of carbonaceous products other than CNTs, as non-catalyzed decomposition is promoted.

In a second set of experiments, each precursor was heated to 30 °C under its boiling point (except for methane, which was not heated) to try to obtain approximately the same vapor pressure for all of the precursors

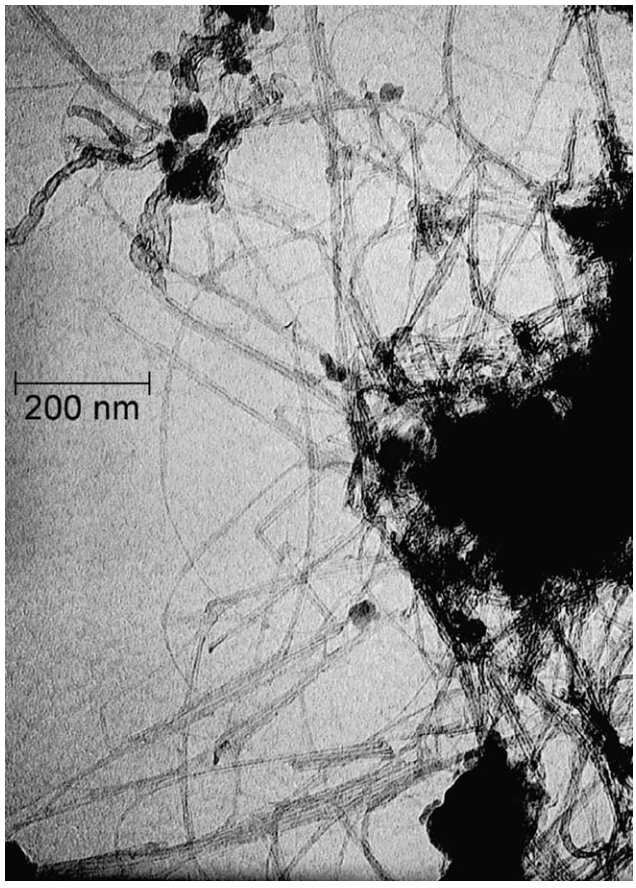

Fig. 2. TEM image of the camphor CVD product, representative for all the precursors, except methane. Both MWNTs and SWNTs can be seen.

so as to remove its effect on the quality of the tubes. Enthalpies of vaporization and Antoine constants for the precursor compounds were obtained from the DETHERM Database.[1] From the thermodynamic data it was established that each precursor heated to ca. 30 °C below its boiling point would have the same vapor pressure of ca. 350 Torr. The CVD products were all found to contain MWNTs and SWNTs, a representative TEM image is shown in Fig. 2. Methane seems to be mostly comprised of SWNTS as can be seen from Fig. 3. Fig. 4 shows that the Raman spectra of the CVD products are all very similar: they all have D, G and RBM bands that confirm that SWNTs are present in the samples. In these results (Table 2) we observe very little difference among the I_D/I_G ratios or the yields, except for methane and benzene. There appears to be no obvious direct relationship between the molecular structure (Fig. 5) and the quality of CNTs formed. The bicyclic structure is not vital to the production of CNTs as

[1] The DETHERM Database (http://i-systems.dechema.de/detherm/) maintained by DECHEMA (Society for Chemical Engineering and Biotechnology), Theodor-Heuss-Allee 25, D-60486 Frankfurt am Main. http://www.dechema.de/.

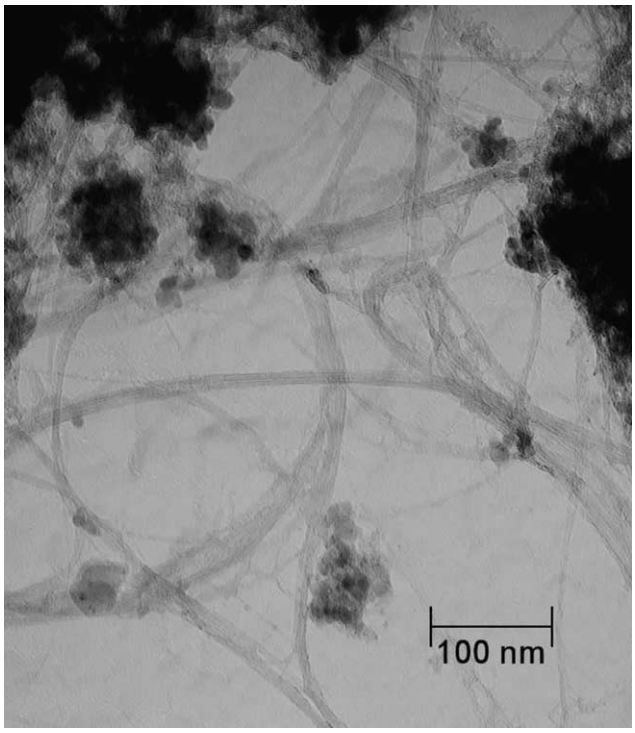

Fig. 3. TEM image of the methane CVD product. Only bundles of SWNTs were observed.

Table 2
Analysis of CVD products from syntheses where precursors were heated to 30 °C below their boiling points

Precursor	I_D/I_G ratio	% Yield
Camphor	0.21	14
Fenchone	0.18	12
Camphorquinone	0.23	14
Camphene	0.24	10
Norcamphor	0.27	14
Norbornane	0.26	15
Menthone	0.16	11
2-Decanone	0.16	12
Benzene	0.23	7
Methane	0.08	3

The I_D/I_G ratios and yields of these precursors (except methane) are very similar, suggesting that the quality of the tubes produced is not directly related to the structure of the precursors. The lower yields for methane and benzene can be explained by their greater stability (see text for details).

both menthone and 2-decanone produce CNTs comparable to the other precursors. More evidence against the *ring addition* mechanism relates specifically to fenchone and camphor. It has been shown that under flash pyrolysis conditions, camphor gave no five-member rings while fenchone did [15]. Therefore, if the inclusion of five-member rings is detrimental to the quality of tubes produced [4] then the tubes from fenchone should be worse than those of camphor, which we do not observe. It should be noted that during flash pyrolysis, decomposition of the precursors is assumed to occur in the gas phase whereas in the CVD process, decomposition can occur at a surface.

It has been suggested that the presence of oxygen in the precursor improves the quality of the tubes produced [7,16]. It is believed that oxygen contained in the precursor may produce O radicals that react with amorphous carbon to be subsequently transported away as gas-phase CO_x. We find no evidence of an improvement in quality in those samples from oxygen-contain-

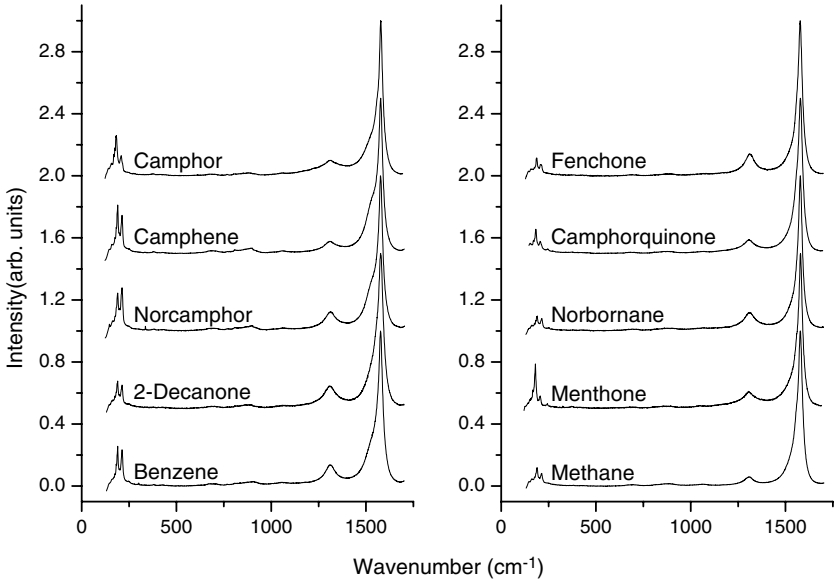

Fig. 4. Raman spectra of CVD products from syntheses where precursors were heated to 30 °C below boiling point. The presence of the D and G bands and radial breathing modes (RBMs) indicate the presence of SWNTs. All the samples (except methane) show similar I_D/I_G ratios, suggesting that the tubes produced have similar amounts of graphitization.

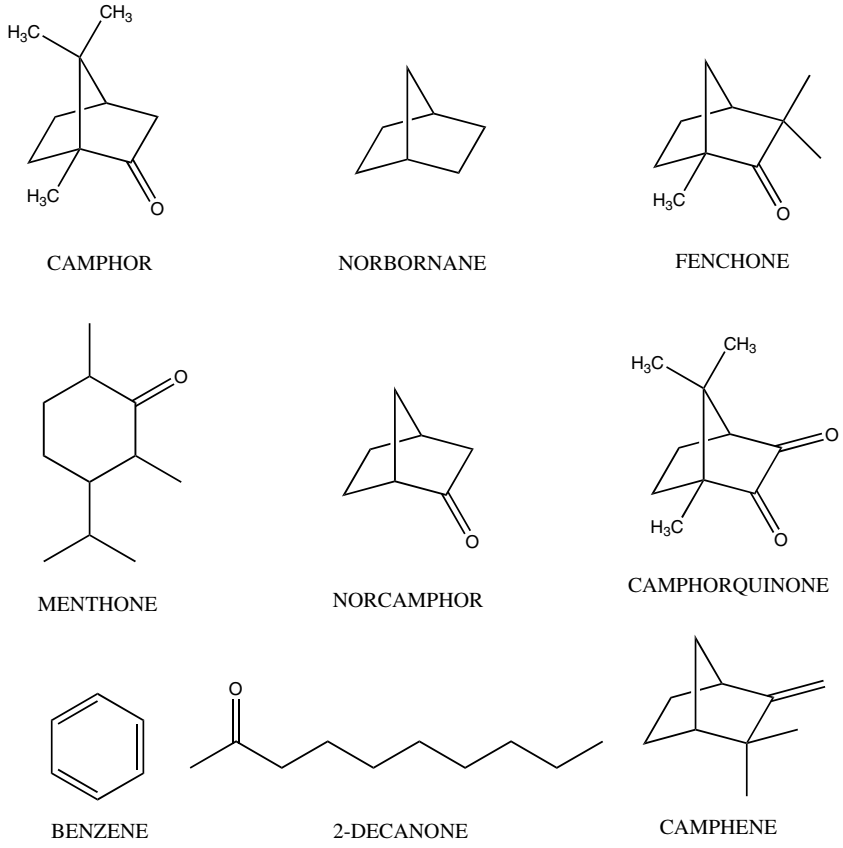

Fig. 5. Molecular structures of the precursors used in the present study.

ing precursors as we see little difference in the I_D/I_G ratios or yields for camphorquinone (which has two O atoms), camphor (single O atom), or for camphene and norbornane (both have no O atoms).

The smaller CNT yields for benzene and methane are most likely due to their greater kinetic stability than the other precursors at higher temperatures. For instance, methane has only C–H bonds to break during decomposition, which require much more energy to break compared to single C–C bonds in the other precursors [17]. Methane gives a product with the lowest I_D/I_G ratio: this can also be rationalized in terms of the stability of methane. Firstly, more methane is likely to pass over without reacting. Secondly, as has been noted before, the high kinetic stability of methane means it will only decompose at the metal nanoparticle and not anywhere where it would form amorphous carbon [18].

In studies where it has been inferred that benzene forms CNTs through the ring addition mechanism, the experiments have been carried out at lower temperatures (~700 °C) and only multi-walled tubes were observed [8,9]. In the present study, due to the similarity of the I_D/I_G ratios for all the precursors, and the relatively high temperature of the CVD conditions optimized for SWNT growth, we suggest that benzene formed CNTs by the *decomposition mechanism* rather than the *ring addition mechanism*. We posit that the formation of SWNTs requires high temperature because they can only form by the decomposition mechanism. Clearly, it would be of interest to vary the temperature of the CVD to see if different mechanisms come into play, and to see if different types of CNTs are formed in different temperature regimes: this remains a goal of our ongoing studies.

It is intriguing to note that we see evidence for differences in the distribution of tube diameters in the different samples; for example, the G band of the benzene sample is much *wider* than that in the methane sample, shown in Fig. 6. The G bands for SWNTs include two main contributions [13]: the highest frequency band is referred to as ω^+, and is best fitted to a Lorentzian function, the other contribution (ω^-) is actually two bands that depend on the electronic properties of the individual tubes from which they arise. The ω^- band for semiconducting tubes, which appears ~50 cm^{-1} below ω^+, is also usually best fitted by a Lorentzian function. The ω^- for metallic tubes, which appears ~80 cm^{-1} below ω^+, can be described best by a Breit–Wigner–Fano function. Fitting the appropriate lineshapes to the G bands shows that the sample from benzene has a much larger contribution from metallic tubes: see Table 3 and Fig. 6.

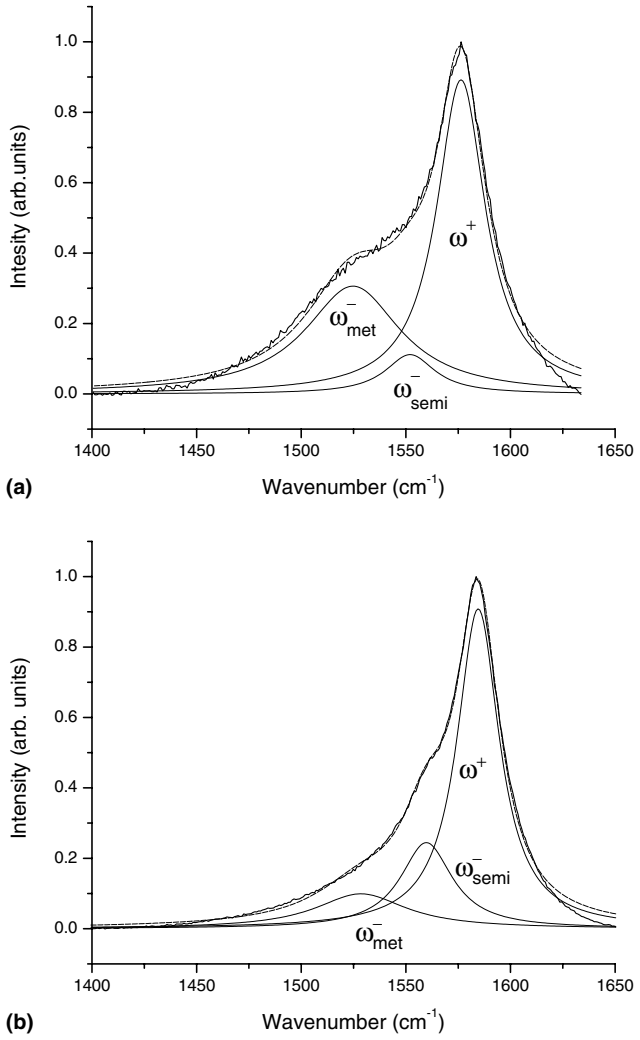

Fig. 6. Raman spectra of samples from (a) benzene, and (b) methane, showing fits of two Lorentzian and one Breit–Wigner–Fano curves to G band region. The larger area of the metallic ω^-_{met} peak in the benzene spectra (~1525 cm^{-1}) suggests the presence of more metallic tubes than the methane sample (see also Table 3).

Table 3
Integrated intensities of ω^-_{met} and ω^-_{semi} for CVD products grown from methane and benzene

Precursor	Area of peaks (normalized to area of ω^+)		
	ω^-_{met}	ω^-_{semi}	$\omega^-_{met}/\omega^-_{semi}$
Methane	0.22	0.33	0.68
Benzene	0.68	0.13	5.22

The results indicate that the precursors produce different distributions of tube diameters, with a larger fraction of metallic tubes grown from benzene.

The ratio of intensities of the RBMs to the G band in the benzene spectrum is greater than that for the methane sample. The frequency of an RBM depends on the diameter of the tube from which arises [13]. The intensity of an RBM in the Raman spectra is not simply proportional to the number of tubes in the sample, but depends also on the wavelength of the laser used and the Raman-scattering cross section (dependent on CNT chirality) [19]. At some excitation wavelengths, some RBMs show a resonance enhancement effect [13], so we note that single walled tubes with diameters other than those suggested by the RBMs are likely to be present. The integrated intensity of a particular RBM compared to the ω^+ of the G band can indicate the presence of tubes in the sample with a diameter corresponding the RBM; for example, we may attribute the RBM at 188 cm^{-1}[19] to a tube with (15,0) structure, which is a metallic zig-zag tube. An increase in the population of this tube would increase the intensities of both the metallic ω^-_{met} contribution of the G band, and the RBM at 188 cm^{-1}. Previously published Raman spectra of samples prepared from methane and benzene (under similar Raman excitation conditions) show differences similar to those observed here [10]. In the previous work, the differences in the benzene and methane spectra were not discussed in terms of a different distribution of metallic and semiconducting tubes; however, it was suggested that samples produced from naphthalene and anthracene would have more metallic tubes as they showed a pronounced splitting of the G band compared with a methane-grown sample. In the results presented here, we find that the CVD product from all the precursors can be qualitatively classified into two distinct groups that have Raman spectra that are either similar to that of methane or to that of benzene: see Fig. 4. We see no obvious way to correlate these groups with the molecular structure or bulk properties of the precursor, however.

Although we conclude that there is no effect of precursor structure on the quality of tubes or growth mechanism, we have found evidence that the structure does influence the distribution of tube diameters. In previous studies, the size of a metal nanoparticle has been directly related to the diameter of a tube that has grown from it [11]. The different precursors in our CVD process could reduce the metal salts of the catalyst to form nanoparticles with different size distributions. The resulting tubes would have correspondingly different distributions of diameters.

To rationalize our findings, we assume that the growth process must be under kinetic control. As discussed previously, the decomposition mechanism of CNT growth depends upon production of atomic carbon that goes on to form the CNTs. For competitive growth of CNTs, the catalytic decomposition of the precursors has to be faster than the gas phase decomposition or decomposition on interior walls of the furnace. The formation of graphitic carbon tubes has been suggested to involve the dissolution and precipitation of carbon through the metal nanoparticle [11]. The rates of precursor decomposition and tube formation are vital to the formation process. The rate of tube formation would

be directly dependent on the concentration of available atomic carbon, which in turn would depend on the passing flux of precursor and the rate of decomposition. If decomposition occurs too fast, for instance, by too much of the precursor arriving at the metal particle surface, then the nanoparticle could become inactive by formation of a layer of carbon around the nanoparticle: such coated particles are often visible in TEM images [11]. We speculate that the kinetics of the catalytic decomposition process is influenced by the structure of the precursor. If the rate of decomposition is slow enough at the beginning of the tube formation, then the forming CNT has enough time to organize itself into a more stable nanotube structure. If the rate of decomposition is high, then the tube starts to grow whether or not the tube has an optimal structure. This view of the tube growth mechanism has the interesting feature that the part of the tube which forms first (the seed, or possibly the end-cap) would control the chirality of the tubes. Further experiments to probe the effect of the flux of different precursors on the Raman spectra are being carried out presently as part of an ongoing study.

4. Conclusions

Several precursors including camphor and related molecules were used as the carbon source in chemical vapor deposition experiments. The conditions for the synthesis were typical of those used to prepare single walled carbon nanotubes (SWNTs). Raman spectra of the products suggest no obvious direct relationship between the structure of the molecule and the quality of the tubes produced, as would be expected if the growth of tubes involved the addition of pre-formed rings. Therefore, we suggest that the formation of SWNTs from camphor does not occur through the addition of precursor rings of carbon. Detailed inspection of the Raman spectra shows that there are differences in the distribution of tube diameters from different precursors. Differences between the distributions have been rationalized in two ways: (1) the metal salts of the catalyst may be reduced to metal particles with different size distributions, depending on the precursor used, and (2) the tube diameter distribution depends on the kinetics of the tube growth, which is dominated by the kinetics of decomposition of the precursor on the catalyst surface.

Acknowledgements

We thank Gavin Forrest and John Findlay (University of Edinburgh) for useful discussions and help with TEM, and Dr. Mukal Kumar (Meijo University) for sending a preprint of his work. Financial support from the EPSRC (studentship for RJA) and The Royal Society (University Research Fellowship for AJA) is gratefully acknowledged.

References

[1] Mukhopadhyay K, Krishna KM, Sharon M. Fullerenes from camphor: a natural source. Phys Rev Lett 1994;72(20):3182–5.
[2] Sharon M, Mukhopadhyay K, Mukhopadhyay I, Krishna KM. Semiconducting mutlichannel-multilayer camphoric tubes. Carbon 1996;33(3):331–3.
[3] Sharon M, Mukhopadhyay K, Yase K, Iijima S, Ando Y, Zhao X. Spongy carbon nanobeads a new material. Carbon 1998; 36(5–6):507–11.
[4] Kumar M, Ando Y. Single-wall and multi-wall carbon nanotubes from camphor–a botanical hydrocarbon. Diam Rel Mater 2003;12(10–11):1845–50.
[5] Kumar M, Ando Y. A simple method of producing aligned carbon nanotubes from an unconventional precursor—camphor. Chem Phys Lett 2003;374(3–4):521–6.
[6] Kumar M, Ando Y. Camphor—a botanical precursor producing garden of carbon nanotubes. Diam Rel Mater 2003;12(3–7): 998–1002.
[7] Kumar M, Ando Y. Controlling the diameter distribution of carbon nanotubes grown from camphor on a zeolite support. Carbon 2005;43(3):533–40.
[8] Tian Y, Hu Z, Yang Y, Wang X, Chen X, Xu H, et al. In situ TA-MS study of the six-membered-ring-based growth of carbon nanotubes with benzene precursor. J Am Chem Soc 2004;126(4):1180–3.
[9] Tian Y, Hu Z, Yang Y, Chen X, Ji W, Chen Y. Thermal analysis–mass spectroscopy coupling as a powerful technique to study the growth of carbon nanotubes from benzene. Chem Phys Lett 2004;388(4–6):259–62.
[10] Li Q, Yan H, Zhang J, Liu J. Effect of hydrocarbons precursors on the formation of carbon nanotubes in chemical vapor deposition. Carbon 2004;42(4):829–35.
[11] Moisala A, Nasibulin AG, Kauppinen EI. The role of metal nanoparticles in the catalytic production of single-walled carbon nanotubes—a review. J Phys: Condens Matter 2003;15(42): s3011–35.
[12] Cassell AM, Raymakers JA, Kong J, Dai H. Large scale CVD synthesis of single-walled carbon nanotubes. J Phys Chem B 1999;103(31):6484–92.
[13] Dresselhaus MS, Dresselhaus G, Jorio A, Souza Filho AG, Saito R. Raman spectroscopy on isolated single wall carbon nanotubes. Carbon 2002;40(12):2043–61.
[14] Qian W, Liu T, Wei F, Yuan H. Quantitative Raman characterization of the mixed samples of the single and multi-wall carbon nanotubes. Carbon 2003;41(9):1851–64.
[15] Sato T, Murata K, Nishimura A, Tsuchiya T, Wasada N. Pyrolysis of organic compounds—II : The flash pyrolysis of camphor and its related compounds. Tetrahedron 1967;23:1791–8.
[16] Maruyama S, Kojima R, Miyauchi Y, Chiashi S, Kohno M. Low temperature synthesis of high-purity single-walled carbon nanotubes from alcohol. Chem Phys Lett 2002;360(3,4):229–34.
[17] Bond strengths in polyatomic molecules. In: Linde DR, editor. Handbook of chemistry and physics. Boca Raton: CRC Press; 1993. p. 9-136–41.
[18] Kong J, Cassell AM, Dai H. Chemical vapor deposition of methane for single-walled carbon nanotubes. Chem Phys Lett 1998;292(4–6):567–74.
[19] Machon M, Reich S, Telg H, Maultzsch J, Ordejon P, Thomsen C. Strength of radial breathing mode in single-walled carbon nanotubes. Phys Rev B 2005;71:035416-1–4.